Characterization and Modification of Electrospun Fiber Mats for Use in Composite Proton Exchange Membranes

by
Matthew Marchand Mannarino

Bachelor of Science in Plastics Engineering, University of Massachusetts Lowell (2007)
Master of Science in Plastics Engineering, University of Massachusetts Lowell (2008)

SUBMITTED TO THE DEPARTMENT OF MATERIALS SCIENCE AND ENGINEERING
IN PARTIAL FULFILLMENT OF THE REQUIREMENTS FOR THE DEGREE OF

DOCTOR OF PHILOSOPHY IN MATERIALS SCIENCE AND ENGINEERING

AT THE

MASSACHUSETTS INSTITUTE OF TECHNOLOGY
(JUNE 2013)

Signature of Author: _____
Matthew M. Mannarino
Department of Materials Science and Engineering
Program in Polymer Science & Technology
May 15, 2013

Certified by: _____
Gregory C. Rutledge
Lammot du Pont Professor of Chemical Engineering
Thesis Supervisor

Certified by: _____
Yang Shao-Horn
Gail E. Kendall Chair of Mechanical Engineering
Associate Professor of Materials Science and Engineering
Thesis Supervisor

Accepted by: _____
Gerbrand Ceder
R.P. Simmons Professor of Materials Science and Engineering
Chair, Departmental Committee on Graduate Students

Characterization and Modification of Electrospun Fiber Mats for Use in Composite Proton Exchange Membranes

by

Matthew Marchand Mannarino

Submitted to the Department of Materials Science and Engineering on May 15, 2013
in partial fulfillment of the requirements for the degree of Doctor of Philosophy in Materials Science and Engineering

Abstract

Electrostatic fiber formation, or electrospinning, offers a particularly simple and robust method to create polymeric nanofibers of various sizes and morphologies. In electrospinning, a viscoelastic fluid is charged so that a liquid jet is ejected from the surface of the fluid (typically in the form of a drop supplied by a needle or spinneret) and collected on a grounded plate, creating a nonwoven fiber mat. Modification of the diameter of the fibers as well as the porosity, specific surface area, and mechanical properties of the mat allows one to tailor electrospun mats for specific applications. Despite the widespread and rapidly growing use of electrospinning in the fabrication of novel nanomaterials, there are no simple, universal methods of predicting, a priori, the properties of electrospun fibers from knowledge of the polymer solution properties and electrospinning operating conditions alone. Changing a single fluid or processing parameter can affect the jet and fiber formation through several mechanisms. For example, using a different solvent can change several properties of the electrospinning fluid, such as the dielectric constant, conductivity, surface tension, and solute-solvent interaction. The work in this thesis seeks to develop a simple relation for predicting terminal jet diameter during electrospinning, which accounts for solution viscoelasticity as well as solution conductivity and operating parameters that can be easily measured and controlled.

The mechanical and tribological properties of electrospun fiber mats are of paramount importance to their utility as components in a variety of applications. Although some mechanical properties of these mats have been investigated previously, reports of their tribological properties are essentially nonexistent. In this thesis, electrospun nanofiber mats of poly(trimethyl hexamethylene terephthalamide) (PA 6(3)T) and poly(hexamethylene adipamide) (PA 6,6) are characterized mechanically and tribologically. Post-spin thermal annealing was used to modify the fiber morphology, inter-fiber welding, and crystallinity within the fibers. Morphological changes, in-plane tensile response, friction coefficient, and wear rate were characterized as functions of the annealing temperature. The Young's moduli, yield stresses and toughnesses of the PA 6(3)T nonwoven mats improved by two- to ten-fold when annealed slightly above the glass transition temperature, but at the expense of mat porosity. The mechanical and tribological properties of the thermally annealed PA 6,6 fiber mats exhibited significant improvements through the Brill transition temperature, comparable to the improvements observed for amorphous PA 6(3)T electrospun mats annealed near the glass transition temperature. The wear rates for both polymer systems correlate with the yield properties of the mat, in accordance with a modified Ratner-Lancaster model. The variation in mechanical and tribological properties of

the mats with increasing annealing temperature is consistent with the formation of fiber-to-fiber junctions and a mechanism of abrasive wear that involves the breakage of these junctions between fibers.

A mechanically robust proton exchange membrane with high ionic conductivity and selectivity is an important component in many electrochemical energy devices such as fuel cells, batteries, and photovoltaics. The ability to control and improve independently the mechanical response, ionic conductivity, and selectivity properties of a membrane is highly desirable in the development of next generation electrochemical devices. In this thesis, the use of layer-by-layer (LbL) assembly of polyelectrolytes is used to generate three different polymer film morphologies on highly porous electrospun fiber mats: webbed, conformal coating, and pore-bridging films. Specifically, depending on whether a vacuum is applied to the backside of the mat or not, the spray-LbL assembly either fills the voids of the mat with the proton conducting material or forms a continuous fuel-blocking film. The LbL component consists of a proton-conducting, methanol-impermeable poly(diallyl dimethyl ammonium chloride)/sulfonated poly(2,6-dimethyl 1,4-phenylene oxide) (PDAC/sPPO) thin film. The electrospun fiber component consists of PA 6(3)T fibers of average diameter between 400 and 800 nm, in a nonwoven matrix of 60-90% porosity depending on the temperature of thermal annealing utilized to improve the mechanical properties. This thesis demonstrates the versatility and flexibility of this fabrication technique, since any ion conducting LbL system may be sprayed onto any electrospun fiber mat, allowing for independent control of functionality and mechanical properties. The mechanical properties of the spray coated electrospun mats are shown to be superior to the LbL-only system, and possess intrinsically greater dimensional stability and lower mechanical hysteresis than Nafion under hydration cycling. The electrochemical selectivity of the composite LbL-electrospun membrane is found to be superior to Nafion, which makes them a viable alternative proton exchange membrane for fuel cell applications. The composite proton exchange membranes fabricated in this work were tested in an operational direct methanol fuel cell, with results showing the capability for higher open circuit voltages (OCV) and comparable cell resistances when compared to Nafion.

Thesis Supervisor: Gregory C. Rutledge
Lammot du Pont Professor of Chemical Engineering

Thesis Supervisor: Yang Shao-Horn
Gail E. Kendall Chair of Mechanical Engineering,
Associate Professor of Materials Science and Engineering

Acknowledgments

In the final scene of Frank Capra's 1946 classic, *It's a Wonderful Life*, George Bailey opens up a copy of *Tom Sawyer* left for him by his guardian angel, Clarence, and inside the front cover it reads: "Dear George- Remember no man is a failure who has friends. Thanks for the wings! Love, Clarence." Never in my life have these words been truer than over my past five years at MIT. This work and thesis would never have come to fruition if it were not for the help and support of all of my friends and family.

I would first like to thank my thesis advisor, Professor Gregory Rutledge, for always pushing me to delve further into a problem and to explore every other possible explanation for a given result before reaching a definitive conclusion. Each member of my thesis committee has been extremely helpful during my time at MIT: Prof. Yang Shao-Horn served as my DMSE co-advisor, without whom I could not have performed my work under a Chemical Engineering professor; Prof. Paula Hammond served as an "honorary co-advisor" in that I worked very closely with her students and often in her lab, in truth, I sometimes felt as much a member of the Hammond group as the Rutledge group depending on how much time I spent in each lab during a given week; and Prof. Alfredo Alexander-Katz, whom was very helpful and welcoming when experimental failures became too overwhelming, I often sought refuge with his students in the basement of Building 12. David Liu, with whom most of the fuel cell portion of this work was done in conjunction with, deserves a significant amount of thanks for all his help in fabrication, testing, and analysis of the composite membranes. Several other collaborators provided significant contributions to this work, including: Prof. Mary Boyce, Dr. Nathan Ashcraft, Dr. Avni Argun, Dr. Meredith Silberstein, and Jonathan Harding. The members of the Rutledge group have also been a significant source of help over the years, and I would like to thank all of them for the assistance over the years, especially: Dr. Joseph Lowery, Dr. Liang Chen, Dr. Ying Yang, and Dr. Chia-Ling Pai for teaching me how to electrospin, Dr. P.K. Bhattacharjee, Dr. Jung Ah Lee, and Dr. Keith Forward for useful discussions and insight, Dr. Jason Lee, Dr. Peng Yi, Simon Choong, Yuxi Zhang, Reika Katsumata and Salvador Aznar for assistance and discussions on various experiments. The Program in Polymer Science & Technology (PPST) proved to be an excellent option for me to pursue my graduate school education and I would like to thank Prof. Robert E. Cohen, Prof. Gareth McKinley, Prof. Darrell Irvine, Gregory Sands, Dr. Charles Sing, Dr. Jane Wang, Dr. Ben Wang, Dr. Wuisiew Tan, Adam Zeiger, Alex Scott, Yin Fan, Charlotte Stewart-Sloan, Eun Seon Cho, Derek Smith, Eric Arndt, Jisam Wong, Michelle Sing, Lionel Moh, Samantha Collins, and all the 2012-2013 First Years for the their friendship and support. I would also like to acknowledge the MIT Institute for Soldier Nanotechnology (ISN) and the Center for Materials Science & Engineering (CMSE) for use of facilities and specifically William DiNatale and Tim McClure for assistance on equipment use.

I am certain that I would never have even been accepted to MIT if it were not for the excellent education I received at the University of Massachusetts Lowell. I would most like to thank the Plastics Engineering Department and specifically Professor Stephen Burke Driscoll for all his help serving as the greatest mentor a college student could ask for and one of the best colleagues anyone could hope to have. I would also like to thank my roommates from Lowell, Brendan Zarechian, Pat Taylor, Michael Sutherland, and Matt MacDonald for putting up with me for 4-5 years when I was studying constantly to get into graduate school and serving as some strong academic support in college. I would also like to thank my bosses and co-workers from the engineering jobs and internships I had during my five years at UML, from Nova Biomedical:

Dan Oullette, Ron Venooker, Matthew MacDonald, and David Yeo, from the U.S. Army Natick Soldier Center: Dr. JoAnn Ratto, Dr. Christopher Thellen, Sarah Schirmer, Danielle Froio, and Dr. Jeanne Lucciarini and from the Charles Stark Draper Laboratory: John LeBlanc, Dave Hagerstrom, Jason Haley, Dr. Livia Racz, Mike Rickley, Rick Pastena, and Alex Orsi.

Outside of academia, there are numerous other people that helped to contribute to this work by giving me their friendship and support. I would like to thank my best friend from middle school through college, Edward Settle for all the support he gave me throughout adolescence and truly helping me to break out of my shell. I would like to thank Ugochukwu Ewulonu who was my best friend for much of the past ten years, we shared so many hopes and dreams together, and I wish nothing but the best for him. All of my friends that I have played ultimate frisbee with (competitively or for fun), I found the stress from school that was relieved during ultimate was always cathartic, so thank you to: James Pitts, Matthew Anderson, Jeff Lee, Andrey Ostapchenko, Tom Burkley, David Isman, Vadim Frishman, Viet Ngyuen, Dana Grandoni, Scott Walfield, and all the members of the NNHS, UML, and Newton Sunday Ultimate teams. I also want to thank the regular trivia crew, with whom we have amassed more than 50 wins (to my count) over 5 years at Flann O'briens: King Chuck, Chairman Brad, Flo, Ashley Marcotte, Dave Goldstein, Rotem Rabinovich, and Justin LaBreque. Lastly, I want to thank all of the friends I have made over the years that I did not have enough room in these two pages to detail their impact: Yusheng Yang, BDP, Matt Alie, Tom Tierney, Annie Hartnett, Marika Plater, Jon Qi, Nate Pangburn, Matthew St. Marie, Eugene Rueben, Ryan Johnson, Salvador LoGrasso, Brian Paliwoda, Hassan Sleiman, Eric Webb, Jennifer Grady, Cheri Lynn, David Lai, Rachel Julien, Dorothy Louisos, the Boldogs, Reid Van Lehn, Joe McCarthy, JT, and BAZ's Brew House.

There are so many important members of my family that I would like to acknowledge for their time and commitment to my success. Thank you to my grandmothers Ann Marchand (Todero) and Josephine Mannarino (Grella) for always being there for me and always willing to give me that extra compliment, hug, or cookie when it was needed most. Thank you to my grandfathers, Arthur (Mike) and Dominic, neither of whom I got the chance to meet, for serving our country in WWII and for working hard to make lives better for your children and raising my wonderful parents. Thank you to all my aunts, uncles and cousins for their love and support over the years: Arthur, Cindy, Elizabeth, Oden, Vanessa, Adam, Sarah, Donna, Jim, Kate, Kerry, Carolyn, Carol, Patrick, Johnathan, Stephanie, Ted, Mickey, Samantha, JoAnn, Ray, JoAnn Marie, Tom, Deb, Jessica, and Marcy. I would also like to thank all of my fiancé's family for welcoming me and helping me through some of the most stressful years in my life: Bud, Deb, Erin, Joe, Phil, Larry, Jean, Jack, Cheryl, Ed, Carolyn, Jeremy, Cathy, Cliff, Nicole, Billy, Heather, Jimmy, Dan, Chaz, Linda, Andy, Colleen, Jeannie, Wayne, Wayne Paul, Stephanie, Terry, Bob, Meg, Ray, Marissa, Billy, and Larry.

I would like to thank most of all, my parents Joan Marchand and Alan Mannarino. Without their unconditional love, encouragement, and constant support whenever I was going through tough times, this work certainly would never have been completed. I would also like to thank my sister Alana for her great friendship and love for most of my life and all of hers. Lastly, I want to thank my fiancé, Kelly Keegan, whom has been the most important person in my life for the past four and a half years, and will continue to be for the rest of our lives together. To everyone that has helped me achieve in life, you have my thanks and my love.

-Matthew M. Mannarino
May 2013

Table of Contents

List of Figures

List of Tables

In the beginning, the Universe was created.
This has made a lot of people very angry and has been widely regarded as a bad move.

-Douglas Adams

1. Introduction

1.1 Motivation

There is an ever-increasing need for clean and sustainable energy worldwide for stationary power generation, distributed power in buildings, and lightweight portable power for transportation and portable electronics applications. As of 2002, nearly 85% of the developed world's energy was provided by fossil fuels (mostly petroleum, natural gas and coal) [1]. The combustion of fossil fuels produces significant amounts of greenhouse gases that need to be mitigated in order to prevent adverse climate effects from occurring. While there is no single solution to the greenhouse gas problem, CO_2 emissions can be reduced by improving combustion efficiencies, carbon sequestration, or switching to alternative fuels and/or energy sources. Alternative energy sources such as solar, wind, geothermal, and hydropower may be able to provide more sustainable energy on a large scale to buildings and houses, but there is no clear alternative to portable energy applications that currently rely on gasoline-powered internal combustion engines (ICE) as indicated by the Ragone Plot [2] in Figure 1-1. Capacitors typically exhibit very high specific power, but a low specific energy while fuel cells and batteries can possess exceptional specific energies, but relatively low specific power as compared to ICEs. Gasoline is a very energy dense fuel, but can only convert up to ~30% of its energy to useful energy (limited by Carnot efficiency), while a significant amount of heat and CO_2 are released to the atmosphere.

Fuel cells offer an efficient, clean, and safe energy conversion technology that can be part of a strategy to reduce the dependence on limited resources, and enhance energy security in the United States as well as developing countries. Fuels cells provide one of the most promising alternative energy solutions because they convert chemical energy directly into electrical energy; therefore, fuel cell efficiencies can exceed the Carnot Cycle limit even when operating at relatively low temperatures (~80°C) [3]. Although fuel cells can be utilized for a range of potential power requirements, the development of small, low-temperature, portable fuel cells is of high importance. Applications for such fuel cells include commercial products such as laptops

and cell phones as well as military use for portable soldier power or other non-conventional small geometry power products. Direct methanol fuel cells (DMFCs) are one of the most promising types of proton exchange membrane fuel cells, exhibiting higher utilization efficiencies and intrinsically lower polluting emissions as compared to internal combustion engines [4]. Methanol is a cheap and easily distributed fuel that can be quickly incorporated into the present infrastructure for liquid fuels. Despite the practical system advantages, DMFCs typically exhibit lower power density and efficiency than hydrogen fuel cells due to the slow oxidation kinetics of methanol and the difficulty in preventing methanol crossover from the anode to the cathode [5].

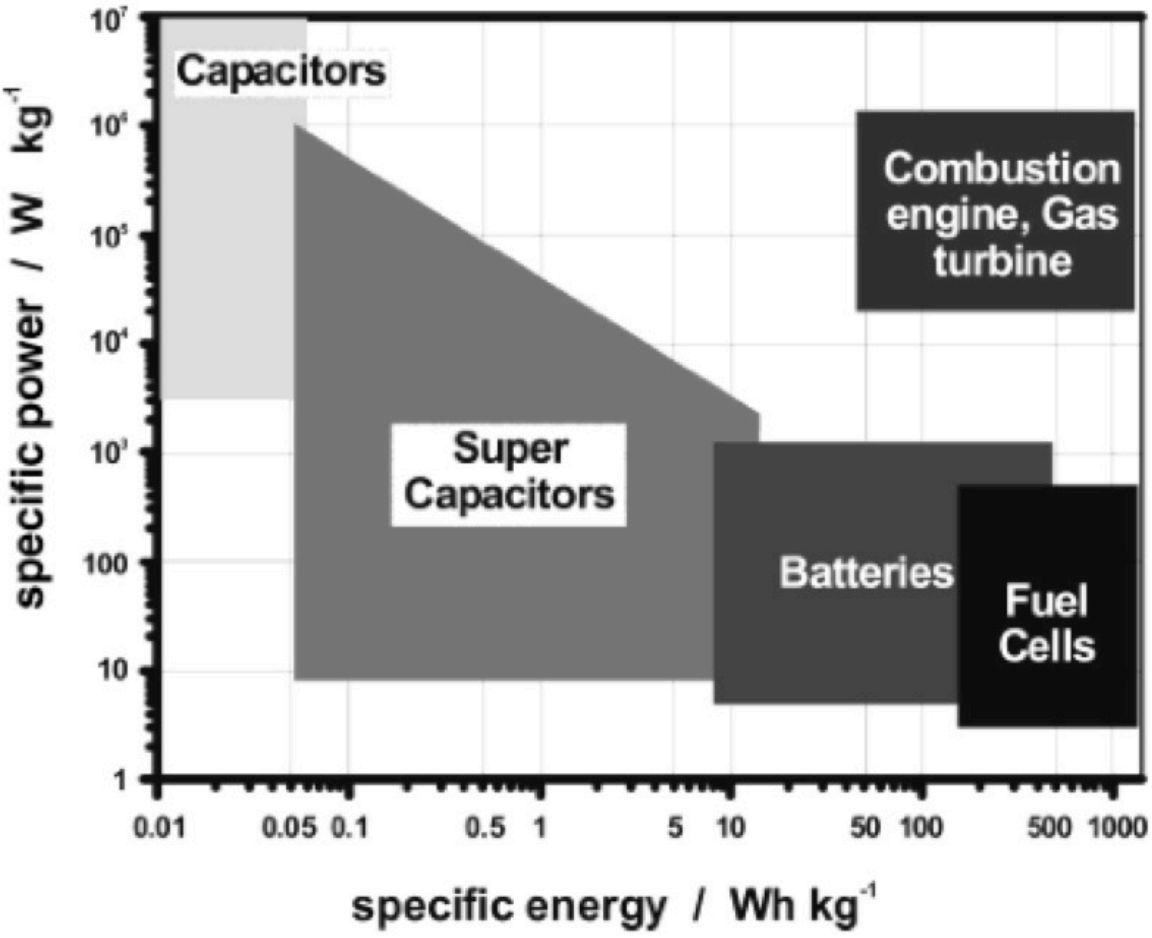

Figure 1-1. Ragone plot of energy storage, fuel cells offer high specific energy, however low specific power as compared to batteries and capacitors [2].

At the core of any fuel cell is an electrolyte that is used to facilitate charge transport between electrodes. Several different types of electrolytes have been used in current fuel cell technologies, including alkaline (AFC), phosphoric acid (PAFC), molten carbonate (MCFC),

solid oxide (SOFC), and polymer electrolyte membrane (PEMFC) fuel cells. PEMFCs are the preferred alternative for stationary power generation, lightweight portable power for transport, and portable electronics applications. Properly engineered, they can be used as reversible electrolysis-power generation units coupled with solar energy to generate hydrogen for carbon-free energy storage. The current state-of-the-art PEMs are DuPont's Nafion family of perfluorosulfonic acid membranes, which have existed for nearly 50 years; however, Nafion has several major drawbacks which prevent their widespread use for DMFCs: (i) high cost of production and processing, (ii) high methanol permeability, and (iii) Poor durability due to hydration cycling fatigue. The development of a novel material for use as the PEM, which does not possess the same disadvantages as Nafion, could make DMFCs a strong candidate for alternative energy devices in the United States and around the world.

This thesis work utilizes an integrated multi-scale materials design and processing approach for the development of a superior proton exchange membrane. Two relatively new processing capabilities, electrospinning of nonwoven nanofibrous mats and layer-by-layer assembly of polyelectrolyte based membranes, are further developed and combined to generate nanoscale assemblies of polymers via the control of thin film architectures on the 1 to 100 nanometer length scale. Decoupling of the mechanical properties and assembly surface area (electrospun fiber matrix) from the transport properties (layer-by-layer assembled polyelectrolytes) facilitates the ability to control the final composite membrane properties independently. Development and design of these systems are closely coupled with morphological, mechanical, and electrochemical characterization of these unique nanoscale layered membranes to finely tune their properties for optimized fuel cell performance. In looking to the future, to when fuel cells would be commercialized and mass-produced, the mechanical properties, durability and life cycle of the proton exchange membrane would become increasingly important. In such a case, the composite membrane consisting of a mechanically robust nanofiber endoskeleton stands a much better chance of withstanding fuel cell cycling (and thus increasing its life-span) at increasingly thin conditions (<30 μm) than any homogeneous polymer or polymer blend that is swollen from water and plasticized to increase conductivity. The separation of the conductive element from the structural element is thus most likely the only way to achieve truly long membrane life spans.

1.2 Background

1.2.1 Fuel Cells

Sir William Grove constructed the first fuel cell (which he called the gas voltaic battery); the device produced electrical energy by combining hydrogen and oxygen, and was the result of reversing the direction of the electrolysis reaction of water. He showed that steam could be disassociated into oxygen and hydrogen, and by reversing the process, he was able to demonstrate the thermal dissociation of molecules into their constituent atoms. Fuel cells did not receive significant attention at the time due to the advent of cheap fossil fuels and steam engines for power generation. It was not until over a century later, when in the 1960's, the National Aeronautics and Space Administration (NASA) began using fuel cells to power systems on spacecrafts that they garnered significant commercial and academic interest [3]. Fuel cells are an attractive alternative power system because they offer an efficient, clean, and safe energy conversion technology that can be part of an environmentally friendly strategy to produce power from renewable resources and reduce dependence on limited resources. They also offer the advantage of minimal maintenance due to the fact that there are no moving parts in the power generating stacks of the fuel cell system.

Methanol fuel cells utilize liquid or gaseous methanol as the fuel supplied to the anode, which is attractive for portable applications. The methanol fuel can be reformed to hydrogen before being supplied to the fuel cell as in reformed methanol fuel cells (RMFC) or supplied directly as a methanol water mixture in DMFCs. Direct methanol fuel cells can convert methanol directly to carbon dioxide, water, and electricity at ambient conditions. They are considered strong candidates to replace Li-ion batteries in many portable devices, especially for applications where recharging would be difficult such as out in the wilderness or in a battlefield. A DMFC only consists of a few components: a flow controller, electrodes, catalyst layer, and a proton exchange membrane (See Figure 1-2). Methanol is directly oxidized to carbon dioxide, although the formation of other compounds such as formaldehyde, formic acid, carbon monoxide or other organic molecules is possible. The formation of these molecules during operation can poison the electrodes and decrease the overall fuel cell performance. A scheme for the half cell reactions is shown in Figure 1-2, leading to the overall reaction occurring in a DMFC, outlined as:

$$CH_3OH + 3/2\ O_2 \rightarrow CO_2 + 2H_2O \qquad \text{(Equation 1-1)}$$

The thermodynamic efficiency of the process is given by the ratio between the Gibbs free energy (maximum value for the electrical work, $\Delta G°$) and the total available energy of the process (the standard enthalpy of the reaction, $\Delta H°$):

$$\eta_{rev} = \Delta G° / \Delta H° \quad \text{(Equation 1-2)}$$

with

$$\Delta G° = \Delta H° - (T \times \Delta S°) \quad \text{(Equation 1-3)}$$

and

$$\Delta G° = -nF \times \Delta E_{rev} \quad \text{(Equation 1-4)}$$

Where T is the temperature of the reaction, $\Delta S°$ is the standard entropy of the reaction, n is the number of electrons that balance the half-cell reactions, F is Faraday's constant, and ΔE_{rev} is the reversible cell voltage, which is determined by the half reactions at the anode and cathode. Fuel cells exhibit high thermodynamic efficiencies, especially at low temperatures; however, these efficiencies are typically never achieved due to internal resistance losses, interfacial losses between the PEM and electrodes, overpotentials, mass transport limitations, and fuel crossover [6]. At 25 °C and 1 atm, with pure oxygen feed, the reversible potential for methanol oxidation is 1.18 V, which does not vary significantly over the operating range of 20-130 °C [5].

Even though methanol is roughly four times the energy density of Lithium ions, the effective energy density (energy obtained per total device volume) can be almost an order of magnitude greater than Li-ion rechargeable batteries. Additionally, rechargeable batteries must never be fully discharged to preserve cycle longevity, require time to recharge between power cycles, and typically loses charge capacity over time, lowering its effective energy density further. Taking into account the cycle constraints and the total device volume as well as energy storage losses over time, rechargeable batteries can only achieve ~30-40% efficiencies, while fuel cells can achieve up to 70% efficiencies [2]. First generation commercial fuel cells have also been found to last over six times as long as current Li-ion rechargeable batteries of similar size and weight. DMFCs also produce very little non-recyclable waste as compared to Li-ion batteries, and future advances in fuel cell technology could greatly improve the performance and recyclability of these devices.

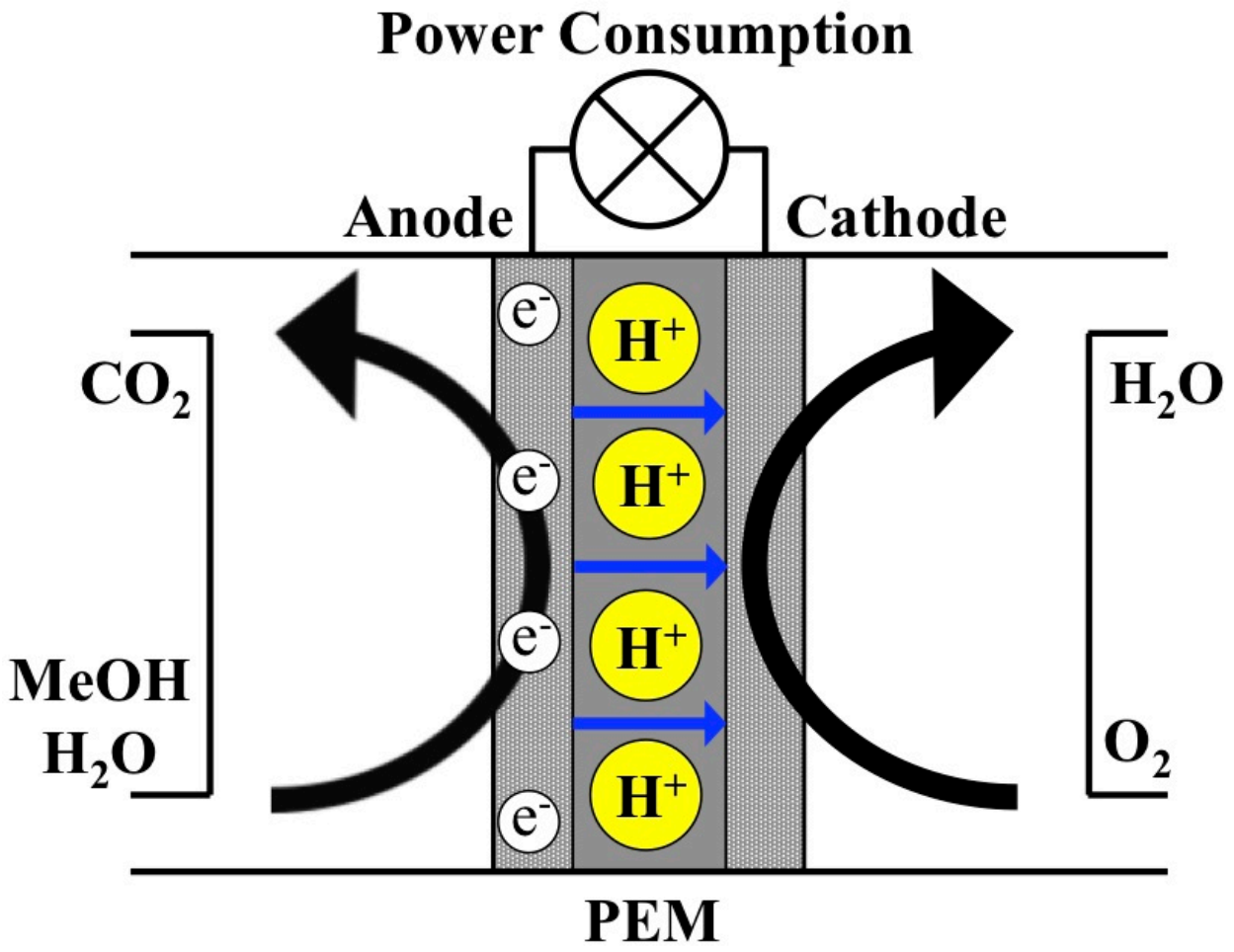

Anode: $CH_3OH + H_2O \rightarrow CO_2 + 6H^+ + 6e^-$

Cathode: $3/2O_2 + 6H^+ + 6e^- \rightarrow 3H_2O$

Figure 1-2. Schematic and half-cell reactions of a Direct Methanol Fuel Cell. The Membrane Electrode Assembly is composed of the PEM, anode, and cathode. Methanol is oxidized at the anode and protons are transported through the PEM to the cathode, while electrons travel through an external circuit to generate power.

The cost, performance, and lifetime of a fuel cell are primarily governed by the membrane electrode assembly (MEA), where electrochemical oxidation of the methanol and reduction of oxygen molecules occurs. The MEA consists of a proton conducting, electrically insulating polymeric membrane sandwiched between two electrically conductive electrode layers

with supported electrocatalysts (typically Pt, Pt-Ru, or Au). The catalyst layer for a DMFC requires a high loading of platinum and platinum-ruthenium to stabilize the electrochemical reaction and prevent the production of carbon monoxide that would reduce the efficiency of the reaction. The proton exchange membrane must be both high in proton conductivity and low in methanol permeability to prevent methanol from crossing over to the other side and reacting with the catalyst. Polymer electrolyte membranes offer higher mechanical strength, lower operating temperatures, and greater fabrication flexibility as compared to conventional liquid or gel electrolytes; however, PEMFCs often require high loadings of expensive metal catalysts and possess a high sensitivity to fuel impurities. The current PEMFC technology is highly restricted by temperature and humidity constraints, since the mechanical and chemical degradation of the polyelectrolyte membranes are both very sensitive to these parameters.

Fuel cell performance is commonly analyzed by inspection of voltage-current (V-I) polarization curves. A representative polarization curve for a DMFC is shown in Figure 1-3. The cell voltage and current density (current normalized by the active area of the MEA) are used to evaluate the performances of various PEMs. Several key features of the polarization curve are important for evaluating MEAs:

1) Open Circuit Voltage (OCV): the cell potential when no current is drawn through the fuel cell. The operational OCV is lower than the theoretical electromotive force (EMF) due to fuel crossover, contact resistances, and irreversibilities.
2) Activation Losses: a sharp drop in the operation voltage at low current densities is attributed to slow electrode or catalyst activation kinetics.
3) Resistance or Ohmic Losses: a linear decrease in the operating voltage with increasing current being drawn is seen after the activation losses; this is attributed to the resistance of ion transport through the PEM.
4) Gas Transport Losses: a sharp drop in operating voltage, which is seen at high current densities, occurs due to transport limitations at the electrodes being too low.

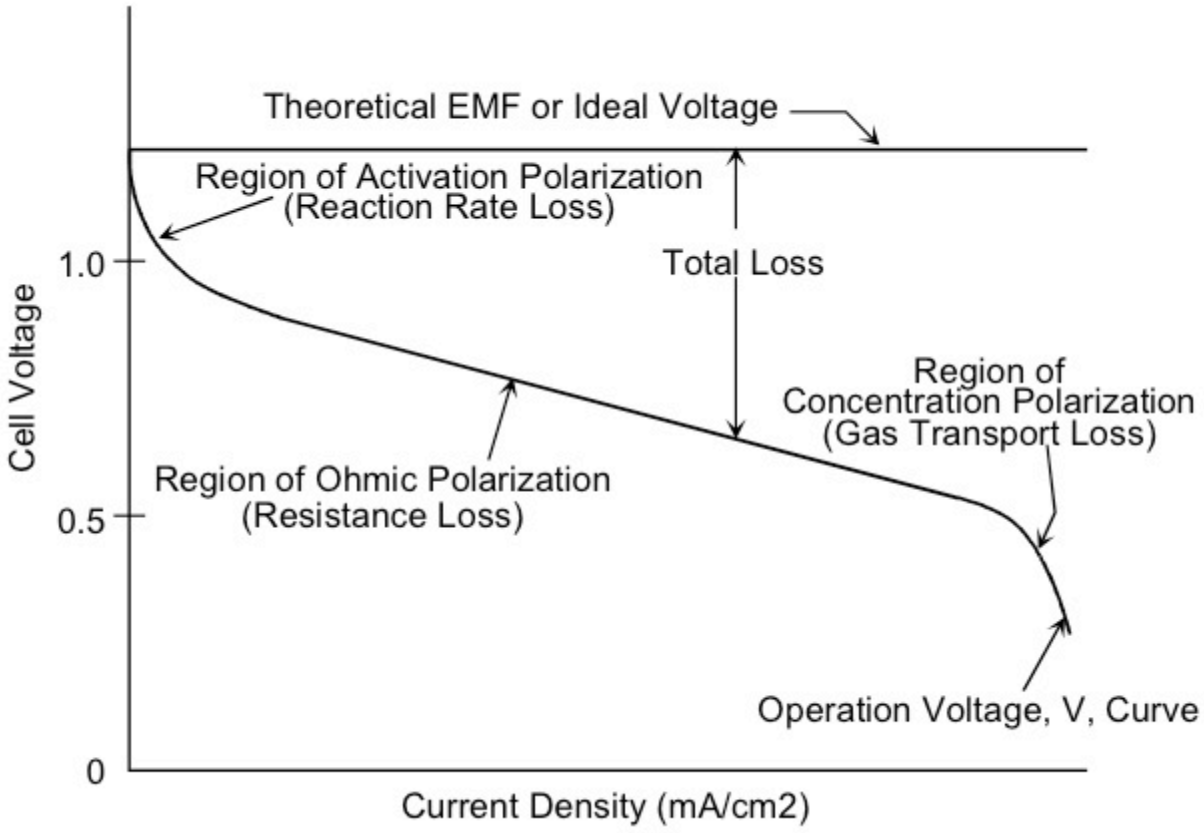

Figure 1-3. Representative fuel cell voltage-current polarization curve with theoretical electromotive force (EMF) plotted as well. The important features of the polarization curve are labeled: OCV, activation losses, resistance losses, gas transport losses, and operation voltage [7].

1.2.2 Proton Exchange Membranes

The efficiency of DMFCs is primarily constrained by protons being trapped on the catalyst and prevented from being transported into or out of the PEM fast enough as a result of a poor connection between the smoother PEM and rough catalyst layer. The cost of the fuel cell is thus a function of the amount of catalyst loading needed, the effectiveness of the binder, the membrane conductivity, and the methanol permeability of the PEM. Improvements to the catalyst, binder, or PEM would reduce the price of DMFCs and help to make them a more commercially practical alternative energy source. The research conducted for this thesis focuses on the development of a novel composite fuel cell membrane that exhibits high proton conductivity and low methanol permeability while exhibiting greater mechanical stability and at a lower production cost than current PEM materials.

Polymer electrolyte membranes generally take the form of thin films that facilitate the transport of ions at specified operating conditions. The development of new polymers for PEMs

have been a significant area of research for DMFCs in order to decrease fuel crossover, increase proton conductivity, and improve water management. The ideal PEM for use in a DMFC would possess the following properties: (1) complete inhibition of unreacted fuel diffusing through the PEM and crossing over to the counter electrode (fuel crossover), (2) high proton conductivity and low electron conductivity, (3) long-term stability in fuel cell environment (subject to fluctuations in temperature, humidity, mechanical stress, electrical load), (4) ability to operate at ambient conditions, and (5) low materials and processing costs. For the past several decades, the primary materials utilized for low temperature fuel cell membranes have been perfluorosulfonated ionomers, specifically DuPont's Nafion, which exhibits high ionic conductivity when fully hydrated as well as mechanical, chemical, and thermal stability [8]. For most state-of-the-art PEMs, is has been observed that as the proton conductivity is increased, larger transport channels are opened that can also increase the amount of fuel crossover as illustrated in Figure 1-4; typically, membranes with the highest conductivities also exhibit the highest crossover [9]. A measure of the transport efficiency of these PEMs is the electrochemical selectivity defined as the ratio of proton conductivity to the methanol permeability.

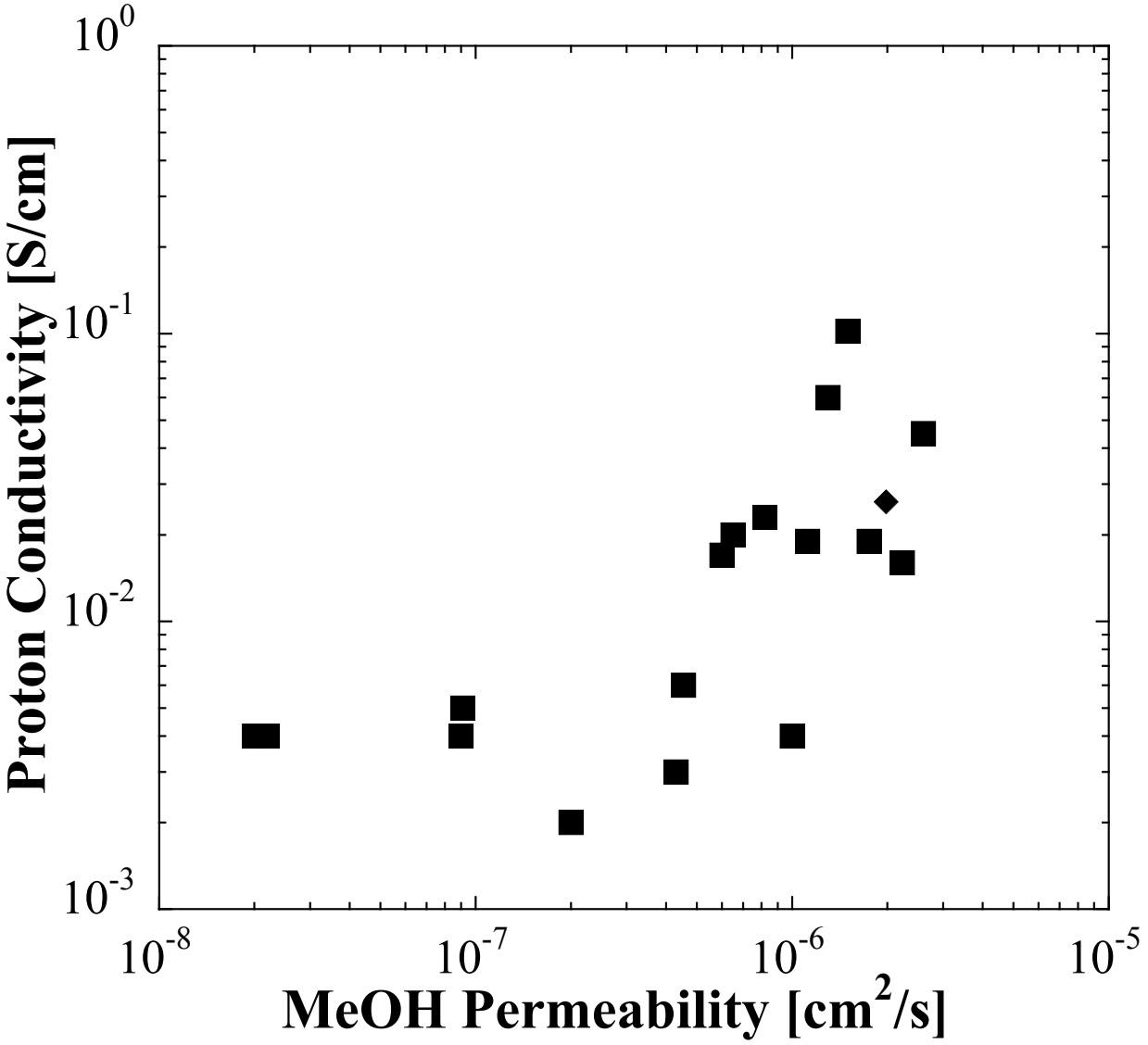

Figure 1-4. Proton conductivity vs. methanol permeability of various PEMs. For most potential PEMs, an increase in proton conductivity also increases the amount of methanol crossover, which can lower fuel cell performance (Data adapted from reference [9]).

1.2.2.1 Nafion

The current benchmark material and "gold standard" for PEMs is DuPont's perfluorinated polymer, Nafion, whose general chemical structure is shown in Figure 1-5. Proton conductivities for Nafion are on the order of 0.1 S/cm when fully hydrated, which is the target value for replacement membranes [6]. This proton conductivity is highly sensitive to the water content of the membrane and the membrane microstructure, which consists of hydrophilic and hydrophobic domains on the nanometer length scale. Microphase separation of Nafion yields

sulfonic acid “channels”, which allow protons to easily travel through the membrane [10]. New insights into the microstructure of Nafion membranes have shown that: 1) The Nafion membranes possess an intrinsic fibrillar structure with cylindrical aggregates screened by ionic charges. 2) These aggregates have a sub-micrometer coherent length. 3) Water uptake in the Nafion membranes is not confined in spherical cavities but rather among fibrillar objects and at high hydration levels, becomes one continuous medium [11,12,13].

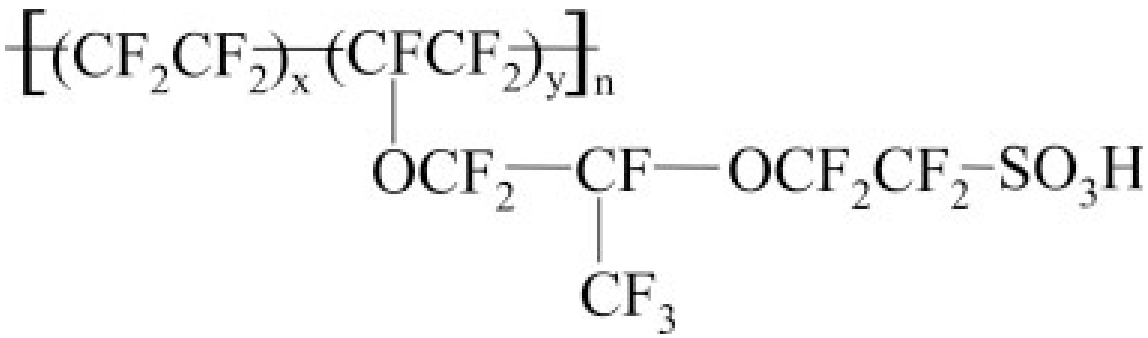

Figure 1-5. Chemical structure of Nafion (x~5-13.5, y~1000). The sulfonic acid groups form nanoscale channels for rapid ion transport, while the perfluorinated backbone and side chains give strong chemical and mechanical stability.

Several models for the structure of Nafion have been proposed to explain the transport mechanism of these membranes and how they change with degree of hydration. One of the earliest structure models proposed was the Cluster-Network Model, consisting of sulfonate ion clusters (typically 10-50 Å wide) connected by a continuous fluorocarbon lattice [14,15] as shown in Figure 1-6. The sulfonate ion clusters in this model can swell and deswell depending on the degree of hydration, allowing for changes to the proton and methanol transport rates. More advanced morphological models proposed include: a Core-Shell Model consisting of an ion-poor shell surrounding an ion-rich core [16,17], a Rod Model where the sulfonate groups arrange in crystal-like rods [12,13], and a Sandwich Model where the polymer forms two layers where sulfonic groups can attract across an aqueous layer where transport occurs [18]. Though the exact mechanism is widely debated in the scientific community, it is known that Nafion’s unique nanoporous channel structure lined with sulfonic acid groups does provide outstanding proton conducting pathways [8]; these nanoporous channels however, are also responsible for the high methanol permeability of Nafion, leading to expedited poisoning of the catalyst.

Physical diffusion and electro-osmotic drag of methanol through the polymer exchange membrane to the cathode side of the DMFC lowers the OCV of the system. Most of the methanol

that crosses over is electrochemically oxidized at the cathode, lowering the cathode potential and consuming some cathode reactant [19]. The crossover problem is so severe that power output of a DMFC with a Nafion proton exchange membrane actually decreases with increasing methanol concentrations above 2.0M [20]; therefore, to use Nafion in a DMFC would require either a highly diluted methanol fuel cartridge or the addition of a complex on-board methanol dilution system, either of which would require excess weight and increase the cost of a DMFC. The methanol permeability issue has compounded with high production costs of Nafion in preventing the widespread commercial use of DMFCs.

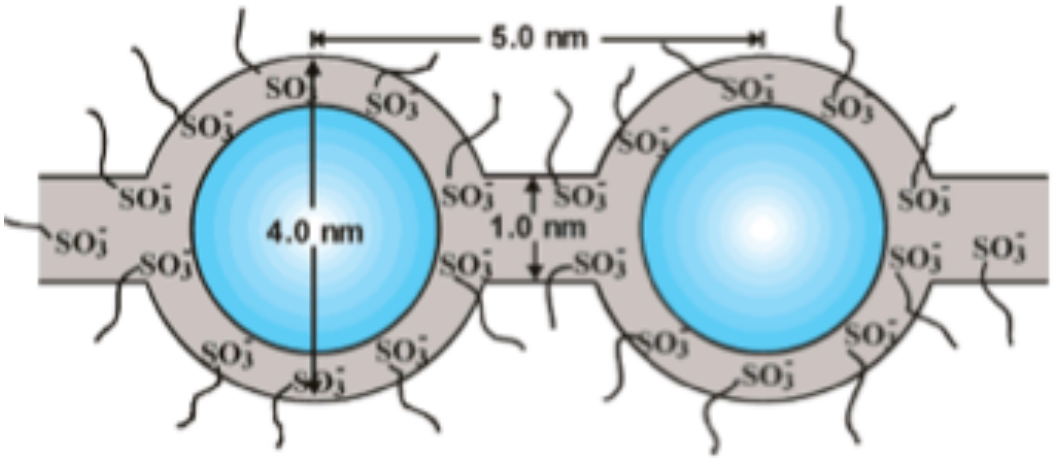

Figure 1-6. Sulfonate ion clusters forming 10-50 Å wide water transport channels in a continuous fluorocarbon lattice of Nafion [15].

Several methods have been used to reduce the methanol permeability of Nafion; however, many of these processes have also been shown to lower the proton conductivity as well as the chemical and thermal stability of the membranes, which make them inadequate solutions for the methanol crossover problem. To help describe the interplay between conductivity and methanol permeability, researchers have started using selectivity ($S=\sigma/P$), which is the ratio of proton conductivity (σ) to methanol permeability (P) [21], Nafion has a selectivity of 3.5×10^4 $S*sec/cm^3$ when fully hydrated; any proton exchange membrane with a selectivity greater than that is considered an improvement over Nafion in terms of transport properties. Many of the research approaches to addressing these PEM issues have relied primarily on the modification and improvement of conventionally synthesized polymer systems. The problem with these approaches is that they often do not lead to systems that are mechanically robust enough to withstand fuel cell cycling, or they fail to significantly lower the cost and effort required in

membrane processing. To date, no system has been able to achieve the overall fuel cell performance of Nafion-based proton exchange membranes.

1.2.2.2 Composite Proton Exchange Membranes

In order to meet both transport and mechanical integrity requirements of an operational fuel cell membrane, the nanoscopically tailored conductive layer-by-layer (LbL) thin films can be integrated into a nanofibrous network. The deposition of polyelectrolytes onto electrospun mats can create ultrathin film bridges across nanopores if a high molecular weight polymer is used; alternatively, utilizing lower molecular weight polyelectrolytes and appropriate surface treatment of the electrospun network could produce a conformal coating of the nanofibers. An example of thin film bridging of nanopores in a Polycaprolactone (PCL) electrospun mat with 50 bilayers of poly(diallyl dimethyl ammonium chloride)/sulfonated poly(2,6-dimethyl-1,4-phenylene oxide) (PDAC/sPPO) LbL dip coated layers is shown in Figure 1-7. Modification of nanofiber surfaces by LbL deposition has been previously demonstrated to achieve stable superhydrophobic fabrics [22] and fiber mats for use as catalysts, filters, and sensors [23]. The combination of the two processes to create a composite LbL/nanofiber membrane allows for decoupling of the structure and mechanical properties of the membrane from the chemical and transport properties. Thus, the electrospun fiber mat and LbL polyelectrolyte deposition can each be tailored independently of each other and then combined to create the optimal composite PEM.

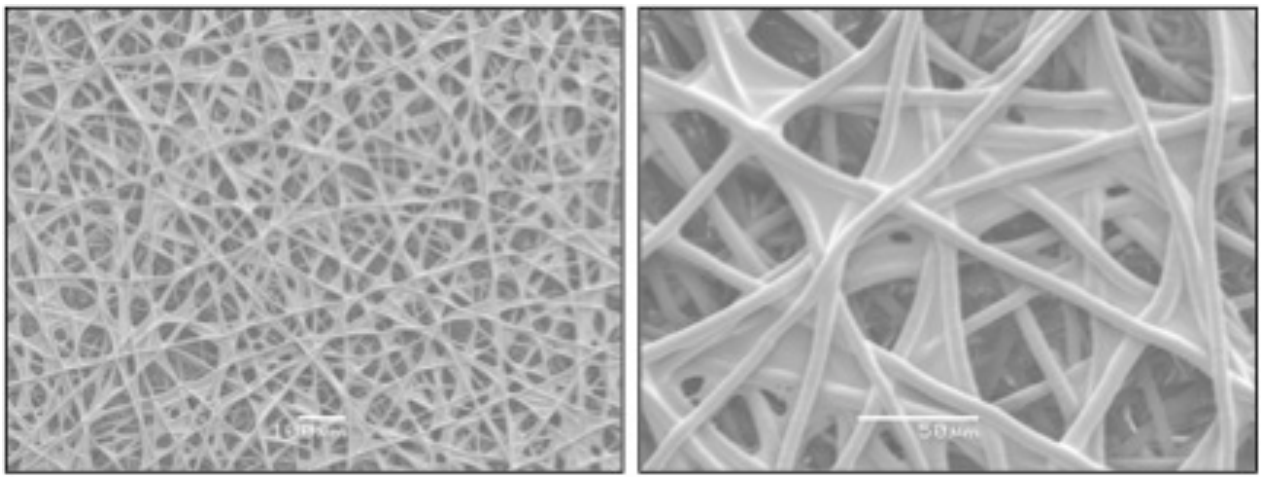

Figure 1-7. SEM micrograph of $(PDAC/sPPO)_{50}$ on ~2 μm diameter PCL Nanofibers. Scale bar for the left image is 100 μm, scale bar for the right image is 50 μm.

To reduce the cycle time of LbL fabrication as well as to improve process control, use of an automated spray-assisted LbL deposition technique has been investigated in recent years.

Krogman et al., in collaboration between the Hammond and Rutledge group, combined the LbL deposition technique with electrospinning of nanofiber mats to create asymmetrical functional membranes through automated spray-assisted LbL deposition [24,25]. By drawing a pressure gradient across the electrospun mat during the spray-assisted LbL process, they were able to obtain highly conformal coatings on the individual fibers without webbing or liquid bridging. The automated cycle time for deposition of each layer was greatly reduced by the spray-assisted LbL deposition technique as compared to the conventional dip-assembly process.

1.2.3 Electrospinning of Nanofiber Mats

Electrostatic fiber formation, or electrospinning, offers a particularly simple and robust method to create porous polymer scaffolds that can provide mechanical support as well as mimic the percolated, fibrillar structure of water-swollen Nafion. The method of producing electrically driven liquid jets into solid polymeric fibers has been a topic of significant interest for many years. In the 1880's, Lord Rayleigh calculated the maximum amount of charge which a drop of liquid can hold before the applied electrical forces overcome the surface tension of the drop [26]. Zeleny then described and photographed the electrospraying phenomena of ethyl alcohol and glycerine droplets in 1917 [27]. Sir Geoffrey Taylor analyzed the conditions at the point of a droplet that is deformed by an electric field and showed that a conical interface between two fluids is stable if the cone has a semi-angle of 49.3°, thus creating stable jets [28]. It was not until the 1990's when the art of electrospinning garnered significant attention for the production of polymeric nanofibers, led by the work of Reneker et al. [29,30,31]; subsequent research in the field of electrostatic fiber formation has increased exponentially over the past 20 years.

In electrospinning, a viscoelastic fluid is charged so that a liquid jet is ejected from the free surface of the fluid (typically supplied by a spinneret) and collected on a grounded plate, creating nonwoven fiber matrices. Charges at the free surface repel each other, working against the surface tension and deform the surface into a conical shape (known as the Taylor cone). At a critical stress, a liquid jet (or jets) is ejected from the apex of the cone and drawn through the action of electrostatic forces such as charge repulsion and charge acceleration in an external electric field to very small diameters. In this region, the liquid jet becomes unstable and deviates from its straight path, undergoing a bending instability known as whipping. The jet stretches during the whipping instability resulting in continuous fibers with diameters in the range of ~50 nm to ~10 μm upon solidification by solvent evaporation. An illustration of a parallel-plate

electrospinning apparatus, showing the fluid jet and whipping instability, can be seen in Figure 1-8. In this set-up, the polymeric solution is pumped at a continuous flow rate from a syringe through a Teflon tube and needle tip imbedded in the top charged plate.

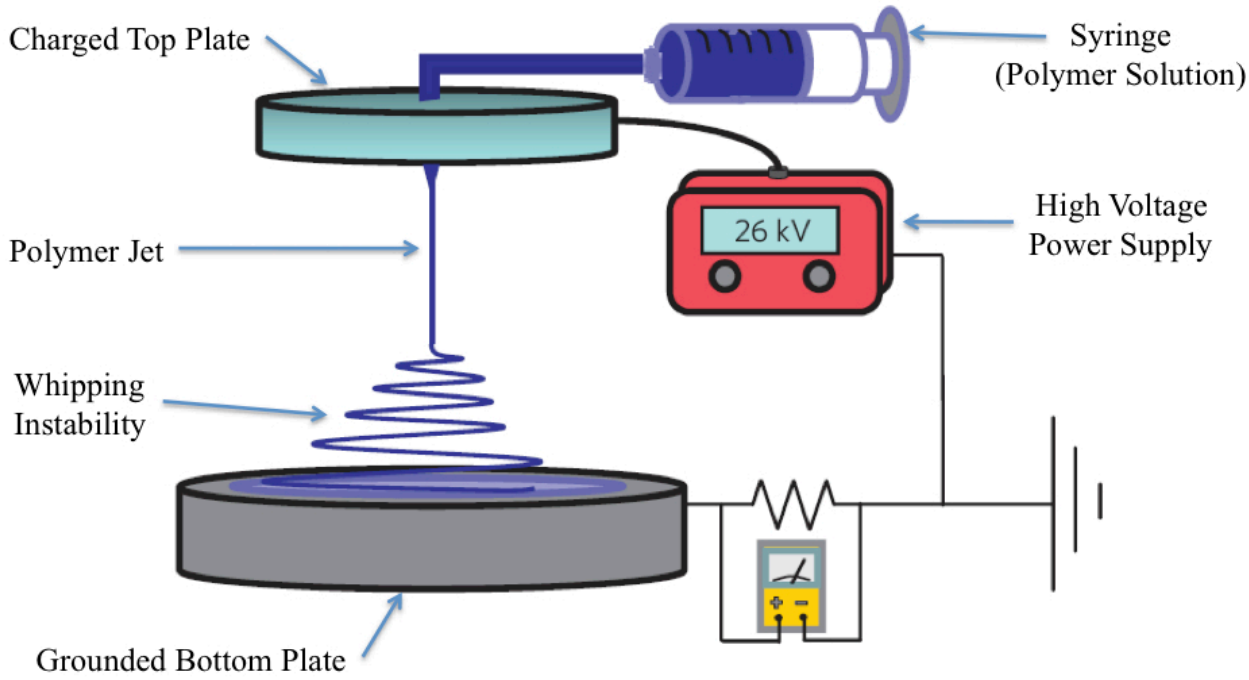

Figure 1-8. Diagram of a typical parallel plate single needle electrospinning apparatus [32]. A polymer solution is pumped through a charged top plate and propelled to the grounded bottom plate by an applied electric field resulting in a randomly oriented nanofiber mat.

The processing and solution parameters can be tuned to create electrospun mats of various fiber diameters and porosity for a wide range of polymers; however, the dynamics of the electrospinning process become extremely complex after the onset of the whipping instability. Changing a single fluid or processing parameter can affect the jet and/or fiber formation through several mechanisms. For example, using a different solvent can change several aspects of the electrospinning jet, such as the dielectric constant, the conductivity, the surface tension, and the solute-solvent interaction. The flow chart in Figure 1-9 attempts to serve as a general guide on how varying certain parameters can modify the fiber radius [33]. There are a few general trends that seem to exist for electrospinning of most solutions. Increasing the solute concentration typically reduces the mass lost due to evaporation and increases the elasticity of the solution, both of which contribute to a larger fiber diameter. Increasing the charge density of the solution

provides a greater stretching force on the jet, resulting in smaller diameter fibers. Similarly, by reducing the surface tension of the solution, this decreases the forces resisting the creation of additional surface area, decreasing the terminal fiber diameter.

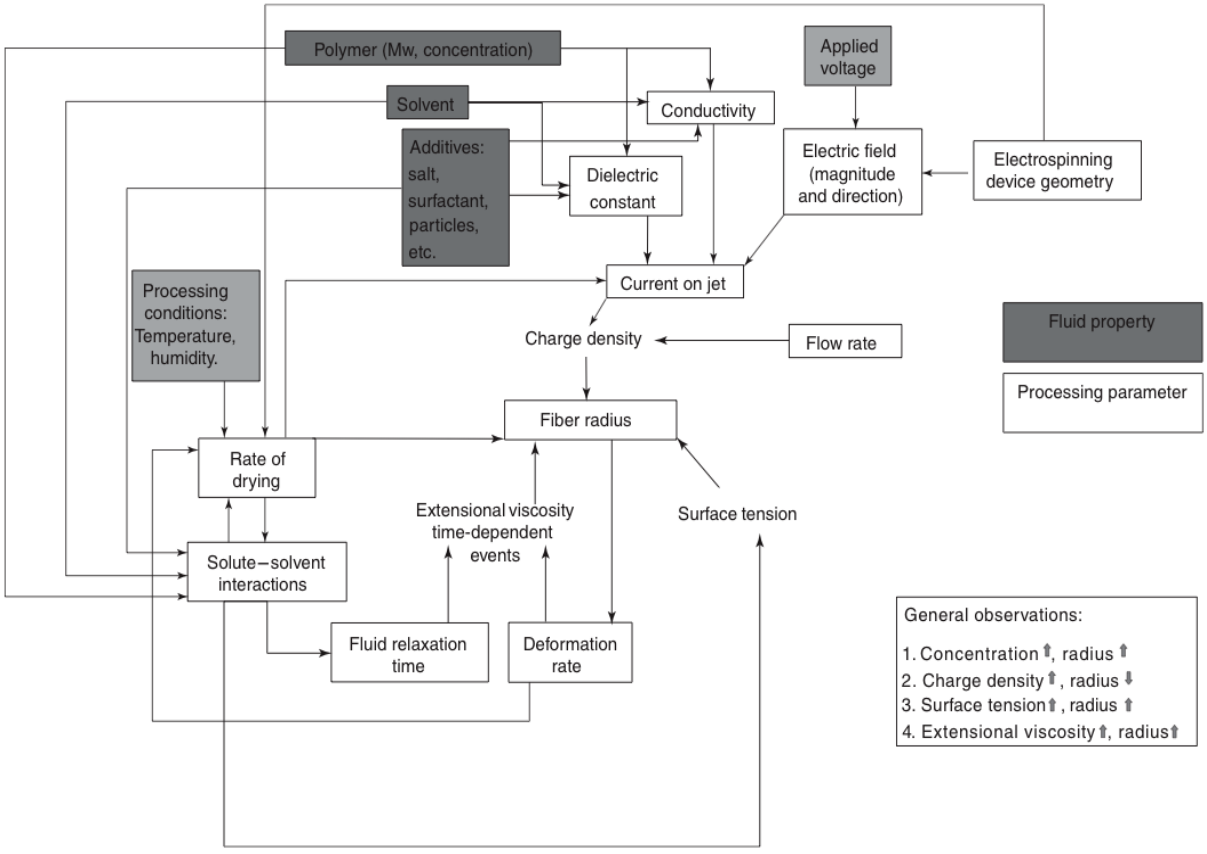

Figure 1-9. The effect of fluid properties and processing parameters on the terminal fiber radius in electrospun fibers [33].

Electrospun nanofiber mats can be tailored for specific applications by modification of the fiber diameter, porosity, surface area, mechanical properties, and degradation kinetics. Because of these unique properties and relative ease of fabrication, electrospun fibers have attracted a significant amount of attention in recent years for a broad range of applications. The most active application of electrospun nanofibers to date has been in tissue engineering scaffolds [34,35]. The nonwoven electrospun mats are desirable for this application due to their extremely high surface area and porosity; the pores sizes are ~1-10 μm, roughly the same size as cells. Electrospun fiber mats have also been used to create superhydrophobic nonwoven fabrics exhibiting contact angles as high as 175° [36]. Numerous other applications for electrospun

nanofiber mats have been investigated over the past decade including (but not limited to): drug release agents [37], optical sensors [38], and ion-exchange membranes [39,40].

1.2.4 Layer-by-layer Deposition of Polyelectrolytes

The technique of polymer thin-film deposition known as layer-by-layer assembly (LbL) is a versatile process that consists of the repeated, sequential electrostatic deposition of the complementary functionalized materials on a substrate. The process was first developed by Decher in the early 1990's and it consisted of the sequential build up of a polyelectrolyte thin film in a step-wise fashion [41,42]. Typically, the process involves exposing an inherently charged substrate sequentially to solutions of oppositely charged polyelectrolytes, to create an insoluble polymer thin film network at diffusion time scales that enable nanometer-level control of film thickness. A diagram illustrating the layer-by-layer deposition process is shown in Figure 1-10. The substrate containing a surface charge (either inherently or added via plasma treatment) is brought in contact with an aqueous polyelectrolyte solution of opposite charge, where the polyelectrolyte is allowed to diffuse and adsorb to the substrate. Enough polyelectrolyte adsorbs to overcompensate the surface charge, which results in a reversal of the surface charge of the substrate. The substrate is then dipped in a series of rinse baths to remove any polyelectrolyte (or salt) that is not tightly bound to the substrate. Next, the substrate is contacted with a polyelectrolyte solution of opposite charge to that of the surface, followed by dipping in a second series of rinse baths, and the cycle is repeated. The overall process can be reiterated as many times as required to produce a film of desired thickness. Adjusting assembly parameters such as ionic strength, salt concentration, and pH can control the composition, morphology, and bulk properties of the LbL film [43].

The layer-by-layer process has several major assembly advantages including: automated processing, assembly at ambient conditions, and the ability to conformally coat to complex geometries. One other major advantage of the LbL technique is its ability to incorporate water-soluble polymers into stable homogeneous films. This allows the use of highly sulfonated, high proton-conducting, aromatic polymers like sulfonated polystyrene (sPS) or sulfonated poly(2,6-dimethyl-1,4-phenylene oxide) (sPPO). In its most conductive state, the bulk version of sPPO becomes highly water swollen and ultimately soluble, making it unusable as a membrane by itself despite its outstanding ionic properties. Several research groups have avoided this problem by using low degrees of sulfonation (~30%) to make the membrane water-insoluble; however, by

doing this, the proton conductivity of the membrane is compromised [44]. The LbL technique can be used to incorporate the highly sulfonated polymers as one of the two components in a water-stable thin film, thus maintaining a large portion of the polyelectrolyte's inherently high proton conductivity. Because the LbL assembled films are essentially homogeneous polyelectrolyte blends and not actually stratified layers, having only one of the components be conductive is sufficient for the entire film to conduct protons through. The homogeneous LbL thin-films also tend to exhibit relatively low methanol permeability as compared to Nafion membranes.

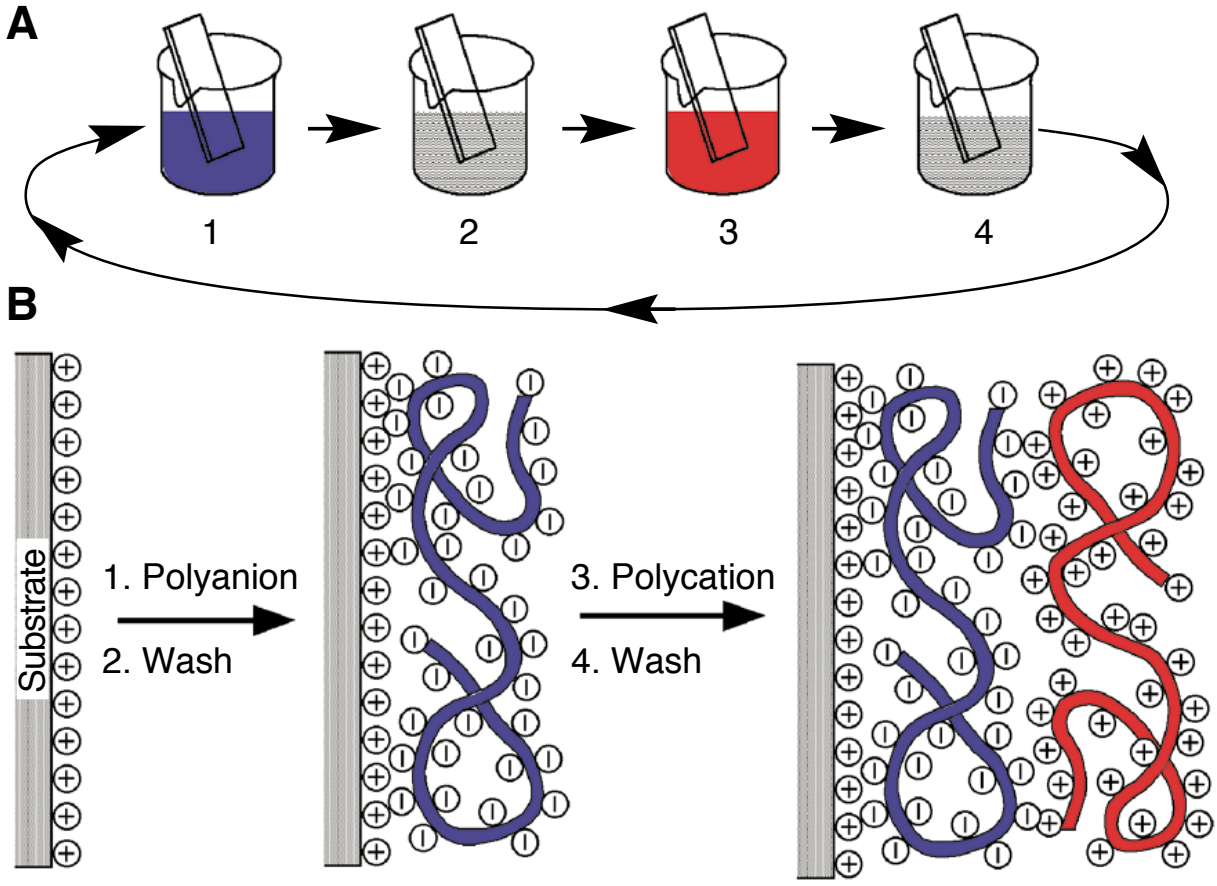

Figure 1-10. Schematic of the layer-by-layer deposition process of polyelectrolyte thin-films. The substrate containing a positive surface charge is brought in contact with an aqueous polyanion solution (blue), where the oppositely charged polyelectrolyte is allowed to diffuse and absorb to the substrate until enough polyanion absorbs to overcompensate the surface charge, resulting in a reversal of the substrate surface charge. The substrate is then dipped in a rinse bath followed by contact with a polycation solution (red), followed by dipping in a second rinse bath. The overall process is repeated many times to produce a film of desired thickness [41].

1.3 Thesis Objectives

This thesis seeks to take an integrated multi-scale materials design and processing approach to the development of a superior composite proton exchange membrane. Two relatively new processing capabilities, electrospinning of nanofibrous mats and layer-by-layer assembly of polyelectrolyte based membranes, are further developed and combined to generate nanoscale assemblies of polymers via the control of thin film architectures on the 1 to 100 nanometer length scale. Development and design of these systems will be closely coupled with morphological, mechanical, and electrochemical characterization of these unique nanoscale layer assemblies to optimize fuel cell performance. In looking to the future, to when fuel cells would be commercialized and mass-produced, the mechanical properties, durability and life cycle of the proton exchange membrane would become increasingly important. In such a case, the proposed composite membrane consisting of a mechanically robust endoskeleton stands a much better chance of withstanding fuel cell cycling (and thus increasing its life-span) at increasingly thin conditions (<30 μm) than any homogeneous polymer or polymer blend that is swollen from water and plasticized to increase conductivity. The separation of the conductive element from the structural element is thus the most promising method to achieve truly long membrane life spans. To achieve these desired membrane properties, the specific objectives involved in this work are as follows:

1) To elucidate the relationship between electrospun fiber morphology and the fabrication process and more specifically, how to manipulate terminal fiber diameter based on the solution properties and processing parameters. Previous work on terminal fiber diameter analysis of electrospun fibers has been performed; however, this work seeks to evaluate the effects of highly viscoelastic solutions on the electrostatic fiber forming process.

2) To investigate the mechanical and tribological properties of electrospun fiber mats and methods of improving their durability and wear resistance by techniques such as thermal annealing. Quantification of tribological properties and development of an accurate wear mechanism for amorphous and semi-crystalline nonwoven polymeric fiber mats is the desired outcome.

3) To incorporate the finely controlled, mechanically robust electrospun fiber mats as a structural scaffold for composite fuel cell membranes. Part of this objective includes the

exploration of the fabrication process for these novel composite LbL-electrospun fiber proton exchange membranes and evaluation of how the transport and mechanical properties of the composite PEM compare with Nafion and free-standing LbL polyelectrolyte film. Optimization of the electrochemical selectivity and mechanical response of the composite PEM will be performed with the ultimate goal of comparing the performance of the composite membrane against Nafion in an operational direct methanol fuel cell.

1.4 References

[1] J.W. Tester, E.M. Drake, M.J. Driscoll, M.W. Golay, W.A. Peters, *Sustainable Energy Choosing Among Options*. Cambridge: The MIT Press (2005).

[2] M. Winter, R.J. Brodd, What are batteries, fuel cells, and supercapacitors?, Chemical Reviews 104 (2004) 4245-4269.

[3] S. Thomas, M. Zalbowitz, Fuel Cells-Green Power, Los Alamos National Laboratory, Los Alamos, NM, (2000).

[4] A.S. Arico, S. Srinivasan, V. Antonucci, DMFCs: from fundamental aspects to technology development, Fuel Cells 1 (2001) 133-161.

[5] A.S. Arico, V. Baglio, V. Anotonucci, Direct Methanol Fuel Cells: History, Status, and Perpectives, *Electrocatalysis of Direct Methanol Fuel Cells*, Wiley VCH (2009) 1-78.

[6] M. Doyle, G. Rajendran, Perfluorinated Membranes, *Handbook of Fuel Cells: Fundamentals, Technology, and Applications*, Wiley VCH (2003) 351-411.

[7] EG&G Technical Services, Inc., Fuel Cell Handbook (7^{th} Edition), U.S. Department of Energy, (2004).

[8] K.A. Mauritz, R.B. Moore, State of understanding of Nafion, Chemical Reviews 104 (2004) 4535-4585.

[9] N.W. Deluca, Y.A. Elabd, Polymer electrolyte membranes for the direct methanol fuel cell: a review, Journal of Polymer Science: Part B: Polymer Physics 44 (2006) 2201-2225.

[10] M. Fujimura, T. Hashimoto, H. Kawai, Small-angle X-ray scattering study of perfluorinated ionomer membranes 2. Models for ionic scattering maximum, Macromolecules 15 (1982) 136-144.

[11] A.L. Rollet, O. Diat, G. Gebel, A new insight into Nafion structure, Journal of Physical Chemistry B 106 (2002) 3033-3036.

[12] L. Rubatat, A.L. Rollet, G. Gebel, O. Diat, Evidence of elongated polymeric aggregates in Nafion, Macromolecules 35 (2002) 4050-4055.

[13] L. Rubatat, A.L. Rollet, O. Diat, G. Gebel, Characterization of ionomer membrane structure (Nafion) by small-andle x-ray scattering, Journal De Physique Iv 12 (2002) 197-205.

[14] T.D. Gierke, W.S. Hsu, The cluster–network model of ion clustering in perfluorosulphonated membranes in perfluorinated ionomer membranes, ACS Symposium Series 180 (1982).

[15] W.S. Hsu, T.D. Gierke, Ion transport and clustering in Nafion perfluorinated membranes, Journal of Membrane Science 13 (1983) 307-326.

[16] M. Fujimura, T. Hashimoto, H. Kawai, Small-angle X-ray scattering study of perfluorinated ionomer membranes. 1. Origin of two scattering maxima, Macromolecules 14 (1981) 1309-1315.

[17] M. Fujimura, T. Hashimoto, H. Kawai, Small-angle X-ray scattering study of perfluorinated ionomer membranes 2. Models for ionic scattering maximum, Macromolecules 15 (1982) 136-144.

[18] H.-G. Haubold, T. Vad, H. Jungbluth, P. Hiller, Nano structure of Nafion: a SAXS study, Electrochimica Acta 46 (2001) 1559-1563.

[19] Z. Qi, A. Kaufman, Open circuit voltage and methanol crossover in DMFCs, Journal of Power Sources 110 (2002) 177-185.

[20] J.N. Ashcraft, Tuning the Transport Properties of Layer-by-Layer Thin Films for Fuel Cell Application, MIT PhD Thesis (2009).

[21] B.S. Pivovar, Y. Wang, E.L. Cussler, Pervaporation membranes in direct methanol fuel cells, Journal of Membrane Science 154 (1999) 155-162.

[22] M. Ma, M. Gupta, Z. Li, L. Zhai, K.K. Gleason, R.E. Cohen, M.F. Rubner, G.C. Rutledge, Decorated electrospun superhydrophobicity, Advanced Materials 19 (2007) 255-259.

[23] B. Ding, J. Kim, E. Kimura, S. Shriatori, Layer-by-layer structured films of TiO2 nanoparticles and poly(acrylic acid) on electrospun nanofibers, Nanotechnology 15 (2004) 913-917.

[24] K.C. Krogman, N.S. Zacharia, S. Schroeder, P.T. Hammond, Automated process for improved uniformity and versatility of layer-by-layer deposition, Langmuir 23 (2007) 3137-3141.

[25] K.C. Krogman, J.L. Lowery, N.S. Zacharia, G.C. Rutledge, P.T. Hammond, Spraying asymmetry into functional membranes layer-by-layer, Nature Materials 8 (2009) 512-518.

[26] Lord Rayleigh, On the equilibrium of liquid conducting masses charged with electricity, The London, Edinburgh, and Dublin Philosophical Magazine and Journal of Science 44 (1882) 184–186.

[27] J. Zeleny, Instability of electrified liquid surfaces, Physical Review 10 (1917) 1-6.

[28] G. Taylor, Electrically driven jets, Proceedings of the Royal Society of London: Series A 313 (1969) 453-475.

[29] J. Doshi, D.H. Reneker, Electrospinning process and applications of electrospun fibers, Journal of Electrostatics 35 (1995) 151-160.

[30] D.H. Reneker, I. Chun, Nanometre diameter fibers of polymer, produced by electrospinning, Nanotechnology 7 (1996) 216-223.

[31] D.H. Reneker, A.L. Yarin, H. Fong, S. Koombhongse, Bending instability of electrically charged liquid jets of polymer solutions in electrospinning, Journal of Applied Physics 87 (2000) 4531-4547.

[32] K.C. Krogman, J.L. Lowery, N.S. Zacharia, G.C. Rutledge, P.T. Hammond, Spraying asymmetry into functional membranes layer-by-layer, Nature Materials 8 (2009) 512-518.

[33] J.H. Yu, G.C. Rutledge, Electrospinning, *Encyclopedia of Polymer Science & Technology* (2008) 1-20.

[34] R.G. Fleming, C.J. Murphy, G.A. Abrams, S.L. Goodman, P.F. Nealy, Effects of synthetic micro- and nano-structured surfaces on cell behavior, Biomaterials 20 (1999) 573-588.

[35] J.A. Matthews, G.E. Wnek, D.G. Simpson, G.L. Bowlin, Electrospinning of collagen nanofibers, Biomacromolecules 3 (2002) 232-238.

[36] M.L. Ma, Y. Mao, M. Gupta, K.K. Gleason, G.C. Rutledge, Superhydrophobic fabrics produced by electrospinning and chemical vapor deposition, Macromolecules 38 (2005) 9742-9748.

[37] E.R. Kenawy, G.L. Bowlin, K. Mansfield, J. Layman, D.G. Simpson, E.H. Sanders, G.E. Wnek, Release of tetracycline hydrochloride from electrospun poly(ethylene-co-vinylacetate), poly(lactic acid), and a blend, Journal of Controlled Release 81 (2002) 57-64.

[38] X.Y. Wang, C. Drew, S.H. Lee, K.J. Senecal, J. Kumar, L.A. Samuelson, Electrospinning technology: a novel approach to sensor application, Journal of Macromolecular Science-Pure and Applied Chemistry A39 (2002) 1251-1258.

[39] S.W. Choi, Y.Z. Fu, Y.R. Ahn, S.M. Jo, A. Manthiram, Nafion-impregnated electrospun polyvinylidene fluoride composite membranes for direct methanol fuel cells, Journal of Power Sources 180 (2008) 167-171.

[40] R. Bajon, S. Balaji, S.M. Guo, Electrospun Nafion nanofiber for proton exchange membrane fuel cell application, Journal of Fuel Cell Science Technology 6 (2009) 031004.

[41] G. Decher, Fuzzy nanoassemblies: toward layered polymeric multicomposites, Science 277 (1997) 1232-1237.

[42] J.T. Lutkenhaus, P.T. Hammond, Electrochemically enabled polyelectrolyte multilayer devices: from fuel cells to sensors, Soft Matter 3 (2007) 804-816.

[43] P.T. Hammond, Form and function in multilayer assembly: new applications at the nanoscale, Advanced Materials 16 (2004) 1271-1293.

[44] T. Xu, D. Wu, L. Wu, Poly(2,6-dimethyl-1,4-phenylene oxide) (PPO) – aversatile starting polymer for proton conducting membranes (PCMs), Progress in Polymer Science 33 (2008) 894-915.

2. Controlling Terminal Fiber Diameter in Electrospinning

Portions of this chapter are reproduced from M.M. Mannarino, G.C. Rutledge, Applied Physics Letters (2013) [In Preparation].

2.1 Introduction

Electrostatic fiber formation, or electrospinning, offers a particularly simple and robust method to create polymeric nanofibers of various morphologies and sizes, inexpensively and in large quantities. In electrospinning, a viscoelastic fluid is charged so that a liquid jet is ejected from the surface of the fluid (typically in the form of a drop supplied by a needle or spinneret) and collected on a grounded plate, thus creating nonwoven fiber matrices [1]. Under an applied voltage to the fluid, charges accumulate at the surface and repel each other, working against the surface tension to deform the surface into a conical shape (known as the Taylor cone) [2]. As the surface charge increases, a critical condition is reached at which electrical stresses overcome the surface tension; at this point, a jet is ejected from the apex of the Taylor cone and drawn to very small diameters through the action of electrostatic forces such as charge-charge repulsion and interaction of charge with an external electric field. In this region, the liquid jet becomes unstable and deviates from its straight path, undergoing a whipping instability. The jet stretches during the whipping instability, resulting in continuous fibers with diameters in the range of approximately 0.05 to 10 μm upon solidification by solvent evaporation or cooling.

Modification of the fiber diameter, mat porosity, specific surface area, and mechanical properties of the nonwoven mat allows one to tailor electrospun nanofiber mats for specific applications. Because of these unique properties and relative ease of fabrication, electrospun fibers have attracted a significant amount of attention in recent years for a broad range of applications. The most active area of development of electrospun nanofibers to date has been for tissue engineering scaffolds [3,4]. The nonwoven electrospun mats are desirable for this application due to their extremely high surface area and porosity; the pores sizes are typically 1-10 μm, roughly the same size as many common cells. Electrospun fiber mats have also been used to create superhydrophobic nonwoven fabrics exhibiting contact angles as high as 175°, which could be used for oil/water separation membranes [5,6]. Numerous other applications for

electrospun nanofiber mats have been investigated over the past decade, including (but not limited to): drug release agents [7], optical sensors [8], carbonized fiber electrodes [9,10], and ion-exchange membranes [11,12]. In many of these applications, the diameter of the fibers used is of critical importance.

Despite the widespread and rapidly growing use of electrospinning in the fabrication of novel nanomaterials, there has been no universal method of predicting, a priori, the size and morphology of electrospun fibers from knowledge of the polymer solution properties and electrospinning operating conditions alone. Changing a single fluid property, processing parameter, or environmental condition can affect the jet and fiber formation through several mechanisms. For example, using a different solvent can change several properties of the electrospinning fluid, such as the dielectric constant, conductivity, surface tension, and solute-solvent interaction. Determining the dominant parameters for a given system is a non-trivial task and analysis of various processing parameters in electrospinning to determine governing parameters typically yields numerous potential scaling laws [13]. There are a few general trends that seem to exist for electrospinning of most solutions based on the parameters with the strongest effect on fiber diameter: viscosity, conductivity, and surface tension [14]. Increasing the solute concentration typically reduces the mass lost due to evaporation and increases both the elasticity and viscosity of the solution, which leads to larger fiber diameters [15]. Increasing the charge density of the solution provides a greater stretching force on the jet, resulting in smaller diameter fibers. Similarly, reducing the surface tension of the solution decreases the forces resisting the creation of additional surface area, resulting in smaller fiber diameters [16]. The electrospinning of new polymeric fibers typically follows a trial-and-error approach of varying fluid properties and processing variables until nanofibers of a desired size and morphology are achieved. Thus, a simple analysis leading to estimation of fiber size (or terminal jet diameter) for novel systems would be highly beneficial to nanomaterial development.

Electrohydrodynamic theory in the slender thinning jet approximation has been previously employed to develop several analytical models for electrospinning in an attempt to predict jet behavior [17]. Hohman et al. used a stability analysis of electrostatically driven jets to develop maps over which different operating regimes, characterized by the occurrence (or lack thereof) and nature of particular instabilities such as whipping and varicose instability, could be predicted [18,19]. More detailed analyses have been developed to predict the so-called “terminal

diameter" of electrospinning jets; however, most of these models involve internal parameters that are impossible to know a priori and are difficult to measure or control experimentally. Fridrikh et al. proposed a force balance model for the terminal diameter of an electrospun jet that requires knowledge of the charge density on the jet, which is typically obtained empirically by measuring the jet current for a known flow rate, so that the relation is not really predictive [20]. To overcome this limitation, Bhattacharjee et al. proposed a scaling relation between jet current and the solution conductivity, flow rate, and applied electric field [21]; however, when combined with the model of Fridrikh et al. to predict fiber diameter, the relation was found to work best for organic solutions of low conductivity (<200 μS/cm). Other models to predict the asymptotic rate of decrease of the jet radius were developed by Feng [22] and Spivak et al. [23]; however, these models were determined in terms of an initial radius of jet formation, which is not easily measurable, and apply only to the case of stable, steady jets. Consequently, these models and analyses do not allow for a priori prediction of electrospun nanofiber diameters. Helgeson et al. used these models as a theoretical foundation for the development of a simple scaling analysis relating the fiber size and morphology to spinning solution properties and controllable processing parameters [24]. In its original form, this model did not include a flow-rate term, nor did it take into account non-Newtonian fluid behavior; it was subsequently revised to be applicable to a wider range of solution conductivities [25]; however, even with these corrections the model still does not predict fiber sizes for a wide range of solutions with significant accuracy. The work performed in this chapter seeks to extend the work of Fridrikh et al. and Bhattacharjee et al. to develop a simple relation for predicting jet diameter of an electrospun fiber that accounts for solution viscoelasticity as well as solution conductivity and operating parameters that are easily measured and controlled.

2.2 Experimental Method

2.2.1 Materials

Poly(trimethyl hexamethylene terephthalamide) (Nylon 6(3)T, henceforth abbreviated PA 6(3)T) was purchased from Scientific Polymer Products, Inc. Bisphenol A polysulfone (UDEL® P3500, henceforth abbreviated PSU) was obtained from Solvay Advanced Polymers, LLC. Both PA 6(3)T and PSU are amorphous polymers with aromatic moieties and high glass transition

temperatures (T_g= 426 K and Tg= 463 K, respectively) and outstanding mechanical properties. The chemical structures of both polymers used for this chapter are shown in Figure 2-1. N,N-dimethyl formamide (DMF), N,N-dimethyl acetamide (DMAc), and N-methyl pyrrolidone (NMP) were used as primary solvents for creating polymeric solutions. Formic acid (FA) and acetic acid (AA) were added in small amounts (~1 wt.%) in order to modify the electrical properties of the solutions. All solvents were obtained from Sigma-Aldrich and used as received without any further purification.

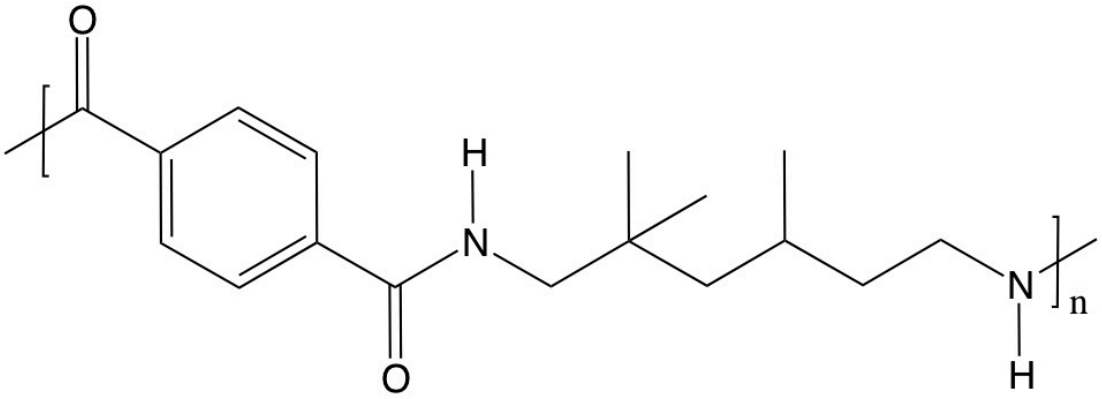

Poly(trimethyl hexamethylene terephthalamide) **[PA 6(3)T]**

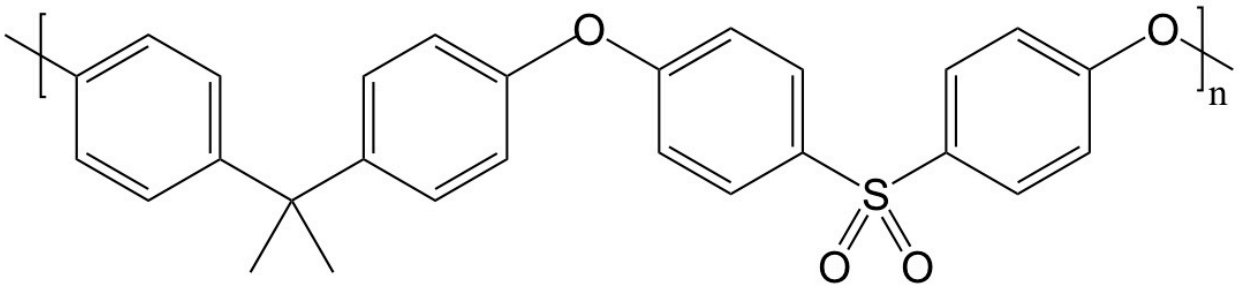

Bisphenol A polysulfone **[PSU]**

Figure 2-1. Chemical structure of poly(trimethyl hexamethylene terephthalamide) [PA 6(3)T] and bisphenol A polysulfone [PSU].

2.2.2 Electrospinning of Nanofibers

Electrospinning was conducted using a parallel-plate apparatus that consists of two aluminum disks, each with a diameter of 12 cm. The spinneret consists of a stainless steel capillary tube (1.6 mm OD, 1.0 mm ID) (Upchurch Scientific) inserted through the center of the top plate. A digitally controlled syringe pump (Harvard Apparatus, PHD 2000) was used to obtain flow rates of 0.1-1.5 mL/hr. The bottom plate was adjusted manually to achieve spinneret

tip-to-collector distances of 15-35 cm. A high voltage power supply (Gamma High Voltage Research, ES40P) was used to realize voltages of 10-30 kV at the top plate. The jet current was measured as the voltage drop across a 1 MΩ resistor inserted between the bottom plate and ground (Fluke, 287 true RMS multimeter). The voltage readings were then converted to electrical current using Ohm's law. The entire apparatus was contained within a fume hood to ensure proper ventilation. Electrospinning parameters that were varied during the course of this work included the applied voltage (V), solution flow rate (Q), and tip-to-collector distance (TCD). The relative humidity (RH) and temperature (T) were monitored using a Digital Humidity/Temperature Monitor (VWR).

2.2.3 Solution Characterization

The variables in electrospinning have been previously categorized as fluid properties, operating parameters, or equipment geometry [26]. The relevant fluid properties are the density (ρ), dielectric permittivity (ε), electrical conductivity (K), surface tension (γ), viscosity (η) and the characteristic relaxation time, τ_R. The static electrical conductivity of each solution was measured using a digital conductivity meter (VWR; Model 23226). Surface tension of each solution was measured with a Krüss DSA10-MK2 Drop-Shape Analyzer, using the pendant drop method [27]. Polymer bulk density and solvent dielectric permittivity values were taken from the literature.

2.2.3.1 Rheology

The viscosity of the electrospinning solution is known to be an important parameter in predicting fiber diameter. The shear viscosity (scanning shear rates between 10^{-1} s^{-1} and 10^{3} s^{-1}) for each solution was measured using a TA Instruments AR-2000 cone and plate shear rheometer. Sample plots of $\eta(\dot{\gamma})$ as a function of shear rate for PSU solutions in NMP are shown in Figure 2-2. The limit of the shear viscosity as the shear rate approaches zero is taken to be the zero shear rate viscosity (η_0); for all of the polymer solutions, the shear viscosity was found to be shear-rate independent below $\dot{\gamma}$=10 s^{-1}. The higher concentration solutions exhibit a shear-thinning fluid response at higher shear rates, while the lower concentrations solutions typically exhibit Newtonian behavior up to shear rates of 1000 s^{-1}. The zero-shear viscosity of polymer solutions typically increases with increasing molecular weight or polymer concentration (wt.%).

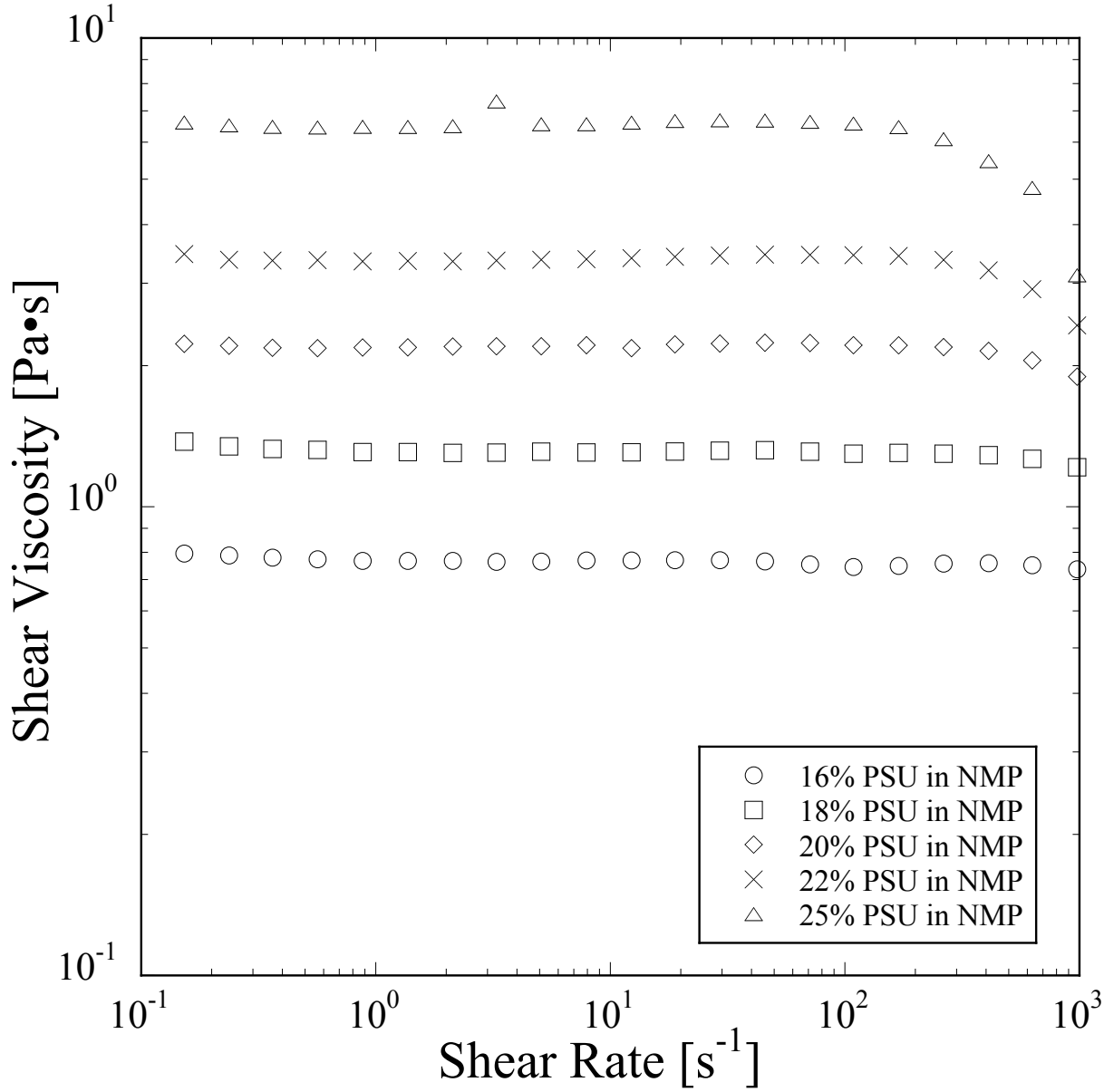

Figure 2-2. Representative plots of the shear viscosity vs. shear rate for PSU solutions in NMP of varying concentrations (○:16 wt.%, □:18 wt.%, ◇:20 wt.%, ×:22 wt.%, and △:25 wt.%).

2.2.3.2 Capillary Break-Up Extensional Rheometry

A Capillary Breakup Extensional Rheometer (CaBER 1; Thermo Haake) was used to examine the viscoelastic properties of polymer solutions in extension, which were then related to the terminal fiber diameter. The CaBER is a filament stretching apparatus that measures the midpoint diameter, $D_{mid}(t)$, of the thinning filament over time when a fluid filament constrained axially between two coaxial disks is stretched rapidly over a short distance [28]. In these measurements, the time evolution of the filament diameter for a viscoelastic fluid is governed by

a balance between the capillary force, which compresses the jet radially and causes it to extend longitudinally, and viscoelasticity, which resists the deformation caused by the capillary force; $D_{mid}(t)$ can therefore be described by the following model [29]:

$$D_{mid}(t) = D_0 \left(\frac{D_0 G}{4\gamma}\right)^{1/3} e^{\left(-\frac{t}{3\tau_R}\right)} \quad \text{(Equation 2-1)}$$

where D_0 is the midpoint diameter of the fluid filament immediately after imposition of a rapid step strain in the axial direction. G, γ, and τ_R are the elastic modulus, surface tension, and viscoelastic relaxation time of the solution, respectively. Two 6 mm diameter stainless steel plates were used in all measurements, with an initial gap distance of 3 mm, and a linear stretch profile to 10 mm in 20 ms. Data was collected at 2000 Hz, and the CaBER analysis package was used for all rheological calculations. A typical CaBER plot of $D_{mid}(t)$ vs. time is shown in Figure 2-3; the model from Equation 2-1 is fitted to the long time linear region on the semi-log plot to determine τ_R for each solution. The region after the exponential-thinning, where D_{mid} drops off sharply in the semi-log plot, corresponds to the filament break-up region, which is typically not experienced during electrospinning, as the jet would solidify before entering this region for uniform fibers. Increasing the concentration (wt.%) of the polymer in solution typically increases the characteristic relaxation time due to increased chain entanglement and viscoelasticity. Previous research has shown that there is a strong correlation between the characteristic relaxation time of the electrospinning solution and the formation of uniform nanofibers (as opposed to spray, beads-on-string, or ribbon morphology) [30]. The ratio of characteristic relaxation time to the growth rate of the Rayleigh instability defines a Deborah number, De, which serves to identify the transition from droplet breakup (electrospraying) to fiber formation (electrospinning), albeit with beads-on-string morphology. However, the same De has also been found empirically to provide a good predictor for the formation of uniform fibers above De=6 or 7 [30,31]. A conclusive relationship between the characteristic fluid relaxation time and the terminal fiber diameter has not yet been established.

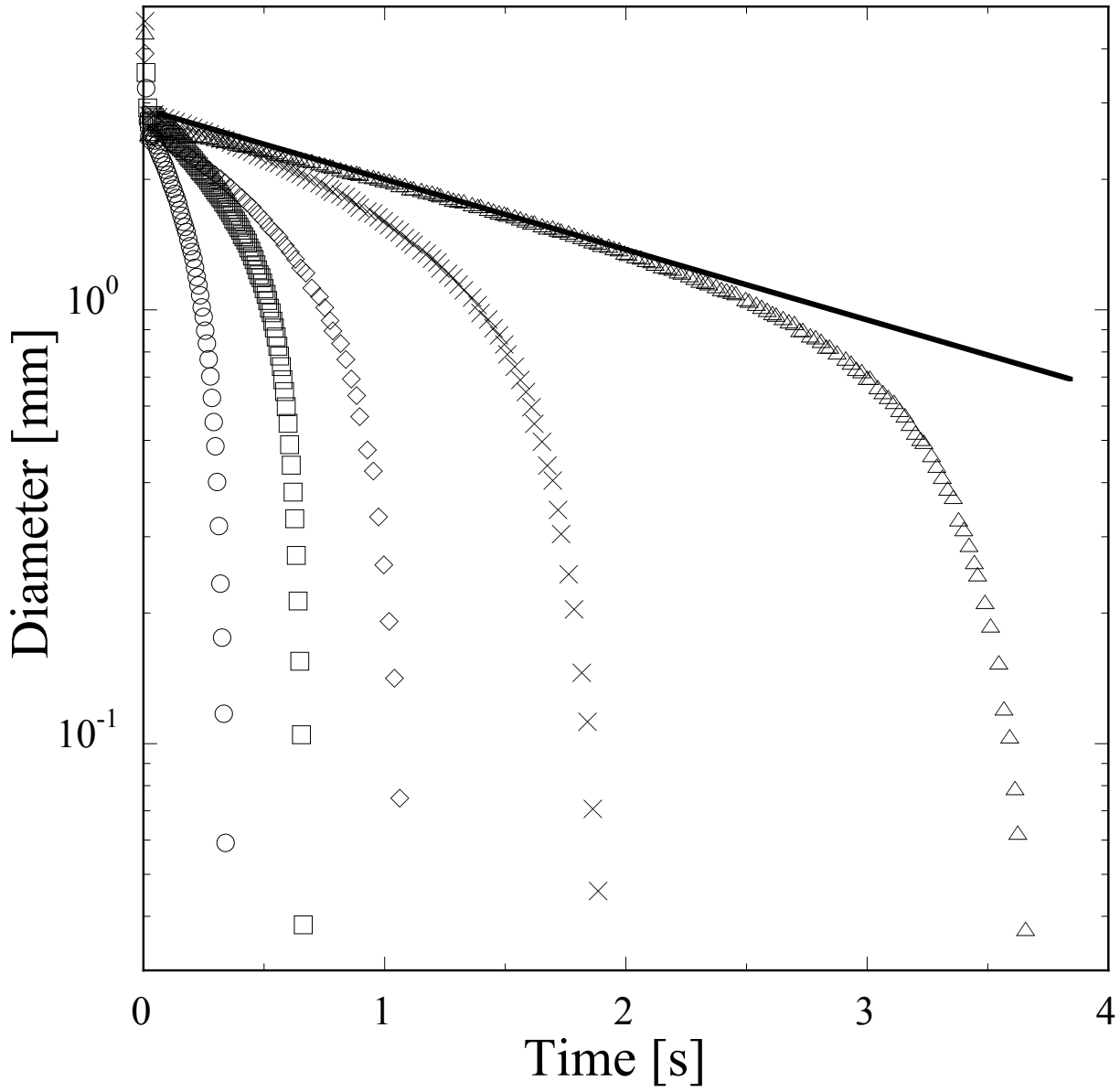

Figure 2-3. Representative CaBER plots of filament diameter evolution over time for five different wt% PSU solutions in NMP (○:16 wt.%, □:18 wt.%, ◇:20 wt.%, ×:22 wt.%, and △:25 wt.%). The solid line demonstrates the region of exponential decay for the 25 wt.% sample, where numerical fitting of Equation 2-1 would yield τ_R.

2.2.4 Fiber Characterization

In the electrospinning process, fluids and operating conditions are selected such that droplet break up modes are suppressed in order to form uniform fibers. In cases where the Rayleigh instability is not sufficiently suppressed, either by strain hardening, premature solidification of the jet, or late stage growth of the surface tension driven instability, the resulting

fiber morphology is characterized as beads-on-string [32]. The non-uniform fiber morphology forms due to the arresting of the droplet breakup instability by strain hardening of the viscoelastic fluid as it drains from the filaments into growing droplets [26]. If the polymer solution is too viscous, the jets will solidify into non-uniform diameter fibers and residual solvent evaporation after collection can yield porous or collapsed fiber shapes; Figure 2-4 shows SEM micrographs indicating both the beads-on-string and roughened non-uniform electrospun fiber morphologies. If the solvent is not sufficiently removed from the polymer jet before reaching the ground plate, "wet" fibers can weld together forming a webbed network morphology; non-cylindrical shapes (ribbons and wrinkled fibers) could also form as residual solvent evaporates after spinning, collapsing the fiber cross-sectional area [33]. Electrospun fibers collected from a parallel-plate electrode configuration exhibit a random nonwoven mesh of fibers with no preferential orientation in the plane of the grounded plate. The fiber size, morphology, and orientation can all be characterized by SEM and analyzed using Matlab and ImageJ image analysis software.

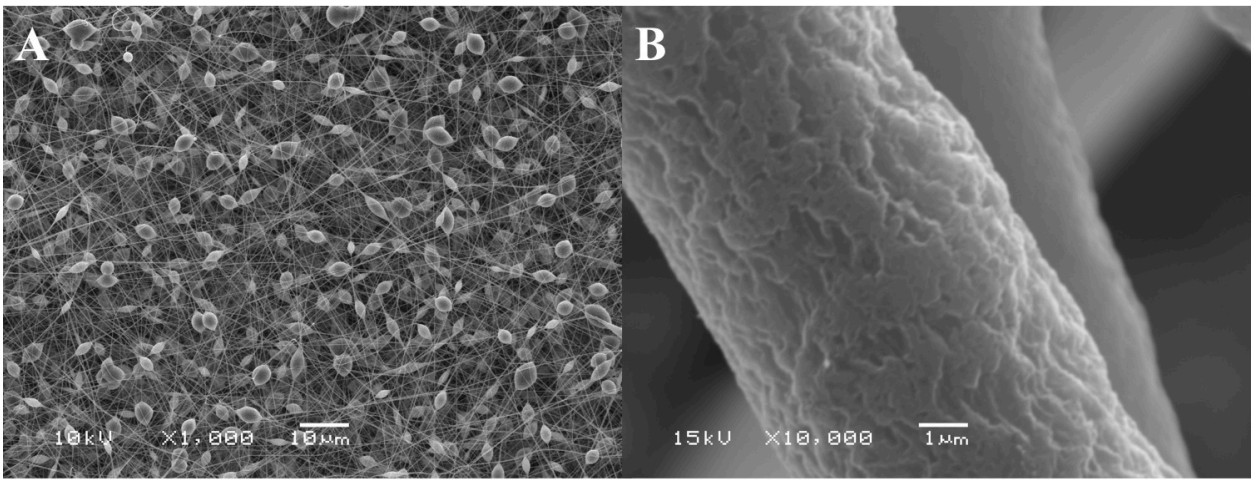

Figure 2-4. SEM micrographs of: (A) PA 6(3)T "beads-on-string" morphology and (B) PSU non-uniform fiber morphology. Scale bar for (A) is 10 μm, scale bar for (B) is 1 μm.

A JEOL JSM-6060 scanning electron microscope (SEM) was used with an accelerating voltage of 10-15 kV and an operating distance of 10 mm to analyze fiber size and morphology. A thin layer of gold (~10 nm) was sputter-coated onto SEM samples prior to imaging. For each sample, ImageJ was used take 100 fiber diameter measurements by manually selecting random fibers from a series of SEM micrographs of 10,000X or higher; the results from which the mean value and standard deviation of the mean were calculated and reported. A representative SEM of

electrospun fibers before and after image analysis using ImageJ (indicating locations of fiber diameter measurements) is shown in Figure 2-5.

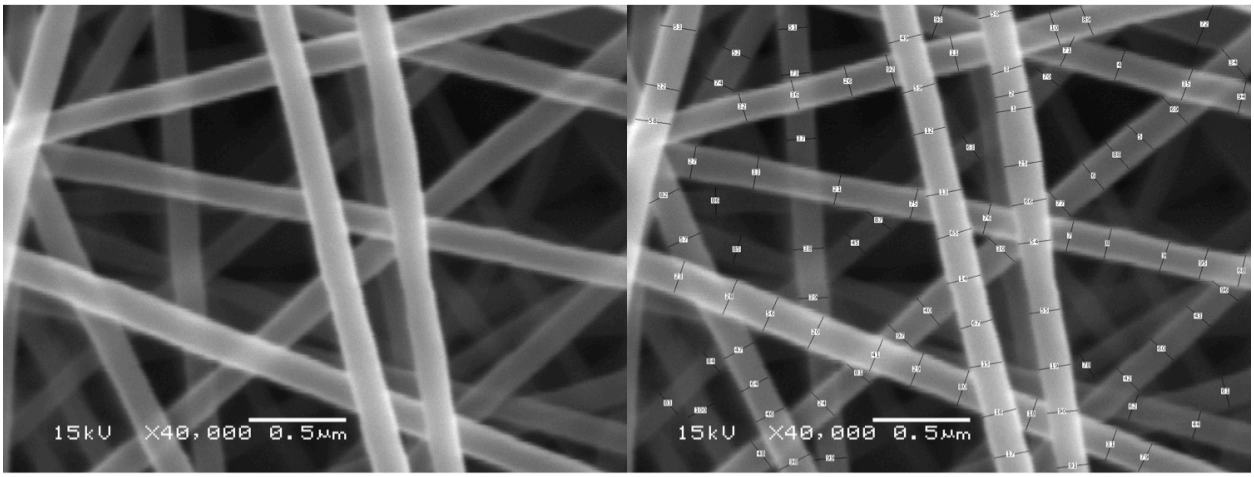

Figure 2-5. SEM micrograph of a representative PA 6(3)T fiber mat (left), and the same image after taking 100 diameter measurements using ImageJ (right). Scale bar for each image is 0.5 μm.

2.3 Results and Discussion

2.3.1 Morphology of Electrospun Nanofibers

Figure 2-6 shows SEM micrographs of electrospun nonwoven mats comprising PA 6(3)T fibers of fairly uniform diameter that span an order of magnitude, from 0.18 ± 0.02 μm up to 1.7 ± 0.13 μm. Similarly, nonwoven mats of PSU fibers were produced with uniform fiber diameters ranging from 0.31 ± 0.06 μm up to 2.2 ± 0.26 μm (Figure 2-7). All of the solution and processing parameters for these experiments are provided at the end of the chapter (Table 2-2 & Table 2-3). Fibers could also be produced from these polymers outside of the specified range of compositions; however, smaller diameter fibers fabricated from solutions with short relaxation times tended to yield the beads-on-string morphology, previously described, due to insufficient suppression of the Rayleigh instability. Larger diameter fibers produced using higher polymer concentrations tended to yield unusual fiber morphologies such as rough and non-uniform surfaces or non-cylindrical fibers. Such non-uniform fibers were excluded from further jet diameter scaling analysis due to the difficulty in accurately measuring a representative fiber diameter.

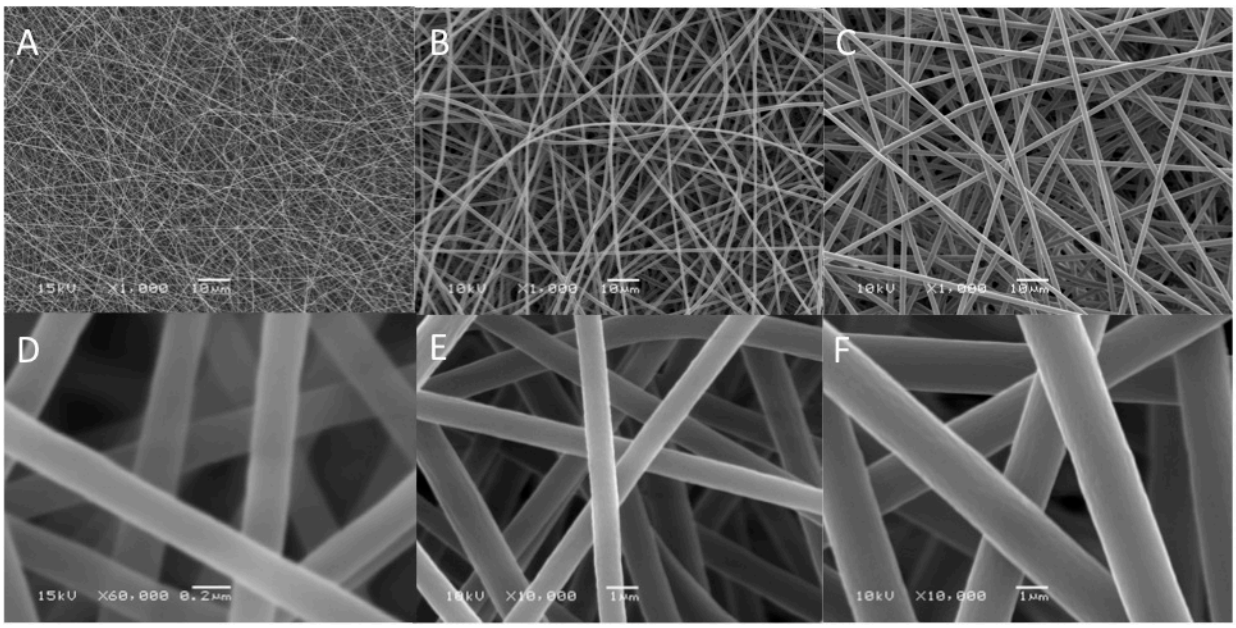

Figure 2-6. SEM micrographs of PA 6(3)T nanofibers illustrating the range of achievable uniform fiber diameters: 0.18 μm fibers (A & D); 0.8 μm (B & E); 2.0 μm fibers (C & F). The scale bars are 10 μm (A, B, C), 1 μm (E, F), and 0.2 μm (D).

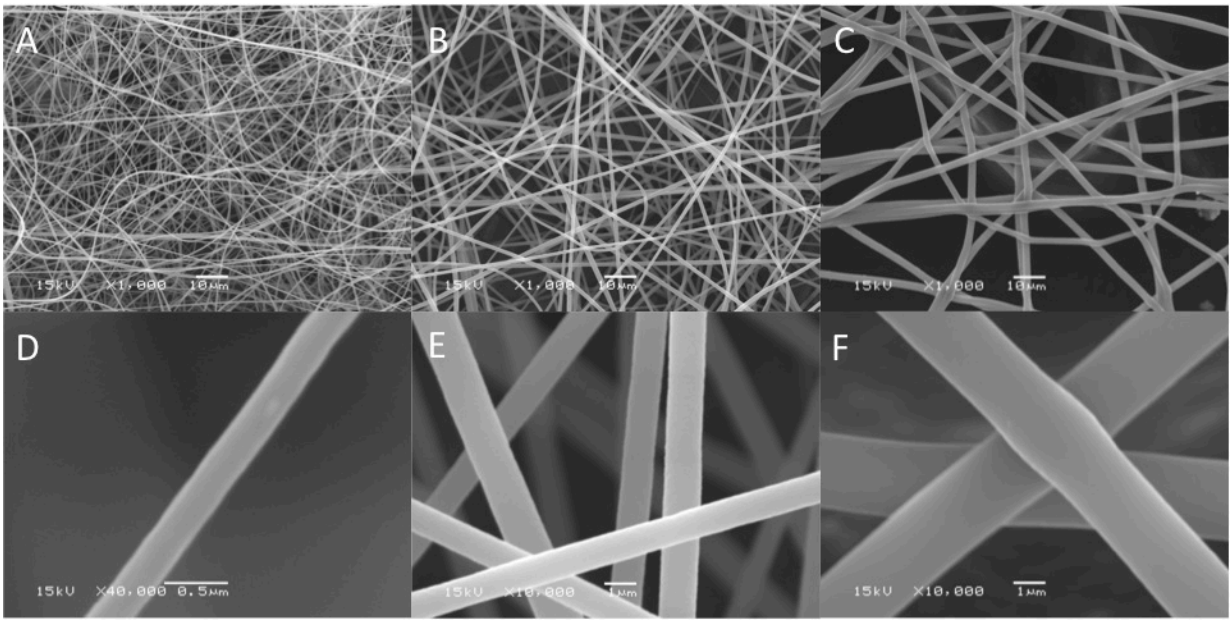

Figure 2-7. SEM micrographs of PSU nanofibers illustrating the range of achievable fiber diameters: 0.31 μm fibers (A & D); 1.0 μm (B & E); 2.4 μm fibers (C & F). The scale bars are 10 μm (A, B, C), 1 μm (E, F), and 0.5 μm (D).

2.3.2 Scaling of Terminal Diameter in Electrospinning

Differences in fiber diameter for a given polymer system were realized by manipulating the solution properties and processing parameters during fabrication of the electrospun fibers. A

summary of the range of solution properties and electrospinning parameters used in this work is shown in Table 1 (complete set of solution properties and electrospinning parameters for PA 6(3)T and PSU are provided in Table 2-2 and Table 2-3 of the Supporting Information). The polymer-solvent systems chosen cover a wide range of conductive properties and viscoelastic regimes; solutions vary over two orders of magnitude in viscosity, conductivity, and relaxation time. Both high surface tension aqueous solutions (PEO-PEG) and lower surface tension organic solutions (PA 6(3)T, PSU, and P(MMA-co-MAA)) were used for dimensional analysis.

Table 2-1. Range of Parameters for Terminal Diameter Analysis

Polymer/Solvent System	η_0 **[Pa s]**	K **[µS/cm]**	γ **[mN/m]**	τ_R **[s]**	E_0 **[V/m]**	h_t **[µm]**
PA 6(3)T in DMF	1.4-10.9	1-3	37.5	0.1-3.4	10^5	1.0-2.5
PA 6(3)T in DMAc	3.6-23.0	0.1-0.2	35.0	0.6-3.6	10^5	1.8-3.2
PA 6(3)T in DMF+FA/AA	1.4-12.7	30-150	37.5	0.2-3.7	10^5	0.4-1.6
PSU in NMP/DMAc	0.8-31.2	0.3-0.7	42.0	0.1-4.8	10^4	1.9-4.8
PSU in NMP/DMAc+FA	0.7-31.5	1-38	42.0	0.2-4.8	10^4	0.9-1.8
PEO-PEG in water [30]	0.1-0.3	55	55.5	0.1-0.6	10^4	4.3-15
P(MMA-co-MAA) in DMF [34]	0.8-1.5	40-112	37.0	0.01-0.07	10^4	0.8-5.3

The diameters of electrospun fibers are affected by a combination of the previously mentioned parameters and since many of the solution parameters are inter-related (either directly or implicitly), determining a universal correlation between these parameters and fiber diameter becomes quite complicated. Figure 2-8 shows how the terminal jet diameter for the organic polymer solutions from this work scales with η_0, τ_R, and K respectively. The terminal jet diameter, h_t, was computed based on the measured (SEM) dry fiber diameter, d_f and the solution concentration according to Equation 2-2:

$$h_t = d_f \sqrt{\frac{1}{c}} \qquad \text{(Equation 2-2)}$$

where c is the concentration of the polymer by volume in the electrospinning solution. As these plots show, the variation in terminal jet diameter cannot be described by any one of these fluid properties alone; however, with the proper manipulation of these parameters along with previously investigated relationships, a generalized terminal diameter scaling law could be achieved.

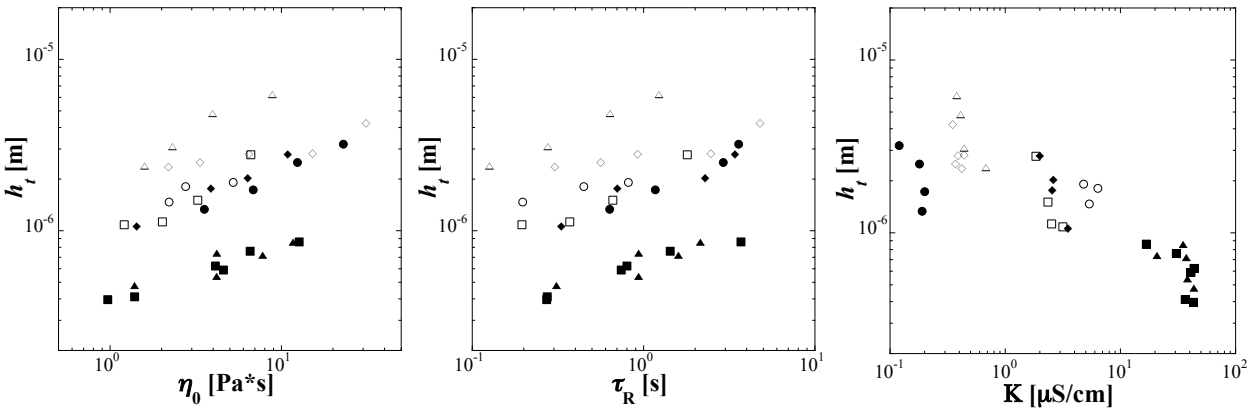

Figure 2-8. Plots of h_t vs. (a) η_0, (b) τ_R, and (c) K for PA 6(3)T and PSU nanofibers. PA 6(3)T in: DMF (◆), DMF+FA (■), DMF+AA (▲), DMAc (●). PSU in: NMP (◇), NMP+FA (□), DMAc (△), DMAc+FA (○).

Fridrikh et al. used a slender thinning viscous jet analysis to argue that stretching of a jet of Newtonian fluid should cease when charge repulsion is balanced by surface tension, and that for a typical electrospinning process Maxwell stresses may be neglected relative to charge repulsion. This analysis led to the following relation between the terminal jet diameter and the key fluid and operating parameters [20]:

$$h_t = \left[\frac{2}{\pi\left(2\ln\chi - 3\right)}\right]^{1/3}\left(\gamma\bar{\varepsilon}\frac{Q^2}{I^2}\right)^{1/3} \qquad \text{(Equation 2-3)}$$

where the pre-factor in brackets is a geometric coefficient of order unity. Bhattacharjee et al. subsequently reported a correlation for electric current I in the form $I \sim EQ^{0.5}K^{0.4}$, and again found good correlation of terminal jet diameter h_t with $(I/Q)^{-2/3}$ for a family of solutions of polymethylmethacrylate (PMMA) with conductivities up to several hundred μS/cm [21]. Combining these observations and assuming that the empirical correlation with conductivity to the 0.4 power is indicative of an underlying scaling to the 1/2 power suggests the following simple correlation for terminal jet diameter entirely in terms of properties that are directly measureable or under operational control:

$$h_t = C\left[\frac{E_{ref}^2 Q_{ref} K_{ref}}{I_{ref}^2}\right]^{1/3}\left[\frac{\gamma\varepsilon Q}{E^2 K}\right]^{1/3} \qquad \text{(Equation 2-4)}$$

where the pre-factor C is again a constant of order unity, and E_{ref}, Q_{ref}, K_{ref}, and I_{ref} are normalizing reference values for a standard fluid (glycerol) as described in Bhattacharjee et al.

[21]. Applying Equation 2-4 to the PA 6(3)T and PSU fibers from this work, as well as to PEO [30] and P(MMA-co-MAA) [34] fibers reported previously by our research group, we obtain the plot of h_t vs. $(\gamma\varepsilon Q/E^2K)^{1/3}$ shown in Figure 2-9. The trend line inserted on the plot shows the expected scaling of the fiber size by Fridrikh's analysis. It should be noted that the deviations from the expected scaling are significant as indiacted by a low coefficient of determination (R^2=0.419).

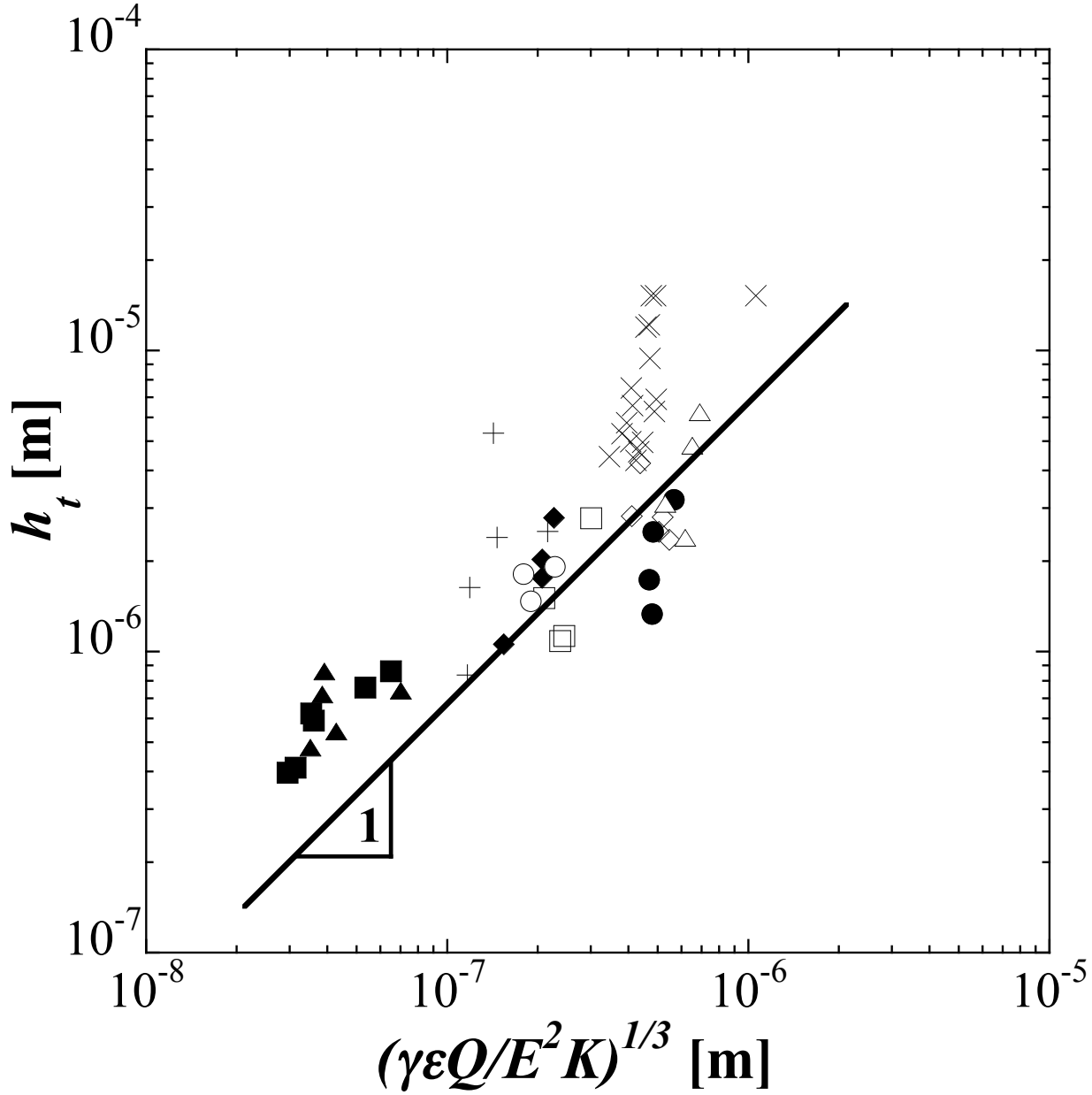

Figure 2-9. Plot of h_t vs. $(\gamma\varepsilon Q/E^2K)^{1/3}$ for PA 6(3)T, PSU, and PEO fibers. PA 6(3)T in: DMF (◆), DMF+FA (■), DMF+AA (▲), DMAc (●). PSU in: NMP (◇), NMP+FA (□), DMAc (△), DMAc+FA (○). PEO-PEG in water (×), P(MMA-co-MAA) in DMF (+).

In the absence of an electric field, a thinning polymer filament can propagate very differently depending on whether the solution exhibits Newtonian or viscoelastic behavior. The relevant model for determining the thinning behavior is based on the relative magnitudes of the visco-capillary, inertio-capillary, and viscoelastic time-scales: $t_v=\eta_0 R_0/\gamma$, $t_R=\rho R_0^3/\gamma$ and τ_R respectively, where R_0 is the radius of a circular nozzle from which the fluid is exiting [35]. For all solutions used in this work, both t_v and τ_R were much larger than t_r suggesting that visco-capillary and viscoelastic time-scales were the dominant factors for the thinning polymer filament in the absence of an electric field. A review by McKinley in 2005 compiled a plot of the inter-relationships between different viscoelastic solutions for filament thinning represented as a function of the Deborah number and the Ohnesorge number [35]. The Deborah number, $De = \tau_R / t^*$, is a ratio of the longest relaxation time of the fluid to the characteristic time scale of the process, taken here to be $t^* = R_0/v$, where the characteristic velocity of the jet is $v = Q/(\pi R_0^2)$. The Ohnesorge number, $Oh = \eta_0 / \sqrt{\rho\gamma R_0}$, captures the behavior of free surface flows whereby small disturbances can lead to capillary breakup in a fluid jet [36,37]. *Oh*, in this form, can be thought of as a characteristic surface stress that expresses the stability and morphology of the electrospinning jet. Capillary thinning for an inviscid fluid thread ($Oh<1$ and $De<1$) would exhibit potential flow (PF) with the minimum dimensionless thickness approaching $De^{2/3}$ close to filament break-up [38]. A viscous Newtonian fluid ($Oh>1$ and $De<1$) would break linearly as a function of time, with the midpoint radius approaching a minimum scaling of Oh^{-1} [39]. For viscoelastic solutions where there are sufficient elasto-capillary (EC) and visco-capillary (VC) contributions to the filament thinning, the dimensionless minimum jet diameter scales as $(De/Oh)^{1/2}$ depending on the limit of the radius length-scale and dynamical regime of capillary thinning [35,40]. Figure 2-10 plots the values of *De* and *Oh* for the solutions used in the electrospinning experiments for this work; note that most of the solutions lie within the viscoelastic regime of both large *De* & *Oh* (>1) and are thus within the regime of visco-elastic-capillary thinning. The aqueous PEO-PEG solutions were significantly less viscous than the PA 6(3)T or the PSU solutions; however, they both exhibited comparable relaxation times.

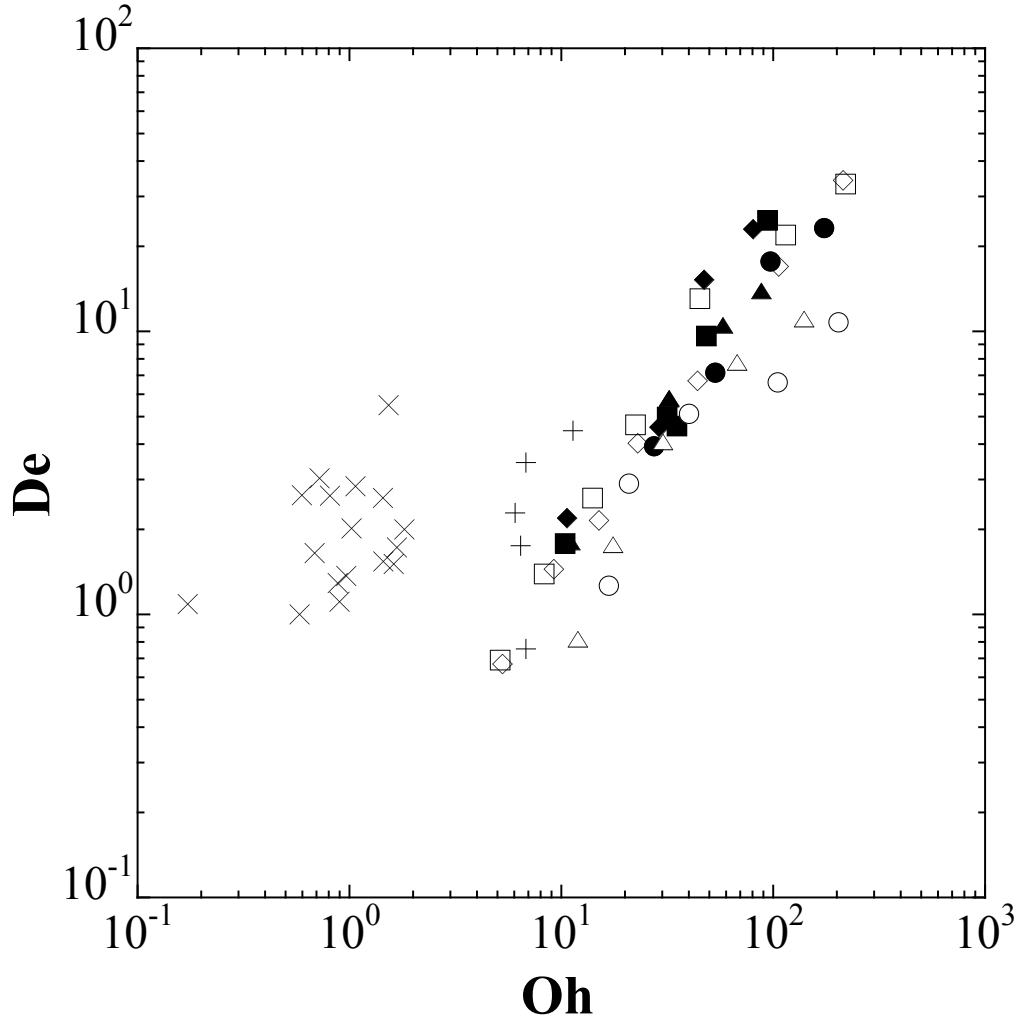

Figure 2-10. Relationship of *De* and *Oh* for solutions of PA 6(3)T in: DMF (◆), DMF+FA (■), DMF+AA (▲), DMAc (●). PSU in: NMP (◇), NMP+FA (□), DMAc (△), DMAc+FA (○). PEO-PEG in water (×), P(MMA-co-MAA) in DMF (+).

We hypothesize that when polymers are electrospun from solutions with significantly different viscoelastic moduli ($G=\eta_0/\tau_R$), large deviations from the Fridrikh scaling (containing no viscoelastic component) become apparent. Combining the scaling argument of the surface tension-charge repulsion balance with a viscoelastic-capillary scaling term, we therefore come to a new scaling law for the terminal jet radius of electrospinning based on a combination of empirical observations and the slender-thinning jet analysis. The additional viscoelastic scaling factor of $[\tau_R^{\,a} \bullet \eta_0^{\,b}]$ was determined by inputting values for the exponents, *a* and *b,* between -5 and +5 (increments of 0.25) and calculating the coefficient of determination (R^2) for the experimental data. A contour plot of the calculated R^2 values for (a,b) in the range of ($-1<a,b<1$) is shown in

Figure 2-11, with the optimum correlation occurring at (a=0.5, b=-0.5) corresponding to a coefficient of determination of 0.741.

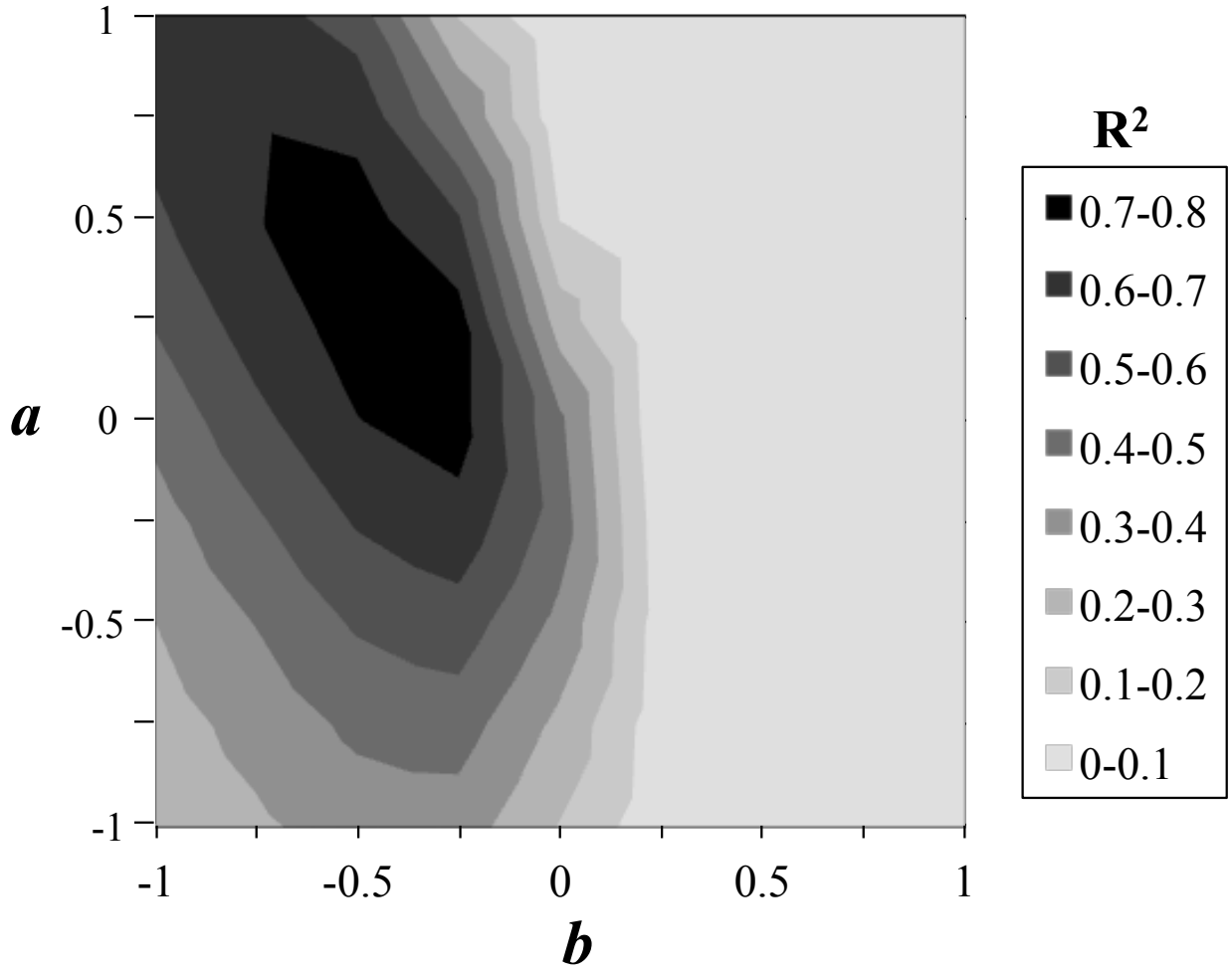

Figure 2-11. 2D contour plot of the coefficient of determination, R^2, as a function of the two proposed scaling parameters, *a* & *b*. Note that the best correlation (largest value for R^2) occurs at the point (a=0.5, b=-0.5).

The empirically determined viscoelastic scaling parameter, $(\tau_R/\eta_0)^{1/2}$, can be interpreted as the inverse of the viscoelastic modulus to the one half power. This scaling factor correlates well with previous theoretical analysis for viscoelastic solutions where there are sufficient elasto-capillary (EC) and visco-capillary (VC) contributions to the filament thinning [40]. By utilizing $(\tau_R/\eta_0)^{1/2}$ as the optimum correction factor for viscoelastic effects of the thinning jet on Fridrikh's analysis (here, non-dimensionalized as $[De/Oh]^{1/2}$ since $\tau_R \sim De$ and $\eta_0 \sim Oh$), we now have a new proposed relationship for the terminal jet diameter, h_t as:

$$h_t = C'\left[\frac{De}{Oh}\right]^{1/2}\left[\frac{\gamma\varepsilon Q}{E^2 K}\right]^{1/3} \qquad \text{(Equation 2-5)}$$

where C' is again, the constant C from Equation 2-4, but now also incorporating the normalizing reference values E_{ref}, Q_{ref}, K_{ref}, and I_{ref} for simplicity. When the observed values for the terminal jet diameter are plotted against this new scaling law in Figure 2-12, we see a better fit (R^2=0.741) for the terminal diameter than from Figure 2-9 (R^2=0.419) which can be attributed to the presence of the new inverse viscoelastic modulus term. One of the most important aspects of this scaling correlation is that all of the variables within the relationship contain only measurable fluid properties and controllable operating parameters; therefore, this accurate and refined scaling law can be utilized to determine electrospun fiber diameters with high precision. The optimal viscoelastic correction factor scaling was found to be (a=0.5, b=-0.5); however, this result was based on the assumption that the Fridrikh analysis is correct and that the viscoelastic term can be optimized independently of the surface tension-charge repulsion term. Further investigation to the validity of these scaling values and the inter-relation between charge repulsion, surface tension, and viscoelastic effects by theoretical determination would be of great utility. The universality of this correlation can be further tested with additional measurements of terminal jet diameters over a broader range of polymers, solvents, and processing parameters.

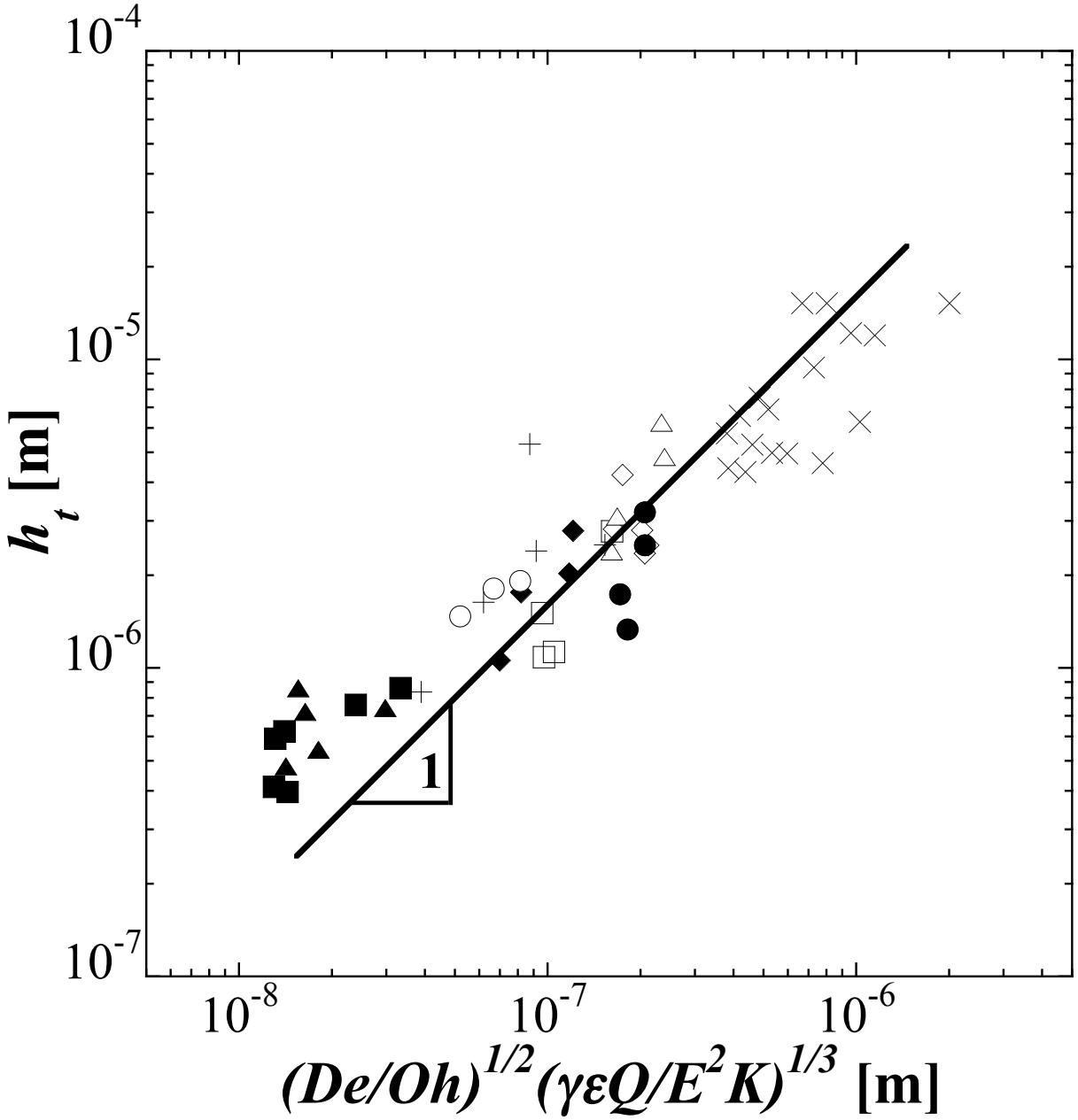

Figure 2-12. Plot of h_t vs. $(De/Oh)^{1/2}(\gamma\varepsilon Q/E^2K)^{1/3}$ for PA 6(3)T in: DMF (◆), DMF+FA (■), DMF+AA (▲), DMAc (●). PSU in: NMP (◇), NMP+FA (□), DMAc (△), DMAc+FA (○). PEO-PEG in water (×), P(MMA-co-MAA) in DMF (+).

2.4 Concluding Remarks

Prediction of the fiber size during electrospinning based on solution properties and operating parameters alone is a non-trivial task, requiring extensive data collection and analysis

to determine accurately. Changes in a single fluid or processing parameter can affect the jet and/or fiber formation through several mechanisms and a universal scaling law would be of high utility for the nanofiber industry. The model presented here predicts a reduced terminal jet diameter by combining previous work on balancing surface charge repulsion and surface tension as well as visco-elastic-capillary thinning analysis with empirical evidence of fiber-size correlation with solution viscoelasticity. The final result, $h_t=C'[De/Oh]^{1/2}[\gamma\varepsilon Q/E^2K]^{1/3}$, is a novel scaling relationship that correlates well with the terminal jet diameter of electrospun fibers based on measurable solution properties and processing parameters not accounted for in previous scaling laws. The scaling presented here was found to predict terminal jet diameters more accurately than the previously proposed Fridrikh analysis for over approximately two orders of magnitude and is applicable for aqueous and organic solutions over a wide range of polymer concentrations, conductivities, viscosities, surface tensions, and relaxation times. Further refining of the proposed model may be required to cover a wider range of solutions and processing parameters; however, the modified scaling law can be used to accurately predict and control electrospun fiber size over a wide range of terminal jet diameters.

2.5 Acknowledgments

Funding for this portion of the thesis was provided by the National Science Foundation through grant number CMMI-0700414 and the Masdar Institute of Science & Technology. The author would like to thank Professor Pradipto K. Bhattacharjee from Monash University, Australia for insightful discussions on terminal jet scaling. The author would also like to acknowledge the MIT Institute of Soldier Nanotechnology for use of facilities.

2.6 Solution Properties and Electrospinning Parameters

This section contains tables for the solution properties (Table 2-2) and electrospinning parameters (Table 2-3) for each solution and electrospinning experiment performed for this section of the thesis work.

Table 2-2. PA 6(3)T & PSU Solution Properties

Polymer	Solvent	Concentration [g/mL]	η_0 [Pa s]	K [µS/cm]	γ [mN/m]	ε_0	τ_R [s]
PA 6(3)T	DMF	0.195	N/A	1.91	36.9	38	0.11
PA 6(3)T	DMF	0.215	1.43	3.51	38.2	38	0.33
PA 6(3)T	DMF	0.246	3.88	2.56	37.7	38	0.70
PA 6(3)T	DMF	0.277	6.36	2.62	38.4	38	2.29
PA 6(3)T	DMF	0.297	10.9	2.00	38.8	38	3.42
PA 6(3)T	DMAc	0.214	3.55	0.19	35.8	37	0.63
PA 6(3)T	DMAc	0.244	6.85	0.20	35.3	37	1.17
PA 6(3)T	DMAc	0.275	12.4	0.18	34.9	37	2.92
PA 6(3)T	DMAc	0.296	23.0	0.12	37.3	37	3.59
PA 6(3)T	DMF/FA	0.195	N/A	43.1	36.9	38	0.27
PA 6(3)T	DMF/FA	0.215	1.39	36.6	37.6	38	0.28
PA 6(3)T	DMF/FA	0.246	4.59	41.0	36.1	38	0.74
PA 6(3)T	DMF/FA	0.277	6.57	30.6	39.0	38	1.43
PA 6(3)T	DMF/FA	0.297	12.7	16.8	38.6	38	3.70
PA 6(3)T	DMF/FA	0.246	4.12	43.6	36.0	38	0.80
PA 6(3)T	DMF/AA	0.215	1.39	43.5	33.5	38	0.31
PA 6(3)T	DMF/AA	0.246	4.19	38.3	35.6	38	0.94
PA 6(3)T	DMF/AA	0.277	7.78	37.4	38.0	38	1.60
PA 6(3)T	DMF/AA	0.297	11.7	35.1	37.4	38	2.15
PA 6(3)T	DMF/AA	0.246	4.20	20.8	35.8	38	0.94
PSU	NMP	0.192	1.33	0.60	40.5	32	0.21
PSU	NMP	0.214	2.19	0.42	41.2	32	0.30
PSU	NMP	0.236	3.35	0.37	41.6	32	0.56
PSU	NMP	0.270	6.47	0.39	42.1	32	0.92
PSU	NMP	0.304	15.2	0.44	39.8	32	2.47
PSU	NMP	0.327	31.2	0.35	41.5	32	4.78
PSU	DMAc	0.200	1.59	0.68	37.5	37	0.13
PSU	DMAc	0.221	2.31	0.44	36.9	37	0.28
PSU	DMAc	0.253	3.97	0.41	36.9	37	0.64
PSU	DMAc	0.286	8.85	0.38	36.5	37	1.23
PSU	DMAc	0.308	18.1	0.36	35.7	37	1.79
PSU	NMP/FA	0.192	1.21	3.17	41.4	32	0.20
PSU	NMP/FA	0.214	2.02	2.53	40.3	32	0.37
PSU	NMP/FA	0.236	3.25	2.35	41.0	32	0.66
PSU	NMP/FA	0.270	6.63	1.85	42.1	32	1.80
PSU	NMP/FA	0.304	16.7	1.58	41.4	32	3.07
PSU	NMP/FA	0.327	31.5	1.31	40.0	32	4.81
PSU	DMAc/FA	0.200	2.21	5.37	37.1	37	0.20
PSU	DMAc/FA	0.221	2.76	6.38	37.4	37	0.45
PSU	DMAc/FA	0.253	5.23	4.79	36.3	37	0.82
PSU	DMAc/FA	0.286	13.6	5.45	35.7	37	1.07

Table 2-3. PA 6(3)T and PSU Electrospinning Parameters

Polymer	Solvent	Concentration [g/mL]	Q [m^3/s]	E_0 [V/m]	h_t [µm]	d_f [µm]
PA 6(3)T	DMF	0.195	1.33E-10	205333	N/A	Beads/String
PA 6(3)T	DMF	0.215	1.33E-10	122400	1.0837	0.4748
PA 6(3)T	DMF	0.246	1.66E-10	102667	1.8905	0.8860
PA 6(3)T	DMF	0.277	1.66E-10	102000	1.9473	0.9684
PA 6(3)T	DMF	0.297	1.66E-10	102667	2.5626	1.3196
PA 6(3)T	DMAc	0.214	1.66E-10	102667	N/A	Beads/String
PA 6(3)T	DMAc	0.244	1.66E-10	102667	1.8202	0.8496
PA 6(3)T	DMAc	0.275	1.66E-10	102667	2.6017	1.2892
PA 6(3)T	DMAc	0.296	1.66E-10	102667	3.2426	1.6670
PA 6(3)T	DMF/FA	0.195	3.33E-11	205333	0.4304	0.1796
PA 6(3)T	DMF/FA	0.215	3.33E-11	205333	0.4368	0.1914
PA 6(3)T	DMF/FA	0.246	3.33E-11	154000	0.5142	0.2410
PA 6(3)T	DMF/FA	0.277	3.33E-11	102667	0.6398	0.3182
PA 6(3)T	DMF/FA	0.297	3.33E-11	102667	0.7706	0.3968
PA 6(3)T	DMF/FA	0.246	3.33E-11	154000	0.6871	0.3220
PA 6(3)T	DMF/AA	0.215	3.33E-11	150000	0.4738	0.2076
PA 6(3)T	DMF/AA	0.246	5.00E-11	150000	0.5019	0.2352
PA 6(3)T	DMF/AA	0.277	3.33E-11	150000	0.5920	0.2944
PA 6(3)T	DMF/AA	0.297	3.33E-11	150000	N/A	Non-uniform
PA 6(3)T	DMF/AA	0.246	8.00E-11	123000	0.7788	0.3650
PSU	NMP	0.192	3.33E-10	72000	N/A	Beads/String
PSU	NMP	0.214	3.33E-10	80000	1.9397	0.8058
PSU	NMP	0.236	1.66E-10	68000	2.4320	1.0610
PSU	NMP	0.270	1.66E-10	64000	2.7345	1.2760
PSU	NMP	0.304	1.66E-10	83333	2.7871	1.3800
PSU	NMP	0.327	1.66E-10	86666	3.7272	1.9140
PSU	DMAc	0.200	8.33E-10	85000	2.2674	0.9106
PSU	DMAc	0.221	3.33E-10	83333	3.0395	1.2832
PSU	DMAc	0.253	3.33E-10	63333	4.7797	2.1590
PSU	DMAc	0.286	3.33E-10	60000	9.1585	4.3984
PSU	DMAc	0.308	3.33E-10	73333	11.7319	5.8470
PSU	NMP/FA	0.192	1.66E-10	72000	0.9327	0.3670
PSU	NMP/FA	0.214	1.66E-10	76000	1.1362	0.4720
PSU	NMP/FA	0.236	1.66E-10	100000	1.5871	0.6924
PSU	NMP/FA	0.270	1.66E-10	66666	2.3895	1.1150
PSU	NMP/FA	0.304	1.66E-10	83333	N/A	Non-uniform
PSU	NMP/FA	0.327	1.66E-10	83333	N/A	Non-uniform
PSU	DMAc/FA	0.200	3.33E-10	112000	1.5239	0.6120
PSU	DMAc/FA	0.221	3.33E-10	112000	1.8192	0.7680
PSU	DMAc/FA	0.253	3.33E-10	88800	1.8264	0.8250
PSU	DMAc/FA	0.286	8.33E-10	110000	N/A	Non-uniform

2.7 References

[1] J. Doshi, D.H. Reneker, Electrospinning process and applications of electrospun fibers, Journal of Electrostatics 35 (1995) 151-160.

[2] G.I. Taylor, Electrically Driven Jets. Proceedings of the royal Society of London. Series A: Mathematical and Physical Sciences 313 (1969) 453-475.

[3] R.G. Fleming, C.J. Murphy, G.A. Abrams, S.L. Goodman, P.F. Nealey, Effects of synthetic micro- and nano-structured surfaces on cell behavior, Biomaterials 20 (1999) 573-588.

[4] J.A. Matthews, G.E. Wnek, D.G. Simpson, and G.L. Bowlin, Electrospinning of Collagen Nanofibers, Biomacromolecules 3 (2002) 232-238.

[5] M.L. Ma, Y. Mao, M. Gupta, K.K. Gleason, and G.C. Rutledge, Superhydrophobic fabrics produced by electrospinning and chemical vapor deposition, Macromolecules 38 (2005) 9742-9748.

[6] A. Tuteja, W. Choi, M.L. Ma, J.M. Mabry, S.A. Mazzella, G.C. Rutledge, G.H. McKinley, R.E. Cohen, Designing superoleophobic surfaces, Science 318 (2007) 1618-1622.

[7] E.R. Kenawy, G.L. Bowlin, K. Mansfield, J. Layman, D.G. Simpson, E.H. Sanders, G.E. Wnek, Release of tetracycline hydrochloride from electrospun poly(ethylene-co-vinylacetate), poly(lactic acid), and a blend, Journal of Controlled Release 81 (2002) 57-64.

[8] X.Y. Wang, C. Drew, S.H. Lee, K.J. Senecal, J. Kumar, and L.A. Samuelson, Electrospun nanofibrous membranes for highly sensitive optical sensors Nano Letters 2 (2002) 1273-1275.

[9] Y. Yang, A. Centrone, L. Chen, F. Simeon, T.A. Hatton, and G.C. Rutledge, Highly porous electrospun polyvinylidene fluoride (PVDF)-based carbon fiber, Carbon 49 (2011) 3395-3403.

[10] Y. Yang, F. Simeon, T.A. Hatton, and G.C. Rutledge, Polyacrylonitrile-based electrospun carbon paper for electrode applications, Journal of Applied Polymer Science 124 (2012) 3861-3870.

[11] S.W. Choi, Y.-Z. Fu, Y.R. Ahn, S.M. Jo, and A. Manthiram, Nafion-impregnated electrospun polyvinylidene fluoride composite membranes for direct methanol fuel cells, Journal of Power Sources 180 (2008) 167-171.

[12] R. Bajon, S. Balaji, and S.M. Guo, Electrospun Nafion Nanofiber for Proton Exchange Membrane Fuel Cell Application, Journal of Fuel Cell Science Technology 6 (2009) 031004.

[13] S.A. Theron, E. Zussman, and A.L. Yarin, Experimental investigation of the governing parameters in the electrospinning of polymer solutions, Polymer 45 (2004) 2017-2030.

[14] C.J. Johnson, G.G. Chase, A.L. Yarin, D.H. Reneker, Effects of parameters on nanofiber diameter determined from electrospinning model, Polymer 48 (2007) 6913-6922.

[15] P. Gupta, C. Elkins, T.E. Long, G.L. Wilkes, Electrospinning of linear homopolymers of poly(methyl methacrylate): exploring relationships between fiber formation, viscosity, molecular weight and concentration in a good solvent, Polymer 46 (2005) 4799-4810.

[16] J.H. Yu, and G.C. Rutledge, Encyclopedia of Polymer Science & Technology (2007).

[17] D. Saville, Electrohydrodynamics: The Taylor-Melcher leaky dielectric model, Annual Review Of Fluid Mechanics 29 (1997) 27-64.

[18] M.M Hohman, M. Shin, G.C. Rutledge, M.P. Brenner, Electrospinning and electrically forced jets. I. Stability theory, Physics of Fluids 13 (2001) 2201-2220.

[19] M.M Hohman, M. Shin, G.C. Rutledge, M.P. Brenner, Electrospinning and electrically forced jets. II. Applications. Physics of Fluids 13 (2001) 2221-2236.

[20] S.V. Fridrikh, J.H. Yu, M.P. Brenner, G.C. Rutledge, Controlling the Fiber Diameter during Electrospinning, Physical Review Letters 90 (2003) 144502.

[21] P.K. Bhattacharjee, T.M. Schneider, M.P. Brenner, G.H. McKinley, G.C. Rutledge, On the measured current in electrospinning, Journal of Applied Physics 107 (2010) 044306.

[22] J.J. Feng, Stretching of a straight electrically charged viscoelastic jet, Journal Of Non-Newtonian Fluid Mechanics 116 (2003) 55-70.

[23] A.F. Spivak, Y.A. Dzenis, D.H. Reneker, A model of steady state jet in the electrospinning process, Mechanics Research Communications 27 (2000) 37-42.

[24] M.E. Helgeson, and N.J. Wagner, A correlation for the diameter of electrospun polymer nanofibers, AIChE Journal 53 (2007) 51-55.

[25] M.E. Helgeson, K.N. Grammatikos, J.M Deitzel, N.J. Wagner, Theory and kinematic measurements of the mechanics of stable electrospun polymer jets, Polymer 49 (2008) 2924-2936.

[26] G.C. Rutledge, S.V. Fridrikh, Formation of Fibers by Electrospinning, Advanced Drug Delivery Reviews 59 (2007) 1384-1391.

[27] F.K. Hansen, and G. Rødsrud, Surface-tension by pendant drop 1. A fast standard instrument using computer image analysis, Journal of Colloid and Interface Science 141 (1991) 1-9.

[28] S. Anna, G. H. McKinley, Elasto-capillary thinning and breakup of model elastic liquids, Journal Of Rheology 45 (2001) 115-138.

[29] L. Rodd, T. Scott, J. Cooper-White, G. H. McKinley, Capillary break-up rheometry of low-viscosity elastic fluids, Applied Rheology 15 (2005) 12-27.

[30] J.H. Yu, S.V. Fridrikh, G.C. Rutledge, The role of elasticity in the formation of electrospun fibers, Polymer 47 (2006) 4789-4797.

[31] L. Chen, L. Bromberg, T.A. Hatton, G.C. Rutledge, Electrospun cellulose acetate fibers containing chlorhexidine as a bactericide Polymer, 49 (2008) 1266-1275.

[32] R. Jaeger, H. Schonherr, G.J. Vansco, Chain packing in electro-spun poly(ethylene oxide) visualized by atomic force microscopy, Macromolecules 29 (1996) 7634-36.

[33] C.L. Pai, M.C. Boyce, G.C. Rutledge, Morphology of porous and wrinkled fibers of polystyrene electrospun from dimethylformamide, Macromolecules 42 (2009) 2102-2114.

[34] M. Wang, A.J. Hsieh, and G.C. Rutledge, Electrospinning of poly(MMA-co-MAA) copolymers and their layered silicate nanocomposites for improved thermal properties, Polymer 46 (2005) 3407-3418.

[35] G.H. McKinley, Visco-elasto-capillary thinning and break-up of complex fluids, HML Report Number 05-P-04, (2005).

[36] Y. Christanti, and L.M. Walker, Effect of fluid relaxation time of dilute polymer solutions on jet breakup due to a forced disturbance, Journal of Rheology 46 (2002) 733–748.

[37] J.M. Lopez-Herrera, and A.M. Ganan-Calvo, A note on charged capillary jet breakup of conducting liquids: experimental validation of a viscous one-dimensional model, Journal of Fluid Mechanics 501 (2004) 303–326.

[38] L. Ting, and J.B. Keller, Slender Jets and Thin Sheets with Surface Tension, SIAM Journal on Applied Mathematics 50 (1990) 1533-1546.

[39] J.T. Papageorgiou, Analytical Description of the Break-up of Liquid Jets, Journal of Fluid Mechanics 301 (1995) 109-132.

[40] J.R. Lister, H.A. Stone, Capillary break-up of a viscous thread surrounded by another viscous fluid, Physics of Fluids 10 (1998) 2758-2764.

3. Mechanical and Tribological Properties of Electrospun PA 6(3)T Fiber Mats

Portions of this chapter are reproduced from M.M. Mannarino, G.C. Rutledge, Polymer 52 (2012) 3017-3025, with permission of Elsevier Limited.

3.1 Introduction

Electrostatic fiber formation, or electrospinning, offers a particularly simple and robust method to create polymeric nanofibers of various morphologies and sizes, inexpensively and in large quantities. In electrospinning, a viscoelastic fluid is charged so that a liquid jet is ejected from the surface of the fluid (typically supplied by a needle or spinneret) and accelerated by an electric field towards a collector, typically a grounded plate, thus creating a nonwoven fiber mat or membrane [1]. Modification of the fiber diameter, porosity, surface area, and mechanical properties of the mat by adjusting the processing and solution parameters can be used to tailor electrospun nanofiber mats for various applications. Because of these unique properties and relative ease of fabrication, electrospun fibers and their mats have attracted a significant amount of attention in recent years for a broad range of applications [2,3] including (but not limited to): drug release agents [4], optical sensors [5], and ion-exchange membranes [6,7]. In each of these applications the mechanical response and tribology of the nanofiber mat is likely to be critical to the performance and/or success of the device in service.

Electrospun nanofibers have been reported to exhibit some remarkable increases in elastic stiffness and yield stress for fibers below a critical diameter, whose value varies from material to material [8,9]. The origin of these increases in fiber mechanical properties remains a topic of some debate. Regardless of the diameter-dependent changes in fiber properties, the as-spun mats tend to exhibit consistently low yield stresses (typically 0.5-3 MPa), Young's moduli (typically 20-60 MPa) and toughnesses (typically 0.5-2 MJ/m^3) [10,11]; as-spun untreated nanofiber mats also exhibit low mechanical resilience (<50%) even at small strains of less than 0.02 mm/mm [12]. Occasionally this is an advantage for applications such as tissue engineering where a soft, porous matrix is desirable; however, for many applications of nonwoven mats,

modest improvements in the stiffness or mechanical integrity without significant losses in the porosity would be highly desirable to ensure durable and robust performance. Although many experimental studies have been conducted on the mechanical properties of conventional nonwoven fabrics, there are a limited number of reports that account adequately for the observed mechanical properties of mats comprising electrospun nanofibers. In recent years several research groups have demonstrated significant improvements to the Young's modulus and yield stress of electrospun polymeric fiber mats by various forms of post-spinning techniques such as thermal annealing [13], mechanical drawing [14], hot pressing [15], and solvent vapor treatment [16]. Subjecting a semi-crystalline polymer fiber to heat treatment at a temperature above the crystallization temperature (T_c) of that fiber, but below the equilibrium melting temperature (T_m) of the polymer, can cause the melting of small, imperfect crystals, and the formation of larger, more perfect crystals within the fibers, thus creating a stiffer and tougher matrix [17,18]. With some amorphous polymer nonwovens, annealing has been shown to allow air or gas pockets within the fibers to diffuse out, creating stronger more uniform fibers [19]. In addition, if the heat-treatment of the amorphous polymer nanofiber mats is conducted above the material's glass transition temperature (T_g), deformation and welding between fibers can be observed that would also contribute to changes in mechanical properties due to the increase in the number of junctions, analogous to an increase in the cross-link density of an elastomer.

Various post-spin treatments can improve the mechanical strength and expand the utility of nonwoven nanofiber mats; however, the resistance of electrospun mats to wear remains a significant issue. Figure 3-1 shows an optical photograph of loose fibers, which have been easily removed from the surface of an electrospun mat by gentle contact with fingers in a nitrile glove. In order to improve the robustness of nanofiber mats, both mechanical strengthening and tribological tailoring is required to keep the membrane intact. Investigation of the tribological properties of textiles and fabrics is not unprecedented; Derler et al. measured the friction coefficient and hardness of conventional textiles in contact with human skin equivalents [20], and Gerhardt et al. measured the frictional properties and contact pressure of skin-fabric interactions, for example [21]. The textile industry has used various abrasive and wear testing techniques (such as the Taber abraser) to evaluate the durability of fabrics. Such quantitative testing would be invaluable to the development and commercialization of nanofiber mats. Despite the need for improving the wear resistance of nanofiber mats, to our knowledge there has

still not been any published investigation of their tribological properties or methods for improvement. Quantitative evaluation of the wear resistance of the nanofiber mats is critical for a better understanding of the trends and underlying mechanism of wear occurring in the nanofiber mats. This chapter seeks to quantify the tribology of nanofiber mats, and to demonstrate the improvement of mechanical integrity and wear resistance of electrospun mats by post-spinning thermal treatments, to generate robust membranes.

Figure 3-1. Optical photograph of loose fibers being removed from the surface of an electrospun fiber mat due to gentle contact with a nitrile glove. Scale bar for this image is 1 cm.

3.2 Experimental Method

3.2.1 Materials

Poly(trimethyl hexamethylene terephthalamide) (PA 6(3)T) was purchased from Scientific Polymer Products, Inc. It is an aromatic, amorphous polyamide with a high glass transition temperature (T_g=425 K) and outstanding mechanical properties. The substituent methyl groups in PA 6(3)T suppress crystallization, yielding an amorphous material at all temperatures that is more soluble in organic solvents and easier to process than semi-crystalline

polyamides. As solvent, N,N-dimethyl formamide (DMF) was purchased from Sigma-Aldrich and used as received for creating polymeric solutions. The tensile modulus and yield stress of electrospun PA 6(3)T fibers and mats have been examined in some detail and reported previously [9,22].

3.2.2 Electrospinning of Nanofiber Mats

Nanofiber mats were fabricated by electrospinning from organic polymer solutions using a vertically aligned parallel plate geometry as shown in Figure 3-2. Two aluminum plates, each 12 cm in diameter, were positioned one above the other to achieve a tip-to-collector distance of 25 cm. A high voltage power supply (Gamma High Voltage Research, ES40P) was used to apply an electrical potential of 22 kV to the polymer solution and the top plate. The nozzle consisted of a stainless steel capillary tube (1.6 mm OD, 1.0 mm ID) (Upchurch Scientific) in the center of the top plate. A digitally controlled syringe pump (Harvard Apparatus, PHD 2000) was used to obtain a flow rate of 0.010 mL/min. The jet current was measured as the voltage drop across a 1 MΩ resistor placed in series between the bottom plate and ground (Fluke, 287 true RMS multimeter). The voltage readings were then converted to electrical current using Ohm's law. The entire apparatus was contained within a fume hood to ensure proper ventilation. An anti-stick agent (CP Fluoroglide® from Saint-Gobain Performance Plastics) was sprayed onto the aluminum collector plate to facilitate removal of the electrospun mat.

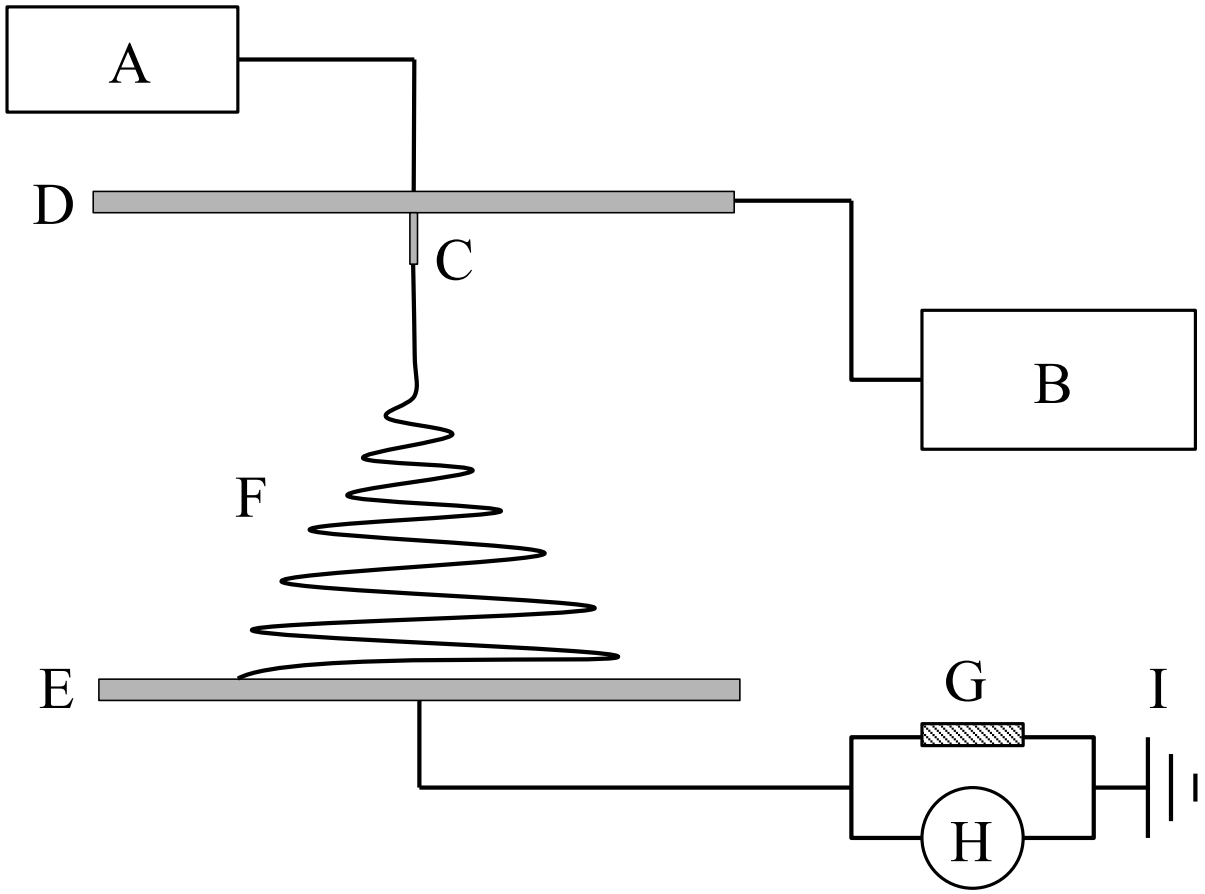

Figure 3-2. Schematic representation of parallel-plate electrospinning apparatus: (A) solution pump; (B) high voltage power supply; (C) capillary tip; (D) upper plate; (E) lower grounding collector plate; (F) whipping polymer fiber jet; (G) resistor; (H) voltage meter; (I) ground.

3.2.3 Morphological Characterization of Nanofiber Mats

A JEOL JSM-6060 scanning electron microscope (SEM) was used to determine the diameter and morphology of the fibers. A thin layer of gold (~10 nm) was sputter-coated onto SEM samples prior to imaging. Fiber diameter was determined by taking 100 diameter measurements of the fibers from a set of SEM micrographs at 10,000X magnification using ImageJ, from which the mean value and standard deviation of the mean were calculated. Porosity of the fiber mats was determined gravimetrically by cutting out rectangular sections and measuring the mass and dimensions of the mat specimen and converting to porosity. Sample thickness was measured with a Mitutoyo digital micrometer with a constant measuring force of 0.5 N. Lateral sample dimensions were determined using a digital caliper. The volume and mass of the specimen were then converted to a porosity using the bulk density of PA 6(3)T (1.12 g/cm^3) and the following equations [23,24],

$$\rho_{app} = \frac{m_{mat}}{h_{mat} \times A_{mat}} \quad \text{(Equation 3-1)}$$

$$\phi = \left(1 - \frac{\rho_{app}}{\rho_{bulk}}\right) \times 100\% \quad \text{(Equation 3-2)}$$

where ρ_{app} is the apparent density, m_{mat} is the mass of mat, h_{mat} is the thickness of mat, A_{mat} is the area of mat, ϕ is the mat porosity (%) and ρ_{bulk} is the bulk density.

3.2.4 Post-electrospinning Treatment of Electrospun Mats

Heat treatment of the electrospun mats was carried out in a Thermolyne lab oven by draping the mat over a 100 mm diameter Pyrex dish and placing it in the oven for 2 hours at a specified temperature. Contact of the mat with the rim of the Pyrex dish was sufficient to prevent the mats from contracting and/or tearing during heat treatment and suspended the sample so that it did not contact or stick to any surfaces. After heat treatment, samples were removed from the oven and allowed to cool before carefully cutting the mat off of the Pyrex dish.

3.2.5 Mechanical Testing

Uniaxial tensile testing of electrospun fiber mats was measured with a Zwick Roell Z2.5 tensile testing machine using a 2.5 kN load cell. Rectangular specimens were cut to 100 mm × 12.5 mm and extended at a constant crosshead speed of 0.50 mm/s with a 50 mm gauge length. Five specimens were tested for each temperature of thermal treatment to determine the mean value; error bars on all plots represent one standard deviation of the mean. The thickness of each specimen was determined from the average of three measurements taken along the gauge length with a Mitutoyo digital micrometer with a constant measuring force of 0.5 N. The force–displacement data as taken from the Zwick was converted to engineering stress–engineering strain results. Engineering stress is defined as the ratio of force to the initial cross-sectional area, and engineering strain is defined as the ratio of the change in length to the original gauge length.

3.2.6 Tribological Testing

The coefficient of friction was measured according to ASTM D-1894-11 [Standard Test Method for Static and Kinetic Coefficients of Friction of Plastic Film and Sheeting] using a custom-made “sled and spring gauge” apparatus. Friction force measurements were taken at a series of normal forces ranging from 0.25-2.5 N with an IMADA push-pull force gauge (10 N capacity and 0.05 N precision), at a testing speed of 0.25 m/s. Five measurements were taken for

each set of heat-treated mats to determine the mean value and standard deviation of the mean. The counter-face used for coefficient of friction measurements was the H-38 Calibrade® standardized abrasion testing wheel used in the abrasive wear testing experiments.

The surface roughness of the nanofiber mats and polymer film were measured using a Veeco surface profiling system, Model "Dektak 150". A 2.5 μm stylus with 3.0 mg tip force was used to scan across 5.0 mm of sample in 30 seconds. The arithmetic average roughness (R_a) was recorded for each sample analysis and the average of five scans was used to determine the mean R_a.

The abrasive wear resistance of the electrospun mats was measured by subjecting the mats to a modified ASTM D-3884-09 [Standard Test Method for Abrasion Resistance of Textile Fabrics (Rotary Platform, Double-Head Method)]. A picture of the Taber abraser and a schematic of the test dimensions are shown in Figure 3-3. Test samples were prepared by carefully cutting out 100 mm diameter circles from an electrospun mat and attaching them to the adhesive side of a 100 mm diameter Polyken® 339 duct closure foil. This prevents the mats from bunching up or shifting during testing. For comparison, a solution cast film was made by depositing 3.0 mL of 20 wt.% PA 6(3)T in DMF on a 100 mm diameter Kapton® sheet and allowing the solvent to evaporate overnight in a fume hood. Five 100 mm specimens were prepared for each temperature of thermal treatment and for each specified number of abrasion cycles to determine the mean value and standard deviation of the mean. H-38 Calibrade® standardized abrasion testing wheels were used with an applied load of 25 or 100 g for 10, 50, 100, 250, 500, and 1000 cycles at 1 revolution per second (25 cm/s). The H-38 Calibrade® standardized Taber abrasion wheel is classified in ASTM D-3884-09 as a very fine-grained abrasive wheel for use in testing woven and nonwoven fabrics as well as delicate textiles. Samples were analyzed for abrasive wear by visual inspection and mass loss using an Ohaus E11140 analytical balance. By measuring the mass loss of the nanofiber mats after a specified number of cycles (or sliding distance), the effective wear rates of the membranes were determined. With the exception of the as-spun sample, the data for mass loss vs. number of cycles for each sample was fitted to a second order polynomial forced through the origin, using the method of least squares. An effective wear rate for each sample was then calculated by taking the value of the tangent to the second order polynomial at 100 cycles. The as-spun sample deteriorated too quickly to measure the mass loss reliably beyond the first 50 cycles; therefore,

the slope of a linear fit through the first three data points was used in calculating the effective wear rate for the untreated nanofiber mat.

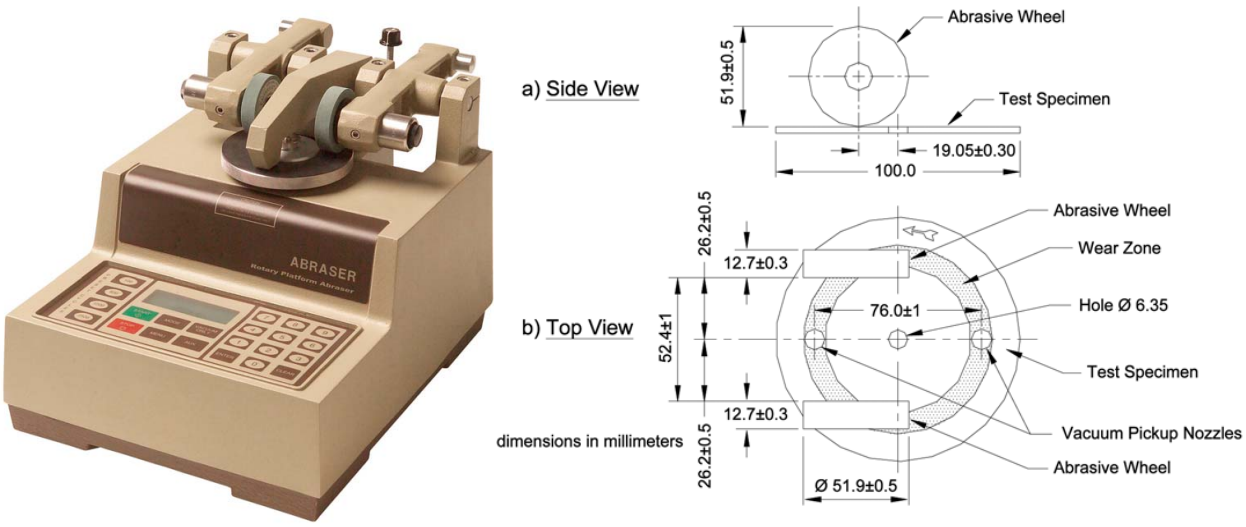

Figure 3-3. Isometric view of the Taber Abraser used (left) and a schematic of the Taber dimensions for the abrading wheel and rotating plate (adapted from ASTM D-3884-09).

3.3 Results and Discussion

3.3.1 Morphology/Porosity of Heat-Treated Electrospun Mats

Electrospun fibers of PA 6(3)T with diameters ranging from 150 nm up to 3.6 μm and their tensile properties have been reported previously by our group [22]. This order of magnitude variation in fiber diameters was achieved by varying solvent composition and polymer concentration as well as processing parameters. Uniform PA 6(3)T fibers having a mean diameter of 463±64 nm were fabricated from a 22 wt.% solution of DMF for use in all of the tests described here. Each nonwoven fiber mat was produced using 1.0 mL of polymer solution to generate a mat of roughly 100 μm thickness and 15 cm in diameter. The mats were then heat-treated at various temperatures close to the T_g of PA 6(3)T (~153 °C as determined by differential scanning calorimetry), which we believe serves to increase the number of weld points between fibers as well as remove any residual solvent and air pockets from the interior of the fibers. Figure 3-4 shows SEM micrographs of PA 6(3)T fibers after 2 hours of heat-treatment at various temperatures spanning a range from below to above T_g. There are no discernable weld points between fibers on the untreated SEM; however at 150 °C thermal treatment, several weld

points become visible, with even more weld points at 160 °C. The 170 °C heat-treated nanofiber mat exhibited extensive fusion between fibers, leading to considerable loss of the original fiber morphology and porosity, creating a webbing effect between fibers.

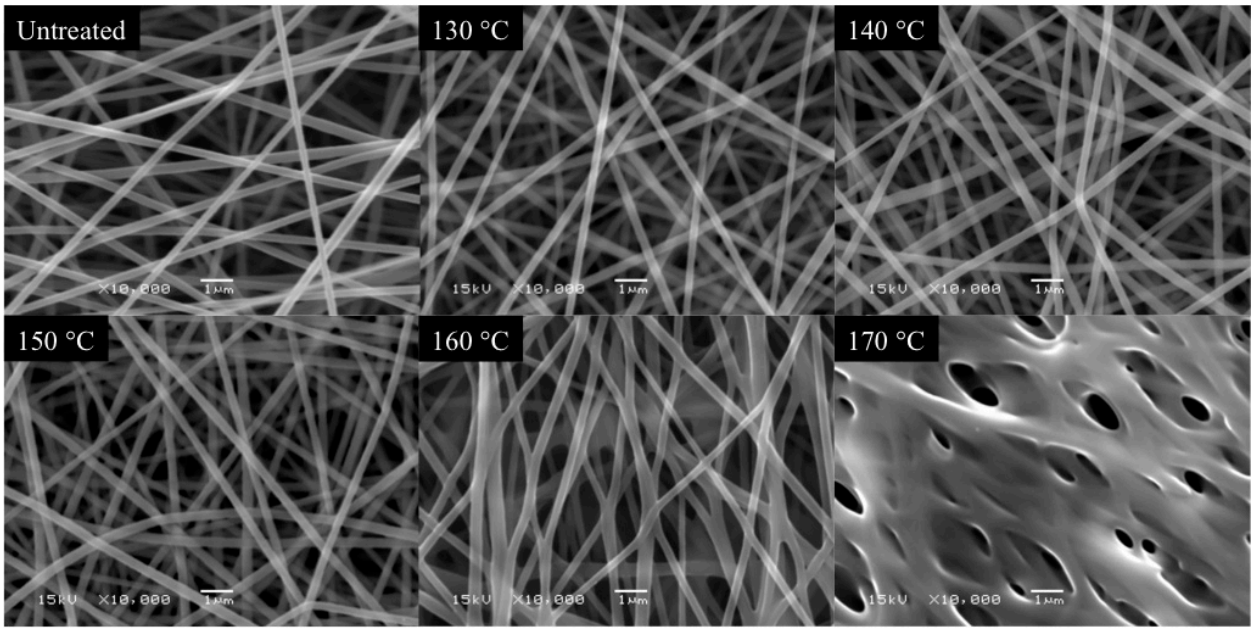

Figure 3-4. SEM Micrographs of PA 6(3)T nanofibers after varying degrees of heat treatment. From upper left to lower right: untreated, and 2 hours thermal annealing at 130, 140, 150, 160 and 170 °C, respectively. Scale bar for each image is 1 μm.

The SEM micrographs show the decrease in pore size between fibers as the temperature of heat-treatment increases, as well as what appears to be a decrease in the overall porosity of the mats. Before the mats were subjected to the heat-treatment, they were typically 100±10 μm in thickness, and it was observed that for the highest annealing temperature (170 °C), the mats can contract to as thin as 60 μm. Figure 3-5 shows a plot of the porosity of PA 6(3)T nanofiber mats after various heat treatments. The nonwoven mats have an inherently high as-spun porosity of 88.5±1.1%, which drops slightly to 85.2±1.5% as the result of mild heat treatment (below the T_g of PA 6(3)T). Annealing at temperatures above the T_g produces a significant drop in porosity. The porosity of the sample after annealing at the highest temperature (170 °C) fell to 62.8±5.1%.

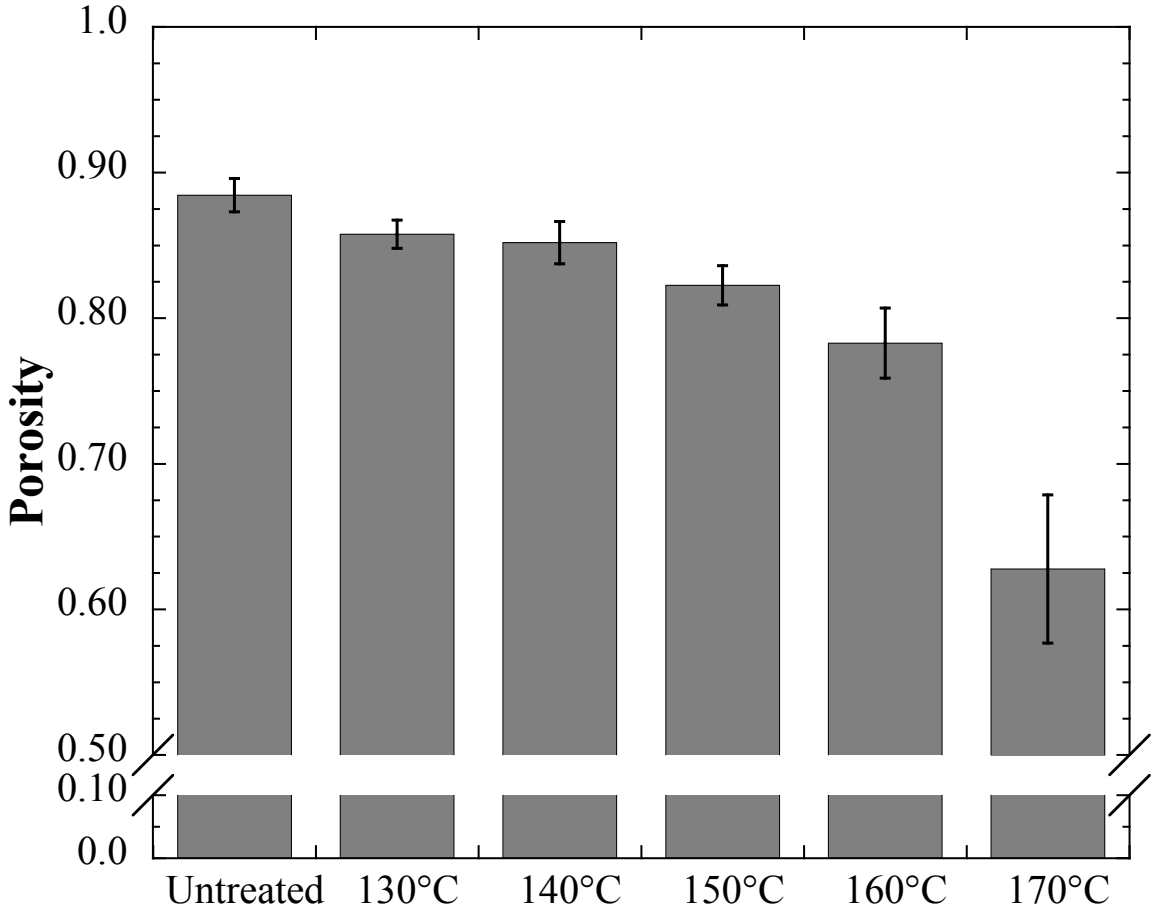

Figure 3-5. Porosity of PA 6(3)T nanofiber mats after 2 hours of thermal annealing at various temperatures.

3.3.2 Mechanical Properties of Heat-Treated Electrospun Mats

Uniaxial, constant strain-rate tensile testing was employed to observe the effect of varying degrees of heat-treatment on the mechanical response of nanofiber mats. Representative plots of the tensile behavior of heat-treated electrospun mats is shown in Figure 3-6; note the increase in modulus and yield stress with increasing temperature of heat-treatment and the transition from somewhat ductile-like failure for materials annealed below 150°C, due to the propagation of tears in the fabric, to brittle fracture for those annealed at or above 150 °C.

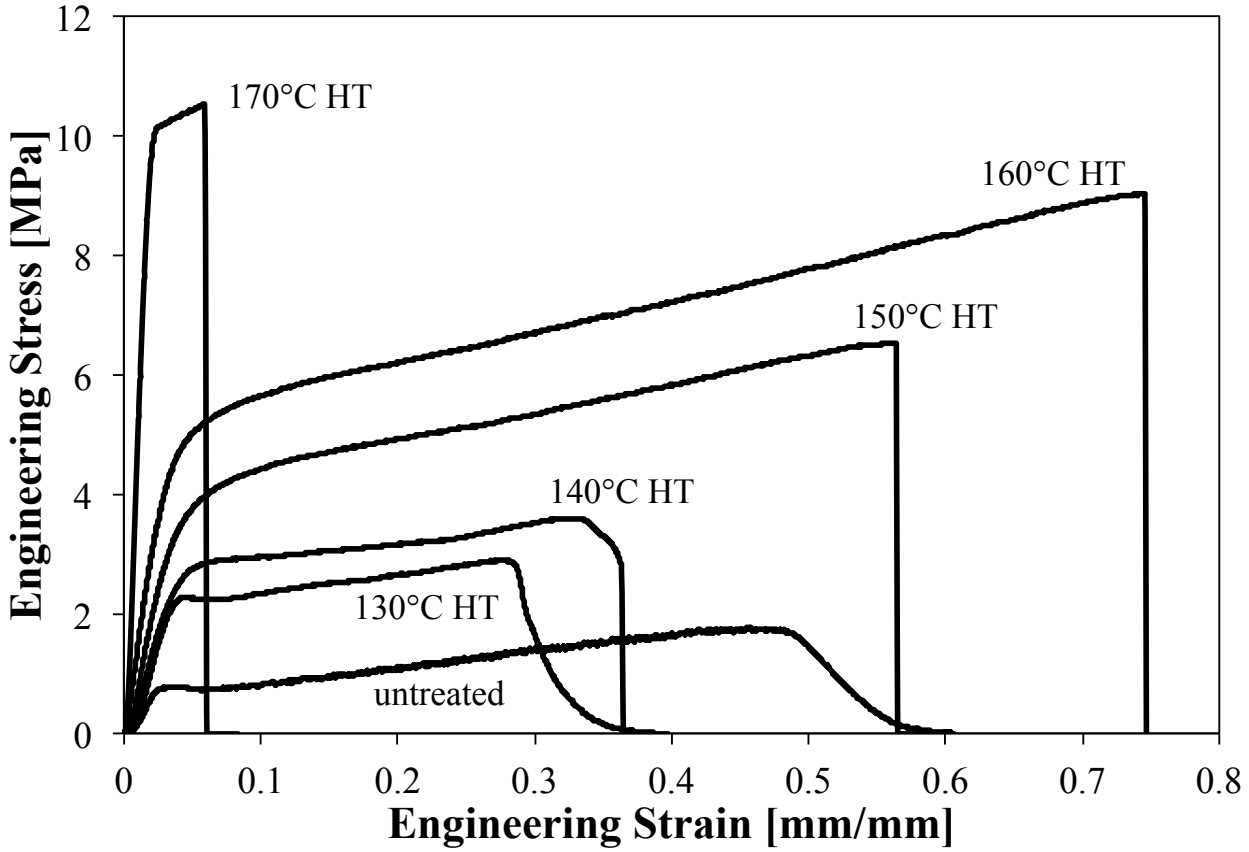

Figure 3-6. Representative stress-strain curves for PA 6(3)T fiber mats with varying degrees of heat-treatment (2 hours each at 130-170 °C).

Analysis of the results of the nonwoven mat tensile testing show that subjecting the samples to thermal treatment can dramatically improve their mechanical properties. Histograms showing the improvements to the Young's modulus, yield stress, strain at break, and tensile energy-to-break (toughness) are plotted in Figures 3-7 and 3-8. The Young's modulus and yield stress for the as-spun material were 40.56 ± 4.82 MPa and 0.75 ± 0.02 MPa, respectively. These results are consistent with those reported by Pai et al. for mats comprising fibers with diameters around 400 nm [9]. The Young's modulus and yield stress of the mats increases modestly from the as-spun state to the heat-treated samples below T_g (130-140 °C), then increases even further for samples treated above 150 °C and shoots up dramatically after thermal annealing at 170 °C, as shown in Figure 3-7. The histogram for the yield stress looks very similar to the inverse of the trend in porosity shown in Figure 3-5, with close to a linear increase in the yield stress for mats up to the 160 °C heat-treated samples, before a sharp jump is observed for the 170 °C treated mat. The plots in Figure 3-8 show that the strain at break and tensile energy-to-break for the nanofiber

mats do not follow a simple trend with increasing temperature of heat-treatment. There is a slight drop in the strain at break with the lowest temperature of heat-treatment (130 °C), indicating a possible transition from a ductile fracture response to more brittle behavior; then there is a steady increase in the strain-to-break with increasing heat-treatment, indicating a toughening of the fiber mat that prevents a critical crack from propagating through the sample. The sample annealed at 170 °C breaks very early (<10% strain) and exhibits very little strain after yield, indicating that the material has become very brittle, behaving like a porous film containing large voids that act as stress concentrators to initiate crack formation. The toughness of the heat-treated PA 6(3)T nanofiber mats shows that the as-spun mat and mats annealed at temperatures up to 140°C exhibit low toughness due primarily to their low modulus and yield stress, while the 170 °C HT membrane also has a low toughness due to its small breaking strain. The toughest mats are the ones that have been annealed at a temperature close to the T_g of PA 6(3)T, where there is a significant increase to both the yield stress and the strain-to-break; these mats exhibit a 5-10 fold increase in toughness over the untreated mats.

The changes observed in the mechanical properties of the electrospun mats cannot be explained solely based on changes in mat porosity; for example, a 3.5-fold increase in solidity (=1–porosity) from the untreated sample to that treated at 170°C is accompanied by a change in modulus of over 10-fold. Pai et al [9] previously showed that the curvature of fibers between points of contact ("junctions") with other fibers is also important. The increase in Young's modulus for the heat-treated mats is consistent with thermal welding of the fibers at their junctions, in addition to the reduction in porosity. Using the nonwoven fabric model for curved fibers reported by Pai et al [9] and the values reported there for the fiber modulus and radius of curvature of PA 6(3)T fabrics comprising 407 nm fibers (*c.f.* Table 2 of Ref 9), we calculate distances between junctions that decrease from about 17.5 μm for the as-spun mats to 14.1 μm for the mats heat-treated at 160°C. This corresponds to an increase in junction density, and is at least qualitatively consistent with the images shown in Figure 3-4.

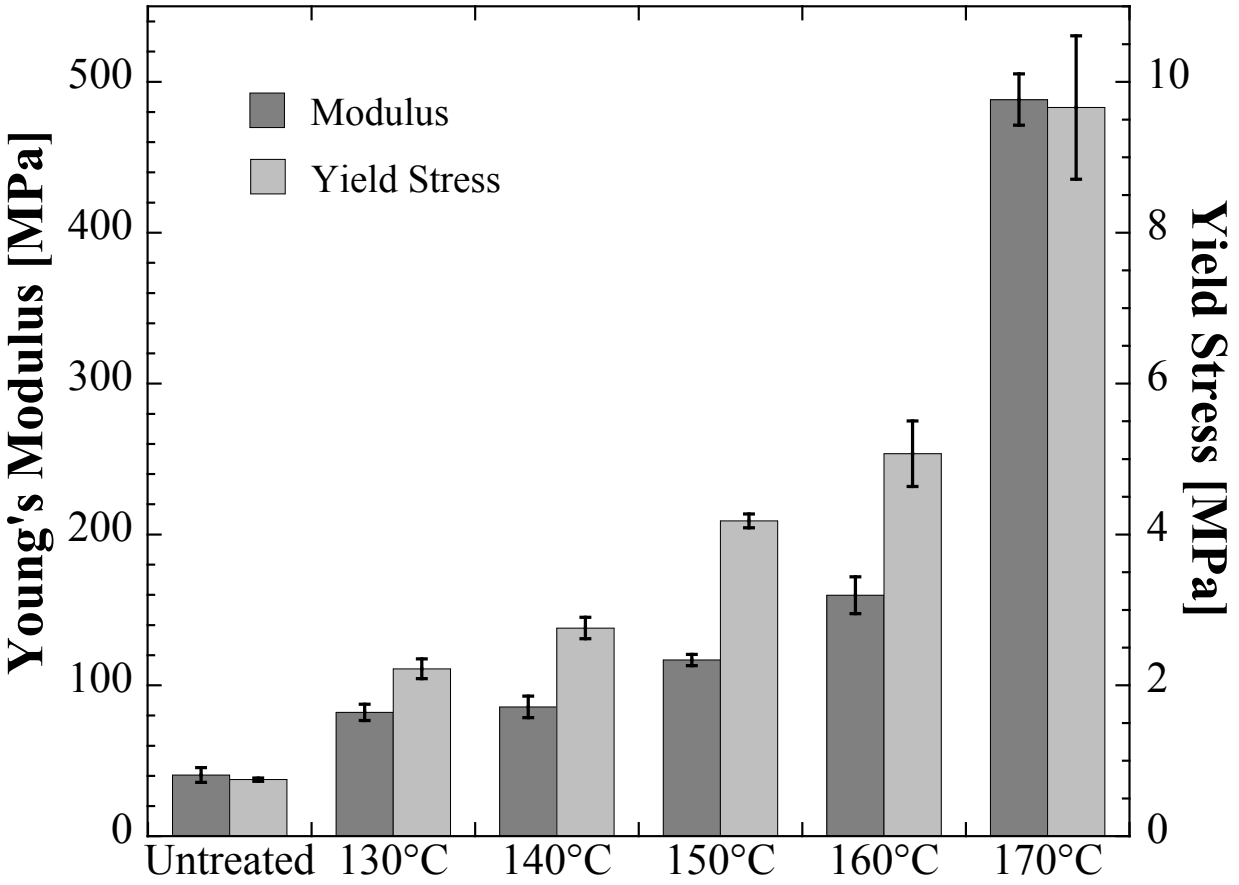

Figure 3-7. Plot of Young's modulus and yield stress vs. temperature of heat-treatment for PA 6(3)T nanofiber mats.

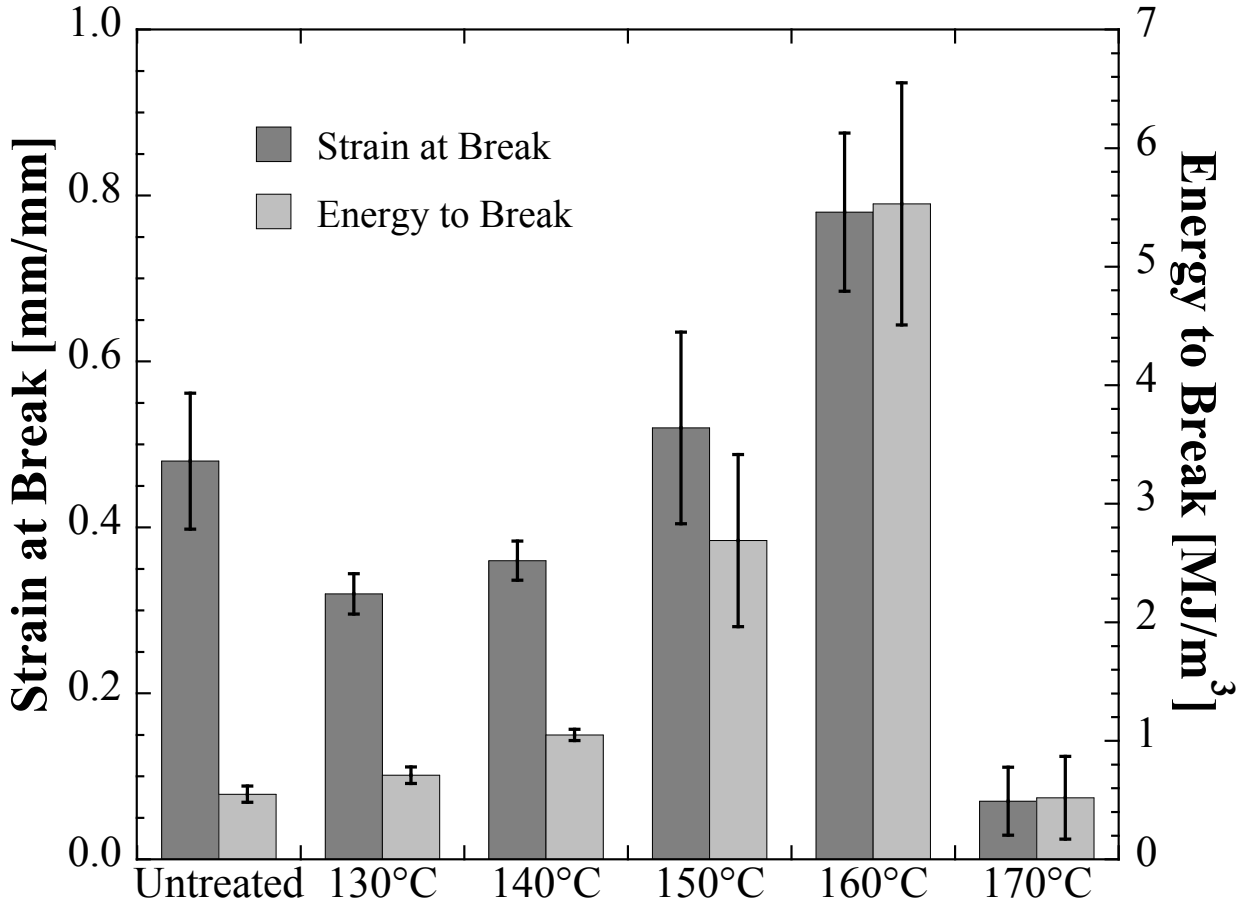

Figure 3-8. Plot of the strain-to-break and tensile energy-to-break vs. temperature of heat-treatment for PA 6(3)T nanofiber mats.

The mechanical resilience of a mat is often of paramount importance for many applications such as filtration, fiber scaffolding, or sensors where the membrane would be subjected to repeated small strain deformations that could result in catastrophic failure if the membrane were not resilient enough to recover. Single load-unload strain cycle tensile testing was performed to determine the resilience of the nanofiber mats and what effect thermal treatment has on the mechanical hysteresis. Representative mechanical hysteresis tensile loops for up to 4% engineering strain are shown in Figure 3-9. The area between the extension curve and recovery curve is a measure of the total energy dissipated over the 4% strain cycle, which when normalized by the toughness yields a measure of the hysteresis of the material. The hysteresis of the heat-treated PA 6(3)T nanofiber mats at single cycle strains of 0.02, 0.04, and 0.10 mm/mm are plotted in Figure 3-10. A sharp decrease in hysteretic losses of the nanofiber mats is observed with samples annealed close to the T_g, especially at low strains. This indicates

that thermal annealing can improve elastic recovery from low strain deformation. Nanofiber mats treated above the T_g began to exhibit an increase in the mechanical hysteresis, indicating that there is some trade-off between the morphological changes that occur during thermal treatment and the resilience of the nanofiber mats. The hysteresis behavior at large strain (10%) is not as drastically affected by the thermal annealing as the low-strain behavior, but modest improvements are still observed with heat-treated fiber mats at 140-150 °C (near the T_g of PA 6(3)T).

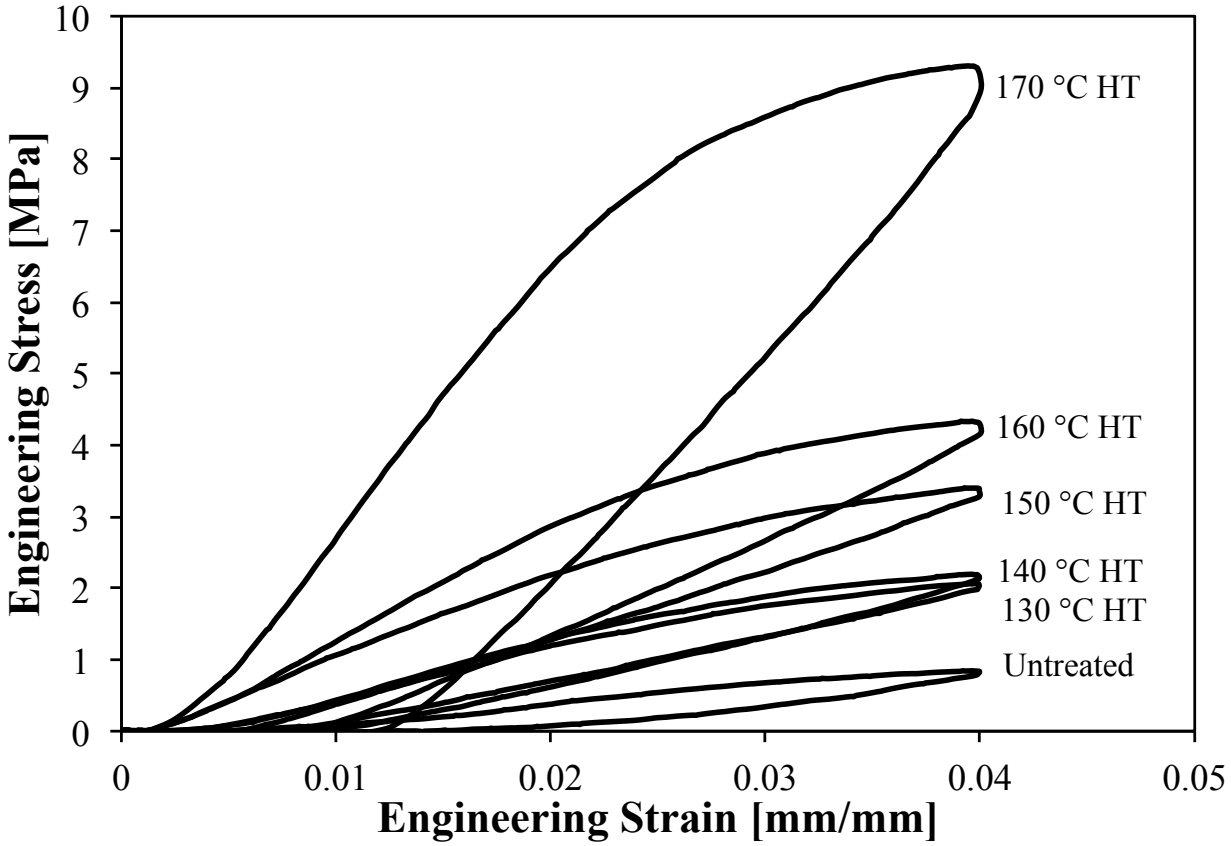

Figure 3-9. Representative 4% strain mechanical hysteresis tensile loops for PA 6(3)T fiber mats with varying temperatures of heat-treatment (2 hours each at 130-170 °C).

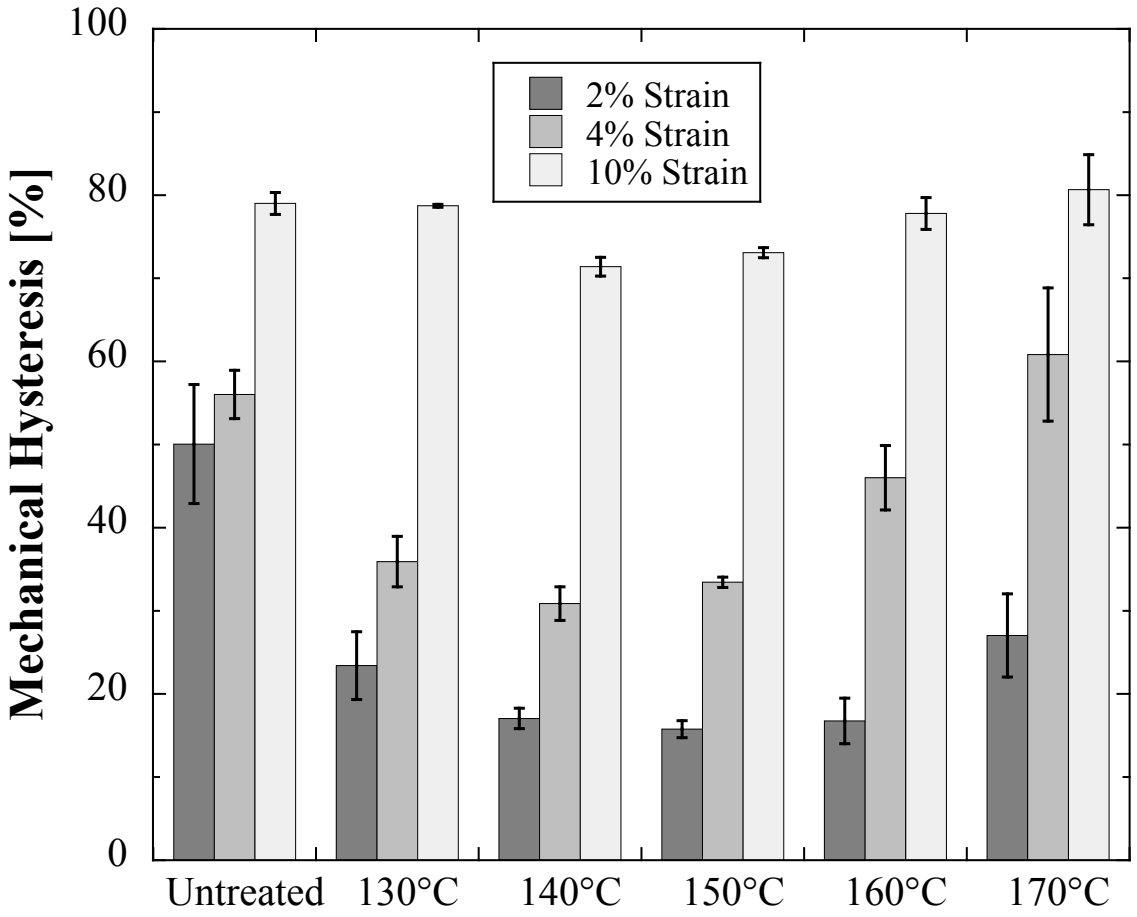

Figure 3-10. Plot of mechanical hysteresis at 2, 4, and 10% strain vs. temperature of heat-treatment for PA 6(3)T nanofiber mats.

3.3.3 Tribology of Electrospun Mats

Electrospun fiber mats are typically fragile and susceptible to wear and delamination even under conditions of gentle handling. This is a concern for the post-spin processing as well as the end-use of such mats and could be a critical limitation to their service lifetime. To quantify this behavior, the coefficient of friction was measured using a standardized testing material (Calibrade® H-38 abrasive wheel) for each of the nanofiber mats, as-spun and after each of the prescribed temperatures of heat treatment. For comparison, the coefficient of friction (μ) was measured for the film of PA 6(3)T cast from solution as well. A plot of the friction force vs. the normal force for each temperature of thermal treatment is shown in Figure 3-11; from this plot, the friction coefficient can be determined by taking the ratio of the average measured friction force to the applied normal force. A plot of the coefficient of friction vs. the normal force is shown in Figure 3-12; note that there is a modest decrease in the coefficient of friction with

increasing normal force at low loads, but that above 1 N (~100 g applied load), the coefficient of friction is approximately constant, especially for the samples annealed at or above 150 °C, as would be expected for typical extruded or cast polymer film samples. The decrease in coefficient of friction with increasing load is typical of compressible polymeric materials, whose shear strength increases with applied load [25]. Mean friction coefficients at 100 g load decreased from 0.86 for the as-spun mat to 0.77 for the 130 °C heat-treatment sample, to 0.49 for the 150 °C heat-treated mat, quickly approaching the coefficient of friction for the cast film (0.45). A lower mean coefficient of friction for the nanofiber mats is typically desirable as it implies that the mat experiences smaller forces during abrasive contact with a counter-face, which could lead to significantly less wear.

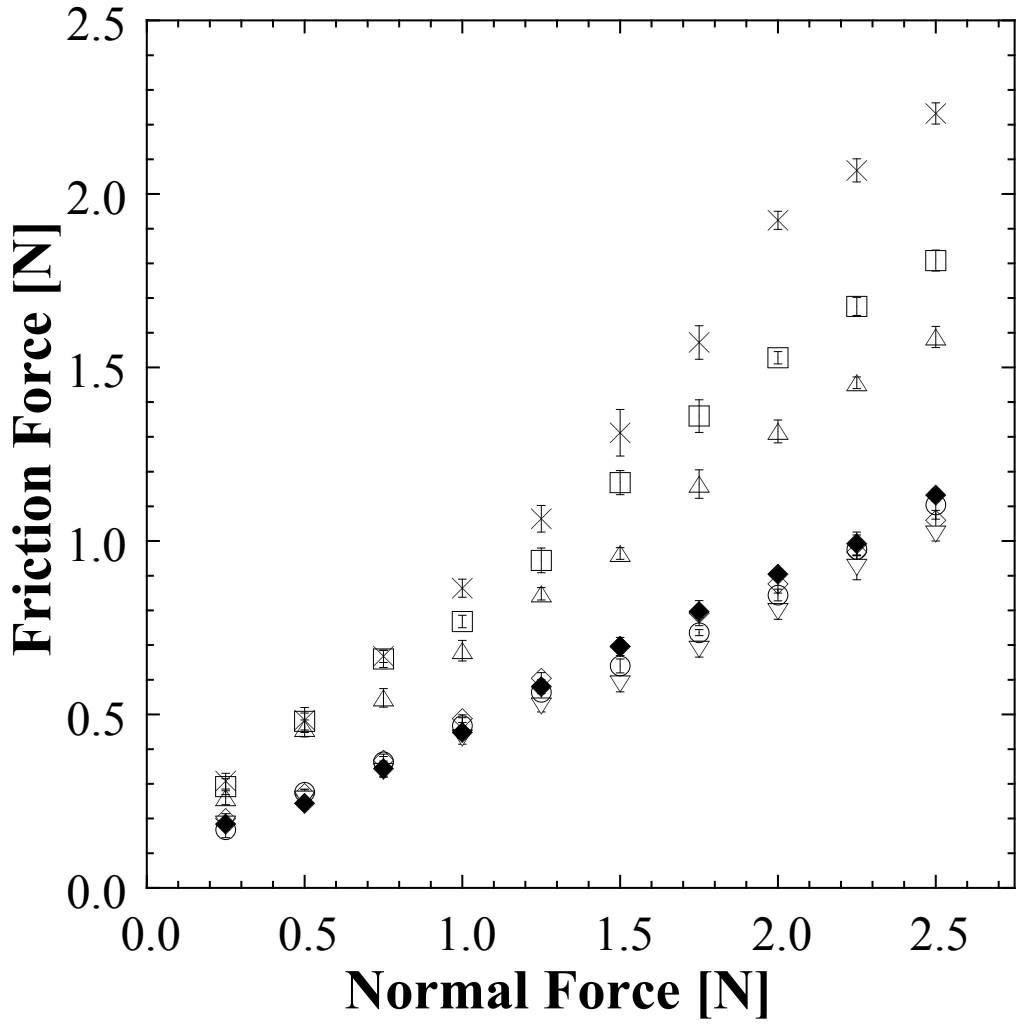

Figure 3-11. Friction force of PA 6(3)T mats as a function of the normal force with varying temperature of heat-treatment: untreated (×), 130 °C (□), 140 °C (△), 150 °C (◇), 160 °C (▽), 170 °C (○), and cast film (◆).

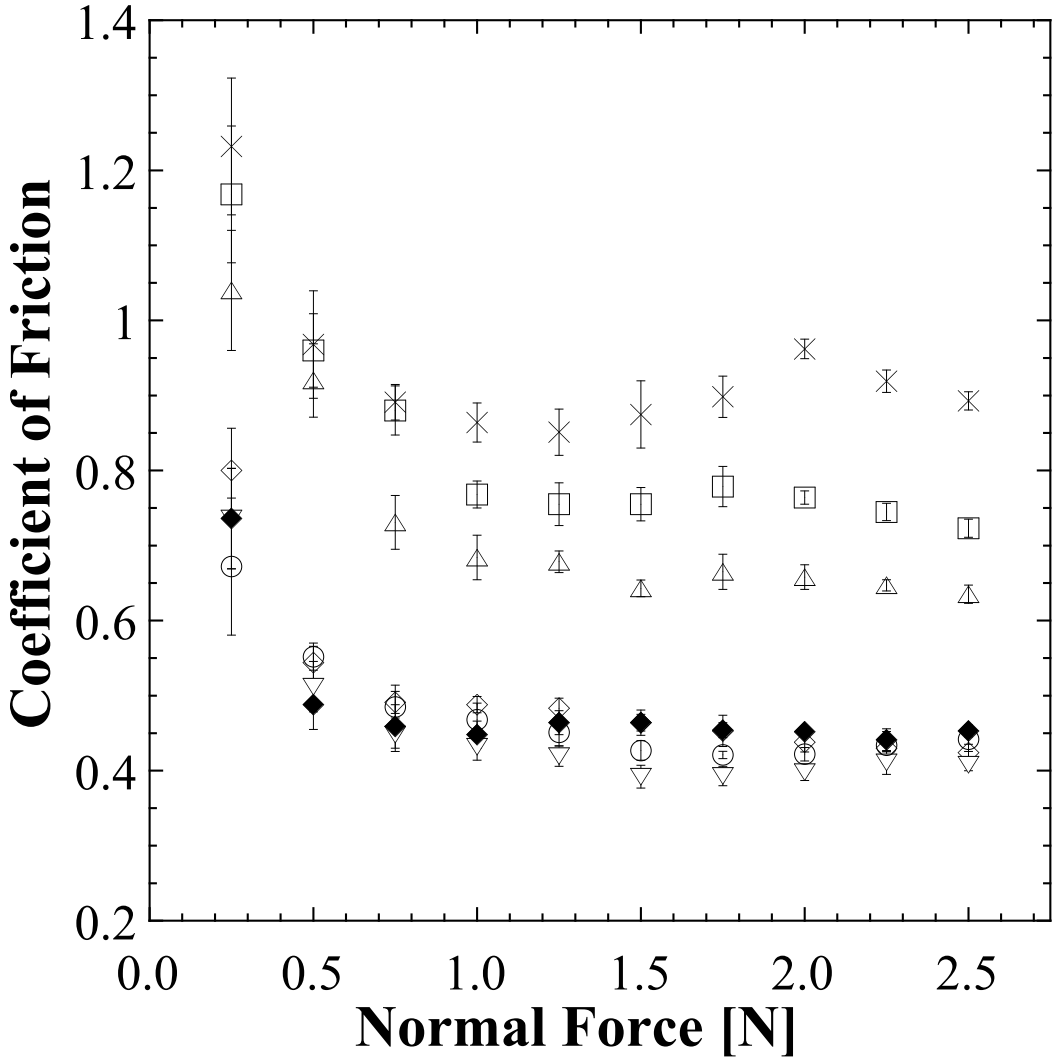

Figure 3-12. Coefficient of Friction of PA 6(3)T mats as a function of the normal force with varying temperature of heat-treatment: untreated (×), 130 °C (□), 140 °C (△), 150 °C (◇), 160 °C (▽), 170 °C (○), and cast film (◆).

The Taber abraser was used to provide uniform, low levels of abrasive wear in order to accurately measure quantitative changes in the tribological response of thermally treated nanofiber mats. All of the mats had a mean-value roughness (R_a) on the order of 1.0-2.3 μm, and the cast film had a R_a of ~0.15 μm. 100 g applied load was used for the first set of testing because it was the lowest load where the mean friction coefficient for each sample had stabilized to an approximately constant value. Visual inspection of the nonwoven membranes after 10, 50, and 100 abrasion cycles qualitatively indicated significant differences in the wear mechanisms between the samples annealed at the various temperatures, as shown in Figure 3-13. The untreated PA 6(3)T sample exhibits an observable amount of wear and distortion after as few as

10 abrasion cycles, and significant levels of deformation and wear after 50 cycles; the sample is completely destroyed (>50% of sample mass removed from the wear path) before reaching 100 cycles. The 150 °C heat-treated sample is significantly more robust, and exhibits only minor wear and abrasive tears at 10-50 cycles, before enduring more significant tearing and delamination after 100 cycles. The 170 °C heat-treated PA 6(3)T samples were even more robust, showing almost no signs of wear at all until 50 abrasion cycles, then exhibiting some moderate levels of tearing after 100 cycles. The cast PA 6(3)T film exhibited almost negligible wear under the same conditions even up to 100 abrasion cycles.

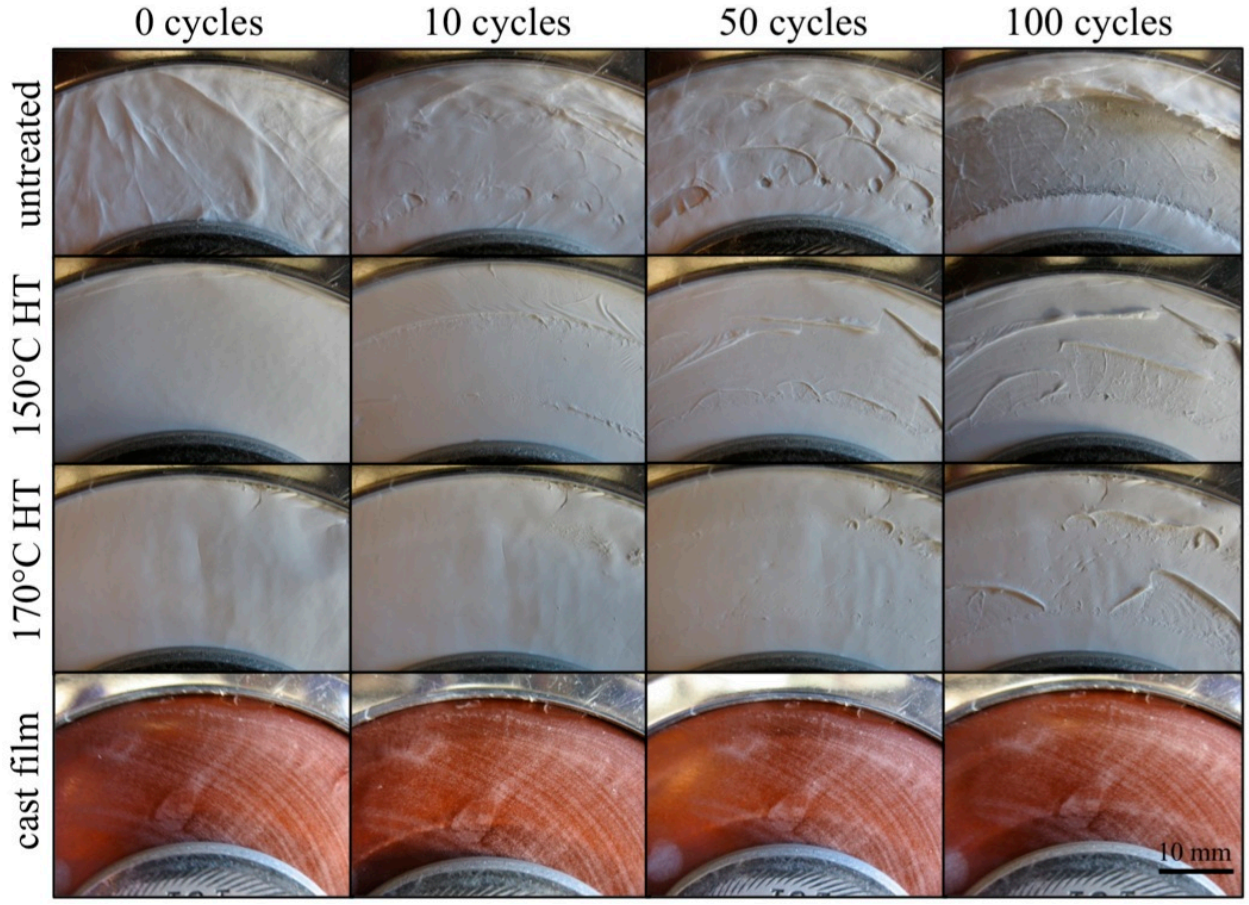

Figure 3-13. Optical images of abrasive wear path for nanofiber mats at 0, 10, 50, and 100 wear cycles under 100 g applied load (top row: as-spun; second row: 150 °C heat-treated; third row: 170 °C heat-treated, bottom row: cast film), scale bar is 10 mm. Note that the PA 6(3)T cast film is transparent and attached to a brown Kapton® polyimide film for support. The white marks seen in these images are indicative of a light haze that forms within the film during solvent evaporation. These are not surface defects, as confirmed by profilometry.

The change in the coefficient of friction as a function of the number of abrasion cycles would indicate how much the surface of the material is changing over time when subjected to abrasive wear. A plot of the friction coefficient vs. number of cycles with a 100 g load is plotted in Figure 3-14 for 10, 50, 100, 250, 500, and 1000 cycles. The coefficient of friction for the untreated mat and the 130 °C heat-treated mat both increase significantly after a minimal number of wear cycles, indicating that the surface of the mat is changing with each wear cycle. The mats heat-treated at 140 and 150 °C exhibit a less sharp increase in the coefficient of friction as a function of the number of abrasion cycles; the coefficients of friction appear to level off after approximately 100 cycles. The mats annealed at 160 and 170 °C do not exhibit significant changes to the friction coefficient as a function of the number cycles, even out to 1000 cycles; a similar effect is observed for the coefficient of friction of the PA 6(3)T cast film.

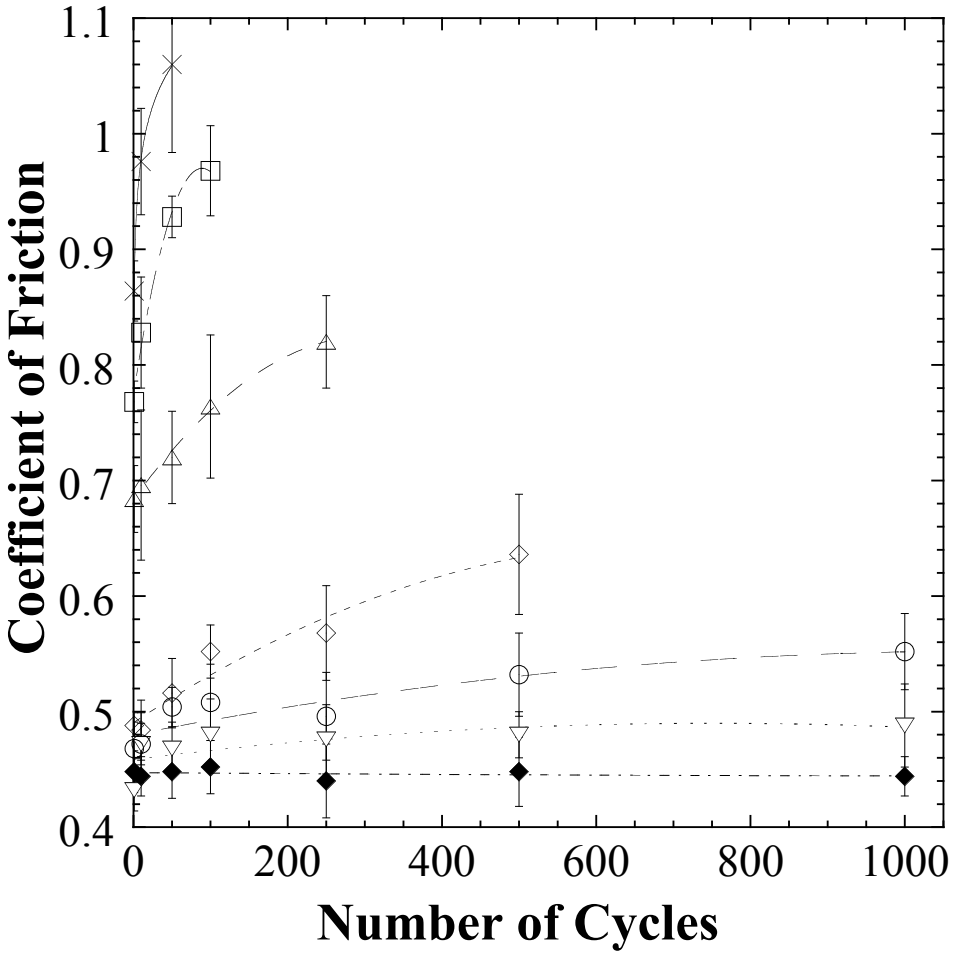

Figure 3-14. Coefficient of Friction of PA 6(3)T mats as a function of the number of abrasion cycles at 100 g applied load with varying temperatures of heat-treatment: untreated (×), 130 °C (□), 140 °C (△), 150 °C (◇), 160 °C (▽), 170 °C (○), and cast film (◆).

A plot of the abrasive mass loss vs. the number of cycles for 100 g applied load is shown in Figure 3-15 for 10, 50, 100, 250, 500, and 1000 cycles. The wear rate was measured up to approximately 50% mass loss within the wear path, or ~35-40 mg for each sample. The wear profiles for the nanofiber mats correlate well with the wear behavior of conventional polymer films.

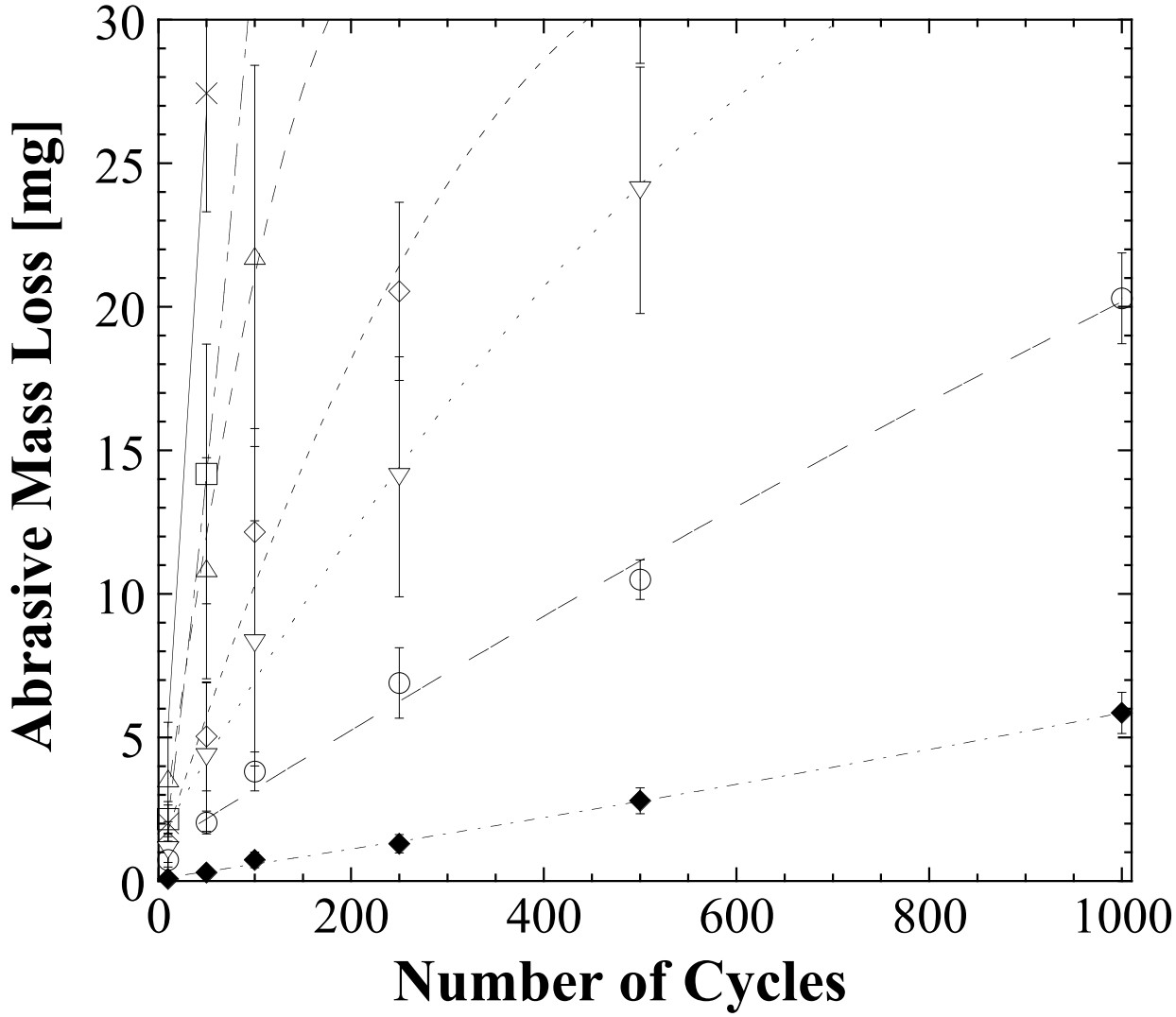

Figure 3-15. Abrasive mass losses of electrospun nanofiber mats as a function of the number of wear cycles under 100 g load: untreated (×), 130 °C (□), 140 °C (△), 150 °C (◇), 160 °C (▽), 170 °C (○), and cast film (◆).

The wear results for the samples under 100 g applied load were adequate for the mats that were annealed above 140 °C; however, since the untreated and 130 °C heat-treated nanofiber mats were completely destroyed by 100 abrasion cycles, a lighter applied load of 25 g was used

to evaluate the less wear-resistant nonwoven mats. The plot of the abrasive mass loss vs. number of cycles for the 25 g applied load is shown in Figure 3-16. Similar trends for the progression of wear for each sample are seen for the 25 g load as was seen with 100 g applied load, though the effective wear rate for each sample is less. A summary of all the tribological data is compiled in Table 3-1. Note that for both the 25 g and 100 g applied load, there is nearly an order of magnitude improvement to the effective wear rate of the 150 °C heat-treated nanofiber mat as compared to the as-spun untreated PA 6(3)T mat; however this wear rate is still about an order of magnitude higher than the effective wear rate of the PA 6(3)T cast film.

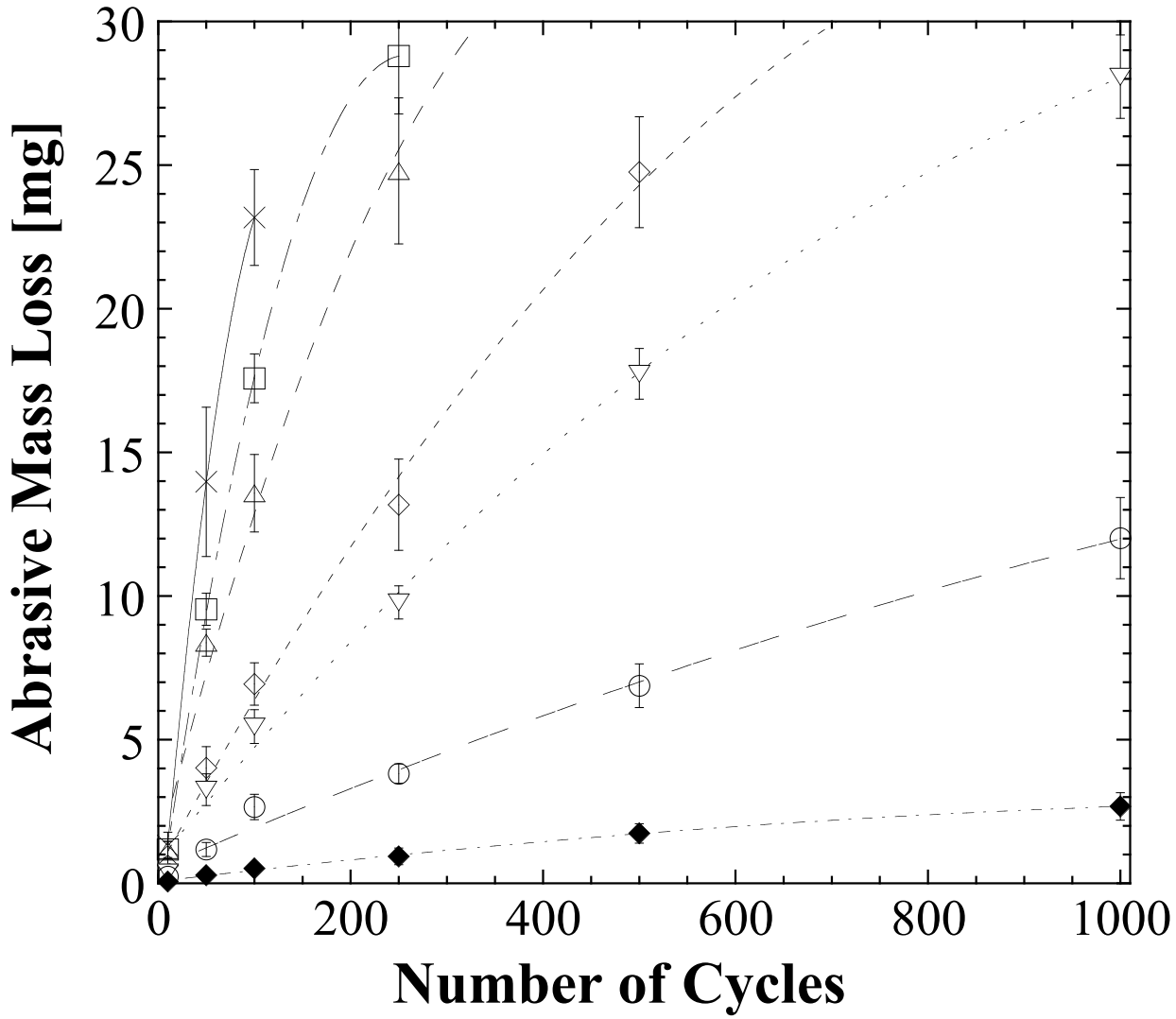

Figure 3-16. Abrasive mass losses of electrospun nanofiber mats as a function of the number of wear cycles under 25 g load: untreated (×), 130 °C (□), 140 °C (△), 150 °C (◇), 160 °C (▽), 170 °C (○), and cast film (◆).

Table 3-1. Summary of Tribological Properties of PA 6(3)T Nanofiber Mats

	R_a [μm]	Coefficient of friction, μ (25 g)	Wear Rate (25 g) [g/cm]	Coefficient of friction, μ (100 g)	Wear Rate (100 g) [g/cm]
Untreated	1.162	1.23	6.38×10^{-6}	0.86	2.14×10^{-5}
130 °C HT	1.030	1.17	5.30×10^{-6}	0.77	1.74×10^{-5}
140 °C HT	2.321	1.04	4.06×10^{-6}	0.68	6.64×10^{-6}
150 °C HT	2.304	0.80	2.32×10^{-6}	0.49	3.66×10^{-6}
160 °C HT	1.478	0.74	1.62×10^{-6}	0.43	2.37×10^{-6}
170 °C HT	1.036	0.67	6.40×10^{-7}	0.47	1.01×10^{-6}
PA 6(3)T film	0.156	0.74	1.62×10^{-7}	0.45	2.19×10^{-7}

The increased effective wear rate observed for the untreated nanofiber mat and samples treated below 150 °C could have a strong correlation with the previously observed increase in the friction coefficient of the mats with number of abrasion cycles (from the plot in Figure 3-14). There appear to be large morphological changes in the surface of the nanofiber mats (especially the untreated, 130 °C, and 140 °C heat treated samples) with increasing number of wear cycles as indicated by the sharp increase in the friction coefficient after 10, 50, and 100 cycles. As more mass is removed per cycle with these samples, there could be a significant amount of fiber distortion and debris accumulation that would consequently roughen the surface and increase the coefficient of friction. It was observed when conducting the wear tests that some fibrous debris would transfer from the sample to the abrading wheel during testing (this was removed between each sample run), and some of the fibers and debris would most likely be re-deposited into the pore spaces within the nanofiber mat. Observable residual fibrous debris on the abrading wheel was most prominent for the untreated nanofiber mats as well as the 130 °C and 140 °C thermally treated samples, which were also the samples with the largest increases in friction coefficient.

Determining the mechanism of friction and wear of polymeric nanofiber mats could prove to be vital to the ability to tailor the tribological properties of nonwovens. The mechanism of wear can be due to physicochemical interactions, asperity interactions, or macroscopic deformation [25]. All of the nanofiber mat samples used in this work consist of identical chemical composition, similar fibrous morphology, and comparable surface roughness; therefore, the mechanism of abrasive wear for these nanofiber mats is most likely due to macroscopic deformation caused by exceeding the yield stress of the mats. Relationships between the

mechanical properties and wear properties of materials have been investigated before, and some strong correlations have been drawn for polymeric materials based on microscopic and macroscopic wear models [26]. In the abrasive wear of polymers, deformation of a surface is generally a function of the indentation hardness, the relative motion opposed by the frictional force, and disruption of material at the contact points involving an amount of work equal to the area under the stress-strain curve. These three processes occur sequentially, and therefore, the total wear should be proportional to a product of the hardness, the frictional force, and the work (energy) of material removal. One of the most commonly used correlations based on this mechanism is the Ratner-Lancaster correlation [27], which predicts the wear rate, W as:

$$W = C\left(\mu \frac{L}{H\sigma_b\varepsilon_b}\right) \qquad \text{(Equation 3-3)}$$

where C is a constant, μ is the coefficient of friction, L is the applied load, H is the hardness, σ_b is the breaking stress of the material, and ε_b is the breaking strain. This relationship includes a term for the indentation hardness of a material; however, for most polymers the dominant parameters have been determined to be σ_b & ε_b [28,29]. For nanofiber mats, we suggest that the breaking stress and breaking strain of individual fibers is reflected in the yield stress and strain of the nonwoven mats; therefore, we propose a modified version of the Ratner-Lancaster relationship in which the yield stress, σ_y, and yield strain, ε_y, of the mat replace the breaking stress and strain of the fibers. The wear rate is furthermore put on a mass basis by the bulk density of PA 6(3)T, ρ, to get:

$$W \propto \left(\frac{\rho\mu L}{\sigma_y\varepsilon_y}\right) \qquad \text{(Equation 3-4)}$$

Figure 3-17 compares the effective wear rates of the treated nanofiber mats to the modified Ratner-Lancaster wear rate relationship from Equation 3-4 and confirms that there is a strong correlation between the wear rate and the quantity $(\sigma_y\varepsilon_y)^{-1}$ for both the 25 g and 100 g applied loads. The effective wear rate for the PA 6(3)T nanofiber mats is seen to increase logarithmically with $(\rho\mu L)/(\sigma_y\varepsilon_y)$ for over an order of magnitude in these quantities. These results show that the mechanical and tribological properties of nanofiber mats are inter-related and are well-described by conventional abrasive wear correlations modified to reflect the yield behavior of fibrous mats.

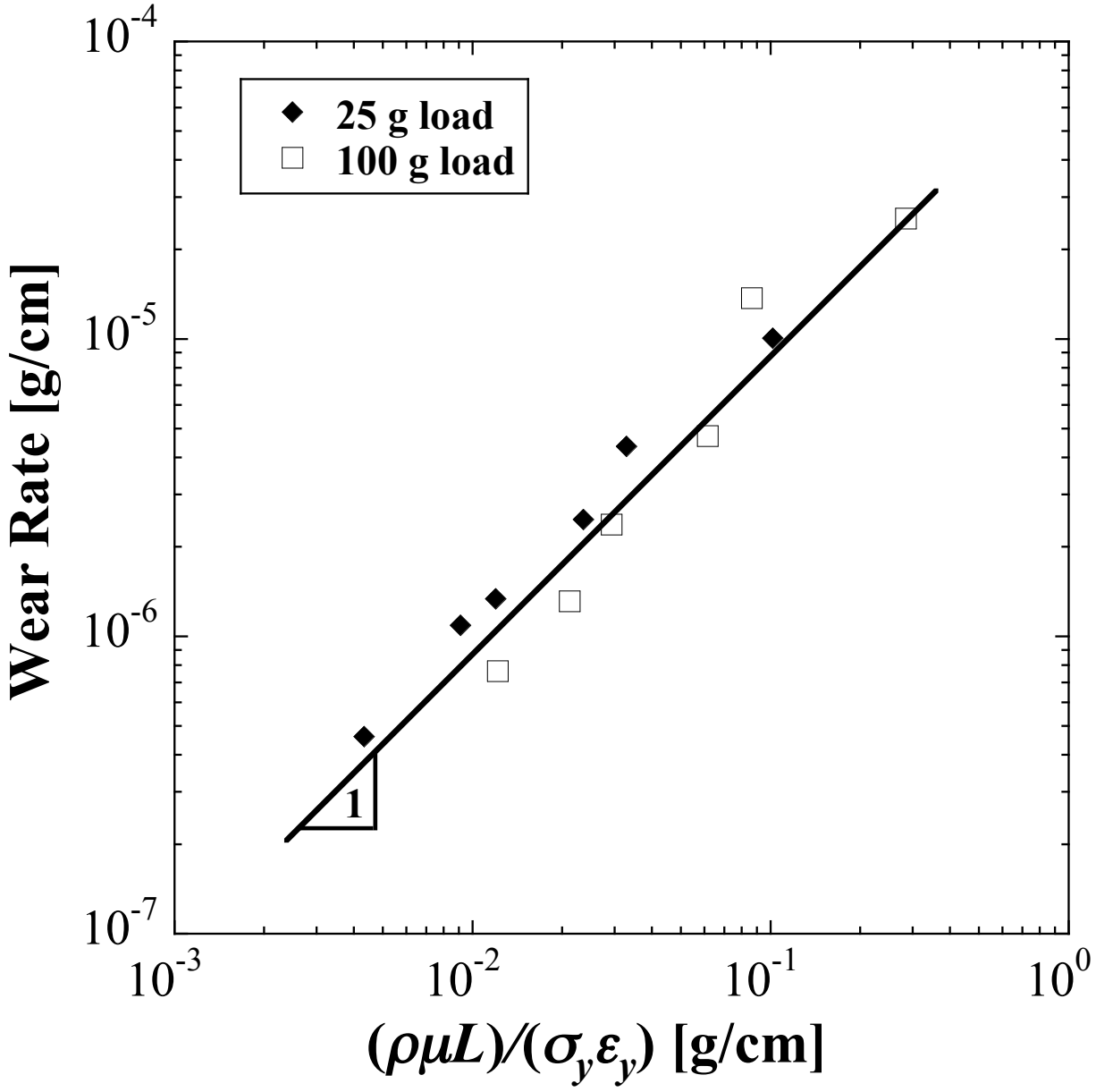

Figure 3-17. Effective wear rate vs. $(\rho\mu L)/(\sigma_y\varepsilon_y)$ of nanofiber mats subjected to varying temperatures of thermal treatment: (◆) 25 g applied load for wear, (□) 100 g applied load wear. The line with slope=1 is drawn as a guide to the eye.

3.4 Concluding Remarks

The tribological and mechanical responses of thermally treated electrospun nanofiber mats were investigated in this chapter. The Young's moduli and yield stresses of the nonwoven mats were found to improve dramatically with an increase in the temperature of heat-treatment at

or above the glass transition temperature, at the expense of mat porosity. The Young's modulus increased significantly from 40 MPa for the untreated PA 6(3)T nanofiber mat, to 82 MPa and 117 MPa after 130 °C and 150 °C heat-treatment, respectively, without suffering a significant loss of porosity; the modulus could be increased further to >400 MPa after 170 °C heat-treatment, but at a substantial loss to the mat porosity (88% to 63%). The annealed nanofiber mats also exhibited less mechanical hysteresis under low-strain deformations than the as-spun mat, indicating that the heat-treated mats can recover more readily and have significantly improved fatigue resistance. In addition to gains in mechanical integrity, there was also an improvement in the wear resistance of the nanofiber mats with thermal treatment. Annealing at 150°C results in an order of magnitude decrease in the effective wear rate relative to that of the as-spun mats, from 2.14 x 10^{-5} g/cm to 3.66 x 10^{-6} g/cm at 100 g applied load, while the porosity decreases only modestly, from 88% to 82%. The effective wear rate of nanofiber mats was well-described by a modified Ratner-Lancaster relationship for wear rate of polymeric materials, $W \sim (\rho \mu L)/(\sigma_y \varepsilon_y)$, suggesting that the mechanism of wear is primarily due to the breakage of fibers that is also responsible for yield in these nonwoven mats. Post-spin treatments such as thermal annealing close to the relevant thermal transition temperature (e.g. the glass transition) serve to weld the fibers to form additional fiber junctions, significantly improving the mechanical and tribological properties of the electrospun mats and greatly improving their utility and service lifetime.

3.5 Acknowledgments

Funding for this portion of the thesis was provided by the National Science Foundation through grant number CMMI-0700414, the Masdar Institute, and the U.S. Army through the Institute for Soldier Nanotechnologies (ISN) under AROW911NF-07-D-0004. The author would like to thank Prof. Stephen Burke Driscoll and the Plastics Engineering Department at the University of Massachusetts Lowell for use of their Taber abraser and discussions about wear testing of textiles. The author would also like to acknowledge the Hammond lab at MIT for use of their Dektak surface profiling system, and the MIT Institute of Soldier Nanotechnology for use of facilities.

3.6 References

[1] J. Doshi, D.H. Reneker, Electrospinning process and applications of electrospun fibers, Journal of Electrostatics, 35 (1995) 151-160.

[2] R.G. Flemming, C.J. Murphy, G.A. Abrams, S.L. Goodman, P.F. Nealey, Effects of synthetic micro- and nano-structured surfaces on cell behavior, Biomaterials 20 (1999) 573-588.

[3] J.A. Matthews, G.E. Wnek, D.G. Simpson, G.L. Bowlin, Electrospinning of collagen nanofibers, Biomacromolecules 3 (2002) 232-238.

[4] E.R. Kenawy, G.L. Bowlin, K. Mansfield, J. Layman, D.G. Simpson, E.H. Sanders, G.E. Wnek, Release of tetracycline hydrochloride from electrospun poly(ethylene-co-vinylacetate), poly(lacic acid), and a blend, Journal of Controlled Release 81 (2002) 57-64.

[5] X.Y. Wang, C. Drew, S.H. Lee, K.J Senecal, J. Kumar, L.A. Samuelson, Electrospinning technology: A novel approach to sensor application, Journal of Macromolecular Science-Pure and Applied Chemistry A39 (2002) 1251-58.

[6] J. Choi, K.M. Lee, R. Wycisk, P.N. Pintauro, P.T. Mather, Nafion-impregnated electrospun polyvinylidene fluoride composite membranes for direct methanol fuel cells, Journal of Power Sources 180 (2008) 167-171.

[7] R. Bajon, S. Balaji, S.M. Guo, Electrospun Nafion Nanofiber for Proton Exchange Membrane Fuel Cell Application, Journal of Fuel Cell Science Technology 6 (2009) 031004.

[8] L. Li, L.M. Bellan, H.G. Craighead, M.W. Frey, Formation and properties of nylon-6 and nylon-6/montmorillonite composite nanofibers, Polymer 47 (2006) 6208-6217.

[9] C.L. Pai, M.C. Boyce, G.C. Rutledge, Mechanical properties of individual electrospun PA 6 (3) T fibers and their variation with fiber diameter, Polymer 52 (2011) 2295-2301.

[10] H.J. Jin, H.S. Chen, V. Karageorgiou, G.H. Altman, D.L. Kaplan, Human bone marrow stromal cell responses on electrospun silk fibroin mats, Biomaterials 25 (2004) 1039-1047.

[11] X.H. Zong, S.F. Ran, D.F. Fang, B.S. Hsiao, B. Chu, Control of structure, morphology and property in electrospun poly (glycolide-*co*-lactide) non-woven membranes via post-draw treatments, Polymer 44 (2003) 4959-4967.

[12] M.N. Silberstein, C.L. Pai, G.C. Rutledge, M.C. Boyce, Elastic-plastic behavior of non-woven fibrous mats, Journal of the Mechanics and Physics of Solids 60 (2012) 295-318.

[13] X. Wang, K. Zhang, M. Zhu, B.S. Hsiao, B. Chu, Enhanced mechanical performance of self-bundled electrospun fiber yarns via post-treatments, Macromolecular Rapid Communications 29 (2008) 826-831.

[14] C. Lai, G. Zhong, Z. Yue, G. Chen, L. Zhang, A. Vakili, Y. Wang, L. Zhu, J. Liu, H. Fong, Investigation of post-spinning stretching process on morphological, structural, and mechanical properties of electrospun polyacrylonitrile copolymer nanofibers, Polymer 52 (2011) 519-528.

[15] H. Na, Y. Zhao, C. Zhao, C. Zhao, X. Yuan, Effect of hot-press on electrospun poly(vinylidene fluoride) membranes, Polymer Engineering And Science 48 (2008) 934-940.

[16] L. Jeong, K.Y. Lee, J.W. Liu, W.H. Park, Time-resolved structural investigation of regenerated silk fibroin nanofibers treated with solvent vapor, International Journal of Biological Macromolecules 38 (2006) 140-144.

[17] K. Gao, X. Hu, C. Dai, T. Yi, Crystal structures of electrospun PVDF membranes and its separator application for rechargeable lithium metal cells, Materials Science & Engineering B 131 (2006) 100-105.

[18] D. Cho, E. Zhmayev, Y.L. Joo, Structural studies of electrospun nylon 6 fibers from solution and melt, Polymer 52 (2011) 4600-4609.

[19] C.L. Pai, M.C. Boyce, G.C. Rutledge, Morphology of porous and wrinkled fibers of polystyrene electrospun from dimethylformamide, Macromolecules 42 (2009) 2102-2114.

[20] S. Derler, G.U. Schrade, L.C. Gerhardt, Tribology of human skin and mechanical skin equivalents in contact with textiles, Wear 263 (2007) 1112-1116.

[21] L.C. Gerhardt, N. Mattle, G.U. Schrade, N.D. Spencer, S. Derler, Study of skin-fabric interactions of relevance to decubitus: friction and contact-pressure measurements, Skin Research and Technology 14 (2007) 77-88.

[22] C.L. Pai, M.C. Boyce, G.C. Rutledge, On the importance of fiber curvature to the elastic moduli of electrospun nonwoven fiber meshes, Polymer 52 (2011) 6126-6133.

[23] W. He, Z.W. Ma, T. Yong, W.E. Teo, S. Ramakrishna, Fabrication of collagen-coated biodegradable polymer nanofiber mesh and its potential for endothelial cells growth, Biomaterials 26 (2005) 7606-7615.

[24] X. Zhu, W. Cui, X. Li, Y. Jin, Electrospun fibrous mats with high porosity as potential scaffolds for skin tissue engineering, Biomacromolecules 9 (2008) 1795-1801.

[25] N.P. Suh, Tribophysics, 1st ed. New Jersey: Prentice-Hall, 1986.

[26] K.G. Budinski, Resistance to particle abrasion of selected plastics, Wear 203 (1997) 302-309.

[27] J.K. Lancaster, Abrasive wear of polymers, Wear 14 (1969) 223-239.

[28] A. Wang, D.C. Sun, C. Stark, J.H. Dumbleton, Wear mechanisms of UHMWPE in total joint replacements, Wear 181 (1995) 241-249.

[29] P.H. Shipway, N.K. Ngao, Microscale abrasive wear of polymeric materials, Wear 255 (2003) 742-750.

4. Structural, Mechanical, and Tribological Properties of Electrospun Poly(hexamethylene adipamide) Fiber Mats

Portions of this chapter are reproduced from M.M. Mannarino, R. Katsumata, and G.C. Rutledge, Wear (2013) [Submitted].

4.1 Introduction

Electrospinning is a simple yet robust method to create highly porous nonwoven fiber mats from polymeric solutions. In this process, a viscoelastic fluid is charged so that a liquid jet is ejected from the surface of the fluid (typically supplied by a needle or spinneret) and accelerated by an electric field toward a collection electrode, typically a grounded plate. The resulting product is a nonwoven mat composed of fibers with small diameters (~100 nm - 10 μm), high specific surface area (~1-100 m^2/g), and high porosity (~90%) [1,2]. By adjusting the processing and solution parameters, the fiber diameter, porosity, specific surface area and mechanical properties of the mat can be tailored for various applications. The unique properties and relative ease of fabrication of electrospun fibers and their nonwoven mats have led to their use in a broad range of applications [3,4] including (but not limited to): degradable biomedical scaffolds [5,6], optical sensors [7], and ion-exchange membranes [8,9]. In each of these applications the mechanical and tribological response of the fiber mat is critical to the utility of the device.

Individual electrospun fibers have been shown to exhibit some remarkable increases in elastic stiffness and yield stress below a critical, submicrometer diameter, the value of which has been found to vary from polymer to polymer [10,11]; however, the origin of these increases in single fiber mechanical properties remains a topic of some debate, and may differ depending on the polymer. For non-crystalline fibers like those formed from poly(trimethyl hexamethylene terephthalamide) (PA 6(3)T), an amorphous nylon, the increases in stiffness and yield stress have been shown conclusively to result from increased molecular orientation, which in turn was attributed to increased strain during formation [9]. Regardless of the diameter-dependent changes in fiber properties, the as-spun mats tend to exhibit consistently low yield stresses

(typically 0.5-3 MPa), Young's moduli (typically 20-60 MPa) and toughnesses (typically 0.5-2 MJ/m^3) [12,13]. For some applications such as tissue engineering, where a soft, porous matrix is desirable, this may be an advantage; however, for many applications of nonwoven mats, notably membranes and textiles, for example, modest improvements to the mechanical integrity without significant losses in the inherently high porosity or specific surface area would be highly desirable. Although many experimental studies have been conducted on the mechanical properties of conventional nonwoven fabrics, there are a limited number of reports that account adequately for the observed mechanical properties of mats comprising electrospun fibers [14,15]. In recent years several research groups have demonstrated significant improvements to the Young's modulus and yield stress of electrospun polymeric fiber mats by various forms of post-spinning techniques such as thermal annealing [16,17], mechanical drawing [18], hot-pressing [19], and solvent vapor treatment [20]. For amorphous polymer nonwovens, thermal annealing has been shown to consolidate the fibers, creating stronger, more uniform materials [21]. In addition, if the amorphous polymer fiber mats are annealed above the material's glass transition temperature (T_g), flow and welding between fibers can be observed, which enhances mechanical properties through the mechanism of increased number (and perhaps rigidity) of junctions.

For a broad range of applications, nonwoven fiber materials must be not only strong, but also wear-resistant. Derler et al. have measured the friction coefficient and hardness of conventional textiles in contact with human skin equivalents [22]. Gerhardt et al. have measured the frictional properties and contact pressure of skin-fabric interactions [23]. The textile industry currently uses several abrasion and wear testing techniques (such as the Taber abraser) to evaluate the durability of fabrics. Such tribological characterization is necessary for electrospun fiber mats as well, if they are to be developed and commercialized. We have recently reported the first quantitative study of friction and wear resistance for electrospun fiber mats of the amorphous nylon PA 6(3)T. We showed that wear correlates well with the yield properties of the nonwoven mat, in accord with a modified Ratner-Lancaster model, and that significant improvements can be realized by thermal annealing in the vicinity of the polymer glass transition [17]. Here, we report the study of friction and wear resistance for electrospun fiber mats of the semi-crystalline nylon, poly(hexamethylene adipamide) (PA 6,6). The crystal structure and polymorphic phase transitions within electrospun Nylon 6 and Nylon 6,6 fibers have been previously investigated [24,25], as have the tensile mechanical properties of the electrospun

Nylon 6,6 fibers [25]. Subjecting a semi-crystalline polymer fiber to heat treatment at a temperature above the crystallization temperature (T_c) of that polymer, but below the equilibrium melting temperature (T_m) can cause the melting of small, imperfect crystals, and the formation of larger, more perfect crystals within the fibers, thus creating a stiffer and tougher matrix [26,27]. The effect of crystallinity on the tribological properties of electrospun nonwoven mats has, to our knowledge, not yet been reported. This chapter reports the tribology of semi-crystalline PA 6,6 electrospun mats, correlates this with mechanical properties, and demonstrates the improvement of both mechanical integrity and wear resistance by post-spin annealing, to generate more robust membranes.

4.2 Experimental Method

4.2.1 Materials

Poly(hexamethylene adipamide) (Nylon 6,6), henceforth referred to as PA 6,6, was purchased from Scientific Polymer Products, Inc. It is a semi-crystalline polyamide with a glass transition temperature of 45 °C (T_g=318 K) and crystal melting temperature of 254 °C (T_m=527 K) as reported by the vendor and confirmed by differential scanning calorimetry. N,N-dimethyl formamide (DMF) and formic acid (FA) were purchased from Sigma-Aldrich and used as received to create solutions with the composition 20:75:5 by weight of PA 6,6:FA:DMF. The less volatile DMF was added to prevent solidification of the solution at the needle tip and to decrease the solution conductivity.

4.2.2 Electrospinning of Nanofiber Mats

Fiber mats were fabricated by electrospinning from organic polymer solutions using a parallel plate geometry inclined at 45° with respect to vertical, as shown in Figure 4-1. Two aluminum plates (the top one 12 cm in diameter, the bottom one a 20 cm square plate) were positioned as illustrated with a tip-to-collector distance of 20 cm. The rotated geometry of the electrospinning process was employed to avoid dripping of solution onto the electrospun fiber mats, which re-dissolves the PA 6,6 fibers and disrupts the uniform fiber matrix morphology; the change in orientation should have no effect on the physics of fiber formation. A high voltage power supply (Gamma High Voltage Research, ES40P) was used to apply an electrical potential of 28 kV to the polymer solution and the top plate. The nozzle consisted of a stainless steel

capillary tube (1.6 mm OD, 1.0 mm ID) (Upchurch Scientific) in the center of the top plate. A digitally controlled syringe pump (Harvard Apparatus, PHD 2000) was used to obtain a constant flow rate of 0.0023 mL/min. The entire apparatus was contained within a fume hood to ensure proper ventilation. PA 6,6 is well known to be hygroscopic, and the spinning process was found to be very sensitive to humidity. All samples fabricated for testing in this work were collected between 15-25% relative humidity (RH) and stored after fabrication in a sealed dry box, containing desiccant to remove any atmospheric moisture. An anti-stick agent (CP Fluoroglide® from Saint-Gobain Performance Plastics) was sprayed onto the aluminum collector plate to facilitate removal of the electrospun mat. Each mat of approximately 11-12 cm in diameter and 100 μm in thickness was produced from 0.5 mL of PA 6,6 solution.

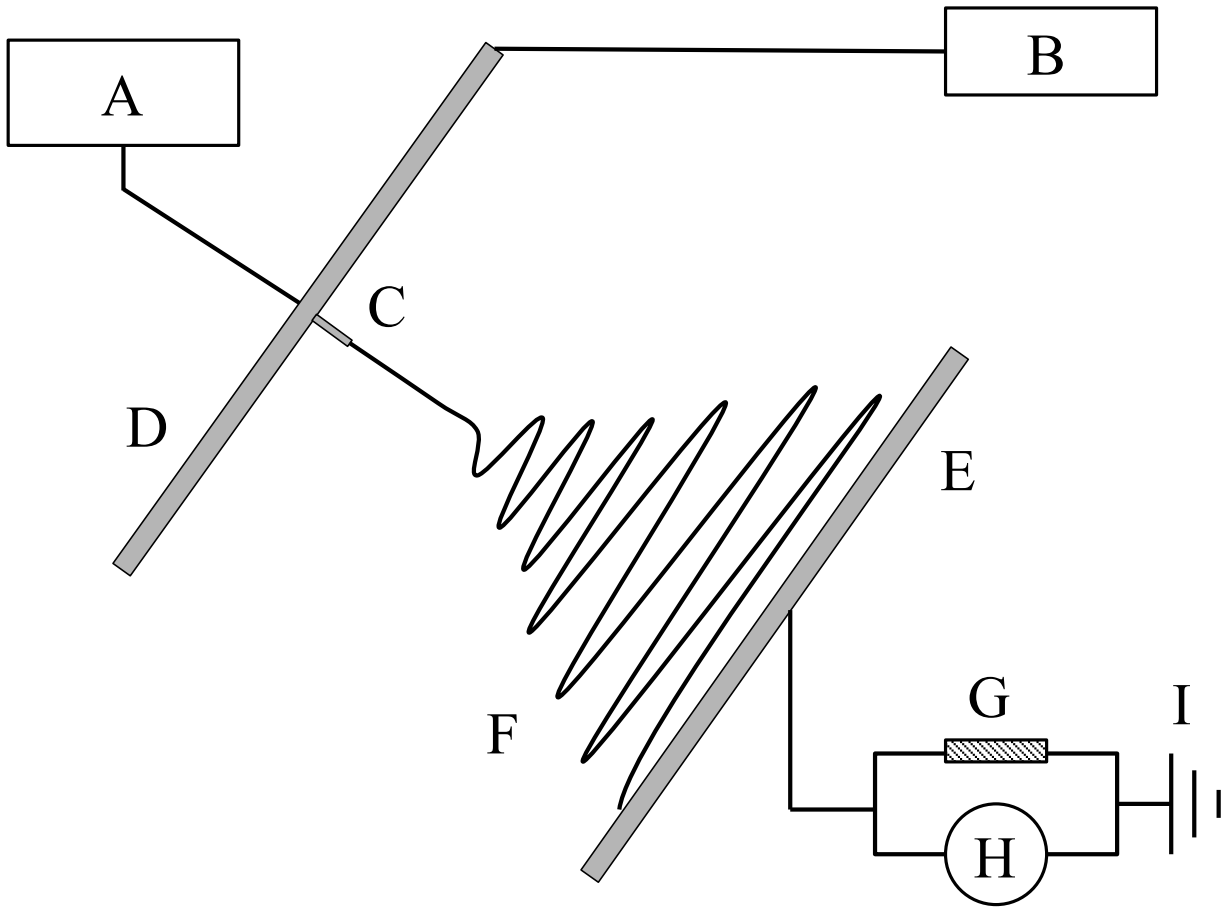

Figure 4-1. Schematic representation of 45°-rotated parallel-plate electrospinning apparatus: (A) solution pump; (B) high voltage power supply; (C) capillary tip; (D) upper plate; (E) lower grounding collector plate; (F) whipping polymer fiber jet; (G) resistor; (H) voltage meter; (I) ground.

4.2.3 Morphological Characterization of Nanofiber Mats

A JEOL JSM-6060 scanning electron microscope (SEM), with an accelerating voltage of 10-15 kV and a working distance of 10 mm, was used to determine the diameter and morphology of the fibers. A thin layer (~10 nm) of gold was sputter-coated onto SEM samples prior to imaging. The mean and standard deviation of fiber diameter were determined based on 100 measurements of fiber diameter from a set of SEM micrographs at 17,000X magnification using ImageJ. Porosity of the fiber mats was determined gravimetrically by cutting out rectangular sections and measuring the mass and dimensions of the mat specimen and converting to porosity. Five mat thickness measurements were taken per sample with a Mitutoyo digital micrometer with a constant measuring force of 0.5 N; the mean thickness was used for porosity calculations. Lateral sample dimensions were determined using a digital caliper with 0.01 mm precision. The volume and mass of the specimen were then converted to a porosity using the bulk density of PA 6,6 (1.14 g/cm^3 for the amorphous nylon; 1.25-1.30 g/cm^3 for specimens of 40-60% crystallinity) and the following equations [28,29],

$$\rho_{app} = \frac{m_{mat}}{h_{mat} \times A_{mat}} \quad \text{(Equation 4-1)}$$

$$\phi = \left(1 - \frac{\rho_{app}}{\rho_{bulk}}\right) \times 100\% \quad \text{(Equation 4-2)}$$

where ρ_{app} is the apparent density, m_{mat} is the mass of mat, h_{mat} is the thickness of mat, A_{mat} is the area of mat, ϕ is the mat porosity (%) and ρ_{bulk} is the bulk density.

4.2.4 Thermal Annealing of Electrospun Mats

The electrospun mats were thermally annealed in a Thermolyne lab oven. Each mat was draped over a 100 mm diameter Pyrex dish and placed in the oven for 60 minutes at a specified temperature. Nitrogen was introduced during annealing at 240 and 270 °C to prevent degradation and charring of the PA 6,6. Contact of the mat with the rim of the Pyrex dish was sufficient to prevent the mats from tearing during heat treatment and suspended the sample so that it did not contact or stick to any surfaces. After annealing, samples were removed from the oven and allowed to cool before carefully cutting the mat off of the Pyrex dish.

4.2.5 Crystallinity and Morphology

Differential scanning calorimetry (DSC) was performed using a TA Instruments Discovery Series DSC Model 972001. Samples of 4-6 mg were prepared in standard aluminum

pans and equilibrated in the DSC under nitrogen purge for 5 minutes at 40 °C before being ramped up to 295 °C at 10 °C/min to determine the crystallinity. Samples were then held isothermally at 295 °C for 5 minutes before ramping back down to 40 °C at 10 °C/min to confirm the crystallization temperature (T_c) of the PA 6,6 samples. TRIOS software version 2.5.0 was used to analyze the DSC data. Crystallinity was calculated from the heat absorbed in the melting endotherm and the heat of fusion of PA 6,6 ($\Delta H°$=191.9 J/g) [30].

Wide-angle X-ray diffraction (WAXD) patterns were obtained using a Molecular Metrology ASSY 610 X-ray diffractometer at 45 kV and 0.66 mA. The distance between the detector and the sample for WAXD was 117 mm. The wavelength of the X-ray beam (Cu-K_α) was λ=1.54 Å, and the beam was aligned and calibrated using a silver behenate standard with the first reflection peak at the scattering vector $q=(4\pi\sin\theta)/\lambda)=1.076$ nm^{-1}, where θ is the scattering half-angle. Fuji imaging plates were used as X-ray detectors with a typical exposure time of 6 hours. Digital WAXD images were obtained using a Fuji BAS-1800II scanner and analyzed using Polar® X-ray Diffraction (XRD) analysis software version 2.7.5, with a Voigt peak-fitting model to deconvolute the crystalline and amorphous regions and determine the percent crystallinity.

Polarized infrared spectra were measured using a Nicolet 6700 Fourier transform infrared (FT-IR) spectrometer equipped with a Nicolet Continuum infrared microscope (Thermo Fisher Scientific, Waltham, MA). An IR polarizer was used in transmission mode, and 128 scans were recorded in the range of wavenumber from 650 to 4000 cm^{-1} for polarization both parallel and perpendicular to the fiber axis. Bundles of aligned fibers were collected as described previously and used for FTIR, due to limitations in sensitivity of the instrument to measure single fibers [9]. OMNIC software was used to analyze the FTIR spectra. The dichroic ratio was used to characterize crystal orientation; it is defined as $D=A_\parallel/A_\perp$, where $A_\parallel$ and $A_\perp$ are the absorbance measured with the incident beam polarized parallel and perpendicular to the fiber bundle axis, respectively. The dichroic ratio can be related to an orientation function, f [9,31]:

$$f = \frac{(D-1)/(D+2)}{(2\cot^2\alpha-1)/(2\cot^2\alpha+2)} \qquad \text{(Equation 4-3)}$$

where α is selected to be the angle between the molecular axis and the transition moment vector of the CH_2 twist-wagging mode around 1200 cm^{-1} in PA 6,6 (α=0°) [32]. The orientation function, f, is related to the second moment of molecular orientation $\langle\cos^2\theta\rangle$ by the expression

$$f = [3\langle \cos^2\theta \rangle - 1]/2 \quad \text{(Equation 4-4)}$$

where $f = 1$ corresponds to perfect uniaxial alignment of molecules in the fiber direction, $f = 0$ corresponds to the absence of preferred molecular orientation, and $f = -1/2$ corresponds to molecular alignment perpendicular to the fiber axis.

4.2.6 Mechanical Testing

Uniaxial tensile testing of electrospun fiber mats was performed with a Zwick Roell Z2.5 tensile testing machine using a 2.5 kN load cell. Rectangular specimens were cut to 50 mm × 12 mm and extended at a constant extension rate of 0.36 mm/s with a 36 mm gauge length (corresponding to a strain rate of 0.01 s^{-1}). Five specimens were tested for each temperature of thermal treatment to determine the mean and standard deviation. The thickness of each specimen was determined from the average of three measurements taken along the gauge length with a Mitutoyo digital micrometer with a constant measuring force of 0.5 N. The force–displacement data was converted to engineering stress versus engineering strain results using the initial thickness, width and gauge length of the test specimen. Young's modulus was determined from the maximum slope of the engineering stress-engineering strain curve in the elastic region. Yield stress was determined from the intersection of the linear fit to the elastic deformation region at small strain with a linear fit to the plastic deformation region at large strain.

4.2.7 Tribological Testing

The coefficient of friction was measured according to ASTM D-1894-11 [Standard Test Method for Static and Kinetic Coefficients of Friction of Plastic Film and Sheeting] using a custom-made "sled and spring gauge" apparatus. Friction force measurements were taken with a series of normal forces ranging from 0.5-2.5 N with an IMADA push-pull force gauge (10 N capacity and 0.05 N precision), at a testing speed of 0.25 m/s. The counter-face used for coefficient of friction measurements was the H-38 Calibrade® standardized abrasion testing wheel used in the abrasive wear testing experiments. The abrading wheel has a contact area of 20 cm^2, corresponding to nominal contact pressures of 0.25-1.25 kPa. Five measurements were taken for each set of heat-treated mats to determine the mean and standard deviation.

The surface roughness of the fiber mats and polymer film were measured using a Veeco surface profiling system, Model "Dektak 150". A 2.5 μm stylus with 3.0 mg tip force was used to scan across 5.0 mm of sample in 30 seconds. The arithmetic average roughness (R_a) was

recorded for each sample analysis, and the average of five scans was used to determine the mean R_a.

The abrasive wear resistance of the electrospun mats was measured by a modified ASTM D-3884-09 [Standard Test Method for Abrasion Resistance of Textile Fabrics (Rotary Platform, Double-Head Method)], similar to the method outlined in Chapter 3 [17]. Test samples were prepared by carefully cutting out 100 mm diameter circles from an electrospun mat and attaching them to the adhesive side of a 100 mm diameter Polyken® 339 duct closure foil. This prevents the mats from bunching up or shifting during testing. Five 100 mm specimens were prepared for each combination of annealing temperature and specified number of abrasion cycles, to determine the mean and standard deviation. H-38 Calibrade® standardized abrasion testing wheels were used with an applied load of 50 g for 10, 50, 100, 250, and 500 cycles at 1 revolution per second (25 cm/s). The H-38 Calibrade® standardized Taber abrasion wheel is classified in ASTM D-3884-09 as a very fine-grained abrasive wheel for use in testing woven and nonwoven fabrics as well as delicate textiles. Samples were conditioned overnight in a sealed box, containing desiccant, to remove any residual atmospheric moisture from the fibers, since moisture is known to affect the mechanical properties of polyamides [33,34]. Abrasive wear testing was conducted entirely within a sealed glove box maintained at <1% RH with a dry air purge, in order to prevent the absorption of water that would disrupt the mass-loss measurements. The temperature of the electrospun mats was monitored during testing using an OSXL450 non-contact infrared thermometer to ensure that there was not a significant amount of frictional heating during the course of abrasive wear testing. Samples were analyzed for abrasive wear by visual inspection and mass loss using an Ohaus E11140 analytical balance with a precision of 0.1 mg. By measuring the mass loss of the fiber mats after a specified number of cycles (or sliding distance), the effective wear rates of the membranes were determined. The data for mass loss vs. number of cycles for each sample were fitted to a second order polynomial forced through the origin, using the method of least squares. An effective wear rate for each sample was then calculated by taking the value of the tangent to the second order polynomial at 100 cycles.

4.3 Results and Discussion

4.3.1 Morphology/Porosity of Heat-Treated Electrospun Mats

Uniform PA 6,6 fibers having a mean diameter of 238 ± 22 nm were fabricated from a 20 wt.% solution in 15:1 FA:DMF for use in all of the tests described here. Each nonwoven fiber mat was produced using 0.5 mL of polymer solution to generate a mat of roughly 100 μm thickness and 12 cm in diameter. The mats were then annealed at one of several temperatures selected to bracket the major thermal transitions of PA 6,6: T_g (45 °C), T_c (240 °C), and T_m (254 °C). PA 6,6 also exhibits a broad thermal transition between 80 and 170°C called the Brill transition, T_B. It is believed that the thermal annealing serves to drive out any residual solvent or air pockets within the fibers, increase the number of weld points between fibers, and alter the crystal morphology and crystalline fraction. Figure 4-2 shows SEM micrographs of PA 6,6 fibers after 1 hour of annealing at various temperatures. There are no discernable weld points between fibers on the untreated SEM, nor are there any observable morphological changes for the 70 °C annealed sample; however at 170 °C and 240 °C thermal treatment, several weld points become visible, as well as some qualitative densification of the fiber mat. The 270 °C annealed PA 6,6 fiber mat exhibits extensive flow and fusion between fibers, leading to considerable loss of the original fiber morphology and porosity, thus creating a webbing effect between fibers similar to that seen previously in the thermal annealing of an amorphous polyamide above T_g [17].

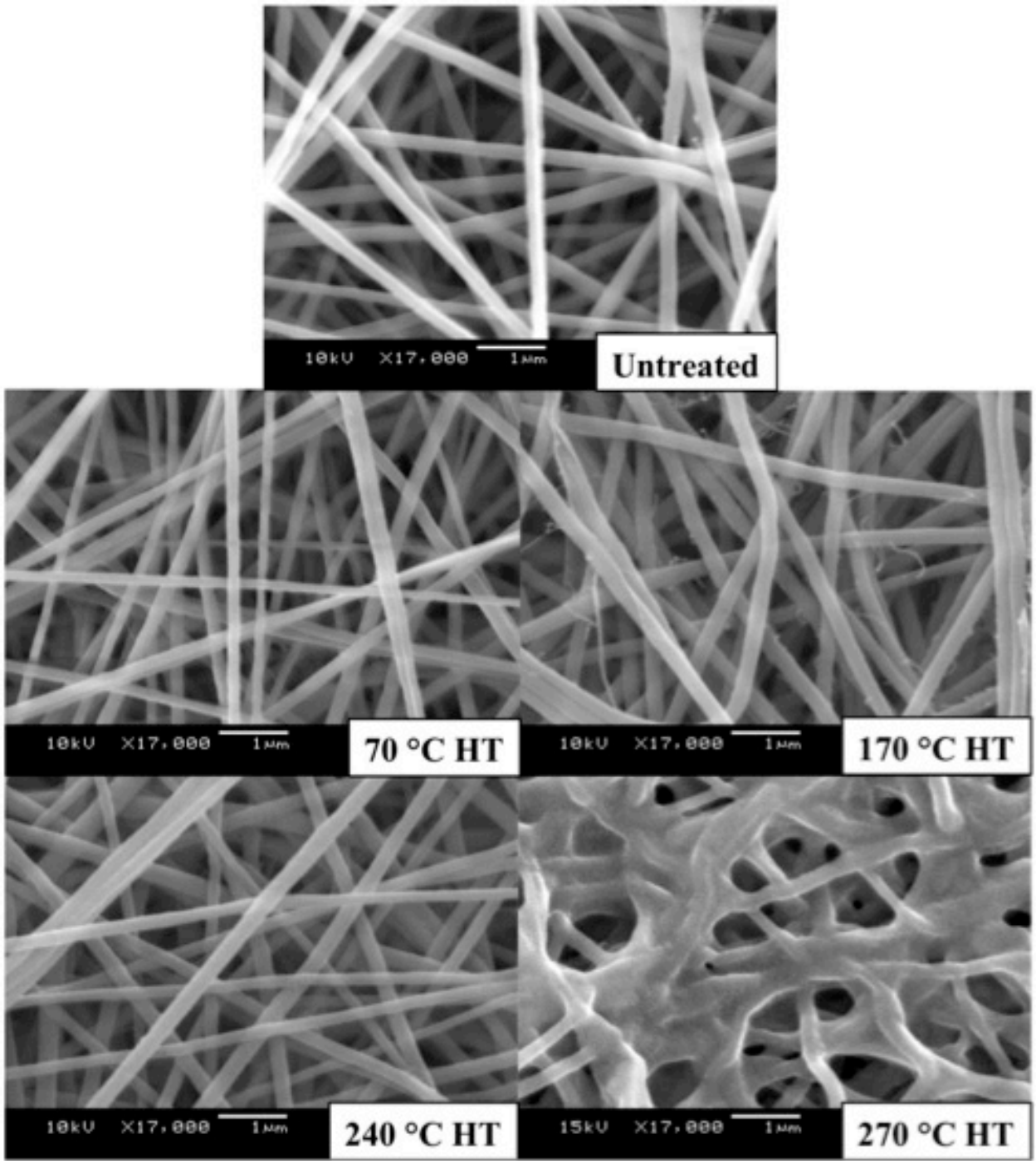

Figure 4-2. SEM micrographs of untreated electrospun PA 6,6 nanofibers (left), and after 60 minutes of thermal treatment at 70, 170, 240, and 270 °C. Scale bar for all images is 1 μm. HT refers to the heat treatment (annealing) temperature.

The SEM micrographs indicate that there may be a decrease in the pore size between fibers as the temperature of annealing increases, as well as what appears to be a decrease in the overall porosity of the mats. Before the mats were subjected to the heat-treatment, they were

typically 100 ± 10 μm in thickness. At the highest annealing temperature (270 °C), the mats were observed to contract to as thin as 55 ± 10 μm, while maintaining a fixed diameter of 100 mm. Figure 4-3 shows the results for porosity of electrospun PA 6,6 fiber mats after annealing at each temperature. The nonwoven mats have an inherently high as-spun porosity of 90.8 ± 1.4%, which drops slightly to 86.8 ± 1.0% as the result of the 170 °C heat treatment (between the T_g and T_c). Annealing at temperatures above the T_m produces a more significant drop in porosity, falling to 72.1 ± 2.6%, which is consistent with the significant changes observed in the SEM micrographs from Figure 4-2.

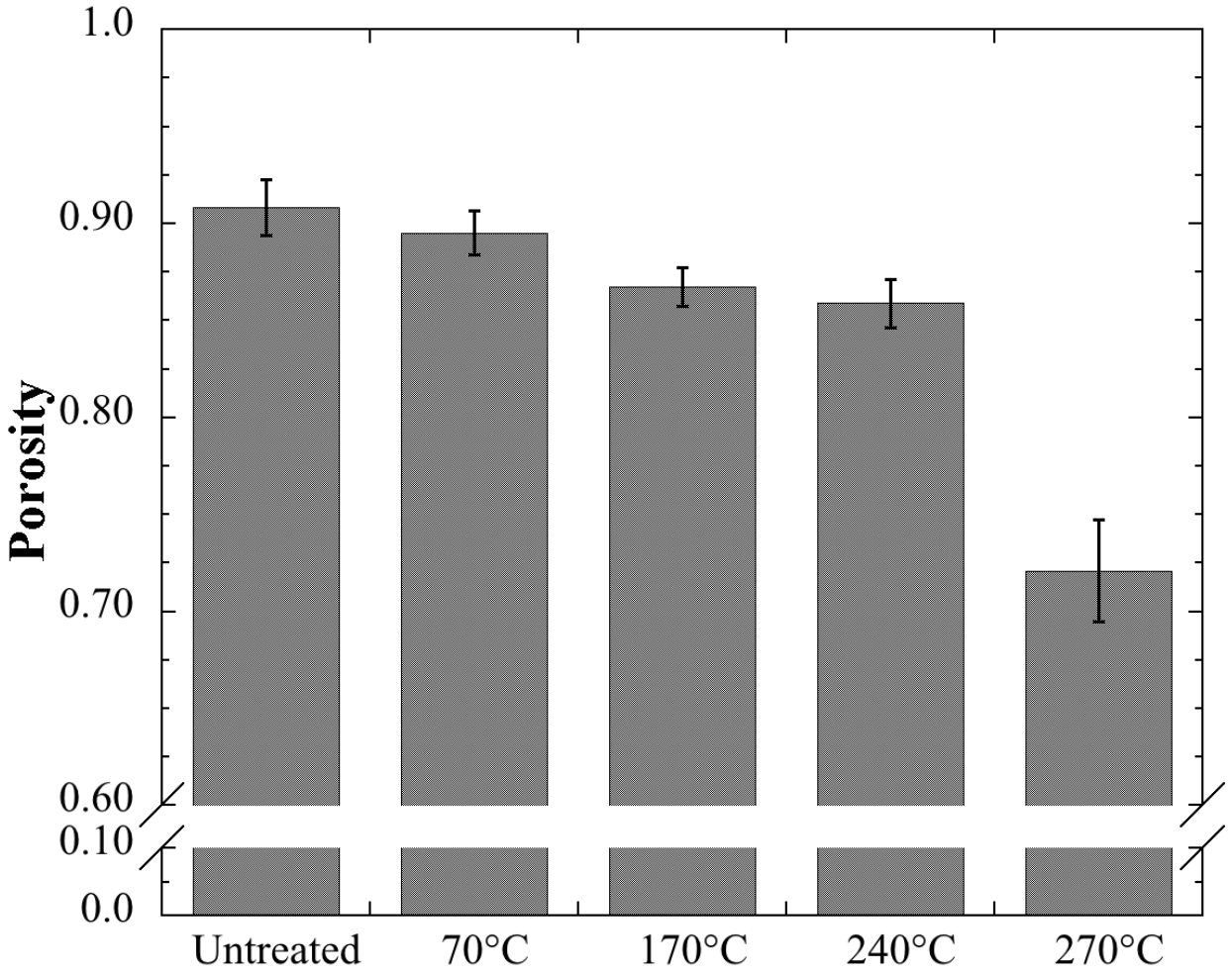

Figure 4-3. Porosity of PA 6,6 nanofiber mats after thermal annealing at various temperatures (1 hour each at 70, 170, 240, and 270 °C).

4.3.2 Crystal Structure of Annealed PA 6,6 Fibers

The crystalline structures of PA 6,6 electrospun fibers were characterized by WAXD at room temperature for each annealing temperature. Figure 4-4 shows the 2D-WAXD patterns that

were collected for each thermally annealed electrospun PA 6,6 sample; the images show broad scattering regions for the as-spun and 70 °C HT samples and two distinct narrow scattering bands for 240 °C and 270 °C heat-treatment, with the 170 °C HT sample exhibiting an intermediate scattering pattern. The azimuthally-integrated WAXD profiles of the annealed PA 6,6 fiber samples are plotted in Figure 4-5; the plots show broad scattering regions for the as-spun and 70 °C HT samples and two distinct narrow scattering peaks for the samples annealed at 240 °C and 270 °C. The sample annealed at 170 °C HT exhibits a scattering pattern intermediate between these two extremes. The as-spun PA 6,6 fiber mat exhibits a relatively strong (100) diffraction peak at a 2θ scattering angle of 20.2 degrees, and a second broader (010)/(110) doublet diffraction peak at a 2θ of 23.0 degrees, corresponding to the triclinic α crystal structure of PA 6,6 [35,36]. Consistent with previous reports, the diffraction peak are relatively broad, indicating that the sizes of PA 6,6 crystallites are small and heterogeneous in the electrospun fibers [24]. The sample annealed at 70 °C shows a shift of the diffraction peaks to 20.9 and 23.6 degrees, with a corresponding loss of intensity, suggestive of some melting out of the least stable crystallites. Meanwhile, the sample annealed at 170 °C HT also exhibits broad, low intensity peaks, but these are shifted back to 20.4 and 22.8 degrees, with both the (100) and (010)/(110) diffraction peak intensities closer in magnitude to each other; this behavior is consistent with transformation of the triclinic α form to a pseudo-hexagonal form above the Brill transition temperature, followed by recovery of the triclinic form upon cooling [36,37,38,39]. The samples annealed at 240 °C and 270 °C exhibit very similar WAXD profiles, but with higher intensity. This is a consequence of the fact that both are cooled following annealing well above T_B. These samples each exhibit a new, small (002) peak at a 2θ of 13.9 and 14.1 degrees, very sharp (100) diffraction peaks at a 2θ of 20.0 and 20.2 degrees, and an additional sharp (010)/(110) doublet diffraction peak at a 2θ of 23.4 and 23.5 degrees, respectively. Sharper peaks (and larger crystallites) are achieved through thermal annealing of the PA 6,6 fiber mats between T_B and T_m.

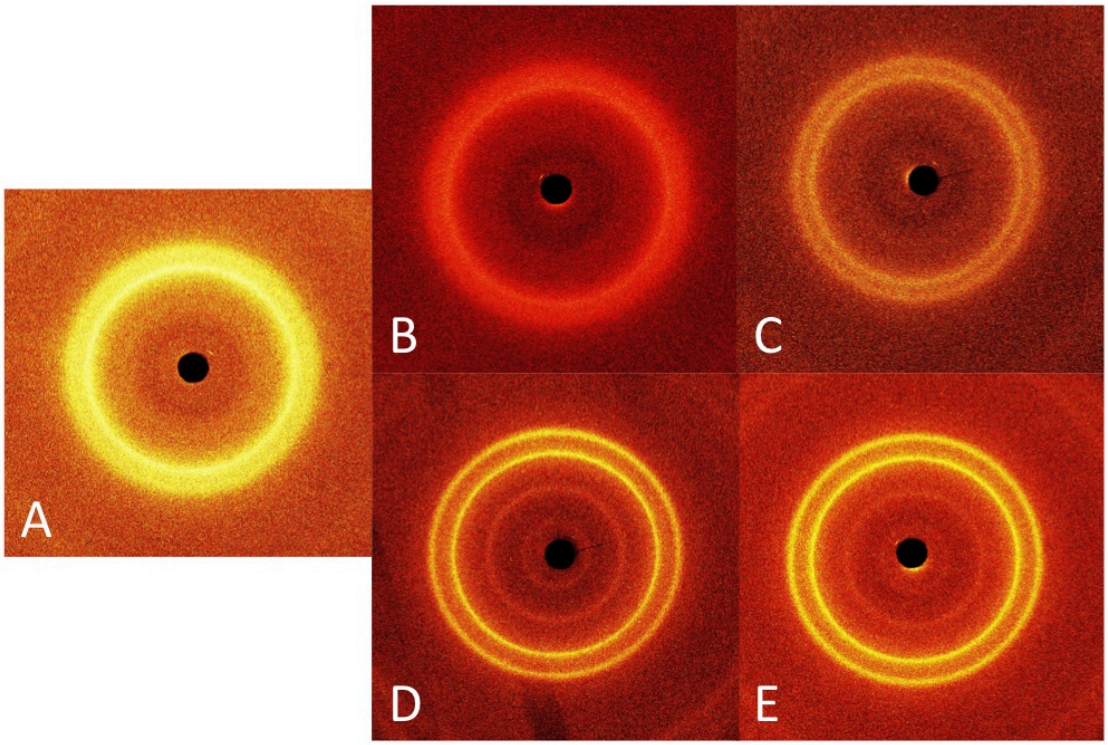

Figure 4-4. 2D-WAXD pattern of electrospun PA 6,6 fiber mats: (A) as-spun, (B) 70°C HT, (C) 170°C HT, (D) 240°C HT, and (E) 270°C HT.

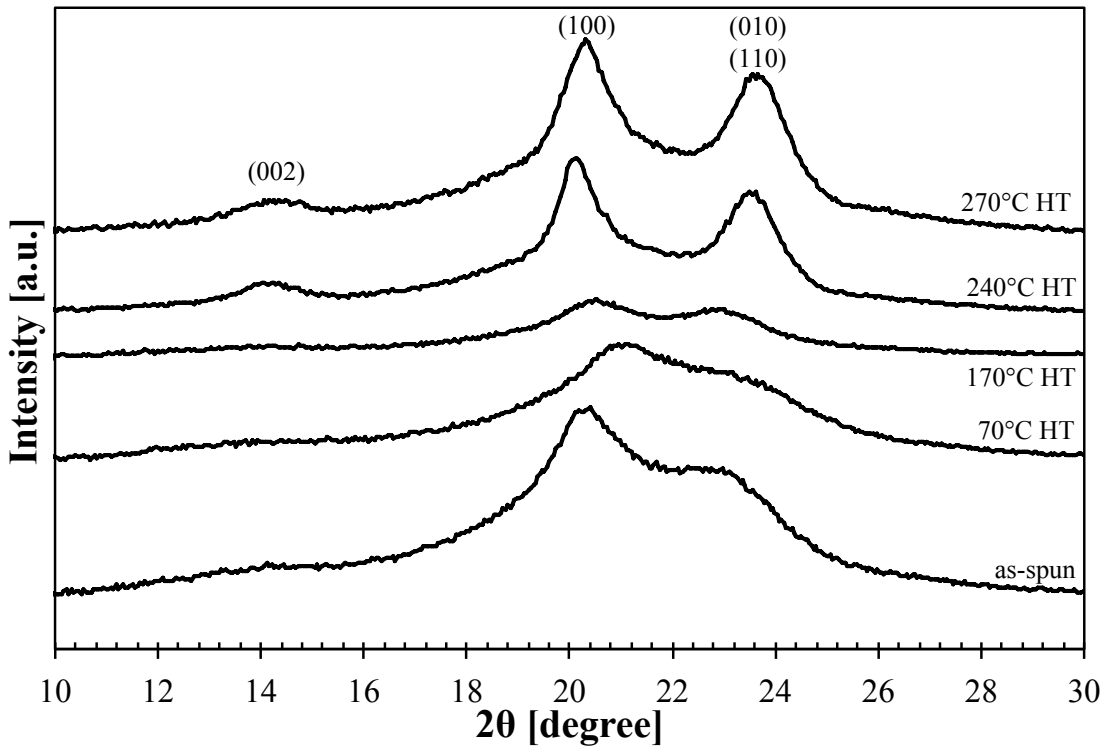

Figure 4-5. WAXD profiles of electrospun PA 6,6 fiber mats: as-spun, 70°C HT, 170°C HT, 240°C HT, and 270°C HT. HT refers to the heat treatment (annealing) temperature.

Polarized IR absorption was used to measure the dichroism of the peak around 1200 cm^{-1}, which is attributed to the CH_2 twist-wagging vibration mode in the α-crystalline phase of PA 6,6 [35,40]. Polarized FTIR spectra for the oriented PA 6,6 fiber bundles at each annealing temperature are shown in Figure 4-6. The solid lines represent the absorbance perpendicular to the fiber axis, $A_{\perp}$, indicative of alignment of the PA 6,6 backbone parallel to the fiber axis, and the dotted lines represent the absorbance parallel to the fiber axis, $A_{\parallel}$, indicative of molecular alignment perpendicular to the fiber axis Visual inspection of the polarized FTIR spectra indicate that the samples annealed below the T_m of PA 6,6 all exhibit a greater absorbance of CH_2 twist-wagging parallel to the fiber axis, while the two samples treated near or above T_m, exhibit higher absorbance perpendicular to the fiber axis. Values for the dichroic ratio and orientation function of PA 6,6 fiber bundles are tabulated in Table 4-1. The orientation function value for the as-spun sample is 0.054, indicating some preferential crystal orientation parallel to the fiber axis. There is a modest increase in *f* for the 70 °C and 170 °C heat-treated samples to 0.109 and 0.074 respectively. When annealed above T_B, the calculated value of *f* drops below 0, to -0.099 for the sample annealed at 240 °C, and even further to -0.181 for the sample annealed at 270 °C. This transition of the molecular orientation function from slightly positive (oriented along fiber axis) to slightly negative (oriented perpendicular to fiber axis) indicates significant changes to the crystal organization within the fibers occur when annealed above the crystal Brill transition temperature.

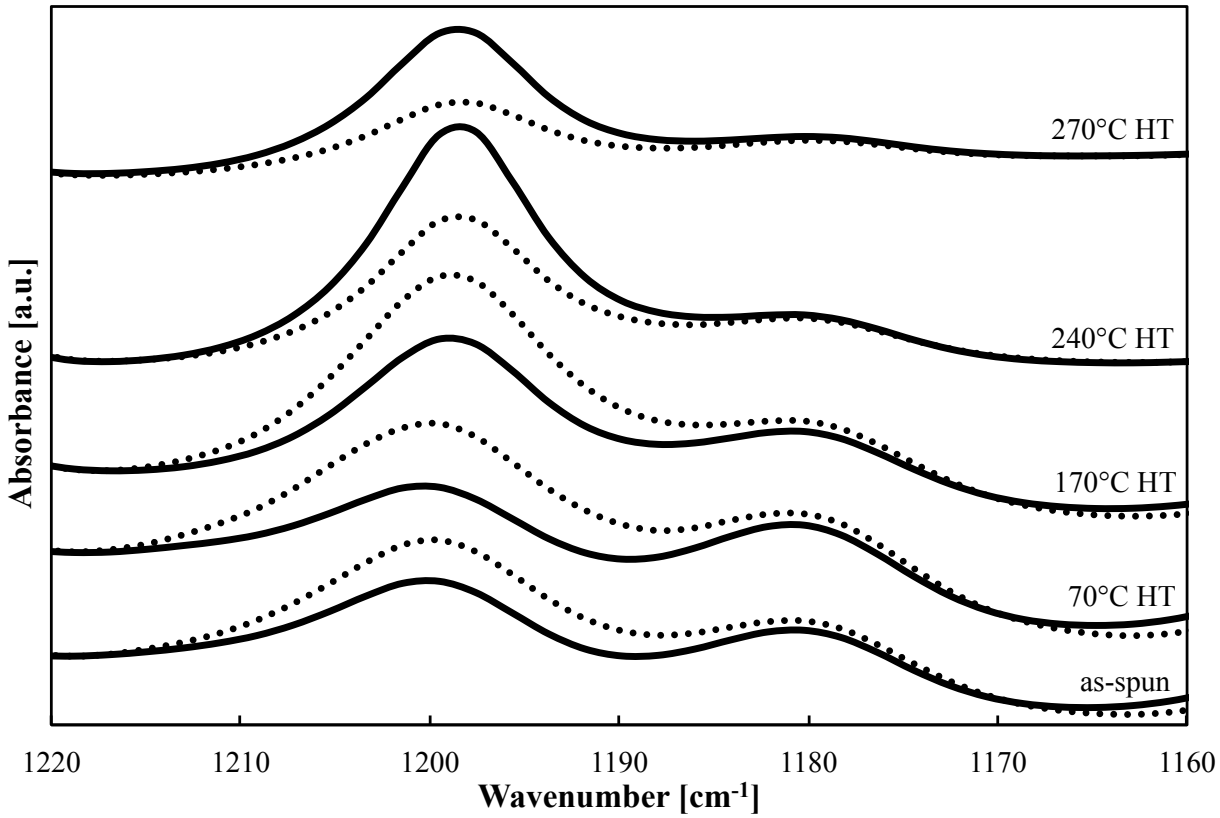

Figure 4-6. Polarized FTIR of oriented PA 6,6 fiber bundles after annealing at various temperatures. Solid lines represent $A_{\perp}$ and dotted lines represent $A_{\parallel}$.

Thermal heating profiles of the electrospun PA 6,6 fiber mats were obtained by DSC. The first heating at 10 °C/min was used in order to determine the T_m of the PA 6,6 crystals as well as the heat required to melt the crystalline regions of the polymer; the first cooling was used to confirm the T_c of the PA 6,6 samples (240 °C), and did not change significantly with annealing temperature. Figure 4-7 shows the first heating thermal profiles from 40 °C to 295 °C for each of the annealed electrospun PA 6,6 mat samples (solid lines), and a typical first cooling profile for the as-spun sample (dotted line). The as-spun sample exhibits a broad melting peak with a T_m of 255.8 °C for the fibers crystallized from solution; this is very close to the reported value from the manufacturer (254 °C). The samples annealed at 70 °C and 170 °C exhibit melting peaks with a similar breadth; however, the peaks are split into two distinct melting points: 252.6 °C and 254.4 °C, respectively, for the first melting peak, and 257.1 °C and 259.2 °C for the second melting peak, which we interpret as indication of cold crystallization within the fibers. The sample annealed at 240 °C exhibits a significant change in the heating profile, with a large shift in the first melting peak to 237.5 °C (close to the annealing temperature of 240 °C), and a second

smaller melting peak at 247.8 °C. This shift in the melting peak indicates that the thermal treatment at 240°C (above the T_B of PA 6,6) leads to substantial melting and recrystallization within the fibers. The sample annealed at 270 °C exhibits a broad melting peak with a single T_m of 253.0 °C, indicating that the sample readily recrystallized during the quench after annealing; however, the heat required to melt the crystallites of the 270 °C was lower than that for any other sample, indicating that some melting of crystallites did take place at this temperature and was not recovered.

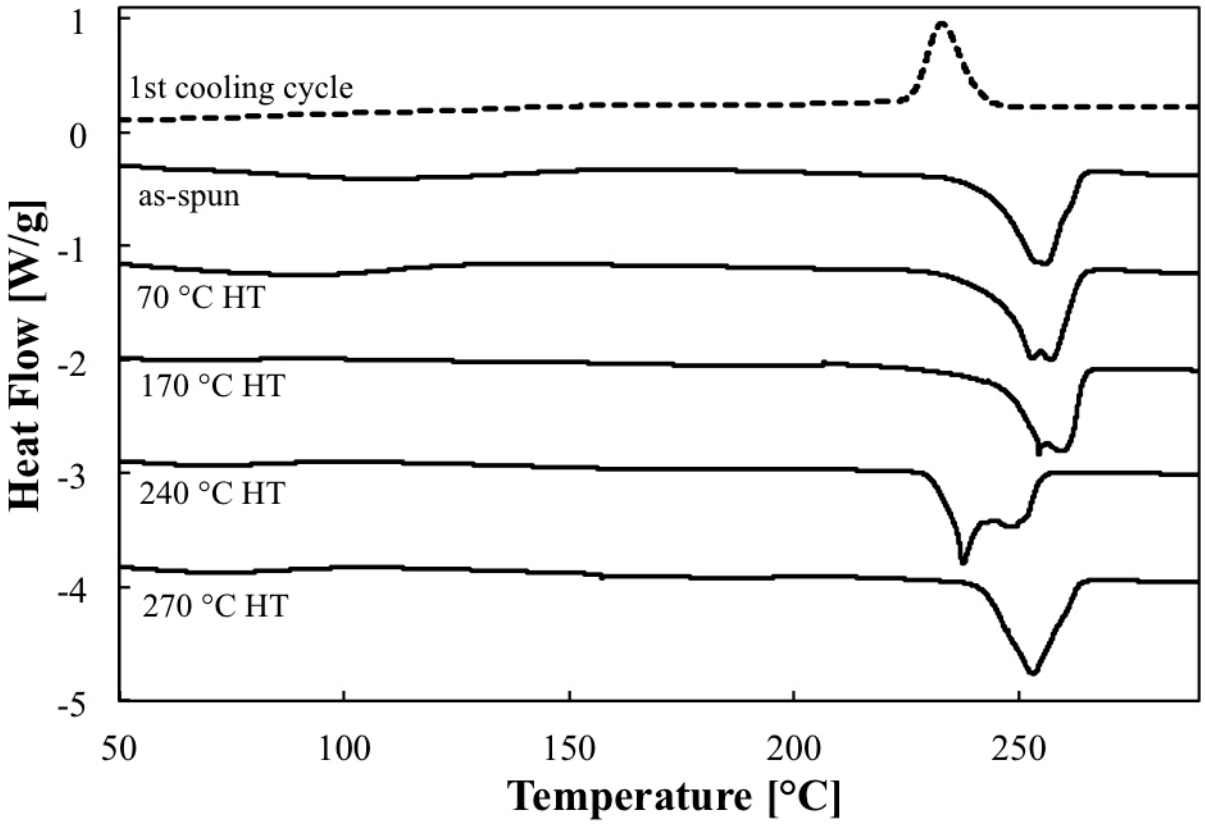

Figure 4-7. DSC Thermographs of electrospun PA 6,6 fiber mats from the first heating: as- spun, 70°C HT, 170°C HT, 240°C HT, and 270°C HT (solid lines); also shown is a typical first cooling cycle for the as-spun fiber mat (dotted line).

A summary of the thermal properties and crystal structure analysis of the electrospun PA 6,6 fiber mats is shown in Table 4-1. The percent crystallinity, as measured from WAXD, was determined by deconvoluting the crystalline and amorphous regions of the 1D-integrated intensity profiles using Polar analysis software and then normalizing the area under the crystal peaks by the total integrated intensity. Percent crystallinity, as determined by DSC, was calculated based on the integrated area of the melting endotherm divided by the heat of fusion of

191.9 J/g for an ideal α-form PA 6,6 crystal [30]. The percent crystallinities of the PA 6,6 fibers determined by WAXD and DSC exhibited differing values and trends. The percent crystallinity of the PA 6,6 fiber mats, as calculated from deconvolution of the WAXD spectra, decreases from 38.8% for the as-spun sample to 34.9% and 35.7% for the 70 °C and 170 °C heat-treated samples, respectively. Thermal annealing above T_B showed an increase in the percent crystallinity to 40.1% for the 240 °C annealed sample and 44.9% crystallinity for the 270 °C thermally annealed sample. The percent crystallinity as measured by DSC, showed the as-spun fibers to be 41.0% crystalline, while the samples annealed at 70 °C exhibited a small drop to 40.1%, indicating that the annealing temperature was too low to cause significant changes to the crystal structure of the polymer. The crystallinity dropped more significantly, to 34.4%, for the samples annealed at 170 °C, and an even further to 32.7% for the samples annealed at 240 °C. These results show that while the annealing process changes the crystal structure of the PA 6,6 fibers, the total percent crystallinity of the samples also changes with temperature of thermal treatment. The relatively high percent crystallinity for the 270 °C (44.9% by WAXD) confirms that the annealing and subsequent quenching process of the fiber mats produced larger, but perhaps less perfect, crystallites.

Table 4-1. Structural Properties of Heat-treated Electrospun PA 6,6 Fiber Mats

Sample	**D**	***f***	**Crystallinity (WAXD) [%]**	**Crystallinity (DSC) [%]**	**T_m (DSC-1st Peak) [°C]**	**T_m (DSC-2nd Peak) [°C]**
As-spun	1.17	0.054	38.8	41.0	255.8	-
70 °C HT	1.37	0.109	34.9	40.1	252.6	257.1
170 °C HT	1.24	0.074	35.7	34.4	254.4	259.2
240 °C HT	0.73	-0.091	40.1	32.7	237.5	247.8
270 °C HT	0.54	-0.181	44.9	32.2	253.0	-

4.3.3 Mechanical Properties of Heat-Treated Electrospun Mats

Uniaxial, constant strain-rate tensile testing was employed to observe the effect of the annealing temperature on the mechanical response of the semi-crystalline electrospun fiber mats. Representative plots of the tensile behavior of heat-treated electrospun mats are shown in Figure 4-8; note the slight increase in modulus and yield stress with increasing temperature of heat-treatment and the transition from more highly extensible, plastic behavior for the untreated sample to more brittle behavior when annealing close to or above T_m. The PA 6,6 mats as-spun

and annealed at 70 °C both exhibited the most ductile behavior, with large plastic deformation regions extending well beyond 50% breaking strain for most of the samples tested. The samples annealed at 170 °C and 240 °C exhibited some ductility, with higher elastic moduli, and breaking strains of 35-45%. The sample annealed at 270 °C exhibited much more brittle behavior, with a very narrow plastic deformation region, breaking very shortly after reaching the yield point. This behavior is similar to that observed for the amorphous nylon electrospun fiber mat annealing above T_g [17].

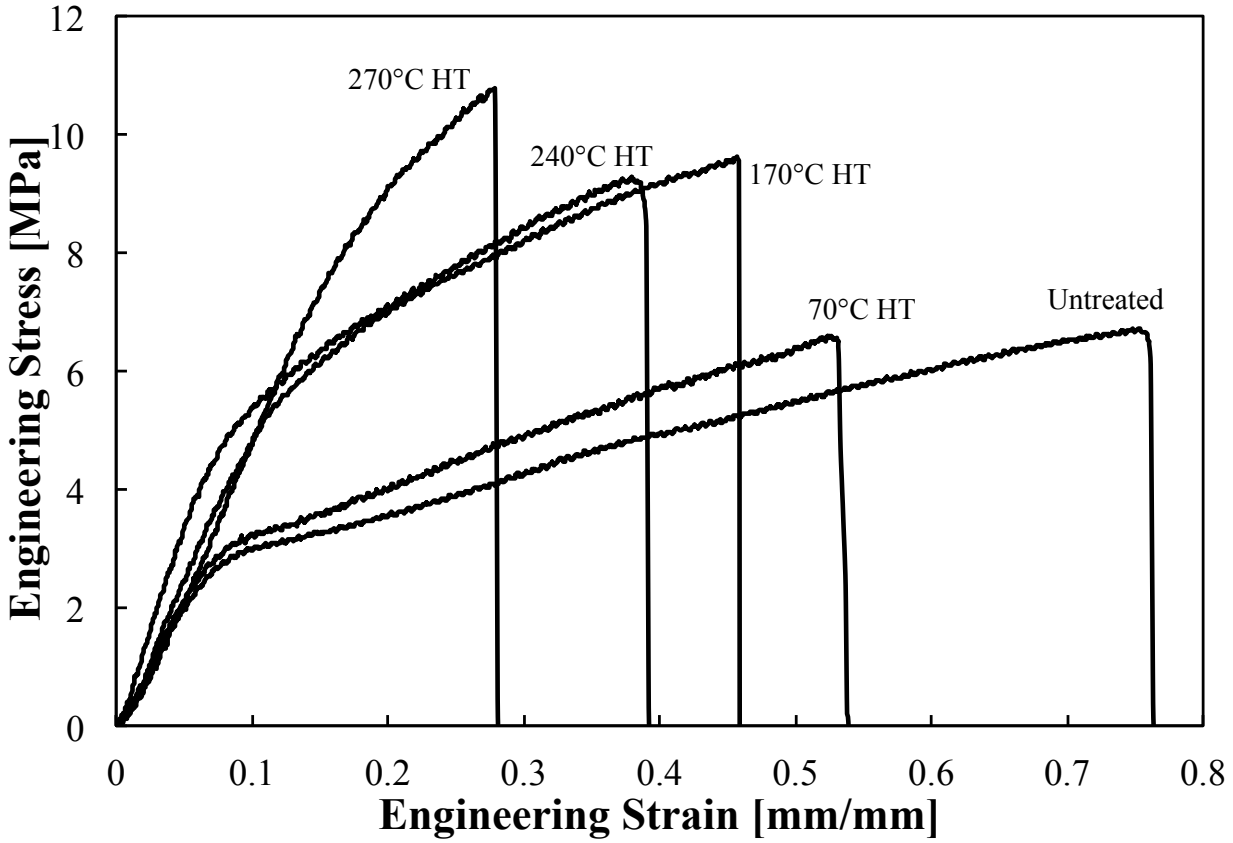

Figure 4-8. Representative stress-strain curves for PA 6,6 fiber mats as-spun and after annealing at various temperatures (1 hour each at 70, 170, 240, and 270 °C).

Analysis of the nonwoven mat tensile testing results indicates that thermal annealing of the electrospun fiber mats can significantly alter their mechanical properties. Plots showing changes to the Young's modulus, yield stress, maximum (breaking) stress, breaking strain, and tensile energy-to-break (toughness) are plotted in Figures 8-10. The Young's modulus for the as-spun material was 45.11 ± 2.30 MPa and did not increase when thermally annealed slightly above T_g (70 °C HT sample); however, it did increase modestly to 67.81 ± 6.53 MPa after annealing at 170 °C (between T_g & T_m), as shown in Figure 4-9. Further improvements to the

Young's modulus were not observed in the samples annealed around the T_m of PA 6,6 (240 °C and 270 °C), indicating that crystal annealing/melting within the fibers does not have a significant effect on the Young's modulus of the nonwoven mat.

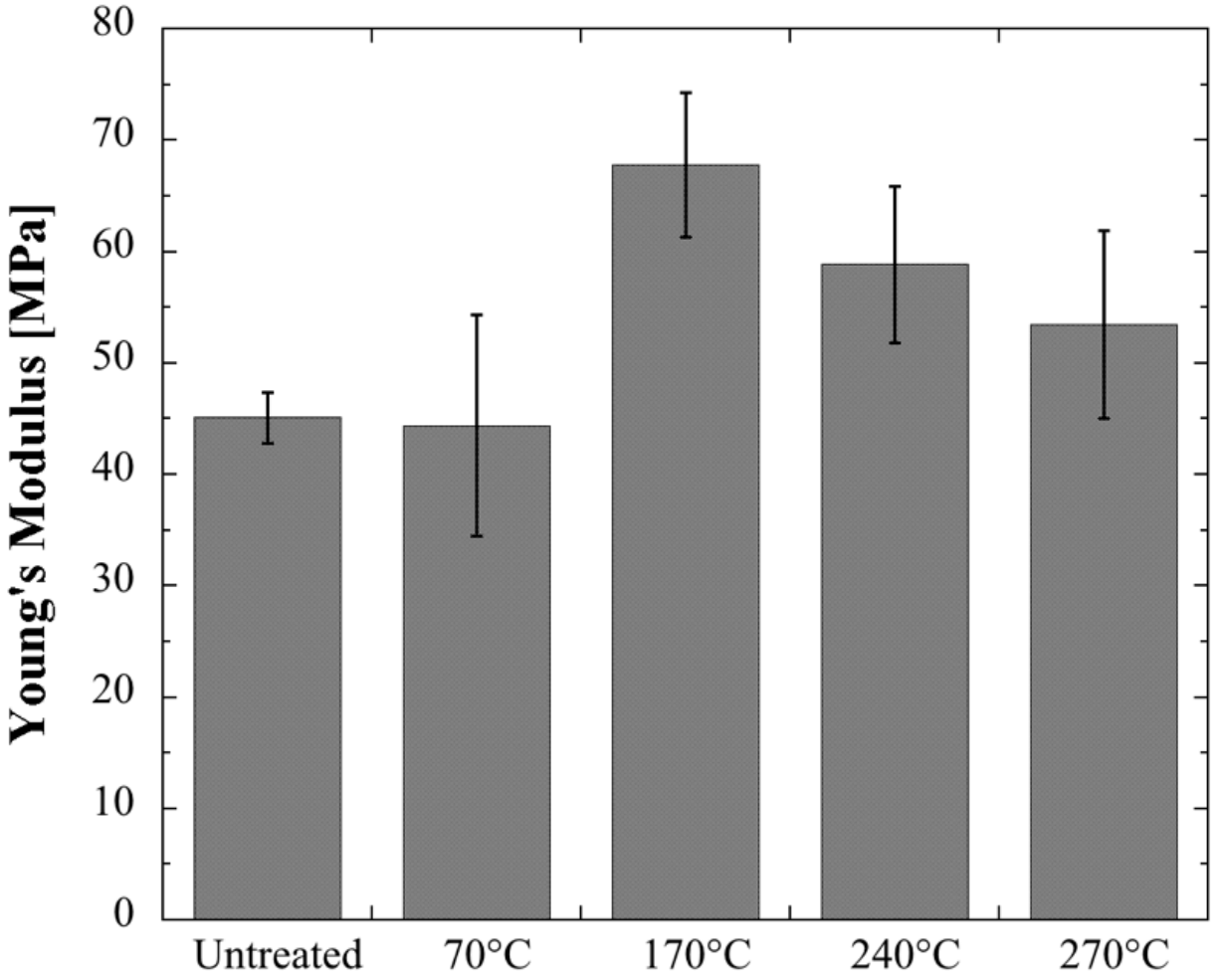

Figure 4-9. Plot of Young's modulus vs. annealing temperature for PA 6,6 nanofiber mats.

The yield stress and maximum (breaking) stress of the mats as a function of annealing temperature is shown in Figure 4-10. Steady increases in the yield stress are observed from the as-spun state at 2.92 ± 0.14 MPa up to 4.54 ± 0.43 MPa for the samples annealed above T_g (170 °C), then increases even further for samples annealed above T_m (7.05 ± 1.10 MPa for the 270 °C HT). The bar graph for the yield stress looks very similar to the inverse of the trend in porosity shown in Figure 4-3, with consistent increases in the yield stress for each increase in the temperature of annealing. The maximum (breaking) tensile stress of the PA 6,6 mats shows a modest increase between 70 °C and 170 °C thermal treatment (increasing from 5.94 ± 0.99 MPa

to 9.03 ± 1.37 MPa); however, no further increases in the breaking stress is observed with annealing at higher temperatures than 170 °C, and all values are statistically identical for samples annealed at 170, 240, or 270 °C.

Bar graphs for strain at break and for toughness of the electrospun fiber mats are shown in Figure 4-11. They do not follow a consistent trend with increasing annealing temperature. There is a slight drop in the strain at break for the sample annealed at 170 °C and another drop for the sample annealed at 240 °C, indicating a possible transition from a ductile fracture response to more brittle behavior or introduction of microstructural flaws or stress concentrators (crystallites) causing premature fracture. The large variations in the data for strain at break, are likely due to the sensitivity of failure to the weakest points in the mats, where stress can build up rapidly; such stress concentrators are common in porous and heterogeneous materials. The toughness of the electrospun mats correlates very closely to the strain at break. This behavior reflects the fact that the breaking stress for all of the samples did not vary by more than 50% from the lowest mean value to the highest, while the strain to break dropped from 0.67 ± 0.11 mm/mm to 0.27 ± 0.05 mm/mm for the as-spun sample and the sample annealed at 270 °C, respectively. This suggests that the breaking strain is the dominant factor in determining the tensile energy-to-break for the PA 6,6 fiber mats.

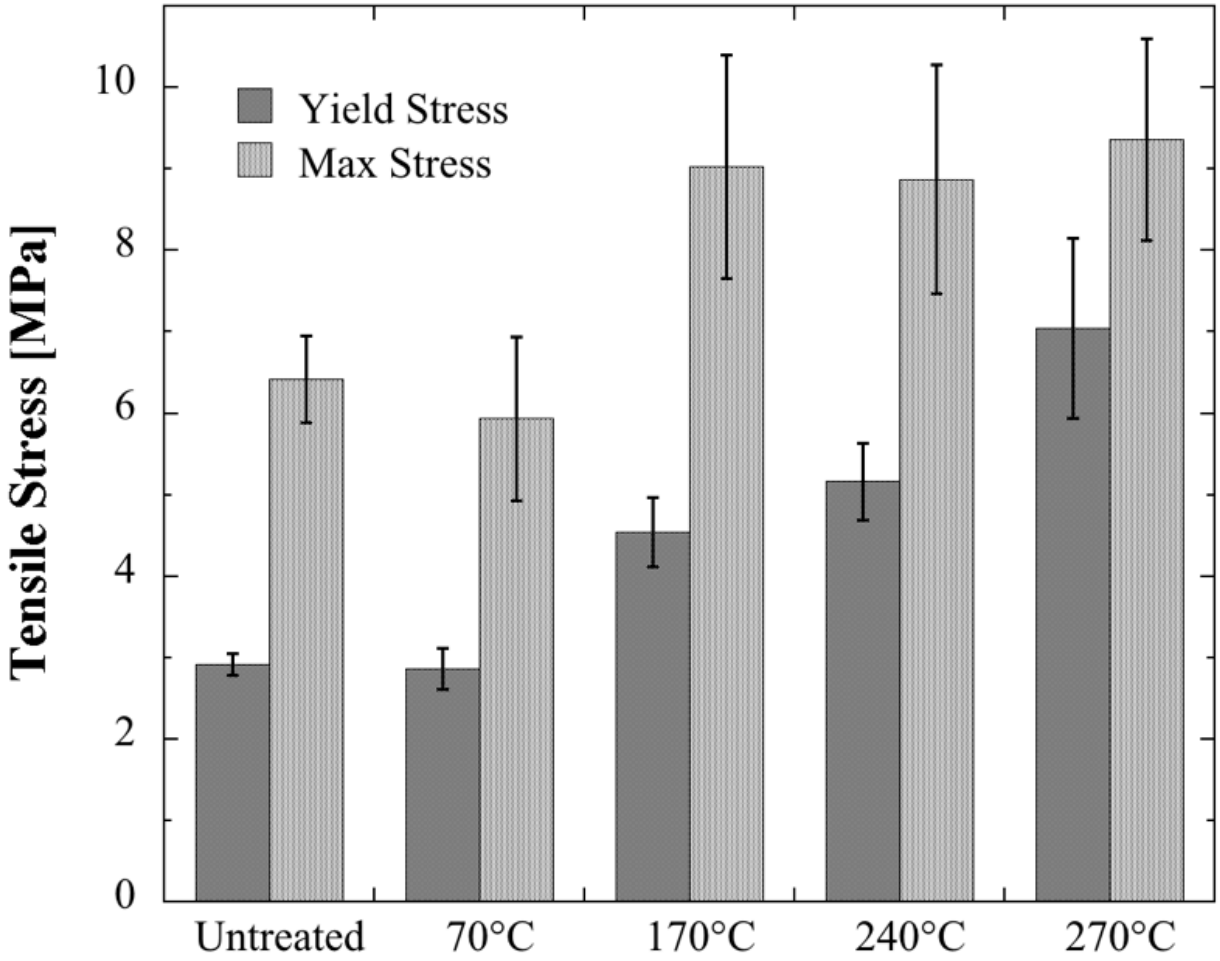

Figure 4-10. Plot of the yield stress and maximum (breaking) stress of PA 6,6 electrospun mats vs. annealing temperature.

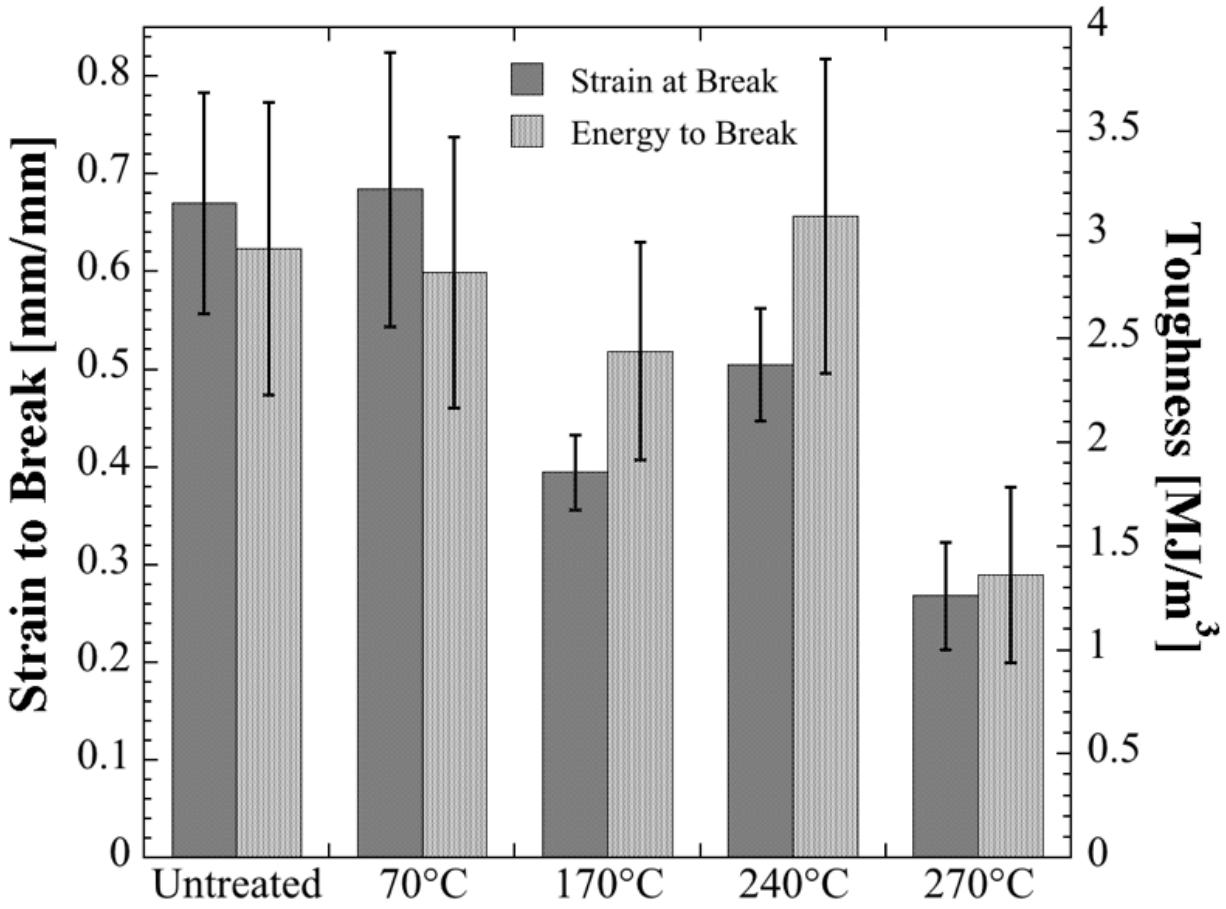

Figure 4-11. Plot of the strain-to-break and tensile energy-to-break (Toughness) vs. annealing temperature for PA 6,6 nanofiber mats.

4.3.4 Tribology of Electrospun Mats

Untreated electrospun fiber mats are typically fragile and susceptible to wear and delamination, even under conditions of gentle handling. This is a source of concern for the post-spin handling as well as the end-use of such mats, and could be a critical limitation to their service lifetime. To quantify the tribological behavior of nonwovens, the coefficient of friction (μ) was measured using a standardized testing material (Calibrade® H-38 abrasive wheel) for each of the fiber mats, as-spun and after each of the prescribed annealing temperatures. A plot of the friction force vs. the normal force for each annealing temperature is shown in Figure 4-12; from this plot, the friction coefficient can be determined by taking the ratio of the average measured friction force to the applied normal force. A plot of the coefficient of friction vs. the normal force is shown in Figure 4-13; note that there is a modest decrease in the coefficient of friction with increasing normal force at low loads, but that above 1.0 N (~100 g applied load),

the friction coefficient becomes relatively constant for each sample. The decrease in coefficient of friction with increasing load is typical of compressible polymeric materials, due to increasing shear strength with applied load in these materials [41]. Mean friction coefficients at 0.5 N load decreased from 0.97 for the as-spun mat to 0.85 for the 170 °C heat-treatment sample, to 0.69 for the 240 °C heat-treated mat. A lower mean coefficient of friction for the fiber mats is typically desirable, as it implies that the mat experiences smaller forces during abrasive contact with a counter-face, which could lead to significantly less wear.

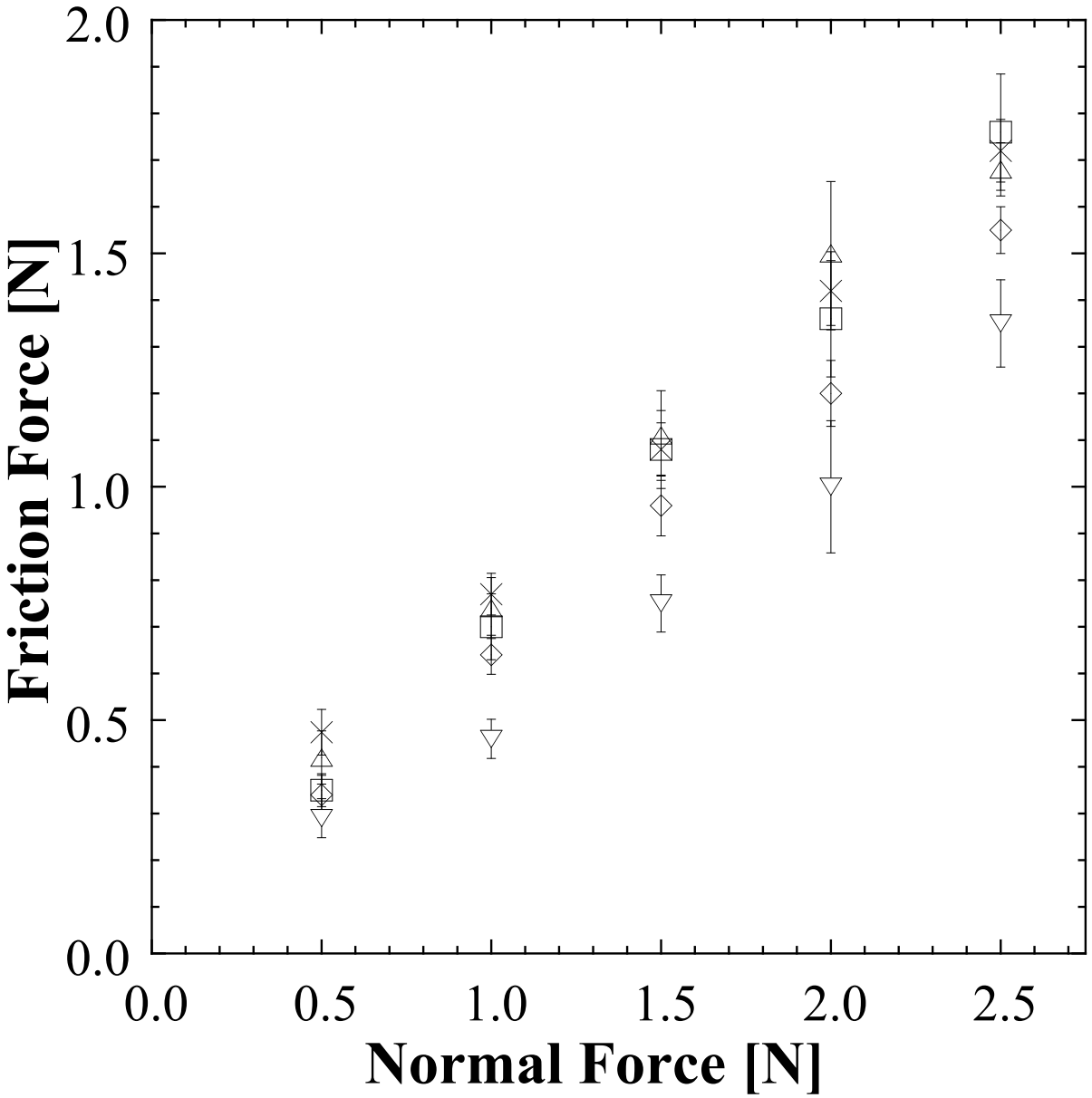

Figure 4-12. Friction force of PA 6,6 mats as a function of the normal force after annealing at various temperatures: as-spun (×), 70 °C (□), 170 °C (△), 240 °C (◇) and 270 °C (▽).

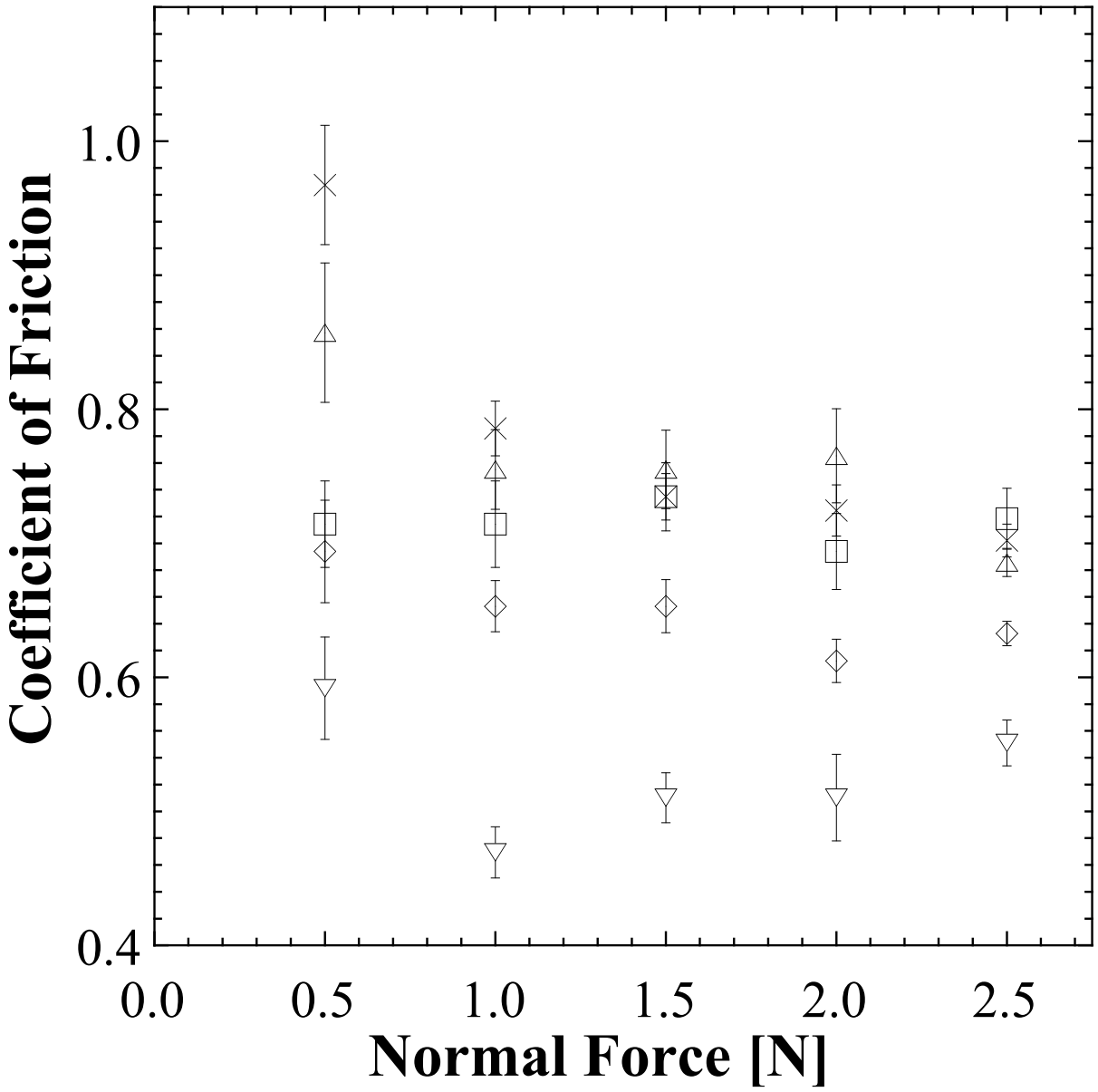

Figure 4-13. Coefficient of Friction of PA 6,6 mats as a function of the normal force after annealing at various temperatures: as-spun (×), 70 °C (□), 170 °C (△), 240 °C (◇) and 270 °C (▽).

The Taber abraser was used to provide uniform, low levels of abrasive wear in order to measure quantitatively the changes in the tribological response of annealed electrospun PA 6,6 fiber mats. The surface roughness of a material can be a major factor in the tribological response, relating to the area of contact between the test material and the abrasive counter-surface; all of the PA 6,6 mats used in these wear tests had a mean-value roughness (R_a) on the order of 1.5-2.5 μm; values are listed in Table 4-2. An applied load of 50 g was used for testing because it was

sufficiently high to yield consistent coefficient of friction values, while being low enough such that more than 100 abrasion cycles could be performed before destruction of each sample. Temperature changes to the fiber mat during abrasive cycling were monitored using a non-contact infrared thermometer. The surface temperature of the mats were measured to be 25.0 ± 0.2 °C before wear testing and typically did not increase by more than 0.4 °C (25.8 °C maximum reading) at any point during testing, even up to 500 continuous abrasion cycles. The mats never approached the T_g (45 °C) or T_m (254 °C) of the bulk PA 6,6 during testing and should therefore not have undergone any thermally induced transformations or deformations due to the wear cycling.

Visual inspection of the nonwoven membranes after 10, 50, and 100 abrasion cycles indicated significant qualitative differences in the wear mechanisms between the samples annealed at the various temperatures, as shown in Figure 4-14. The as-spun sample and the sample annealed at 70 °C exhibited some observable signs of deformation and wear after as few as 10 abrasion cycles, and significant levels of deformation and wear after 50 cycles; the samples typically reached tribological destruction (>50% of sample mass removed from the wear path) by approximately 100 abrasion cycles. The sample annealed at 170 °C exhibited only marginally more wear resistance; however, the mechanism of wear seemed to have changed from a fibrous pulling/displacement-type deformation to more of a tearing and rolling mechanism. The sample annealed at 240 °C exhibited significantly more robust wear resistance, and showed only minor wear and abrasive tears at 10 and 50 cycles, before exhibiting more significant tearing and delamination after 100 cycles. The samples annealed at 240 °C did not reach the 50% mass loss wear destruction until as much as 500 abrasion cycles. The samples annealed at 270 °C were also very robust, showing minimal signs of wear until 50 abrasion cycles (most of which are small tears and holes), then exhibiting some more significant levels of tearing after 100 cycles.

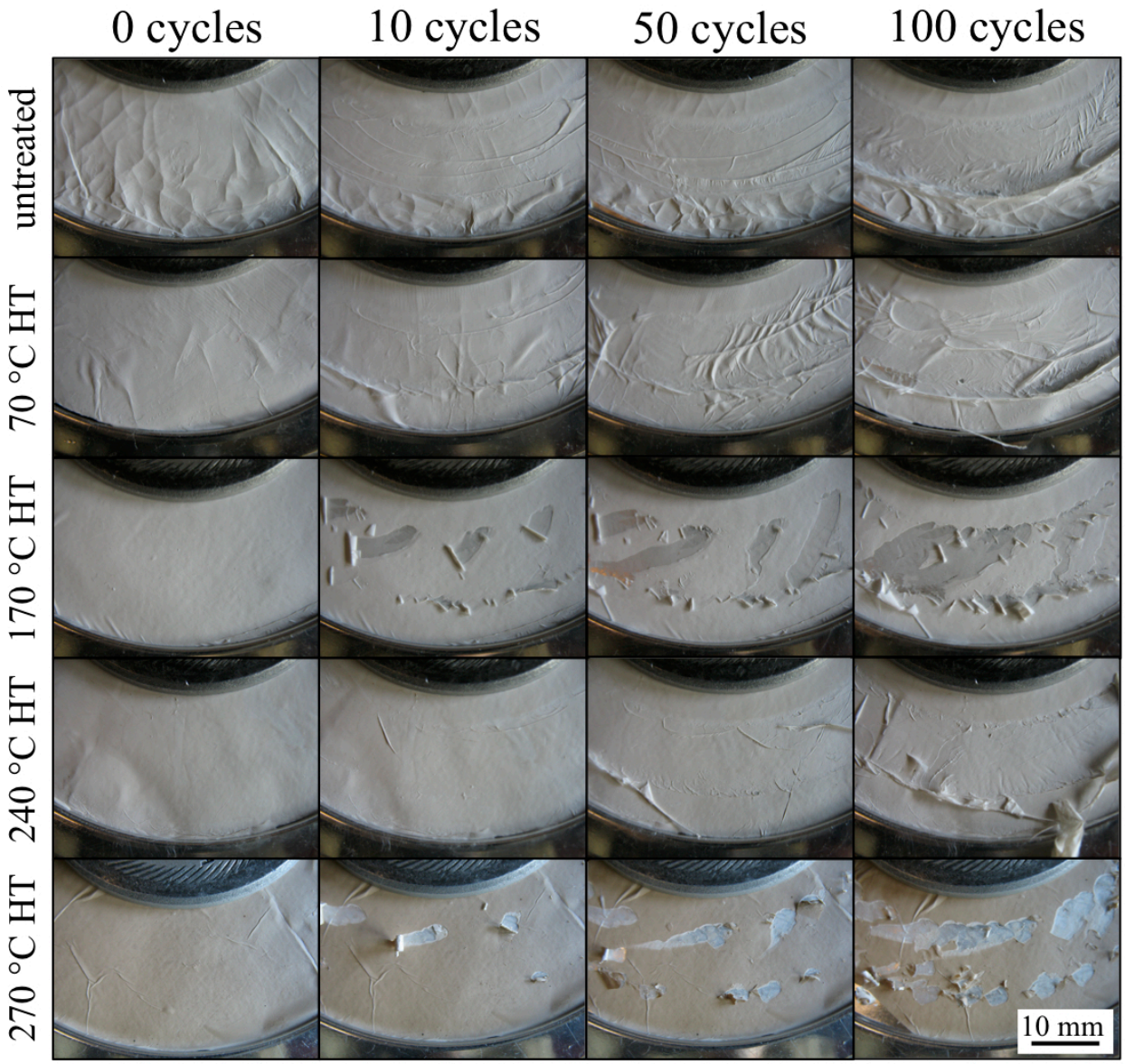

Figure 4-14. Optical images of abrasive wear path for fiber mats at 0, 10, 50, and 100 wear cycles under 50 g applied load (top row: as-spun; second row: 70 °C heat-treated; third row: 170 °C heat-treated, fourth row: 240 °C heat-treated, bottom row: 270 °C heat-treated), scale bar is 10 mm.

Quantitative evaluation of the abrasive wear properties of the electrospun PA 6,6 mats was performed by measuring the mass loss of the samples after a specified number of abrasion cycles. A plot of the abrasive mass loss vs. the number of cycles for 50 g applied load is shown in Figure 4-15 for 10, 50, 100, and 250 cycles. The wear rate was measured up to approximately 50% mass loss within the wear path, or ~35-40 mg for each sample, which was defined as the point of tribological destruction. Significantly more material was removed from the untreated

electrospun mats compared to the thermally annealed samples, with the most wear-resistant mats being those annealed at 240 °C; this is consistent with what was observed qualitatively from visual inspection. Modest decreases in the effective wear rate of the electrospun fiber mats was observed with increasing temperature of thermal annealing for 70 °C, 170 °C, and 240 °C; however, annealing the PA 6,6 mats at 270 °C (above the T_m) yielded an increase in the wear rate compared to the mat annealed at 240 °C, indicating that there could be significant morphological changes in the samples annealed at 270 °C that affected the wear response. The effective wear rate for each sample was calculated as the slope of the tangent to a best-fit second-order polynomial to each set of wear data, evaluated at 100 cycles. The effective wear rate was seen to decrease from 8.10×10^6 g/cm for the as-spun PA 6,6 sample down to 3.01×10^6 g/cm for the mats annealed at 240 °C. The improvements to the wear resistance of electrospun PA 6,6 mats were not as significant as previously seen for poly(trimethyl hexamethylene terephthalamide) [PA 6(3)T] fiber mats [17]. However, the amorphous polyamide samples also had greater changes in mechanical properties with thermal annealing. A summary of all the tribological data including the mean-value roughness (R_a), mean coefficient of friction (μ), and effective wear rate are compiled in Table 4-2.

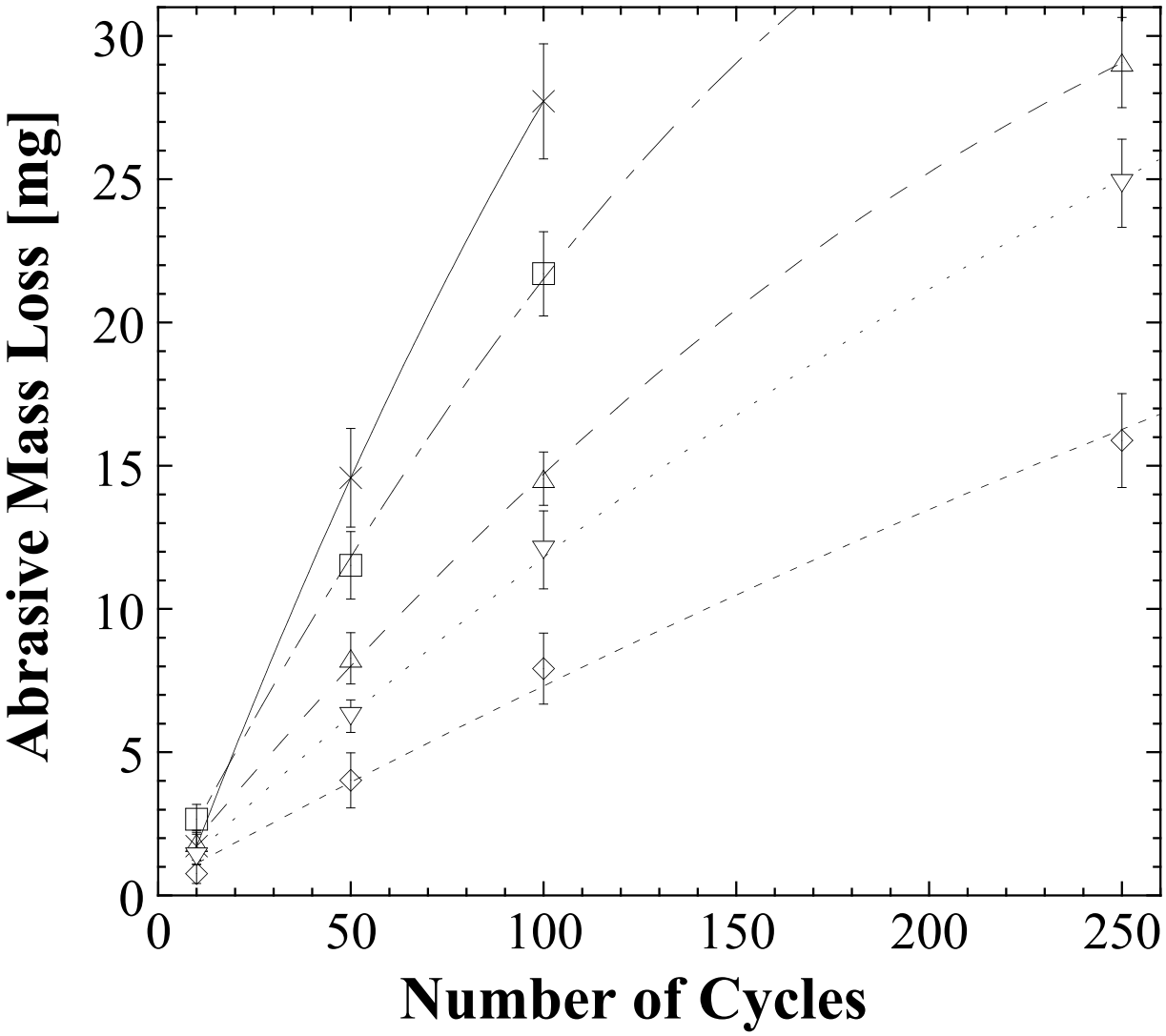

Figure 4-15. Abrasive mass losses of electrospun nanofiber mats as a function of the number of wear cycles under 50 g load: untreated (×), 70 °C heat-treated (□), 170 °C heat-treated (△), 240 °C heat-treated (◇) and 270 °C heat-treated mats (▽).

Table 4-2. Summary of Tribological Properties of PA 6,6 Nanofiber Mats

	R_a [μm]	**Mean coefficient of friction, μ (50 g)**	**Wear rate (50 g) [g/cm]**
Untreated	2.459	0.97	8.10×10^{-6}
70 °C HT	1.887	0.71	7.12×10^{-6}
170 °C HT	2.298	0.85	5.17×10^{-6}
240 °C HT	2.145	0.69	3.01×10^{-6}
270 °C HT	1.581	0.59	4.55×10^{-6}

The tensile mechanical properties and the abrasive wear properties of polymeric materials tend to be strongly correlated. The deformation of a surface is generally a function of the indentation hardness, the relative motion opposed by the frictional force, and disruption of material at the contact points, involving an amount of work equal to the area under the stress-strain curve. One of the most commonly used correlations based on such a mechanism is the Ratner-Lancaster correlation [42,43], which predicts the wear rate, W, as:

$$W = C\left(\mu \frac{L}{H\sigma_b \varepsilon_b}\right) \qquad \text{(Equation 4-5)}$$

where C is a constant, μ is the coefficient of friction, L is the applied load, H is the hardness, σ_b is the breaking stress of the material, and ε_b is the breaking strain. The indentation hardness of most polymer fiber mats is relatively small and does not change significantly between materials; therefore, the dominant parameters tend to be σ_b and ε_b [44,45]. For electrospun fiber mats, we have previously proposed that the breaking stress and breaking strain of individual fibers is reflected in the yield stress and strain of the nonwoven mats; based on this, a modified version of the Ratner-Lancaster relationship is obtained, in which the yield stress, σ_y, and yield strain, ε_y, of the mat replace the breaking stress and strain of the fibers [17]. The wear rate is furthermore put on a mass basis by the density of the polymer mat, ρ, to get:

$$W \propto \left(\frac{\rho \mu L}{\sigma_y \varepsilon_y}\right) \qquad \text{(Equation 4-6)}$$

This modified Ratner-Lancaster relationship has been shown to correlate well the wear results for the electrospun mats of the amorphous polyamide PA 6(3)T [17]. Figure 4-16 compares the effective wear rates of the treated PA 6,6 fiber mats to the modified Ratner-Lancaster wear rate relationship from Equation 4-6, along with the previously reported PA 6(3)T data. The effective wear rate for the PA 6,6 mats increases proportionately with the quantity $(\rho\mu L)/(\sigma_y\varepsilon_y)$ for the samples annealed below the T_m. Only the sample annealed at 270 °C exhibits a wear rate that deviates significantly from the proposed scaling. This deviation from the expected scaling of the wear rate is most likely due to morphological changes of the crystal structure within the fibers, which could significantly alter the fracture mode and breaking strain of the individual fibers. With the exception of the sample annealed above T_m (270 °C heat treatment), the semi-crystalline PA 6,6 electrospun nonwoven mats wear more slowly, by a factor of 2-3, compared to

the amorphous PA 6(3)T electrospun nonwoven mats. These results show that the mechanical and tribological properties of electrospun fiber mats are well correlated by the modified Ratner-Lancaster model, and that the effects on wear resistance due to the crystallinity and crystal morphology within a semi-crystalline polymeric fiber mat cannot be neglected.

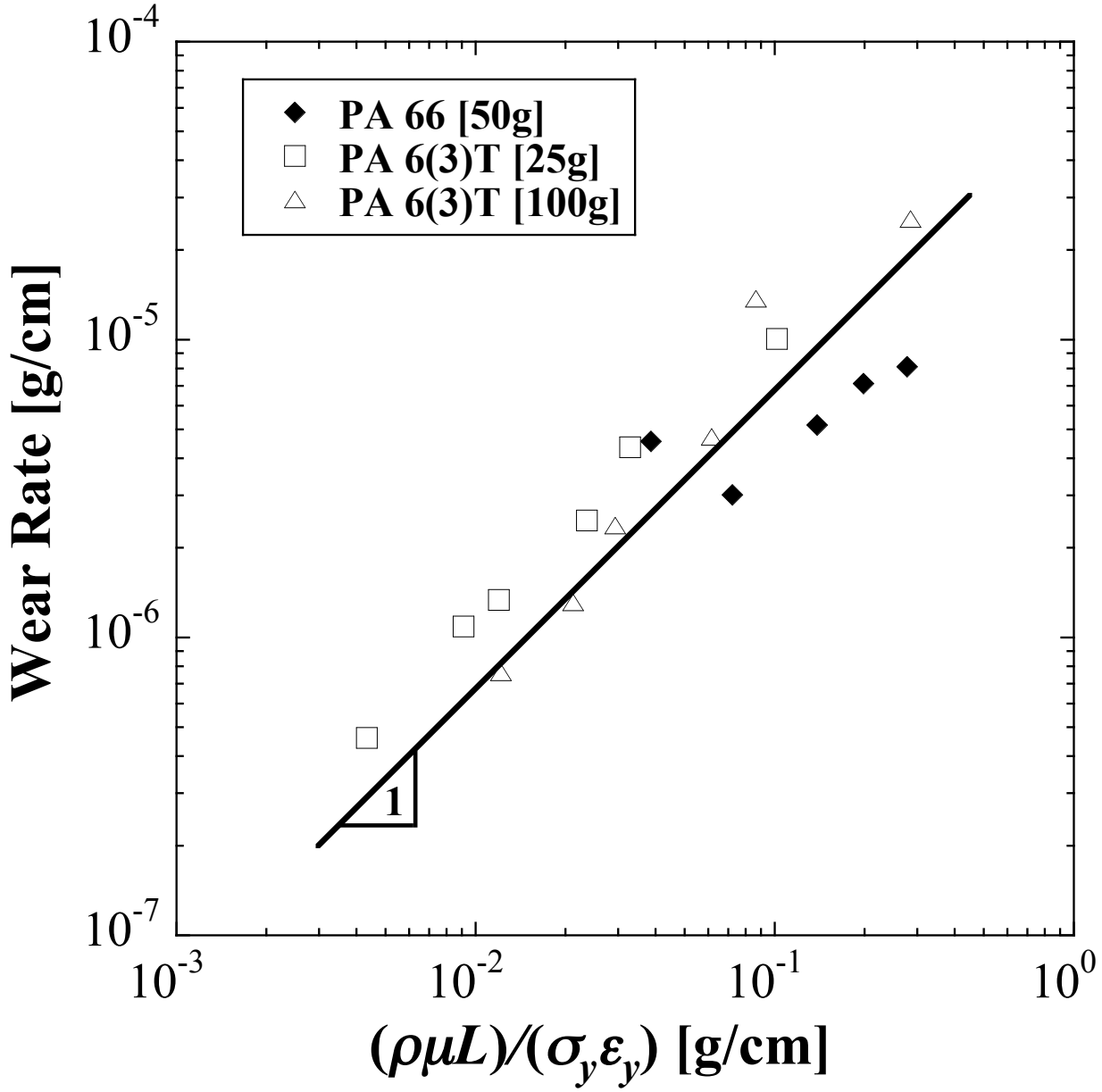

Figure 4-16. Effective wear rate vs. $(\rho\mu L)/(\sigma_y\varepsilon_y)$ of nanofiber mats subjected to varying temperatures of thermal treatment: PA 6,6 at 50 g applied load (◆) [this work], and PA 6(3)T from previous tribology investigation [17] at 25 g (□) and 100 g (△) applied load. The line with slope=1 is drawn as a guide to the eye.

4.4 Concluding Remarks

The tribological and mechanical response of thermally annealed semi-crystalline electrospun PA 6,6 fiber mats were investigated in this chapter. The crystallinity of the fiber mats was observed to exhibit small changes as a function of the annealing temperature, with more pronounced increases to the percent crystallinity, according to WAXD, when samples were treated above T_B. Significant changes to the crystal morphology and orientation were observed within the PA 6,6 fibers as molecular alignment changed from parallel to the fiber axis to perpendicular for samples treated above T_B. The change in molecular orientation is most likely due to the initial strain alignment when forming the crystallites as a result of the jet stretching during the electrospinning process. During the thermal annealing process above T_B, the molecular orientation relaxes as the chains become more mobile. The Young's modulus, yield stress, and toughness of the nonwoven mats were found to change with an increase in the annealing temperature through the glass transition, Brill transition, and crystalline melting points, at the expense of mat porosity. The yield stress increased modestly from 2.9 MPa for the untreated PA 6,6 nanofiber mat, to 4.5 MPa for the 170 °C heat-treatment, without suffering a significant loss of porosity. The yield stress could then be increased further up to 7.1 MPa after 270 °C heat-treatment (above the T_m), at a substantial loss to the mat porosity (90% to 72%). In addition to gains in mechanical integrity, there was also an improvement in the wear resistance of the semi-crystalline electrospun fiber mats with thermal treatment. Annealing at 240 °C results in a significant decrease in the effective wear rate relative to that of the as-spun mats, from 8.10×10^{-6} g/cm to 3.01×10^{-6} g/cm at 50 g applied load, while the porosity decreases only modestly, from 90% to 86%. The mechanical and tribological properties of the thermally annealed PA 6,6 fiber mats were found to exhibit significant improvements through the Brill transition temperature, comparable to the improvements observed when annealing amorphous PA 6(3)T electrospun mats near the glass transition temperature. The effective wear rate of the electrospun PA 6,6 fiber mats was well-described by a modified Ratner-Lancaster relationship for wear rate of polymeric materials, $W \sim (\rho \mu L)/(\sigma_y \varepsilon_y)$ for samples annealed below the T_m, suggesting that the mechanism of wear is primarily due to the breakage of fibers that apparently contributes to yield in these nonwoven mats. Only the sample annealed at 270 °C exhibits a wear rate that deviated significantly from the proposed scaling. The deviation from the modified Ratner-Lancaster correlation is most likely due to the changes observed in the crystal orientation

and morphology; these changes could affect the individual fiber properties such as the fracture mode and breaking strain of the individual fibers, resulting in a lower mechanical energy required to remove material from the surface. The mechanical and tribological properties of electrospun fiber mats are found to be inter-related, and the effects of crystallinity and crystal morphology within semi-crystalline polymeric fiber mats are significant with respect to the wear resistance.

4.5 Acknowledgments

Funding for this portion of the thesis was provided by the U.S. Army through the Institute for Soldier Nanotechnologies (ISN) under AROW911NF-07-D-0004. The author would like to thank Prof. Stephen Burke Driscoll and the Plastics Engineering Department at the University of Massachusetts Lowell for use of their Taber abraser and for discussions about wear testing of textiles. The author would like to thank Dr. Jason Lee for his assistance with X-ray diffraction and Tim McClure for his assistance with FTIR. The author would also like to acknowledge the Hammond lab at MIT for use of their Dektak surface profiling system, and the MIT Institute of Soldier Nanotechnology and Center for Materials Science and Engineering (CMSE) for use of facilities.

4.6 References

[1] J. Doshi, D.H. Reneker, Electrospinning process and applications of electrospun fibers, Journal of Electrostatics 35 (1995) 151-160.

[2] Y.M. Shin, M.M. Hohman, M.P. Brenner, G.C. Rutledge, Electrospinning: a whipping fluid jet generates submicron polymer fibers, Applied Physics Letters 78 (2001) 1149-1151.

[3] R.G. Flemming, C.J. Murphy, G.A. Abrams, S.L. Goodman, P.F. Nealey, Effects of synthetic micro- and nano-structured surfaces on cell behavior, Biomaterials 20 (1999) 573-588.

[4] J.A. Matthews, G.E. Wnek, D.G. Simpson, G.L. Bowlin, Electrospinning of collagen nanofibers, Biomacromolecules 3 (2002) 232-238.

[5] K. Kim, M. Yu, X. Zong, J. Chiu, D. Fang, Y.-S. Seo, B.S. Hsiao, Control of degradation rate and hydrophilicity in electrospun non-woven poly (D, L-lactide) nanofiber scaffolds for biomedical applications, Biomaterials 24 (2003) 4977-4985.

[6] J. Zeng, X. Xu, X. Chen, Q. Liang, X. Bian, L. Yang, X. Jing, Biodegradable electrospun fibers for drug delivery, Journal of Controlled Release 92 (2003) 227-231.

[7] X.Y. Wang, C. Drew, S.H. Lee, K.J Senecal, J. Kumar, L.A. Samuelson, Electrospinning technology: A novel approach to sensor application, Journal of Macromolecular Science-Pure and Applied Chemistry A39 (2002) 1251-58.

[8] J. Choi, K.M. Lee, R. Wycisk, P.N. Pintauro, P.T. Mather, Nafion-impregnated electrospun polyvinylidene fluoride composite membranes for direct methanol fuel cells, Journal of Power Sources 180 (2008) 167-171.

[9] R. Bajon, S. Balaji, S.M. Guo, Electrospun Nafion Nanofiber for Proton Exchange Membrane Fuel Cell Application, Journal of Fuel Cell Science Technology 6 (2009) 031004.

[10] L. Li, L.M. Bellan, H.G. Craighead, M.W. Frey, Formation and properties of nylon-6 and nylon-6/montmorillonite composite nanofibers, Polymer 47 (2006) 6208-6217.

[11] C.L. Pai, M.C. Boyce, G.C. Rutledge, Mechanical properties of individual electrospun PA 6 (3) T fibers and their variation with fiber diameter, Polymer 52 (2011) 2295-2301.

[12] H.J. Jin, H.S. Chen, V. Karageorgiou, G.H. Altman, D.L. Kaplan, Human bone marrow stromal cell responses on electrospun silk fibroin mats, Biomaterials 25 (2004) 1039-1047.

[13] X.H. Zong, S.F. Ran, D.F. Fang, B.S. Hsiao, B. Chu, Control of structure, morphology and property in electrospun poly (glycolide-*co*-lactide) non-woven membranes via post-draw treatments, Polymer 44 (2003) 4959-4967.

[14] G.C. Engelmayr Jr, M.S. Sacks, A structural model for the flexural mechanics of nonwoven tissue engineering scaffolds, Journal of Biomechanical Engineering 128 (2006) 610-622.

[15] C.L. Pai, M.C. Boyce, G.C. Rutledge, On the importance of fiber curvature to the elastic moduli of electrospun nonwoven fiber meshes, Polymer 52 (2011) 6126-6133.

[16] X. Wang, K. Zhang, M. Zhu, B.S. Hsiao, B. Chu, Enhanced mechanical performance of self-bundled electrospun fiber yarns via post-treatments, Macromolecular Rapid Communications 29 (2008) 826-831.

[17] M.M. Mannarino, G.C. Rutledge, Mechanical and tribological properties of electrospun PA 6 (3) T fiber mats, Polymer 53 (2012) 3017-3025.

[18] C. Lai, G. Zhong, Z. Yue, G. Chen, L. Zhang, A. Vakili, Y. Wang, L. Zhu, J. Liu, H. Fong, Investigation of post-spinning stretching process on morphological, structural, and mechanical properties of electrospun polyacrylonitrile copolymer nanofibers, Polymer 52 (2011) 519-528.

[19] H. Na, Y. Zhao, C. Zhao, C. Zhao, X. Yuan, Effect of hot-press on electrospun poly(vinylidene fluoride) membranes, Polymer Engineering And Science 48 (2008) 934-940.

[20] L. Jeong, K.Y. Lee, J.W. Liu, W.H. Park, Time-resolved structural investigation of regenerated silk fibroin nanofibers treated with solvent vapor, International Journal of Biological Macromolecules 38 (2006) 140-144.

[21] C.L. Pai, M.C. Boyce, G.C. Rutledge, Morphology of porous and wrinkled fibers of polystyrene electrospun from dimethylformamide, Macromolecules 42 (2009) 2102-2114.

[22] S. Derler, G.U. Schrade, L.C. Gerhardt, Tribology of human skin and mechanical skin equivalents in contact with textiles, Wear 263 (2007) 1112-1116.

[23] L.C. Gerhardt, N. Mattle, G.U. Schrade, N.D. Spencer, S. Derler, Study of skin-fabric interactions of relevance to decubitus: friction and contact-pressure measurements, Skin Research and Technology 14 (2007) 77-88.

[24] Y. Liu, L. Cui, F. Guan, Y. Gao, N.E. Hedin, L. Zhu, H. Fong, Crystalline morphology and polymorphic phase transitions in electrospun nylon-6 nanofibers, Macromolecules 40 (2007) 6283-6290.

[25] E. Zussman, M. Burman, A.L. Yarin, R. Khalfin, Y. Cohen, Tensile deformation of electrospun nylon-6,6 nanofibers, Journal of Polymer Science Part B-Polymer Physics 44 (2006) 1482-1489.

[26] K. Gao, X. Hu, C. Dai, T. Yi, Crystal structures of electrospun PVDF membranes and its separator application for rechargeable lithium metal cells, Materials Science & Engineering B 131 (2006) 100-105.

[27] D. Cho, E. Zhmayev, Y.L. Joo, Structural studies of electrospun nylon 6 fibers from solution and melt, Polymer 52 (2011) 4600-4609.

[28] W. He, Z.W. Ma, T. Yong, W.E. Teo, S. Ramakrishna, Fabrication of collagen-coated biodegradable polymer nanofiber mesh and its potential for endothelial cells growth, Biomaterials 26 (2005) 7606-7615.

[29] X. Zhu, W. Cui, X. Li, Y. Jin, Electrospun fibrous mats with high porosity as potential scaffolds for skin tissue engineering, Biomacromolecules 9 (2008) 1795-1801.

[30] H.W. Starkweather, P. Zoeller, G.A. Jones, The heat of fusion of 66 nylon, Journal of Polymer Science: Polymer Physics 22 (1984) 1615-1621.

[31] M. Wang, J.H. Yu, D.L. Kaplan, G.C. Rutledge, Production of submicron diameter silk fibers under benign processing conditions by two-fluid electrospinning, Macromolecules 39 (2006) 1102-1107.

[32] S.J. Cooper, M. Coogan, N. Everall, I. Priestnall, A polarized μ-FTIR study on a model system for nylon 6,6: implications for the nylon Brill structure, Polymer 42 (2001) 10119-10132.

[33] N.S. Murty, M. Stamm, J.P. Sibilia, S. Krimm, Structural-changes accompanying hydration in nylon-6, Macromolecules 22 (1989) 1261-1267.

[34] N.Y. Jia, H.A. Frenkel, V.A. Kagan, Effects of moisture conditioning methods on mechanical properties of injection molded nylon 6, Journal of Reinforced Plastics and Composites 23 (2004) 729-737.

[35] D.-J. Lin, C.-L. Chang, C.-K. Lee, L.-P. Cheng, Fine structure and crystallinity of porous Nylon 66 membranes prepared by phase inversion in the water/formic acid/Nylon 66 system, European Polymer Journal 42 (2006) 356-367.

[36] C.W. Bunn, E.V. Garner, The crystal structures of two polyamides ('nylons'), Proceedings of the Royal Society of London A 189 (1947) 39-68.

[37] H.W. Starkweather, G.A. Jones, Crystalline transitions in powders of nylon 66 crystallized from solution, Journal of Polymer Science: Polymer Physics Edition 19 (1981) 467-477.

[38] N.S. Murthy, S.A. Curran, S.M. Aharoni, H. Minor, Premelting crystalline relaxations and phase transitions in nylon 6 and 6, 6, Macromolecules 24 (1991) 3215-3220.

[39] C. Ramesh, A. Keller, S.J.E.A. Eltink, Studies on the crystallization and melting of nylon-6,6: 1. The dependence of the Brill transition on the crystallization temperature, Polymer 35 (1994) 2483-2487.

[40] N. Vasanthan, Crystallinity determination of nylon 66 by density measurement and fourier transform infrared (FTIR) spectroscopy, Journal of Chemical Education 89 (2012) 387-390.

[41] N.P. Suh, Tribophysics, 1st ed. New Jersey: Prentice-Hall, 1986.

[42] K.G. Budinski, Resistance to particle abrasion of selected plastics, Wear 203 (1997) 302-309.

[43] J.K. Lancaster, Abrasive wear of polymers, Wear 14 (1969) 223-239.

[44] A. Wang, D.C. Sun, C. Stark, J.H. Dumbleton, Wear mechanisms of UHMWPE in total joint replacements, Wear 181 (1995) 241-249.

[45] P.H. Shipway, N.K. Ngao, Microscale abrasive wear of polymeric materials, Wear 255 (2003) 742-750.

5. Fabrication of Mechanically Robust, Highly Selective Layer-by-Layer/Electrospun Fiber Composite Proton Exchange Membranes

Portions of this chapter are reproduced from D.S. Liu, J.N. Ashcraft, M.M. Mannarino, M.N. Silberstein, A.A. Argun, G.C. Rutledge, M.C. Boyce, P.T. Hammond, Advanced Functional Materials (2013) [In Press], with permission of John Wiley & Sons, Ltd., and M.M. Mannarino, D.S. Liu, P.T. Hammond, G.C. Rutledge, Applied Materials & Interfaces (2013) [In Preparation].

5.1 Introduction

The development of thin solid polymer electrolytes with improved performance is critical for the advancement of electrochemical energy devices [1]. In recent years, considerable interest has been focused on designing chemically and mechanically stable membranes while maintaining high ionic conductivity with low fuel cross-over [2]. For hydrogen and direct methanol fuel cells, membranes comprising perfluorosulfonic acid polymers such as Nafion have been used because they exhibit superior protonic conductivity with relatively high mechanical integrity and chemical stability, despite their high cost [3]. However, even the perfluorosulfonic acid polymers have shown limited device lifetimes due to chemical and mechanical degradation [4,5,6]. One of the main causes of membrane failure is the poor dimensional stability, caused by repeated swelling/deswelling of the membrane in a fuel cell from the cycling of temperature and humidity, which has been shown to mechanically weaken the membrane after only a few hundred cycles [7,8,9]. Typically, to improve the membrane's mechanical properties, the ionomer (Nafion) is incorporated into dimensionally stable supporting matrices such as polytetrafluoroethylene (PTFE) and expanded polytetrafluoroethylene (ePTFE) [4,10,11,12]. Other researchers have tried incorporating carbon nanotubes, metal oxides, and zirconium phosphates into Nafion matrices to improve lifetime or cell performance [13,14,15].

The difficulty with these bulk composites is the lack of control of composition on the micron scale and the continued reliance on Nafion, with its high cost and relatively high fuel crossover, in particular for methanol. A promising approach is to combine two relatively new

processing techniques, layer-by-layer (LbL) assembly of polymer thin films and electrospinning of nanofiber mats. LbL assembly is an extremely versatile nano-scale fabrication technique that allows for the conformal coating of any wettable substrate with a combination of two or more polymers possessing complementary interactions (e.g. oppositely charged functional groups) [16,17,18]. The films are generated through the alternating adsorption of polyanions and polycations, and can be further tuned by adjusting the pH or adding salt to the polymer solutions during assembly, with typical thickness per bilayer ranging from a few nanometers to over a hundred nanometers. Farhat et al. and Argun et al. recently reported the fabrication of LbL-based proton exchange membranes (PEMs) with high performance in hydrogen and direct methanol fuel cells [19,20]. Further work by Ashcraft et al. reported that the LbL system composed of poly(diallyl dimethyl ammonium chloride) (PDAC) and sulfonated poly(2,6-dimethyl 1,4-phenylene oxide) (sPPO), structures shown in Figure 5-1, yielded the highest ionic conductivity of any LbL assembled system, as high as 70 mS cm^{-1}, which is on the order of Nafion's conductivity (~98 mS cm^{-1}). The PDAC/sPPO system also possessed methanol permeability values less than one hundredth that of Nafion [21]; However, these LbL-based PEMs were not sufficiently robust when hydrated and require a reinforcing mechanical substrate.

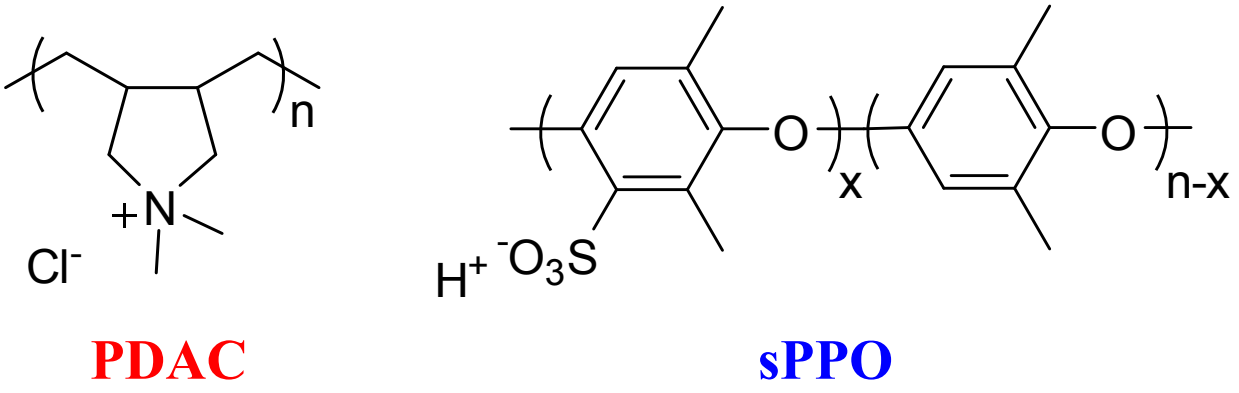

Figure 5-1. Chemical structures of PDAC and sPPO. These two polymers are combined in the LbL assembly process to yield highly conductive PEMs.

An interesting class of materials for reinforcing LbL membranes is the electrospun fiber mat. Electrospun mats are non-woven, highly porous materials with high surface-to-volume ratios and small pore sizes [22,23,24]. A wide range of polymers can be formed into electrospun mats and the fiber diameters can be varied during fabrication depending on solution properties and processing parameters (diameters in range of 0.1–10 μm) [25]. Recently, electrospinning has

been used to produce high proton conductivity fibers from perfluorosulfonic acid (PFSA) and polyethylene oxide (PEO) into mechanically robust membranes [26]; however, a non-swelling, mechanically stable nanofiber mat could also serve as a porous scaffold for deposition of a conducting medium. Figure 5-2 shows a diagram illustrating the steps by which a composite membrane can be fabricated by either dip-LbL or spray-LbL application of polyelectrolytes to an electrospun nanofiber mat. The spray-assisted LbL process enables the coating of complex and porous surfaces, while also significantly reducing the cycle times for multilayer assembly from several minutes to a few seconds, thus making the LbL approach commercially viable [27]. In a recent publication we demonstrated that the spray-LbL process could be used to generate LbL-coated electrospun mats [28]. Individually coated fibers were observed throughout the interior of the mat when assembled with the assistance of a vacuum to control flow through the mat. In the absence of a vacuum, a condensed thin film was found to form at the surface of the mat, resulting in asymmetric composite membranes. This work demonstrated the versatility of combining the spray-LbL assembly process with electrospun mats.

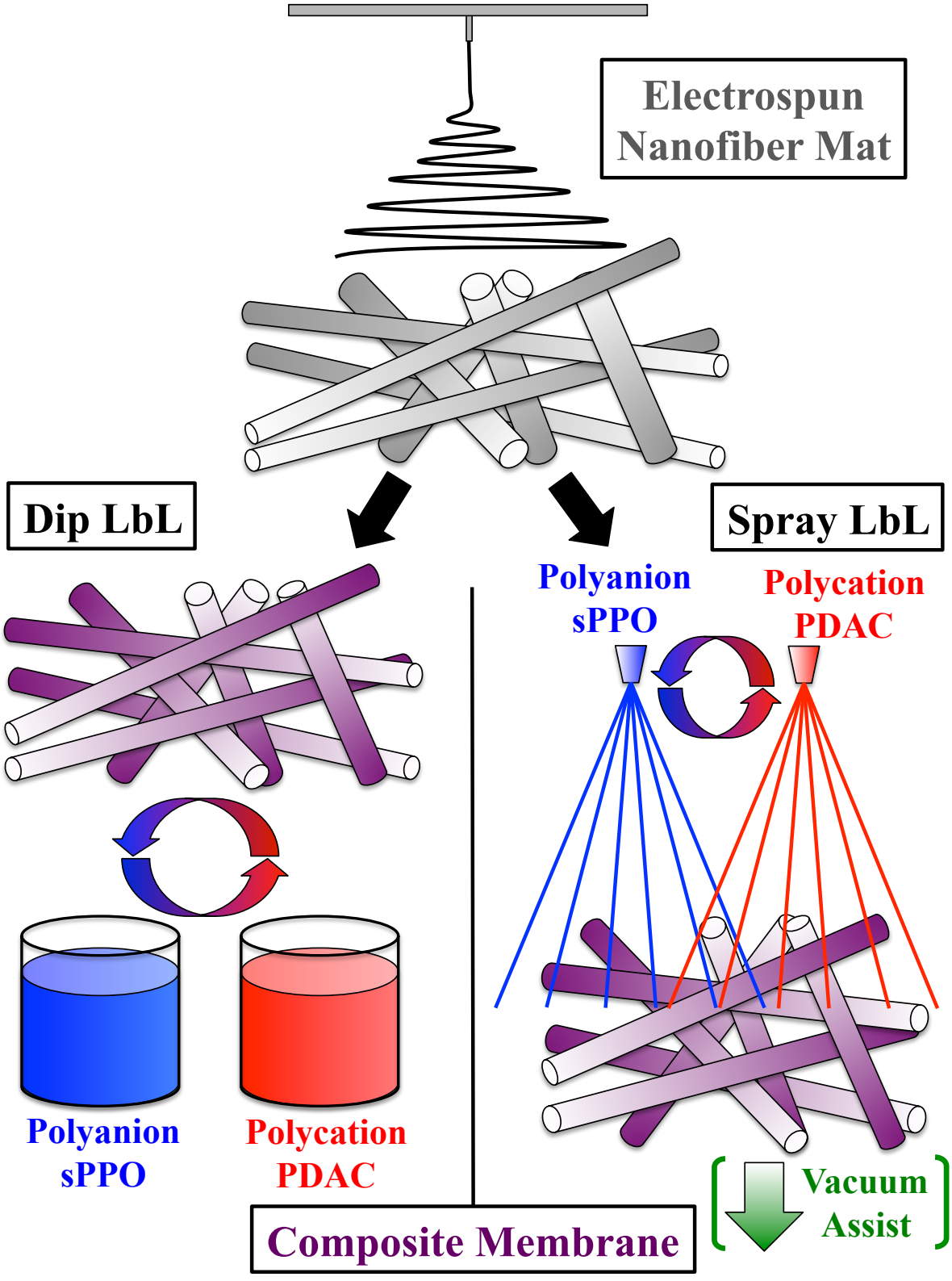

Figure 5-2. Schematic diagram showing the fabrication process of LbL-nanofiber composite membranes by both dip (left) and vacuum-assisted spray (right) processes.

In this chapter the mechanical enhancement of LbL membrane systems with the use of electrospun mats as substrate materials is demonstrated. Specifically, LbL assembly is used to generate selective coatings on and within the electrospun mats, producing thin, mechanically stable composite fuel cell membranes for high power density devices. These material systems can be modified at the molecular level to alter transport properties, simply by changing the relative compositions of each adsorbed bilayer of polymer, while the mechanical and chemical stability can be modified by altering the nature or composition of the underlying electrospun network; the systems are highly controllable and the architectures of the films are modified across the thickness to achieve mechanically robust, highly selective and readily processable ultrathin fuel cell membranes, with the goal of rivaling or exceeding the performance of Nafion. To demonstrate this, the work conducted in this chapter explores three different LbL assembly techniques: traditional dip-LbL, which involves directly dipping into alternate polyelectrolyte solutions, spray-LbL, and vacuum-assisted spray-LbL. We observe that each of these three techniques create distinctively different nano to micron scale morphologies on the fiber scaffold, each contributing different membrane characteristics. The mechanical properties of the composites are investigated, as well as other key properties for a methanol PEM: ionic conductivity and methanol permeability. Poly(trimethyl hexamethylene terephthalamide) (PA 6(3)T) and polycaprolactone (PCL) were the polymers selected for use as the electrospun fiber mats due to their range of fiber sizes (200 nm – 10 μm) and ease of fabrication. The dip-LbL electrospun composite membranes are shown to yield morphologies with less controlled bridging and linking of fibers together. The spray-LbL electrospun composite membranes consist of surface top-coatings that do not penetrate into the bulk of the mat (capping layers); however, when a vacuum is pulled across the electrospun mat during spray-LbL assembly, the process yields conformal coatings of the individual fibers with minimal bridging throughout the bulk of the mat. The mechanical properties of the spray-LbL coated electrospun mats are shown to be superior to the pristine LbL free-standing films previously studied, and controlled by the properties of the underlying electrospun fiber mat.

5.2 Experimental Method

5.2.1 Materials

Poly(2,6-dimethyl 1,4-phenylene oxide) (PPO) (M_w = 23,000), 1,2-dichloroethane (DCE), trichloromethylsilyl chlorosulfonate (TMSCS), acetone, and polycaprolactone (PCL) (M_w = 80,000) were obtained from Sigma-Aldrich, Inc. poly(diallyl dimethyl ammonium chloride) (PDAC) (M_w = 240,000) was obtained from Polysciences, Inc. The amorphous polyamide poly(trimethyl hexamethylene terephthalamide), denoted PA 6(3)T, was obtained from Scientific Polymer Products, Inc. It has a glass transition temperature of 153 °C. N,N-dimethyl formamide (DMF) was purchased from Sigma-Aldrich and used as received for creating polymeric solutions. Sodium chloride (NaCl) salt was purchased from VWR and used as received. PPO was sulfonated as previously reported to yield highly sulfonated sPPO [20].

5.2.2 Electrospinning of Nanofiber Mats

The electrospinning apparatus, similar to that previously reported in Chapters 2 & 3, consisted of two aluminum disks 10 cm in diameter oriented parallel to each other and separated by distance of 35 cm [29]. A 30 vol.% solution of PA 6(3)T was delivered with a syringe pump (Harvard Apparatus PHD 2000) at a rate of 0.01 mL min-1 to a 1.0 mm ID needle in the top aluminum disk. A high voltage power supply (Gamma High Voltage Research, ES40P) provided a 34 kV potential to the upper aluminum disk in contact with the solution. Under these conditions, an electrospun mat about 100 μm thick could be produced in 2 hours. PCL electrospun mats were made using the same setup from a 10 wt.% solution of polymer in chloroform and methanol (3:1 by weight). The PCL mats had an average fiber diameter of 8.6 ± 0.8 μm, while the PA 6(3)T mats had an average fiber diameter of 1.24 ± 0.17 μm. Similar fibers and mats have been produced and characterized previously [30,31].

5.2.3 Contact Angle Measurements

Polymer film and fiber mat contact angle measurements were taken using a Krüss DSA10-MK2 Drop-Shape Analyzer, where both the static and dynamic (advancing and receding) contact angles were measured. The contact angles were determined by fitting the profile of at least five droplets using the Krüss software and determining the mean value. The initial contact angles were recorded within 30 s after placing droplets of a standard volume of 10 μL on the fiber mats via pipette. Contact angles were recorded as the droplets evaporated until

they became too small to make accurate measurements. Thin films of PA 6(3)T and PSU were prepared on glass slides by spin-coating each polymer from a 10 wt.% solution in DMF. Plasma treatment of both the electrospun mats and polymer films were performed using a Harrick Plasma Cleaner with oxygen purge for 45 seconds on the highest setting.

5.2.4 Layer-by-Layer Deposition

5.2.4.1 PPO Sulfonation

The sulfonation process of PPO is similar to previous reports [20]: PPO was sulfonated in anhydrous DCE at 85 °C (reflux) for 4 days using TMSCS as the sulfonating agent (TMSCS:PPO molar ratio was 4:1). Dry nitrogen was bubbled through the reaction to remove the hydrochloric acid generated. Highly sulfonated PPO precipitate was filtered, rinsed with chloroform, dissolved in methanol, and stirred overnight with 1 molar equivalent of sodium methoxide to de-protect the TMSCS group. The sodium form of sPPO (sPPO-Na) was obtained by precipitation into cold acetone followed by filtration. This polymer was then converted to the protonated form (sPPO-H) by dialyzing against 2% HCl for two days and stored until use. Fourier transform infrared (FTIR) spectra of both the PPO and sPPO were obtained using Nicolet Magna-IR 550 spectrometer to confirm the successful sulfonation of PPO. A schematic of the PPO sulfonation process is shown in Figure 5-3.

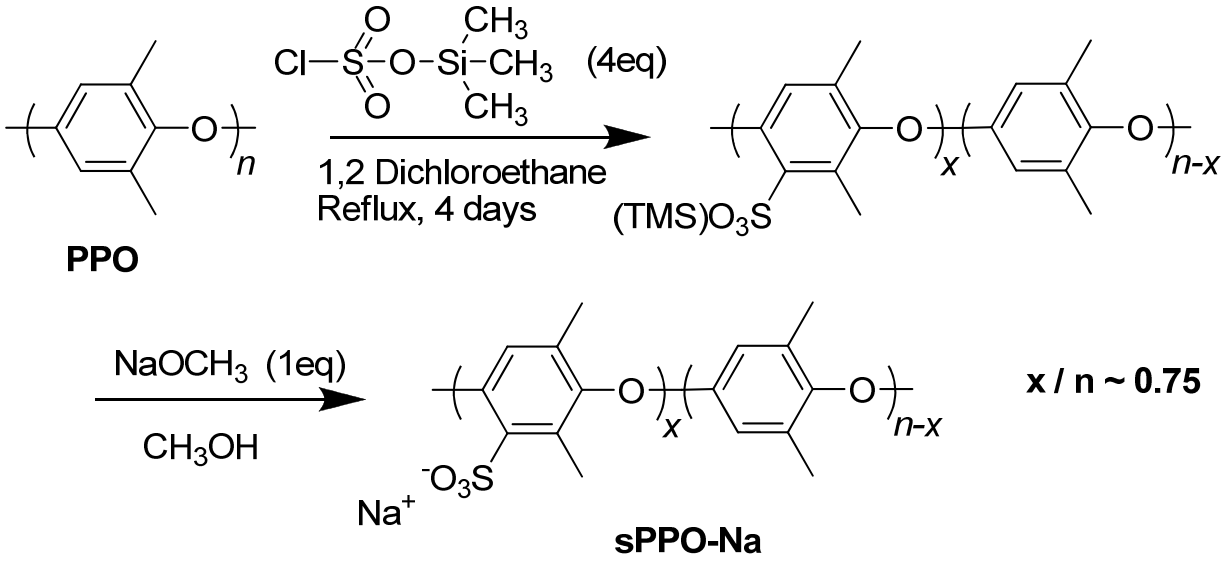

Figure 5-3. Controlled sulfonation of PPO with TMSCS as the sulfonating agent. Highly sulfonated sodium form (sPPO-Na) is water-soluble and can be converted to the proton form (sPPO-H) by dialysis against acidic water [20].

5.2.4.2 LbL Dip Assembly (Dip-LbL)

Dip-LbL assembly was performed using a programmable ZEISS DS50 slide stainer. Electrospun mats about 25 mm x 50 mm in size were used for composite membrane fabrication, and placed into home-built plastic sample holders to ensure the sample remained planar during assembly. The mats were immersed in aqueous PDAC solution for 15 minutes, followed by three (3x) two-minute rinses in water, and then placed in aqueous sPPO solution for 15 minutes, followed by three (3x) two-minute rinses in water; the process was repeated for a specified number of bilayers to yield thick coatings. The PDAC and sPPO solutions were both 10 mM based on the molecular weight of repeat units. All polymer and rinse solutions for dip-LbL had pH 1. The composite membranes were rinsed in deionized water after assembly to remove excess ions from the films. 0.2, 0.5, and 1.0 M sodium chloride solutions were added to polyelectrolyte and rinse solutions to control the growth characteristics and transport properties of the LbL film.

5.2.4.3 LbL Spray Assembly (Spray-LbL)

Electrospun mats about 100 mm x 100 mm in size were placed onto a 75 mm diameter plastic funnel fitted with a steel mesh for support. Sprayed films were fabricated using the same aqueous polymer and rinse solutions described above. The mats were plasma-etched in oxygen for 45 seconds and soaked in the PDAC solution for 5 minutes before spraying. A home-built automated spraying setup, as previously detailed, was used to coat the mats [27]. An automated program run by a logic relay controlled the apparatus, spraying the aqueous PDAC and sPPO solutions for 3 seconds each, with 5 seconds of rinsing with water spray in between the polymer sprays. The process was repeated for the desired number of bilayers. For some samples, a vacuum was applied to the back of the electrospun mat using a venturi pump supplied with nitrogen at 50 psi (vacuum-assisted spray-LbL). Free-standing LbL films were assembled on Teflon substrates or polystyrene-coated silicon wafers and gently peeled off after assembly, similar to a previous report [32].

5.2.5 Morphological Characterization

Scanning Electron Microscopy (SEM) images were obtained on a JEOL JSM-6060 scanning electron microscope after coating the samples with approximately 5 nm of Au/Pd. Cross-sectional images were obtained by cryo-fracturing composite membranes in liquid nitrogen and mounting onto a vertical sample holder.

5.2.6 Post-electrospinning Treatment of Electrospun Mats

Heat treatment of the electrospun mats was carried out in a Thermolyne lab oven by draping the mat over a 100 mm diameter Pyrex dish and placing it in the oven for 2 hours at a specified temperature. Contact of the mat with the rim of the Pyrex dish was sufficient to prevent the mats from contracting and/or tearing during heat treatment and suspended the sample so that it did not contact or stick to any surfaces. After heat treatment, samples were removed from the oven and allowed to cool before carefully cutting the mat off of the Pyrex dish.

5.2.7 Mechanical Testing of Proton Exchange Membranes

Uniaxial tensile testing of dry and fully hydrated electrospun fiber mats and composite membranes was performed with a Zwick Roell Z2.5 tensile testing machine using a 2.5 kN load cell. Rectangular specimens were cut to 100 mm x 12.5 mm and extended at a constant crosshead speed of 0.50 mm/s with a 50 mm gage length (corresponding to a constant strain rate of 0.01 s^{-1}). The thickness of each specimen was determined from the average of three measurements taken along the gauge length with a Mitutoyo digital micrometer at a constant force of 0.5 N. The force–displacement data was converted to engineering stress versus engineering strain results using the initial cross-sectional area and gauge length of the test specimen. Engineering stress is defined as the ratio of force to the initial cross-sectional area and the engineering strain is defined as the ratio of the displacement to the initial gauge length. Samples defined as “dry” were tested at ambient conditions of 25 °C and approximately 40-45% RH, while samples defined as “hydrated” or “wet” were conditioned overnight in deionized water and tested while fully saturated with water. Axial and transverse strain were measured with a Qimaging Retiga 1300 video camera in conjunction with Vic2D video extensometer software, similar to previous reports [33]. The force-displacement data as taken from the Zwick and the video extensometer, respectively, were reduced to true stress-true strain results assuming isotropic incompressible behavior. True stress is defined as the ratio of force to current (deformed) cross-sectional area and true strain is defined as the natural logarithm of the ratio of current length to original length (length being the axial distance between video-imaged marks).

5.2.8 Transport Properties of Proton Exchange Membranes

For a given PEM, the ionic conductivity is related to the number and type of charge carriers and the mobility of the charge species. Increasing the number of charge carriers or the

mobility of the charge carrying species within the membrane can thus increase the ionic conductivity of a material. The equation for determining the conductivity in a PEM is:

$$\sigma = \frac{l}{R \bullet A} \qquad \text{(Equation 5-1)}$$

where l is the distance between electrodes used, A is the cross-sectional area through which protons are moving, and R is the resistance measured. In a fuel cell, protons move through the z-direction of the PEM from the anode to the cathode; however, measuring the through-plane conductivity of a PEM is difficult to perform accurately, so only in-plane conductivity is measured and reported in this chapter. In-plane ionic conductivity measurements of the free-standing films and coated electrospun mats were made by cutting 10 mm x 20 mm samples and placing them in a conductivity cell with two platinum wires 10 mm apart as the electrodes. Temperature and humidity were controlled using a chamber from Electro-tech Systems, Inc. Impedance values were determined by electrochemical impedance spectroscopy (EIS) with a Solartron 1260 impedance analyzer, measuring from 100 kHz down to 10 Hz. When performing in-plane conductivity measurements, it is important to be aware of potential anisotropy in the membrane. For most PEM systems, including polymeric LbL films, it is safe to assume that on a macroscopic scale ion transport is isotropic; however, if there is potential for anisotropy in the PEM, in-depth morphological characterization should be done and reporting in-plane conductivity values as bulk conductivities should be carefully described. Another concern with in-plane measurements is the potential for measuring only surface conductivity. To ensure accurate conductivity measurements, measuring the in-plane conductivity for the same PEM material at several thicknesses can confirm that bulk conductivity is observed. For a given PEM material the ratio of membrane thicknesses for two different samples should equal the inverse ratio of corresponding impedance values measured. If this ratio is observed, then bulk conductivity values are being measured. The thickness of the composite membrane was measured using cross-sectional imaging on an optical microscope and confirmed by a micrometer with 0.5 N applied force.

A model Nyquist plot for a highly conductive PEM measured in-plane is shown in Figure 5-4, along with the corresponding equivalent circuit used to model the impedance data. The details of electrochemical impedance spectroscopy are discussed elsewhere [34]. In the equivalent circuit model, R_S corresponds to the series resistance from the lead wires and platinum electrodes, R_{PEM} is the resistance of the PEM, and C_{PEM} is the capacitance of the PEM.

The diameter of the semicircle, R_{PEM}, is the value that is used in Equation 5-1, along with the geometry of the conductivity cell and PEM sample, to calculate ionic conductivity. Often when modeling the impedance response of actual PEMs, the capacitor, C_{PEM}, is replaced with a constant phase element to account for non-ideal behavior. Constant phase elements are empirical circuit elements that have phase angles independent of frequency and can therefore model non-ideal impedance response. Also, the low frequency response of the electrochemical impedance measurement is not shown in Figure 5-4. Theoretically, double-layer capacitance should lead to a straight vertical line at $R_S + R_{PEM}$, although this is frequently not observed.

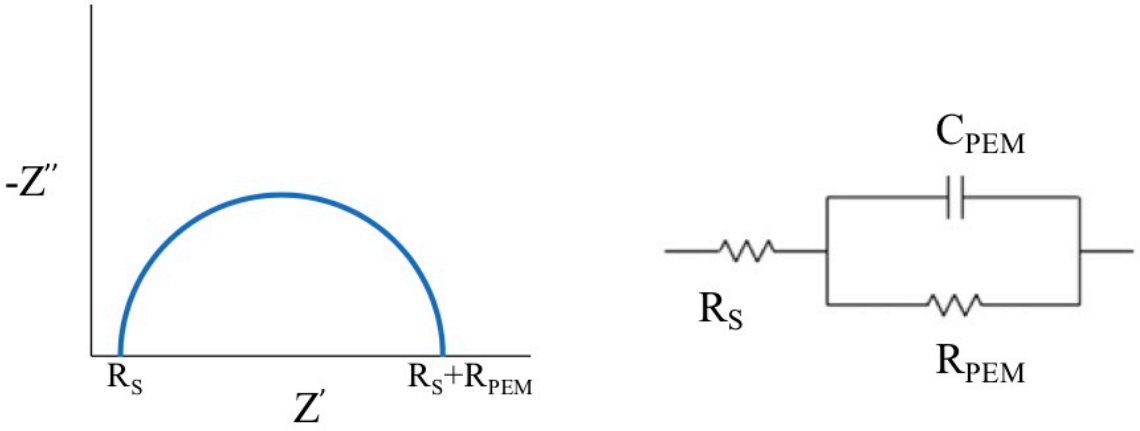

Figure 5-4. A model Nyquist plot for a highly conductive PEM measured in-plane, along with the corresponding equivalent circuit. For the equivalent circuit, R_S corresponds to the series resistance from the lead wires and platinum electrodes, R_{PEM} is the resistance of the PEM, and C_{PEM} is the capacitance of the PEM. The diameter of the semicircle corresponds to R_{PEM} (Image courtesy of J.N. Ashcraft).

5.3 Results and Discussion

5.3.1 Assembly of Free-standing Layer-by-layer Films

Previous methods of LbL deposition of PDAC/sPPO yielded thin-film top layer coatings on Nafion membranes or Nucleopore substrates [20]; however, stable free-standing PDAC/sPPO films could be fabricated by depositing a thick (>5-10 μm) film onto a polystyrene-coated silicone substrate. The thickness of the free-standing film could be finely controlled by the number of bilayers (e.g. 400 bilayers yielded a ~10 μm thick film). Films that are several microns thick or larger can be easily peeled off of the silicone substrate as free-standing films, as

shown in Figure 5-5. Typically, free-standing films with dimensions of 60 mm x 60 mm can be achieved by this method. The free-standing PDAC/sPPO films exhibited hydrolytic stability and possessed enough mechanical stability when dry to be removed from the assembly substrate as a uniform film.

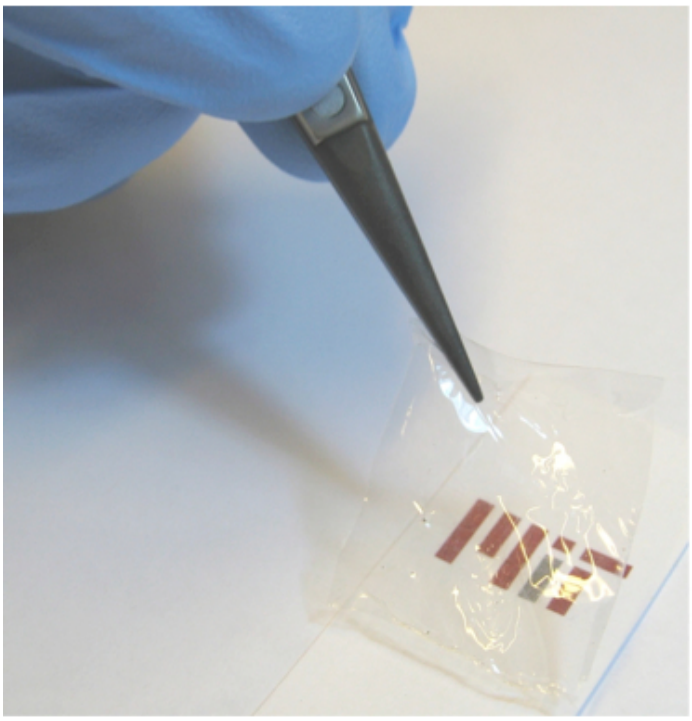

Figure 5-5. An optical image of a free-standing PDAC/sPPO film (~10 μm thickness) assembled on polystyrene coated silicon substrate using the spray-assisted LbL method. Assembly conditions: pH = 2.0, [PDAC] = 10 mM, [sPPO] = 10 mM, [NaCl] = 0.5 M (all solutions) [21].

5.3.2 Transport Properties of Free-standing Layer-by-layer Films

Figure 5-6 shows the relative humidity dependence of in-plane proton conductivity for free-standing PDAC/sPPO films assembled at various ionic strengths. Since LbL assembly yields homogenous blends of polymers rather than stratified layers, the proton conductivity is isotropic and in-plane (parallel to the substrate) measurements yield accurate bulk conductivity values. Both PDAC and sPPO are strong polyelectrolytes, permanently charged in solution, and thus the control of LbL film assembly is possible by screening these charges with salt as discussed previously. All films show similar humidity dependence; the proton conductivity improves approximately 5-7 fold with every 20% increase in humidity. The dependence is also similar to that of pristine sPPO films (not shown here), indicating that the proton conduction mechanism of

the LbL films is analogous to the charge transport mechanism of sulfonate groups in sPPO. With no charge screening (no salt added), the conductivity of PDAC/sPPO is 1.29 mS cm^{-1} at fully humidified conditions. As the ionic strength of the assembly baths is increased, the proton conductivity has benefited from relaxed chain conformation and lighter crosslinking density between polyelectrolytes, consistent with increased growth rates previously investigated [21]. Furthermore, when 1.0 M NaCl is added to the sPPO assembly solution only, PDAC/sPPO yields the highest conductivity value of any LbL system, 70.0 mS cm^{-1}, approaching the values of industry standard PEMs such as Nafion. It is believed that the increased conductivity is a synergistic combination of both better water transport and more free space due to lighter crosslinking density. The extensive list of conductivity values for PDAC/sPPO at various assembly conditions is summarized in Table 5-1, which demonstrates the ability to control the ionic conductivity by simply varying the solution conditions during the LbL assembly.

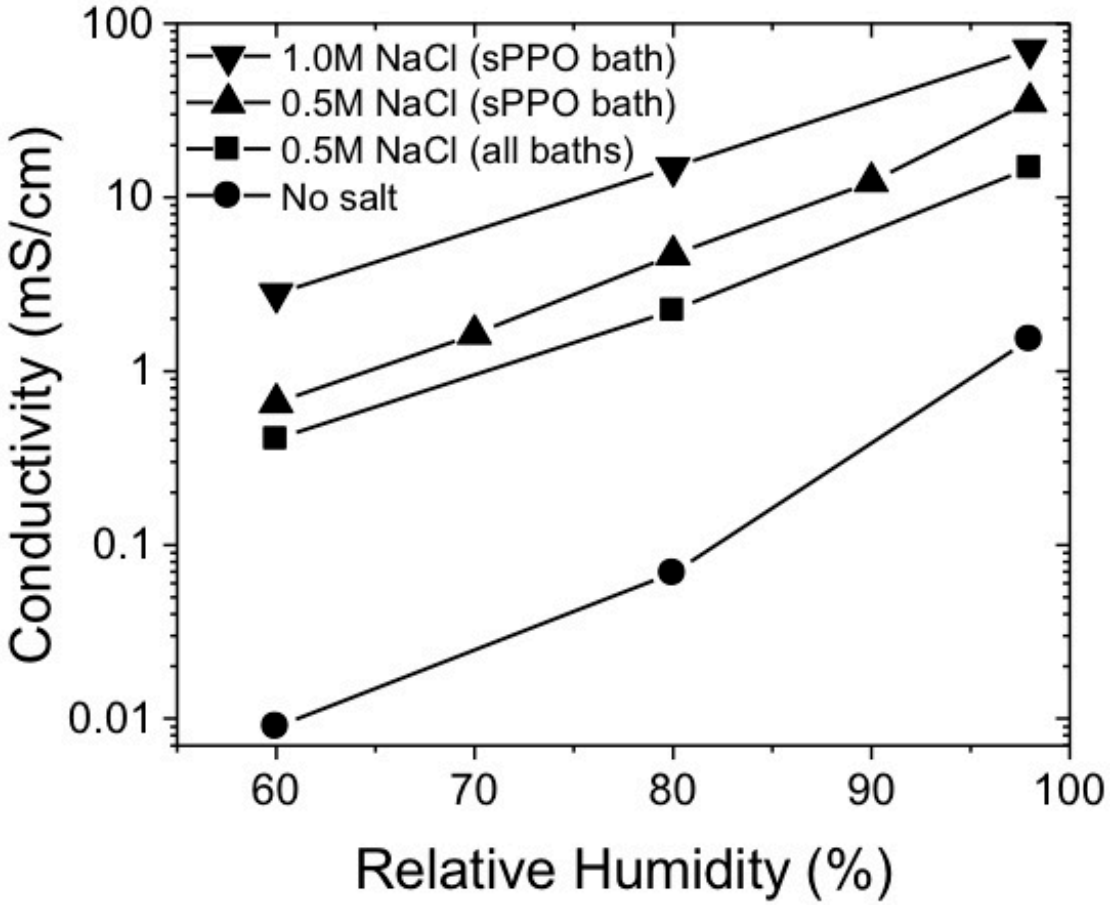

Figure 5-6. Relative humidity dependence of ionic conductivity of PDAC/sPPO films assembled at various ionic strengths. Note that the selective addition of NaCl in sPPO baths result in higher ionic conductivity values [21].

Table 5-1. Assembly Condition Dependence of Ionic Conductivity for PDAC/sPPO Films.

LbL Assembly Conditions	Ionic Conductivity[a] at 98% RH [mS/cm]
No Salt	1.29
0.2 M NaCl (All baths)	5.60
0.5 M NaCl (All baths)	7.09
1.0 M NaCl (All baths)	24.0
0.2 M NaCl (sPPO bath only)	11.2
0.5 M NaCl (sPPO bath only)	35.1
1.0 M NaCl (sPPO bath only)	70.0

In sulfonated PEMs, proton conduction is generally accepted to be through the Grotthuss mechanism, where the protons hop between ionized sulfonate groups. The temperature dependence of conductivity for LbL films in deionized water was investigated to verify the mechanism of conduction [35]. A free-standing PDAC/sPPO film (~9 μm thick) was prepared on a polystyrene substrate followed by careful removal from the substrate and rinsing in deionized water. The proton conductivity dramatically increased from 25.0 mS cm^{-1} at 30 °C to 90.2 mS cm^{-1} at 80 °C. An Arrhenius type dependency was observed with activation energy being about 25.6 kJ mol^{-1}, which is lower than that of pristine sPPO films reported in literature (~40 kJ/mol), suggesting a more favorable medium for proton transport [36,37]. For comparison, the temperature dependent conductivity of a 90 μm thick Nafion film (Nafion 1135) was tested in water over the same temperature range to yield an activation energy of 11.7 kJ/mol. It is also worth mentioning that the activation energy value observed for the PDAC/sPPO film was much lower than the sPPO films measured at low humidity conditions (~70 kJ/mol) [38,39].

5.3.3 Mechanical Properties of Free-standing Layer-by-layer Films

Stress-strain curves of free-standing PDAC/sPPO films are shown in Figure 5-7 for both ambient (dry) and fully hydrated (wet) conditions. It has previously been shown that dry PDAC/sPPO films have higher elastic moduli and strain-to-break than dry pristine sPPO, an indication that the LbL polyelectrolyte complex films are more mechanically durable than sPPO

[a] Ionic conductivity of pristine sPPO at 98% RH is 335.2 mS/cm

alone [21]. The dry, free-standing PDAC/sPPO films exhibit elastic-plastic behavior with elastic modulus values ranging from 250-1100 MPa and yield stress values ranging from 4-40 MPa depending on the processing conditions. LbL assembly at higher salt concentrations forms a more compliant network due to ionic shielding and a lower effective ionic cross-link density, resulting in films with lower elastic modulus and higher yield stress values than films assembled with lower or no salt concentrations, which form highly cross-linked, rigid materials. Overall, under dry conditions, the elastic modulus and yield stress values of PDAC/sPPO compare well with those of Nafion, which has an elastic modulus of 300 MPa and a yield stress of 12 MPa [40]. However, the layer-by-layer films become brittle when dry and tear at small strains. The average true strain-to-break of free-standing PDAC/sPPO films is 0.07 mm/mm, which compares unfavorably to a true strain-to-break greater than 1.0 mm/mm for Nafion under dry conditions. Under hydrated conditions the PDAC/sPPO free-standing films become almost gel-like, and the mechanical strength is lower than the detection threshold of the machine. At the hydrated operating conditions of a fuel cell, these mechanical values would lead to very short MEA lifetimes due to mechanical failure of the membrane. These results motivated the development of electrospun mats as reinforcing substrates in this work.

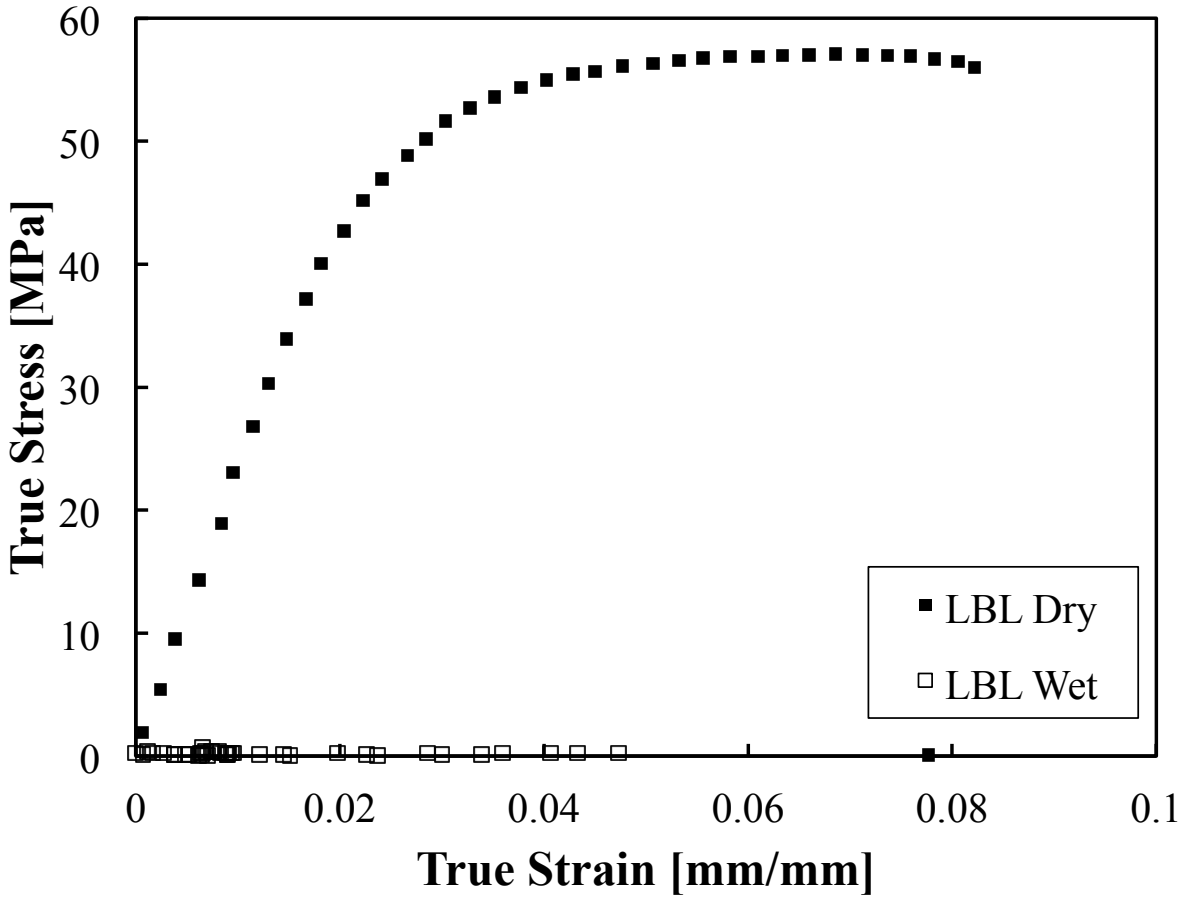

Figure 5-7. Typical stress-strain curves for free-standing PDAC/sPPO films at ambient (dry) and fully humidified (wet) conditions. The PDAC/sPPO films were assembled at pH = 1.0 with 0.5 M NaCl in the sPPO assembly solution. The films were sprayed onto a polystyrene coated silicon wafer and gently removed after assembly.

5.3.4 Electrospun Fiber Mat Contact Angle

Electrospun fiber mats intrinsically provide at least one length scale of roughness for superhydrophobicity because of their small fiber size [41]. In addition, it has been seen that the hydrophobicity of electrospun mats can be further increased with the use of intrinsically hydrophobic polymers such as poly(dimethyl siloxane) (PDMS) [42], by the formation of hierarchically structured fibers [43], or with the additional step of post-spinning surface chemistry modification [44]. These intrinsically hydrophobic nanofiber mats can exhibit contact angles of 110-140°, while the modified superhydrophobic systems can exhibit contact angles in excess of 175°. For fabrication of composite membranes that consisted of conformally coated nanofibers, a hydrophilic fiber matrix would be desirable to allow the aqueous polyelectrolyte solutions to penetrate through easily. To achieve this, reactive oxygen plasma was used to give

the surface of the PA 6(3)T fibers an intrinsic negative charge for the polycation to adhere and form the first polyelectrolyte monolayer. Previous research on the effect of plasma treatment on hydrophobic surfaces have shown that subjecting samples to oxygen plasma for as little as 20 seconds can transform a hydrophobic PDMS surface (contact angle >110°) to being completely wettable [45]. Figure 5-8 shows optical images of a 10 µL water droplet on PA 6(3)T films and electrospun mats both before and after plasma treatment. For the cast PA 6(3)T film, the intrinsic contact angle of 75 ± 2° before plasma treatment is lowered to 37 ± 2° after 45 s of oxygen plasma. The electrospun PA 6(3)T fiber mats exhibit significantly more substantial decrease in contact angle from 122 ± 5° for the as-spun sample to completely wetting after 45 s of plasma treatment, suggesting that the mat has undergone a transition from a Cassie-Baxter state [46] to a Wenzel state [47] as a result of carboxylate formation on the surface of the fibers. The mechanical properties of the plasma treated fiber mats were unaffected by the oxygen plasma.

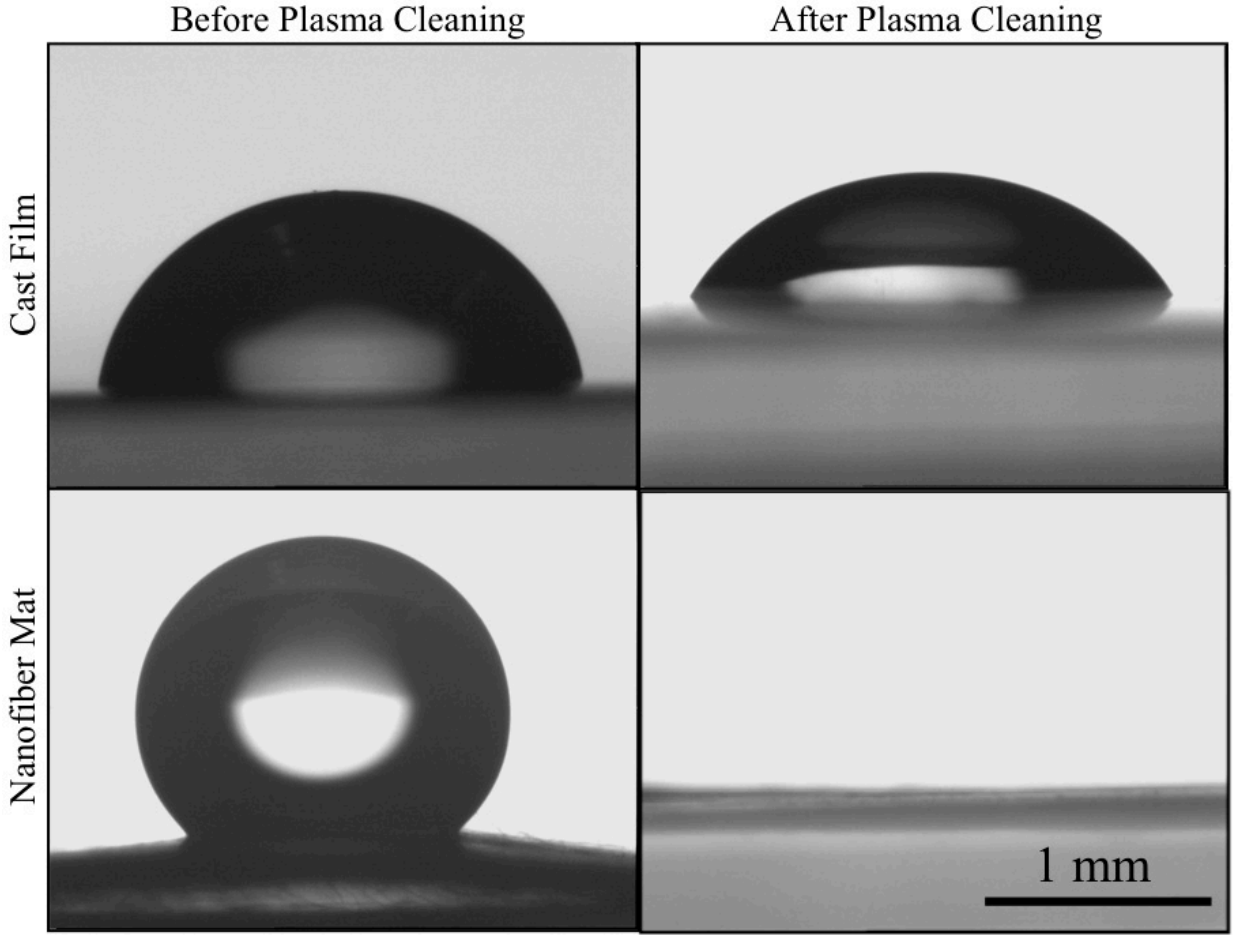

Figure 5-8. Optical images of a 10 µL water droplet on PA 6(3)T cast film and electrospun fiber mats both before and after subjecting to plasma treatment. Scale bar for each image is 1 mm.

5.3.5 Composite Proton Exchange Membrane Fabrication

5.3.5.1 Dipped LbL/Electrospun Fiber Mat Composite Membranes

Figure 5-9 shows top-down SEM micrographs of PCL electrospun mats coated through the dip-LbL assembly process; electrospun mats with 0, 50, 125, and 250 bilayers (BL) of PDAC/sPPO film are shown. The uncoated PCL electrospun mats have fiber diameters of ~8.6 μm as shown in Figure 5-9a. Figure 5-9b-d show that the fibers become coated as more bilayers of PDAC/sPPO are applied to the PCL mats; however, the multilayers form webbed thin films that bridge across the various fibers even at low numbers of bilayers. This webbed morphology is unique to the dip-LbL assembly process. It is believed to be the result of full water immersion followed by the long vertical drain times associated with dipping, which permits the formation of a polymer film joining two fibers starting at their intersection but not bridging across all the fibers in one uniform film. Meanwhile, the fibers that aren't webbed continue to be coated with PDAC/sPPO film and grow thicker until webbing eventually occurs. The result is a surface coating that has a propensity to bridge at fiber intersections and yield a non-uniform, partially bridged morphology. LbL films of PDAC/sPPO fabricated at the same assembly conditions on a planar glass substrate grow at a rate of 24.0 nm/BL; therefore, a 50 BL deposition of PDAC/sPPO corresponds nominally to a 1.2 μm film thickness, and a 250 BL deposition of PDAC/sPPO corresponds nominally to 6 μm in thickness. From Figure 5-9b (50 BL coating) and Figure 5-9d (250 BL), the fibers, particularly those on the top layers, appear to grow in diameter by about 2.4 μm and 12 μm, respectively, while the bridging films connect more fibers with additional layers. Although this non-uniform webbed morphology may eventually allow for the formation of a continuous coating that prevents fuel crossover inside an operating fuel cell, the time frame for deposition would be quite long. In addition it was observed by cross-sectional SEM that the multilayer film did not fully penetrate into the interior of the electrospun mat. For particularly thick mats (>100 μm), there was often a gap in the center of the mat where no LbL coating was seen at all. This results in a gradient in coating across the thickness of the membrane, leading to anisotropy in the ionic conductivity of the composite membrane.

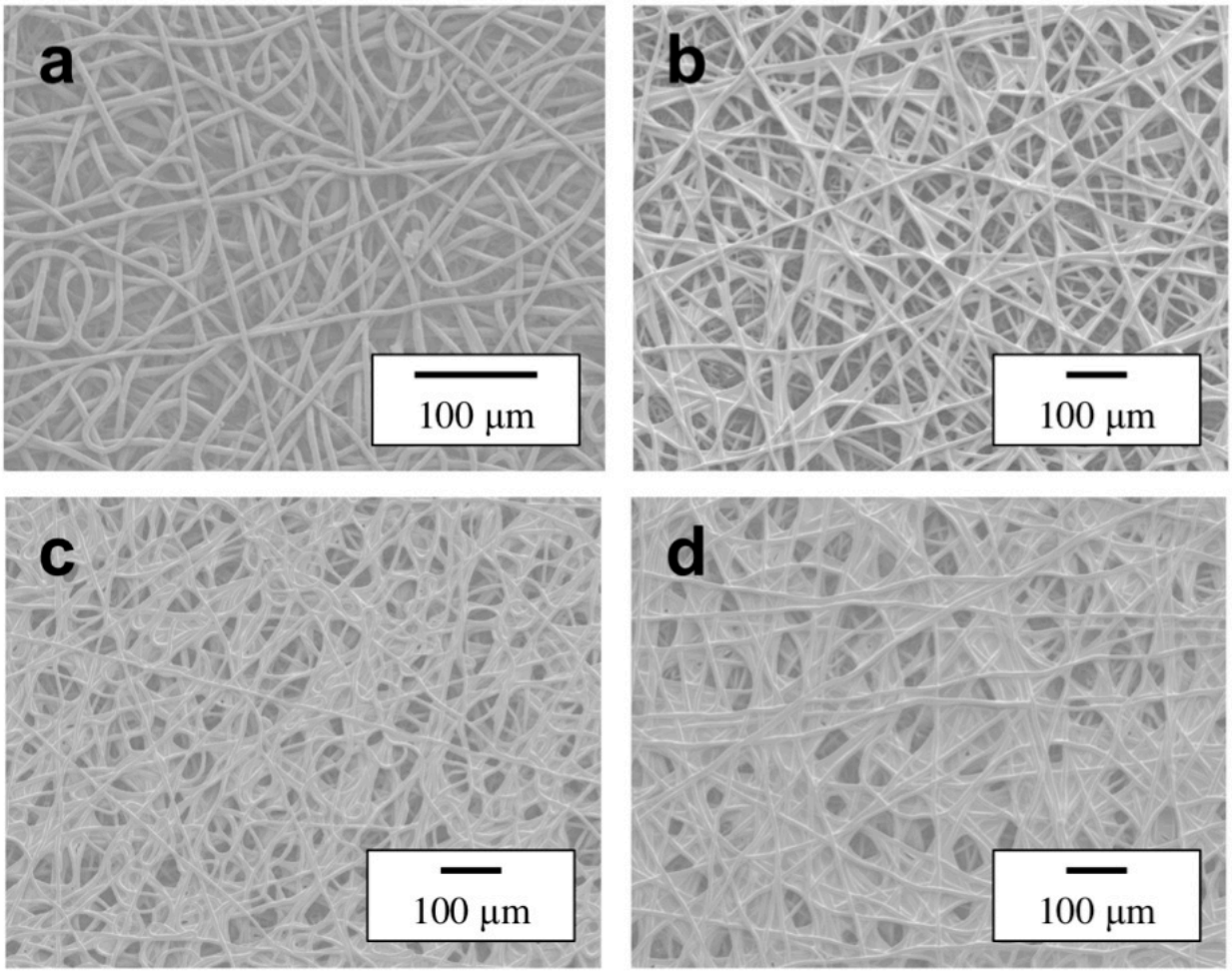

Figure 5-9. SEM images of PCL electrospun mats coated using dip-LbL with (a) 0 BL, (b) 50 BL, (c) 125 BL, and (d) 250 BL of PDAC/sPPO. PCL electrospun mats have fiber diameters of ~8.6 μm. PDAC/sPPO deposition conditions are pH = 1.0, 0.5 M NaCl in sPPO, and no salt in PDAC or any rinse solutions. Scale bar for each SEM micrograph is 100 μm.

The in-plane ionic conductivity values of PCL electrospun mats coated with 125 and 250 BL of PDAC/sPPO are shown in Figure 5-10, along with a PDAC/sPPO film assembled on a glass slide. As the number of bilayers deposited on the electrospun mat increased, the number of webbed bridges increased and the total in-plane ionic conductivity of the composite membrane increased. It appears that after depositing 250 BLs, all of the coated fibers have been connected and the ionic conductivity of the composite approaches that of the pristine PDAC/sPPO thin film; however, due to the lack of penetration into the electrospun mat, the void space in the center of the mat is not completely filled. The slope of the composite membrane ionic conductivity with relative humidity, particularly of the 125 BL dipped electrospun mat, is well

correlated with the pure PDAC/sPPO film, indicating the same mechanism of ion transport through the composite membrane.

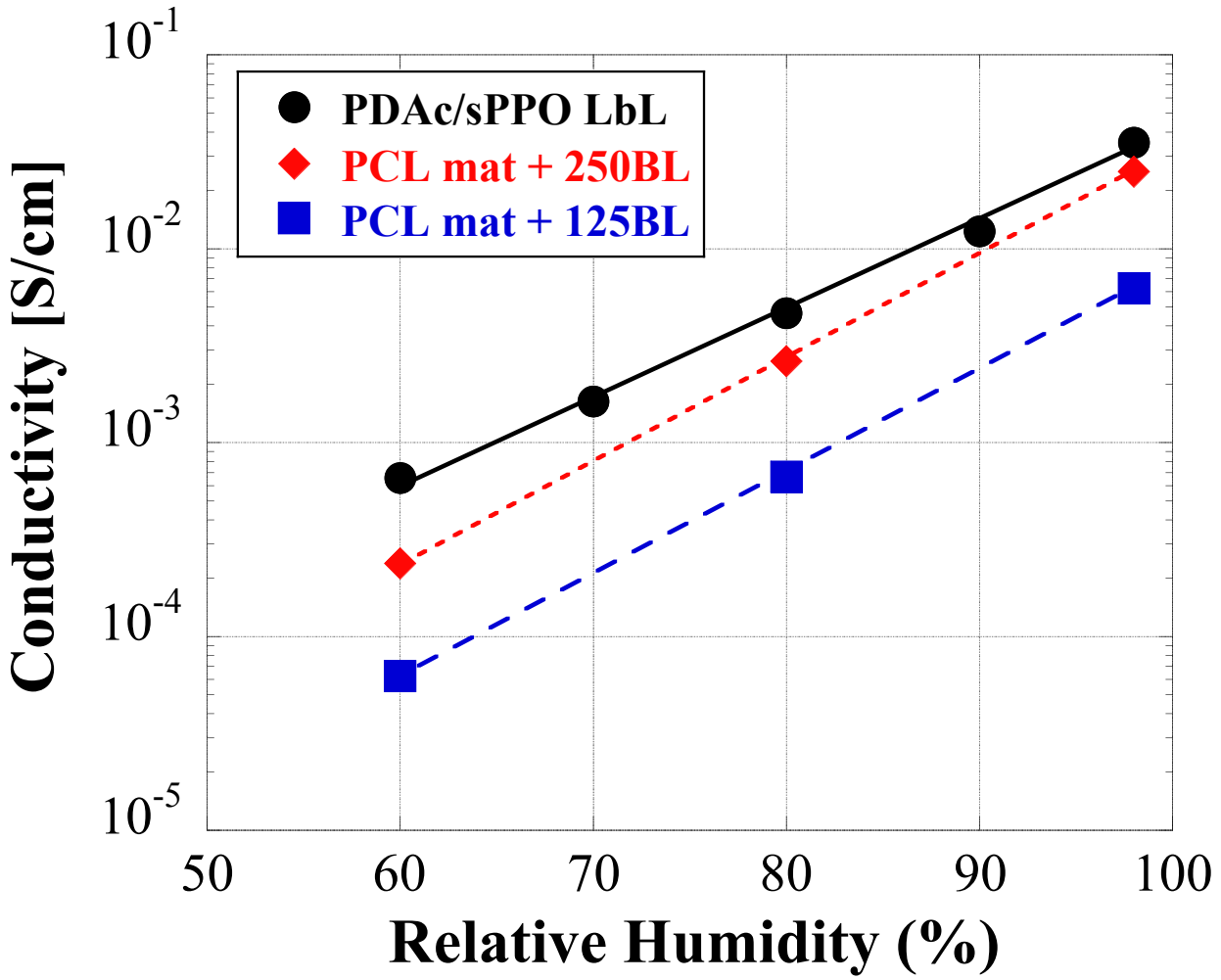

Figure 5-10. Relative humidity dependence of in-plane ionic conductivity of PDAC/sPPO films coated on PCL electrospun mats. PDAC/sPPO deposition conditions are pH = 1.0, 0.5 M NaCl in sPPO, and no salt in PDAC or any rinse solutions. As the number of bilayers deposited on the electrospun mat increases, the webbing of the PDAC/sPPO helps link all the coated fibers and a large increase in conductivity is observed.

5.3.5.2 Spray-assisted LbL/Electrospun Fiber Mat Composite Membranes

To further investigate the potential to achieve highly conductive composite membranes, an improved deposition methodology was adopted. PCL, while a good polymer for the model fiber matrix, is biodegradable and hydrolytically unstable, making it an unsuitable material for use in an operational DMFC; therefore, the more durable, hydrolytically stable PA 6(3)T was selected for producing electrospun mats for the remaining studies. PA 6(3)T fiber diameters can be varied from 2 μm down to 0.2 μm, and the mat mechanical properties have been studied

extensively [29,31,48]. With spray-assisted LbL deposition, it is possible to achieve both pore filling and covering of pores at the surface by using two different spray conditions. Pore filling is achieved when a vacuum is drawn on the downstream side of the electrospun mat during the vacuum-assisted spray-LbL process, effectively coating each fiber conformally through the entire thickness of the mat. By contrast, a superficial film on the exterior of each side of the mat is achieved by simply turning off the vacuum during the spraying process and flipping over the mat to cover each side of the membrane with a thin LbL "capping" layer. Figure 5-11 shows and SEM micrograph of the electrospun mats used prior to any spray coating process; the mean fiber diameter is 1.24 ± 0.15 μm.

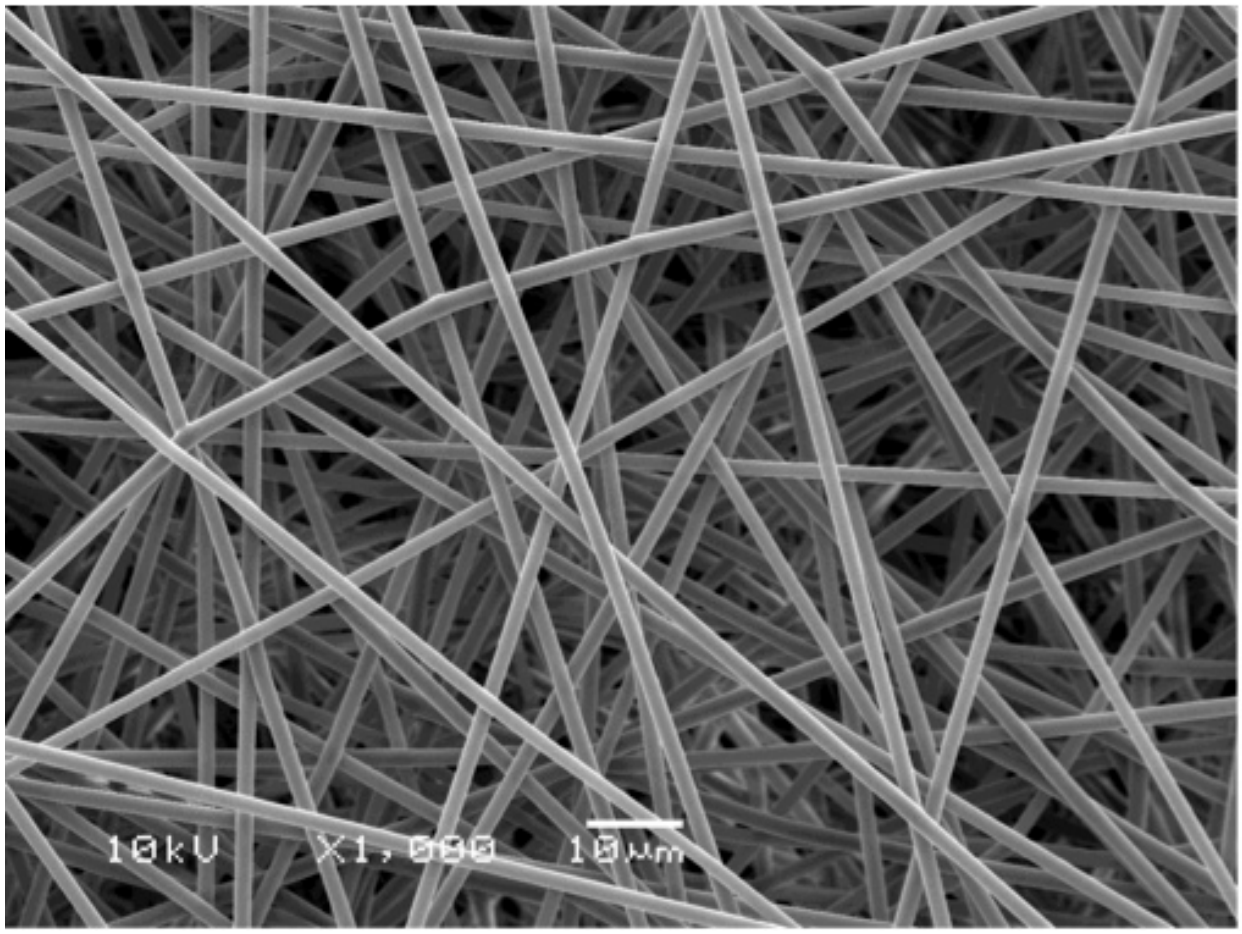

Figure 5-11. Representative SEM micrograph of a PA 6(3)T electrospun mat having mean fiber diameters of 1.24 ± 0.15 μm, scale bar for the micrograph is 10 μm.

To fill the electrospun mat uniformly and impart through-plane conductivity, a vacuum was applied to the downstream side of the mat during assembly, allowing the highly conductive polyelectrolytes to be electrostatically connected within the supporting fiber matrix.

Representative SEM micrographs of the spray-coated electrospun PA 6(3)T mats with and without vacuum are shown in Figure 5-12. Figures 5-12a and 5-12b show images at two different magnifications (1,000X and 7,500X) of an electrospun PA 6(3)T fiber mat coated with 250 bilayers of PDAC/sPPO using the vacuum-assist applied to the back of the mat. When sprayed under vacuum, the individual fibers of the mat are coated conformally, as the deposition occurs below the critical Reynolds number for flow separation from the downstream side of a cylinder [49] using conditions similar to those previously reported [21]. As can be seen in Figure 5-12a, the vacuum-assisted spray-LbL process produces fibers that are smoothly, uniformly, and individually coated with minimal pore blockage. The polyelectrolyte solution is pulled across the entire thickness of the electrospun mat and thus all the fibers, not just those near the surface, are coated. The charged surface of the PA 6(3)T fibers caused by plasma-treatment increases the wettability of the mat and providing an anionic substrate for LbL adhesion. The result is that the LbL penetrates through the void spaces and conformally deposits smooth and uniform LbL films around each fiber. From Figure 5-12b, it is observed that the growth of the multilayer film on the fibers (5.6 ± 0.4 nm/BL) is almost identical to the growth of the film on glass (6.1 nm/BL) under the same salt conditions, indicating a similar growth mechanism. The vacuum-assisted spray-LbL process enables uniform coating by eliminating webbing that would hinder the flow of the polymer solution droplets through the electrospun mat. The vacuum-assisted spray-LbL process allows the precise control of LbL film thickness on each fiber as well as the functional surface area and the degree of porosity of the composite membrane.

To create a film that covers all the pores in the supporting electrospun mat and drastically reduce the methanol permeability of the composite membrane, spray-LbL assembly without vacuum was applied to plasma-treated electrospun PA 6(3)T mats. When there is no vacuum applied during the spray deposition, the polymer solution droplets do not penetrate through the membrane and instead, form a pore-bridging film that spans across all the fibers along the top surface of the membrane. Figure 5-12c and d show images of an electrospun mat after spraying 100 BL (2 μm) and 300 BL (6 μm) with no vacuum, respectively. As can be seen in Figure 5-12c, with 100 BLs, the pores are covered, although the underlying PA 6(3)T fiber structure can still be seen. At 300 BLs, see Figure 5-12d, the LbL coating is so thick that the PA 6(3)T fibers (1.24 μm in diameter) underneath are not visible anymore.

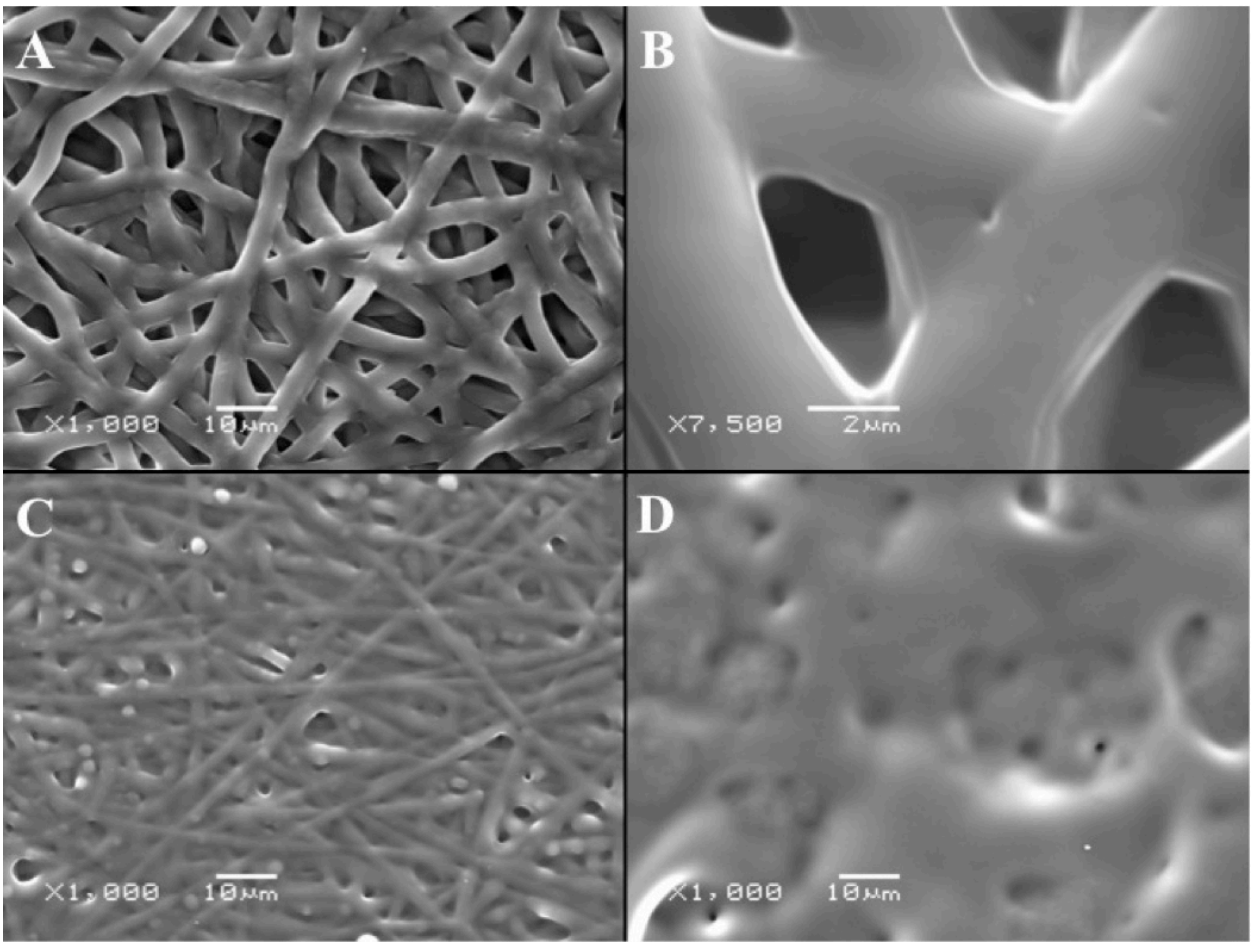

Figure 5-12. SEM images of PA 6(3)T electrospun mat (a – front-side, b – zoomed in) spray-LbL coated with 250 BL of PDAC/sPPO, at pH2 with 0.5M NaCl in the sPPO solution, when a vacuum is applied. The spray coatings provide a uniform coating on the fibers individually without webbing or pore covering. When there is no vacuum applied during the spray deposition, a pore-bridging film is observed after just 100BL (2.0 µm equivalent on glass) is sprayed (c) at pH2 with 1.0M NaCl in all solutions. After 300 BL (6.0 µm equivalent on glass) are deposited, the films have formed such a thick covering that it obscures the fibers underneath (d).

To probe the interior of the spray-coated electrospun mats, cross-sectional SEM micrographs were obtained by cryo-fracturing the composite membranes in liquid nitrogen. Figure 5-13a shows the cross-section of a PA 6(3)T electrospun mat spray-coated with 175 BL of PDAC/sPPO without vacuum (0.46 ± 0.06 µm mean fiber diameter). There is no penetration of the polymer solution into the electrospun mat, while the fibers underneath appear to be unaffected in any way. Figure 5-13b shows an electrospun mat spray-coated with 150 BL of PDAC/sPPO with vacuum. For composite membranes prepared without vacuum, the LbL film starts growing at the surface, bridging across all the pores, and grows outward. For samples

prepared with vacuum, Figure 5-13b shows that the individual fibers of the electrospun mat are coated throughout the film. The enlarged inset shows the conformal nature of the coating and how the LbL film on two adjacent fibers can merge. Because the LbL film grows on each fiber individually throughout the mat, just 150 BL (0.5 μm) were enough to fill the majority of the void spaces of an 80 μm thick membrane, reducing membrane porosity from 80% to 30% as measured gravimetrically based on the apparent density of the membrane and bulk density of the polymer. With further optimization, LbL electrospun fiber composite membranes could be produced with even lower void space. However, an electrospun mat coated only with the vacuum-assisted spray-LbL process can never be completely filled with layer-by-layer assembled polyelectrolyte, and will be highly methanol permeable due to the remaining void space needed for the flow of air to be accommodated through the fiber mat. An ideal composite membrane for methanol fuel cells can be formed with both types of spray-LbL techniques: the vacuum-assisted spray-LbL technique to fill the PA 6(3)T mat with conductive PDAC/sPPO, and the spray-LbL technique without vacuum to form a methanol barrier across the surface of the membrane.

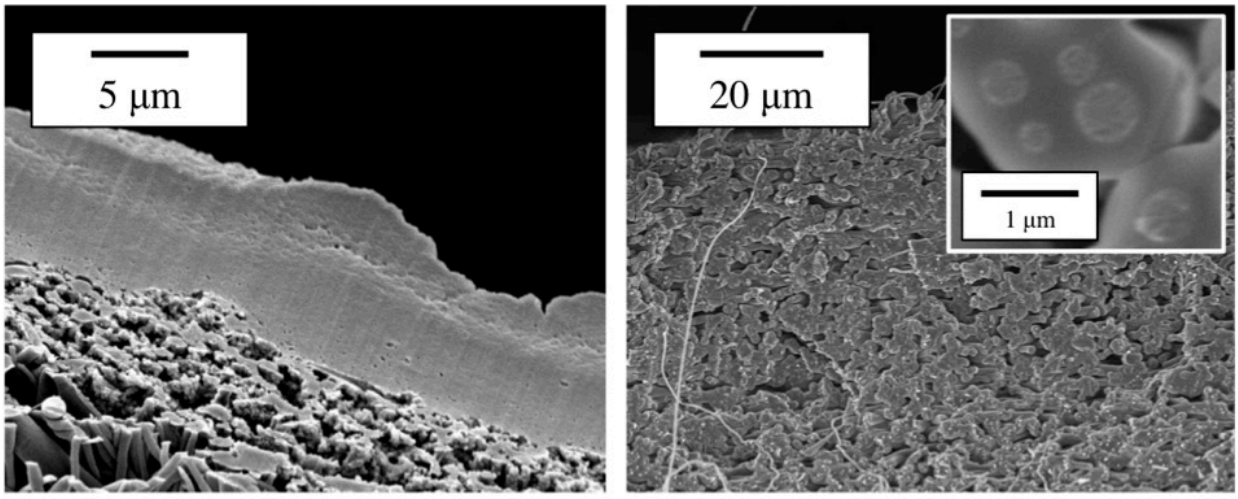

Figure 5-13. Cross-sectional SEM micrographs of 0.46 ± 0.06 mean diameter PA 6(3)T electrospun fiber mats spray coated with 175 BL (6 μm) of PDAC/sPPO without vacuum (left) and spray coated with 150 BL (0.5 μm) of PDAC/sPPO with vacuum (right and inset). Without vacuum, a pore-spanning film over the surface of the mat is formed, leaving the interior of the mat uncoated. With the application of a vacuum across the electrospun mat, the fibers of the mat are conformally coated throughout the mat. Scale bar for the left micrograph is 5 μm, scale bar for the right micrograph is 20 μm, and the scale bar for the inset is 1 μm.

5.3.6 Mechanical Behavior of Composite Membranes

Monotonic and cyclic uniaxial tensile testing was performed on bare PA 6(3)T electrospun mats and vacuum-assisted, PDAC/sPPO spray-coated mats to assess the mechanical behavior of these composite materials (Figure 5-14). Free-standing PDAC/sPPO films exhibit brittle elastic behavior with a Young's modulus up to 1100 MPa and a yield stress of 40-50 MPa under dry testing conditions. Uncoated PA 6(3)T electrospun mats exhibit elastic-plastic behavior with an elastic modulus ranging from 8 - 53 MPa and a yield stress ranging from 0.2 – 2 MPa. In cyclic testing the electrospun mats are seen to unload linearly at the same slope as the initial loading and to reload along nearly the same path, indicating little mechanical hysteresis. The electrospun mats are susceptible to necking and break at strains ranging from 0.3 - 1.0 mm/mm. The mechanical behavior of the PDAC/sPPO vacuum-assisted spray-coated electrospun mats is highly dependent upon the relative humidity, and maintains the characteristics of both the free-standing LbL film and the uncoated mat. When the composite membrane is dry, the mechanical properties of the LbL film impart the composite membrane with its large elastic modulus and low strain-to-break. At failure, the LbL film component fractures first, followed by yielding of the underlying electrospun mat. When the composite membrane is wet, the LbL film provides minimal mechanical strength and the coated electrospun mat behaves like the uncoated PA 6(3)T fiber mat as illustrated in Figure 5-14.

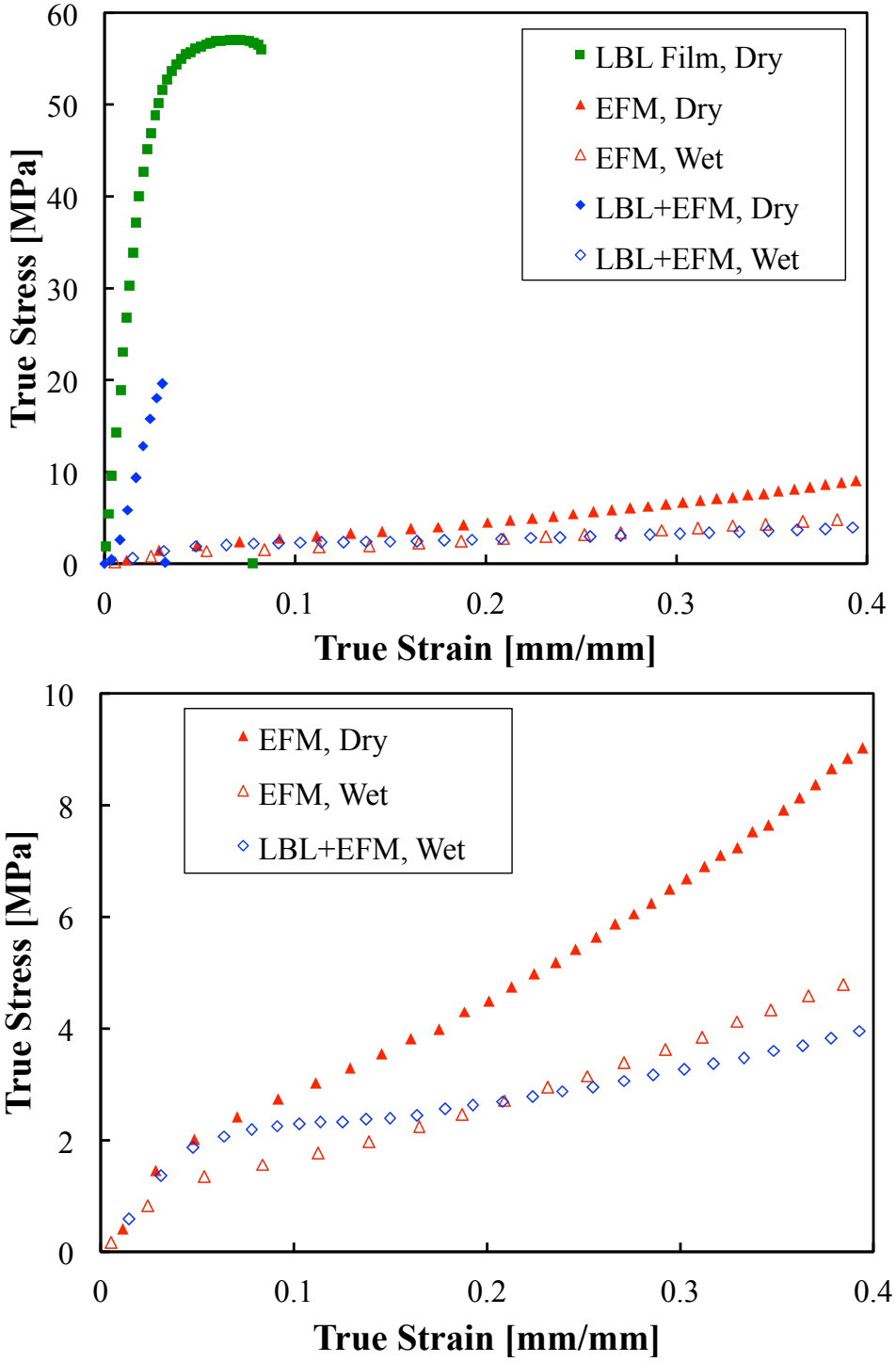

Figure 5-14. Stress-strain curves comparing free-standing LbL film to uncoated and vacuum-assisted spray-coated PA 6(3)T electrospun fiber mats at ambient (dry) and fully humidified (wet) conditions. Shown to the full stress range of the LbL dry film (top). Shown at a lower stress range to better differentiate among the more compliant materials (bottom). The spray-coated mats exhibit composite membrane behavior; the LbL strengthens the mat when dry while the mat provides the supporting base when wet.

The failure mechanisms of the coated fiber mats after mechanical testing for both the dry and hydrated cases were evaluated. It was seen that in the dry case, cracking occurs along the LbL surface, exposing the underlying electrospun mat; however, in the hydrated case the polyelectrolyte coating is able to deform with the rest of the mat without cracking due to the ductile behavior of the LbL films under hydrated conditions, as seen in bare film testing. Figure 5-15 shows SEM micrographs of the fracture plane for composite membranes after tensile testing in both A) "dry" conditions and B) "wet" conditions. The breaking mechanism for the dry sample is brittle fracture as indicated by the minimal plastic deformation of the specimen before breaking and the very smooth conchoidal fracture (normal to the applied tension). The wet membrane (Figure 5-15 B) exhibits significant necking as the fiber matrix deforms plastically before rupture, yielding a very rough fracture surface; these observations indicate that the breaking mechanism for the wet membrane is ductile rupture. Consequently, the spray-coated fiber mats exhibit superior mechanical properties in the hydrated state as compared to the free-standing PDAC/sPPO films, and are comparable to commercial proton exchange membranes such as Nafion. The mechanical properties of the underlying mat may be improved independently from LbL fabrication process; therefore, improving the structural properties of the composite membrane would not affect the key electrochemical properties of the LbL coating, specifically methanol permeability and proton conductivity.

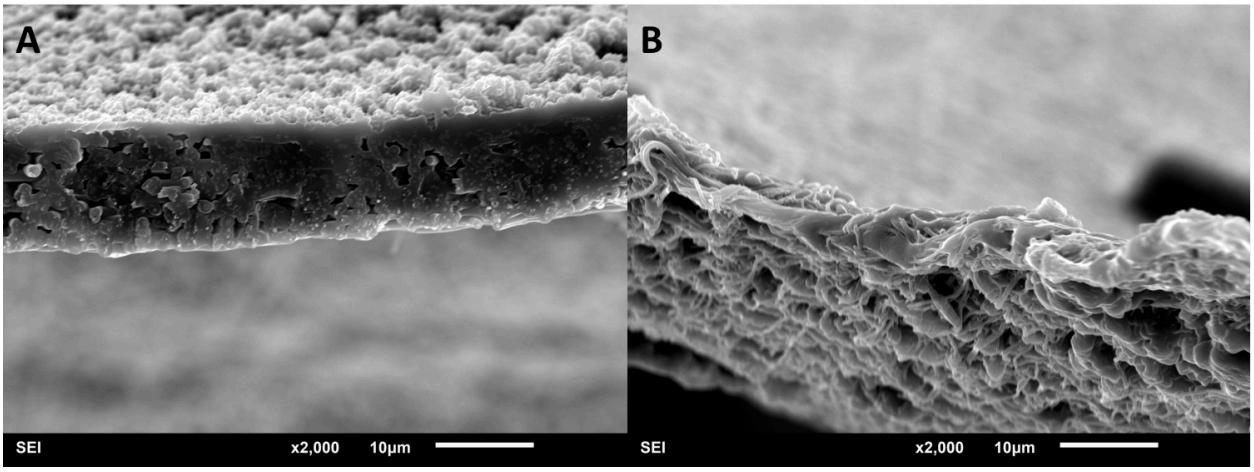

Figure 5-15. Representative SEM micrographs of composite LbL-electrospun fiber membrane fracture surfaces: A) "dry" membrane fracture plane indicating brittle fracture mechanism, B) "wet" membrane fracture plane showing thinning & plastic deformation during ductile rupture. The scale bar for each image is 10 µm.

Table 5-2. Summary of Tensile Properties of Composite PEM at 25 °C and 50 %RH.

	Young's Modulus [MPa]	Yield Stress [MPa]	Strain to Break [mm/mm]
PDAC/sPPO Film	610.4 ± 112.5	12.84 ± 4.53	0.056 ± 0.018
As-spun+LbL	382.6 ± 43.4	8.94 ± 3.46	0.097 ± 0.019
130 °C HT+LbL	403.7 ± 60.9	9.44 ± 3.12	0.086 ± 0.013
150 °C HT+LbL	481.8 ± 70.7	12.26 ± 3.32	0.084 ± 0.011
170 °C HT+LbL	410.4 ± 107.5	9.81 ± 1.82	0.072 ± 0.011
Nafion N112	168.5 ± 21.3	8.24 ± 0.92	1.56 ± 0.15

Annealing of the PA 6(3)T nanofiber mats at temperatures close to the glass transition provides dramatic improvements in the mechanical properties of the electrospun mats. Here we show that these improvements survive during hydration and are reflected in the composite PEMs as well. A summary of the tensile properties of Nafion, PDAC/sPPO free-standing film, and composite LbL/electrospun fiber mat PEMs is shown in Table 5-2. Under dry conditions, the Young's moduli of the composite membranes range from 382.6 ± 43.3 MPa, for the unannealed PA 6(3)T electrospun fiber mat composite PEM, up to 481.8 ± 70.7 MPa, for the composite membrane based on the electrospun fiber mat heat-treated (HT) at 150 °C for 2 hours. Yield stresses range from 8.94 ± 3.46 MPa to 12.26 ± 3.32 MPa for these same composite PEMs. The values for Young's modulus and yield stress are comparable to the values for the free-standing PDAC/sPPO film, at 610 ± 112.5 MPa and 12.84 ± 4.53 MPa, respectively. Even though the Young's moduli and yield stresses of the composite PEMs are greater than those of Nafion at 25 °C and 50 %RH, all of the LbL systems are very brittle and exhibit strains-to-break on the order of 0.05-0.10 mm/mm, significantly lower than that of Nafion, which can extend up to 1.56 mm/mm before breaking at ambient conditions.

During processing, as well as in an operational DMFC, the composite PEMs are in a hydrated state; therefore, tensile testing was also conducted on membranes that have been pre-conditioned in water for 24 hours. A summary of the improvements to the Young's moduli and yield stresses of the composite PEMs when hydrated are shown in Table 5-3 as a function of the annealing temperature of the electrospun mat. An increase of 5-6 fold in the Young's modulus and yield stress of the hydrated composite PEM can be observed for the composite PEMs based on annealed electrospun mats, compared to those based on the as-spun electrospun mats. The mechanical properties of the fully hydrated composite PEMs are comparable to the response of

the uncoated PA 6(3)T electrospun mats under the same testing conditions, confirming that the mechanical response of the composite PEM is controlled by the underlying electrospun nonwoven fiber structure. At 150 °C heat-treatment, the mechanical response of the hydrated composite PEM is comparable to that of hydrated Nafion N112, with Young's moduli of 80.2 ± 9.9 and 74.3 ± 5.7 MPa, and yield stresses of 3.39 ± 0.37 and 5.56 ± 0.22 MPa, respectively. It was reported previously that these increases in the mechanical response of the underlying nanofiber matrix occur at the expense of porosity; however, there was not a significant drop in the porosity of the electrospun mats from the unannealed state to the 150 °C thermally annealed electrospun fiber mat: 82% vs. 88% porosity [29].

Table 5-3. Summary of Tensile Properties of Hydrated Composite PEM at 25 °C and 100 %RH.

	Young's Modulus [MPa]	**Yield Stress [MPa]**
PDAC/sPPO Film	1.70 ± 0.95	0.11 ± 0.04
As-spun+LbL	36.1 ± 5.1	1.07 ± 0.14
130 °C HT+LbL	52.1 ± 10.8	1.69 ± 0.10
150 °C HT+LbL	80.2 ± 9.9	3.39 ± 0.37
170 °C HT+LbL	197.7 ± 54.2	6.51 ± 0.63
Nafion® N112	74.3 ± 5.7	5.56 ± 0.22

Figure 5-16 compares the data for engineering stress vs. engineering strain for a typical composite membrane in which the electrospun mat was annealed at 150 °C vs. Nafion (both PEMs tested in the fully hydrated state); included as well, for reference, are curves for a hydrated uncoated 150 °C heat-treated PA 6(3)T fiber mat and a hydrated free-standing LbL film. When wet, the free-standing LbL film becomes gelatinous and loses most of its mechanical integrity as illustrated in the stress-strain response. The yield stress drops to ~0.1 MPa (close to the lower limit of the load cell sensitivity) and the Young's modulus drops to 1-2 MPa. Figure 5-16 shows that when coated onto the heat-treated PA 6(3)T electrospun fiber scaffold, the composite membrane exhibits the exceptional mechanical response of the underlying fiber mat. At low strains (<0.05 mm/mm), the mechanical response of the composite membrane is nearly identical to that of the hydrated Nafion membrane, and maintains its integrity through the plastic deformation region (>0.05 mm/mm). These results show that the mechanical properties of the composite LbL/electrospun fiber PEM when fully hydrated can be finely tailored solely based on the post-spinning thermal treatment of the underlying electrospun fiber scaffold.

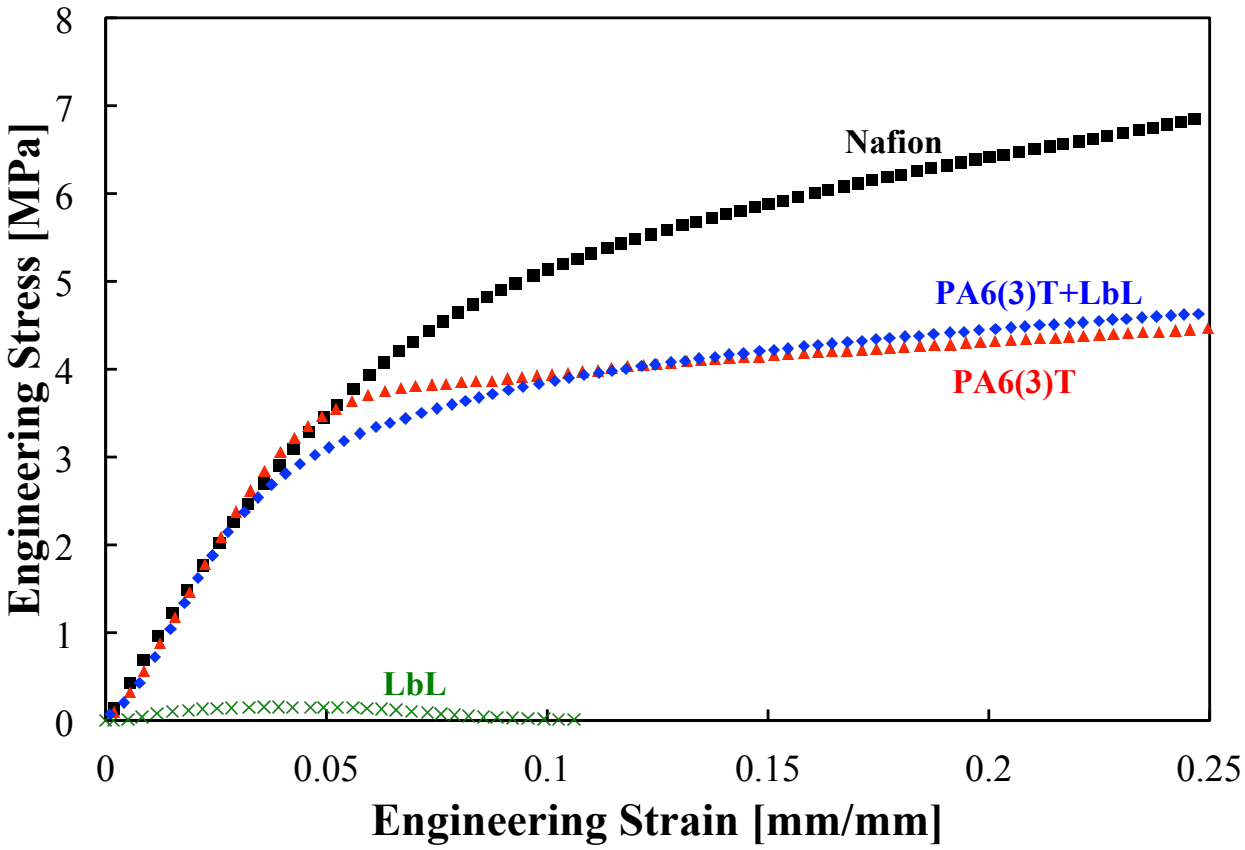

Figure 5-16. Representative stress-strain plots for hydrated membranes of: Nafion (black squares), 150 °C heat-treated PA 6(3)T nanofiber mat (red triangles), free-standing LbL film (green x's), and the composite PA 6(3)T+LbL using 150 °C heat-treated electrospun mat (blue diamonds).

5.4 Concluding Remarks

Composite membranes of highly conductive layer-by-layer films and electrospun fiber mats are fabricated and characterized for mechanical strength and selectivity in this chapter. Free-standing PDAC/sPPO LbL-assembled films have elastic moduli up to 1100 MPa and a maximum yield stress of 40 MPa when tested at ambient conditions. PDAC/sPPO films assembled with more salt in the assembly baths exhibit improved mechanical properties due to the more favorable cross-linked network that is formed. The mechanical properties of PDAC/sPPO free-standing films are on par with commercial proton exchange membranes like Nafion at moderate to low relative humidity conditions; however, the PDAC/sPPO films break at extremely low strains (~ 0.07 mm/mm) and become gel-like with low elastic moduli values when fully hydrated. The mechanical response of highly conducting PDAC/sPPO LbL-assembled

films is improved by depositing the LbL films onto a highly controllable electrospun fiber scaffold. Coating a PCL electrospun mat with PDAC/sPPO using the LbL dipping process produces composite membranes with interesting webbed morphologies that span adjacent fibers. The in-plane ionic conductivity of the composite membrane is similar to the pristine LbL system beyond a critical number of bilayers.

To create a fuel-blocking layer and to fill in more of the void space throughout the electrospun fiber matrix, the spray-LbL assembly is utilized as a means for the rapid formation of LbL films. When the spray-LbL technique is used along with an applied pressure gradient across the electrospun mat during assembly, the resulting LbL electrospun mat composites have conformal coatings on the individual fibers throughout the bulk of the mat. When the spray-LbL technique is used without vacuum, the resulting LbL film bridges across the pores of the electrospun mat, forming a continuous fuel-blocking layer with properties similar to the free-standing LbL by itself. The mechanical properties of the spray coated electrospun mats are shown to be superior to the LbL only system, particularly at hydrated conditions. This shows the versatility of the spray-LbL system to fabricate composite membranes with finely tuned morphology and properties. Future studies are underway to model the mechanical behavior of the LbL/electrospun fiber composite membranes, and to develop future systems with increased mechanical durability and electrochemical selectivity as well as test the composite membrane in an operational direct methanol fuel cell.

5.5 Acknowledgments

This portion of the thesis was supported by the National Science Foundation - Engineering Division Award #0700414, the Masdar Institute of Science and Technology, and the Samsung Advanced Institute of Technology. The author would like to thank Joe Lowery for help preparing PCL electrospun mats, as well as Minglin Ma and Chia-Ling Pai for helpful discussions around electrospinning. The author also acknowledges the Hatton lab for use of drop shape analysis equipment and the MIT Institute of Soldier Nanotechnology for use of facilities.

5.6 References

[1] F. De Brujin, The current status of fuel cell technology for mobile and stationary applications, Green Chemistry 7 (2005) 132-150.

[2] S.G. Chalk, J.F. Miller, Key challenges and recent progress in batteries, fuel cells, and hydrogen storage for clean energy systems, Journal of Power Sources 159 (2006) 73-80.

[3] M. Doyle, G. Rajendran, Handbook of Fuel Cells: Fundamentals, Technololgy and Applications, John Wiley & Sons Ltd., Chichester, England (2005).

[4] J. Wu, X.Z. Yuan, J.J. Martin, H. Wang, J. Zhang, J. Shen, S. Wu, W. Merida, A review of PEM fuel cell durability: Degradation mechanisms and mitigation strategies, Journal of Power Sources 184 (2008) 104-119.

[5] M. Inaba, T. Kinumoto, M. Kiriake, R. Umebayashi, A. Tasaka, Z. Ogumi, Gas crossover and membrane degradation in polymer electrolyte fuel cells, Electrochimica Acta 51 (2006) 5746-5753.

[6] R. Borup, J. Meyers, B. Pivovar, Y. S. Kim, R. Mukundan, N. Garland, D. Myers, M. Wilson, F. Garzon, D. Wood, P. Zelenay, K. More, K. Stroh, T. Zawodzinski, J. Boncella, J. E. McGrath, M. Inaba, K. Miyatake, M. Hori, K. Ota, Z. Ogumi, S. Miyata, A. Nishikata, Z. Siroma, Y. Uchimoto, K. Yasuda, K. I. Kimijima, N. Iwashita, Scientific aspects of polymer electrolyte fuel cell durability and degradation, Chemical Reviews 107 (2007) 3904-3951.

[7] R. Solasi, Y. Zhou, X. Huang, K. Reifsnider, D. Condit, On mechanical behavior and in-plane modeling of constrained PEM fuel cell membranes subjected to hydration and temperature cycles, Journal of Power Sources 167 (2007) 366-377.

[8] A. Kusoglu, A.M. Karlsson, M.H. Santare, S. Cleghorn, W.B. Johnson, Mechanical response of fuel cell membranes subjected to a hygro-thermal cycle, Journal of Power Sources 161 (2006) 987-996.

[9] X. Huang, R. Solasi, Y. Zhou, M. Feshler, K. Reifsnider, D. Condit, S. Burlatsky, T. Madden, Mechanical endurance of polymer electrolyte membrane and PEM fuel cell durability, Journal of Polymer Science Part B: Polymer Physics 44 (2006) 2346-2357.

[10] F.Q. Liu, B.L. Yi, D.M. Xing, J.R. Yu, H.M. Zhang, Nafion/PTFE composite membranes for fuel cell applications, Journal of Membrane Science 212 (2003) 213-223.

[11] K.M. Nouel, P.S. Fedkiw, Nafion-based composite polymer electrolyte membranes, Electrochimica Acta 43 (1998) 2381-2387.

[12] T.L. Yu, H.-L. Lin, K.-S. Shen, L.-N. Huang, Y.-C. Chang, G.-B. Jung, J.C. Huang, Nafion/PTFE composite membranes for fuel cell applications, Journal of Polymer Research 11 (2004) 217-224.

[13] Y.-H. Liu, B. Yi, Z.-G. Shao, D. Xing, H. Zhang, H, Carbon nanotubes reinforced Nafion composite membrane for fuel cell applications, Electrochemical and Solid-State Letters 9 (2006) A356-A359.

[14] E. Chalkova, M.V. Fedkin, D.J. Wesolowski, S.N. Lvov, Effect of TiO2 surface properties on performance of Nafion-based composite membranes in high temperature and low relative humidity PEM fuel cells, Journal of the Electrochemical Society 152 (2005) A1742-A1747.

[15] C. Yang, P. Costamagna, S. Srinivasan, J. Benziger, A.B. Bocarsly, Approaches and technical challenges to high temperature operation of proton exchange membrane fuel cells, Journal of Power Sources 103 (2001) 1-9.

[16] G. Decher, Fuzzy nanoassemblies: toward layered polymeric multicomposites, Science 277 (1997) 1232-1237.

[17] G. Decher, J.D. Hong, J. Schmitt, Buildup of ultrathin multilayer films by a self-assembly process: III. Consecutively alternating adsorption of anionic and cationic polyelectrolytes on charged surfaces, Thin Solid Films 210 (1992) 831-835.

[18] P.T. Hammond, Form and function in multilayer assembly: New applications at the nanoscale, Advanced Materials 16 (2004) 1271-1293.

[19] T.R. Farhat, P.T. Hammond, Designing a new generation of proton-exchange membranes using layer-by-layer deposition of polyelectrolytes, Advanced Functional Materials 15 (2005) 945-954.

[20] A.A. Argun, J.N. Ashcraft, P.T. Hammond, Highly conductive, methanol resistant polyelectrolyte multilayers, Advanced Materials 20 (2008) 1539-1543.

[21] J.N. Ashcraft, A.A. Argun, P.T. Hammond, Structure-property studies of highly conductive layer-by-layer assembled membranes for fuel cell PEM applications Journal of Materials Chemistry 20 (2010) 6250-6257.

[22] J. Doshi, D.H. Reneker, Electrospinning process and applications of electrospun fibers, Journal of Electrostatics 35 (1995) 151-160.

[23] Y.M. Shin, M.M. Hohman, M.P. Brenner, G.C. Rutledge, Experimental characterization of electrospinning: the electrically forced jet and instabilities, Polymer 42 (2001) 9955-9967.

[24] G.C. Rutledge, S.V. Fridrikh, Formation of fibers be electrospinning, Advanced Drug Delivery Reviews 59 (2007) 1384-1391.

[25] S.V. Fridrikh, J.H. Yu, M.P. Brenner, G.C. Rutledge, Controlling the fiber diameter during electrospinning, Physical Review Letters 90 (2003) 144502.

[26] J. Choi, K.M. Lee, R. Wycisk, P.N. Pintauro, P.T. Mather, Nanofiber composite membranes with low equivalent weight perfluorosulfonic acid polymers, Journal of Materials Chemistry 20 (2010) 6282-6290.

[27] K.C. Krogman, N.S. Zacharia, S. Schroeder, P.T. Hammond, Automated process for improved uniformity and versatility of layer-by-layer deposition, Langmuir 23 (2007) 3137-3141.

[28] K.C. Krogman, J.L. Lowery, N.S. Zacharia, G.C. Rutledge, P.T. Hammond, Spraying asymmetry into functional membranes layer-by-layer, Nature Materials 8 (2009) 512-518.

[29] M.M. Mannarino, G.C. Rutledge, Mechanical and tribological properties of electrospun PA 6(3)T fiber mats, Polymer 53 (2012) 3017-3025.

[30] J.L. Lowery, N. Datta, G.C. Rutledge, Effect of fiber diameter, pore size, and seeding method on growth of human dermal fibroblasts in electrospun poly(epsilon-caprolactone) fibrous mats, Biomaterials 31 (2010) 491-504.

[31] C.-L. Pai, M.C. Boyce, G.C. Rutledge, On the importance of fiber curvature to the elastic moduli of electrospun nonwoven fiber meshes, Polymer 52 (2011) 6126-6133.

[32] J.L. Lutkenhaus, K.D. Hrabak, K. McEnnis, P.T. Hammond, Elastomeric flexible free-standing hydrogen-bonded nanoscale assemblies, Journal of the American Chemical Society 127 (2005) 17228-17234.

[33] M.N. Silberstein, C.-L. Pai, G.C. Rutledge, M.C. Boyce, Elastic-plastic behavior of non-woven fibrous mats, Journal of the Mechanics and Physics of Solids 60 (2012) 295-318.

[34] A. Bard, L. Faulkner, *Electrochemical Methods: Fundamentals and Applications*. Second ed. John Wiley and Sons, Inc.: Hoboken, 2001.

[35] T.E. Springer, T.A. Zawdzinski, S. Gottesfeld, Polymer electrolyte fuel cell model, Journal of the Electrochemical Society 138 (1991) 2334-2342.

[36] E. Guzman, H. Ritacco, J.E.F. Rubio, R.G. Rubio, F. Ortega, Salt-induced changes in the growth of polyelectrolyte layers of poly(diallyl-dimethylammonium chloride) and poly(4-styrene sulfonate of sodium), Soft Matter 5 (2009) 2130-2142.

[37] W. Chuanqing, H. Yuhui, C. Guangmin, L. Guo, Z. Shulu, Single-ion conducting polymeric electrolyte based on sulfonated poly(phenylene oxide), Journal of Applied Polymer Science 63 (1997) 559-563.

[38] K.-D. Kreuer, Proton Conductivity: Materials and Applications, Chemistry of Materials 8 (1996) 610-641.

[39] Y. Liu, Q. Yu, J. Yuan, L. Ma, Y. Wu, Brønsted acid–base polymer electrolyte membrane based on sulfonated poly (phenylene oxide) and imidazole, European Polymer Journal 42 (2006) 2199-2203.

[40] S. Kundu, L.C. Simon, M. Fowler, S. Grot, Mechanical properties of Nafion™ electrolyte membranes under hydrated conditions, Polymer 46 (2005) 11707-11715.

[41] M.L. Ma, R.M. Hall, G.C. Rutledge, A review of recent results on superhydrophobic materials based on micro- and nanofibers, Journal of Adhesion Science and Technology 22 (2008) 1799-1817.

[42] M.L. Ma, R.M. Hill, J.L. Lowery, S.V. Fridrikh, G.C. Rutledge, Electrospun poly(styrene-block-dimethylsiloxane) block copolymer fibers exhibiting superhydrophobicity, Langmuir 21 (2005) 5549-5554.

[43] A. Tuteja, W. Choi, M.L. Ma, J.M. Mabry, S.A. Mazzella, G.C. Rutledge, G.H. McKinley, R.E. Cohen, Designing superoleophobic surfaces, Science 318 (2007) 1618-1622.

[44] M.L. Ma, M. Gupta, Z. Li, L. Zhai, K.K. Gleason, R.E. Cohen, M.F. Rubner, G.C. Rutledge, Decorated electrospun fibers exhibiting superhydrophobicity, Advanced Materials 19 (2007) 255-259.

[45] X. Jiang, H. Zheng, S. Gourdin, P.T. Hammond, Polymer-on-polymer stamping: universal approaches to chemically patterned surfaces, Langmuir 18 (2002) 2607-2615.

[46] A.B.D. Cassie, S. Baxter, Wettability of porous surfaces, Transactions of the Faraday Society 40 (1944) 0546-0550.

[47] R.N. Wenzel, Resistance of solid surfaces to wetting by water, Industrial and Engineering Chemistry 28 (1936) 988-994.

[48] C.L. Pai, M.C. Boyce, G.C. Rutledge, Mechanical properties of individual electrospun PA 6 (3) T fibers and their variation with fiber diameter, Polymer 52 (2011) 2295-2301.

[49] W.M. Deen, Analysis of Transport Phenomena, Oxford University Press (1998).

6. Testing and Optimization of Layer-by-Layer/Electrospun Fiber Mat Composite Proton Exchange Membranes in Direct Methanol Fuel Cells

Portions of this chapter are reproduced from D.S. Liu, J.N. Ashcraft, M.M. Mannarino, M.N. Silberstein, A.A. Argun, G.C. Rutledge, M.C. Boyce, P.T. Hammond, Advanced Functional Materials (2013) [In Press], with permission of John Wiley & Sons, Ltd., and M.M. Mannarino, D.S. Liu, P.T. Hammond, G.C. Rutledge, Applied Materials & Interfaces (2013) [In Preparation].

6.1 Introduction

Improvements to the performance of thin-film solid polymer electrolytes for use as proton exchange membranes (PEMs) are critical for the advancement of the electrochemical energy devices [1]. In recent years, there has been considerable interest on designing more chemically stable and mechanically robust membranes while maintaining the high ionic conductivity required of PEMs, and inhibiting fuel crossover [2,3,4]. For current state-of-the-art hydrogen and methanol fuel cells, PEMs comprising perfluorosulfonic acid polymers such as Nafion are the material of choice, primarily because they exhibit superior proton conductivity, relatively high mechanical integrity, and chemical stability; however, even perfluorosulfonic acid polymers have shown limited device lifetimes due to chemical and mechanical degradation [5,6]. One of the main causes of membrane failure is the repeated swelling/deswelling of the membrane during fuel cell operation due to the cycling of temperature and humidity. This cyclic fatigue stress has been shown to weaken the membrane mechanically after as few as a hundred cycles [7,8]. The hydro-thermal mechanical behavior of Nafion during swelling has been extensively studied [9,10]; however, there is a significant need to improve upon the current membrane's durability. Many methods have been proposed to improve the mechanical properties of PEMs, such as incorporating Nafion into a polytetrafluoroethylene (PTFE) supporting matrix [11,12]. Other methods of mechanical reinforcement have led researchers to incorporate metal oxides [13], zirconium phosphates [14], and carbon nanotubes [15] into Nafion matrices in order to improve PEM lifetime or the overall fuel cell performance.

The continued reliance on Nafion, with its high cost and relatively high fuel crossover, as well as the lack of control of the micro-scale composition of previously investigated composite PEMs has proven to be a significant obstacle for development of direct methanol fuel cells (DMFCs). In recent years, alternative composite polyelectrolyte membranes have been investigated as substitutes for Nafion in PEMs such as sulfonated poly(ether ether ketone) (SPEEK)/phenoxy resin (PHR) composites [16], poly(vinyl alcohol)/sulfonated polyhedral oligosilsesquioxane hybrid membranes [17], and sulfonated polystyrene/poly(vinylidene fluoride) blends compatibilized with poly(styrene)-b-poly(methyl methacrylate) block copolymer membranes [18]. More recently, researchers have attempted to fabricate a composite membrane based on sulfonated poly(2,6-dimethyl 1,4-phenylene oxide) (sPPO) reinforced by electrospun and cross-linked bromomethylated poly(2,6-dimetyl-1,4-phenylene oxide) (cBPPO) [19]. While many of these alternative composite PEMs have shown promising results, there are still concerns regarding their mechanical durability, chemical stability, and/or transport properties that prevent them from widespread use in DMFCs.

In recent reports, we have produced layer-by-layer (LbL)-based PEMs that perform well in hydrogen and direct methanol fuel cells [20,21,22]. LbL assembly is a versatile nano-scale fabrication technique that allows for the conformal coating of any wettable substrate with a combination of two or more polymers possessing complementary interactions such as oppositely charged functional groups [23,24]. The films are typically generated by alternating deposition of polyanions and polycations from aqueous solutions, and can be tuned by adjusting the pH or salt content of the polymer solutions; the typical thicknesses per bilayer of films constructed by the LbL method range from as small as a few nanometers to over one hundred nanometers. An LbL system composed of poly(diallyl dimethyl ammonium chloride) (PDAC) and sulfonated poly(2,6-dimethyl 1,4-phenylene oxide) (sPPO) has shown promise for use in a DMFC, with the highest ionic conductivity of any LbL assembled system to date, at 70 mS cm^{-1}, comparable to that of Nafion, while possessing methanol permeability values less than one hundredth that of Nafion. However, this LbL system was found to be mechanically deficient when hydrated [25].

Electrospun fiber (EF) mats are non-woven, highly porous materials with high porosity and a large surface area-to-volume ratio (~1-10 m^2/g) [26,27]. A wide range of polymers can be formed into electrospun mats, and it has been shown that the resulting fiber diameters can be controlled during fabrication in the range of 0.1–10 μm depending on the solution and processing

parameters [28]. In addition, we have previously shown that significant improvements in the mechanical response of EF mats can achieved by thermal annealing with only modest decreases in the porosity of the mats [29]. The spray-assisted LbL process can be used to coat fibers individually throughout the interior of the electrospun mat when assembled with the assistance of a vacuum to control the convection of the spray through the mat; in the absence of a vacuum, the spray-assisted LbL process creates a film that can bridge the pores at the surface of the mat, resulting in an asymmetric composite membrane [22,30]. This versatility in fabrication through the combination of LbL assembly and electrospinning allows for the manufacture of PEMs with controllable transport properties. Previously, we demonstrated the fabrication of LbL films onto electrospun nanofiber mats to produce conductive composite PEMs with superior methanol resistance when compared to Nafion [22].

In this chapter we manipulate the structure of the underlying electrospun nanofiber scaffold to investigate the effects on the mechanical and functional performance of the composite proton exchange membrane. Thermal annealing of the electrospun fiber mats at temperatures near the glass transition was found to improve the mechanical response and dimensional stability of the coated PEMs. The mechanical durability and hysteretic cycling of the composite membranes are investigated as well as the key transport properties of protonic conductivity and methanol permeability for a PEM to be used in methanol fuel cell applications. The transport properties of the composite systems are controllable by manipulation of the fiber mat thickness and LbL deposition parameters. Complete Membrane Electrode Assemblies (MEAs) are constructed and used to evaluate composite PEM performance in an operational DMFC for comparison to Nafion.

6.2 Experimental Method

6.2.1 Materials

Poly(2,6-dimethyl 1,4-phenylene oxide) (PPO) (Mw = 23,000) was obtained from Sigma-Aldrich, Inc. Poly(diallyl dimethyl ammonium chloride) (PDAC) (Mw = 240,000) was obtained from Polysciences, Inc. Poly(trimethyl hexamethylene terephthalamide) [PA 6(3)T] was purchased from Scientific Polymer Products, Inc. N,N-dimethyl formamide (DMF) and isopropyl alcohol (IPA) were purchased from Sigma-Aldrich and used as received for creating

polymeric solutions. PPO was sulfonated as previously reported [20] to yield highly sulfonated sPPO. Magnesium nitrate salt was purchased from Sigma-Aldrich and used as received. E-Tek single side coated 4.0 mg/cm^2 60 wt.% HP Pt on Vulcan XC-72 catalyst coated gas-diffusion layer (GDL) was used for the cathode side of the membrane electrode assembly (MEA) and E-Tek single side coated 4.0 mg/cm^2 30 wt.% Nafion Pt/Ru black catalyst coated GDL was used for the anode side. HP 80% Pt:Ru on Vulcan XC-72 and HP 80 wt.% Pt on Vulcan XC-72 for custom catalyst fabrication were purchased from Fuel Cell Store and used as received. Nafion DE2020 solution was purchased from Ion Power, Inc. and used as the catalyst binder at 0.8:1 wt. ratio to carbon. Catalyst ink slurry of 1:1 mixture by volume of isopropanol:water as solvent was sonicated for five minutes before application. The target catalyst loading was 4.0 mg/cm^2 and the gas diffusion layer was ELAT carbon cloth from Fuel Cell Store.

6.2.2 Electrospinning of Nanofiber Mats

As described in earlier chapters and previous reports [22,29], the electrospinning apparatus consisted of two aluminum disks 10 cm in diameter oriented parallel to each other and separated by a distance of 30 cm. A 22 wt.% solution of PA 6(3)T in DMF was pumped through a Teflon tube with a syringe pump (Harvard Apparatus PHD 2000) at a rate of 0.01 mL/min through a 0.040" ID needle in the top aluminum disk. A high voltage power supply (Gamma High Voltage Research, ES40P) provided 20-24 kV potential to the upper aluminum disk, and the polymer solution was drawn to the bottom grounded disk where ultrafine fibers of approximately 400 nm diameter were collected. The thickness of the mat (from ~10 μm to 80 μm) was controlled by the time allowed for deposition. The EF mats were (optionally) annealed in an oven at a specified temperature between 130-170 °C for 2 hours prior to subsequent coating by the spray-LbL method in order to improve the yield strength of the electrospun mat, as previously reported [29].

6.2.3 Spray Layer-by-Layer Assembly

Samples of EF mats about 100 mm in diameter were first plasma treated in an oxygen atmosphere for 1 minute to make the EF mats hydrophilic and to impart an initial negative charge to the fibers (forming carboxylates on the surface of the fibers). The mats were then placed onto a 75 mm diameter plastic funnel fitted with a steel mesh (2 mm grating) to support the membrane. Sprayed films were fabricated using the same polymer and rinse solutions

described previously [21,22]. A home-built automated spraying setup was used to coat the EF mats using an automated program run by a logic relay, spraying the PDAC and sPPO solutions for 3 seconds each, with 5 seconds of rinse water spray in between the polymer sprays. The process was repeated numerous times to generate thicker coatings. A vacuum was applied to the back of the fiber mat using a Venturi pump supplied with nitrogen, to achieve conformal LbL coatings. For all ES mats 25 μm or thicker, halfway through the desired number of bilayers, the coated mat is flipped over on the steel mesh such that the vacuum is drawn through the opposite side; this is done to provide a more even coating throughout the fiber matrix. The coated fiber mats were then hydrated in deionized water and consolidated in a Carver hot press (15 cm x 15 cm platens) at 100 °C and 50 kN for 30 minutes in order to reduce the remaining pore spaces within the composite membrane. A "capping layer" of LbL film (typically 1 μm thick) was then applied to the composite membrane on both sides by spraying without the vacuum assist, to further inhibit methanol crossover. Free-standing LbL films were also assembled on Teflon substrates or polystyrene-coated silicon wafers and gently peeled off after assembly, similar to a previous report [25].

6.2.4 Characterization

Scanning electron microscopy (SEM) images were obtained on a JEOL JSM-6060 scanning electron microscope after coating the composite membranes with roughly 5 nm of Au/Pd. Cross-sectional images were obtained by cryo-fracturing the composite membranes in liquid nitrogen. Porosities of the fiber mats were determined gravimetrically by cutting out rectangular specimens and measuring the mass and dimensions of the mat sample and converting to porosity. Sample thickness was measured with a Mitutoyo digital micrometer with a constant measuring force of 0.5 N. Lateral sample dimensions were determined using a digital caliper. The volume and mass of the specimen were then converted to a porosity using the following equations [31,32],

$$\rho_{app} = \frac{m_{mat}}{h_{mat} \times A_{mat}} \quad \text{(Equation 6-1)}$$

$$s = \left(\frac{\rho_{app}}{\rho_{bulk}}\right) \times 100\% \quad \text{(Equation 6-2)}$$

where ρ_{app} is the apparent density, m_{mat} is the mass of mat, h_{mat} is the thickness of mat, A_{mat} is the area of mat, s is the mat solidity (%) and ρ_{bulk} is the bulk density. The bulk density was estimated

as the average value for the polymers used: PA 6(3)T (1.12 g/cm^3), sPPO (1.06 g/cm^3), and PDAC (1.04 g/cm^3). The porosity of the composite membranes was defined as 1-solidity.

6.2.5 Mechanical Testing

Uniaxial tensile testing of dry and fully hydrated electrospun fiber mats and composite membranes was performed with a Zwick Roell Z2.5 tensile testing machine using a 2.5 kN load cell. Rectangular specimens were cut to 100 mm x 12.5 mm and extended at a constant crosshead speed of 0.50 mm/s with a 50 mm gauge length (corresponding to a constant strain rate of 0.01 s^{-1}). The thickness of each specimen was determined from the average of three measurements taken along the gauge length with a Mitutoyo digital micrometer at a constant force of 0.5 N. The force–displacement data were converted to engineering stress versus engineering strain using the initial cross-sectional area and gauge length of the test specimen, respectively. Samples defined as "dry" were tested at ambient conditions of 25 °C and approximately 40-45% RH, while samples defined as "hydrated" were conditioned overnight in water and tested while fully saturated with water. Tensile testing under specific humidity conditions was conducted in an EnduraTEC Electroforce 3200 (ELF) with an environmental control chamber. Samples were cut to 4 mm X 30 mm and tested at a constant crosshead speed of 0.12 mm/s with a 0.12 mm gauge length (corresponding to a constant strain rate of 0.01 s^{-1}). The ELF testing grips were completely enclosed in a stainless steel chamber, which was controlled at 25 °C and 50% RH with a magnesium nitrate salt solution, as confirmed by a humidity gauge. Samples were equilibrated in a humidity chamber before being transferred to the testing chamber, and the chamber allowed to re-equilibrate for 1 min after reaching the desired relative humidity prior to being tested.

6.2.6 Swelling Measurements

Swelling measurements were performed by cutting out approximately 10 mm x 10 mm specimens and measuring the precise length and width using a Mitutoyo digital caliper with 0.01 mm precision. Specimens were then placed in boiling water (maintained at 100 °C) for 2 hours, before being removed and re-measured using the digital calipers. The linear swelling was then defined as: swelling %=100% x $(L_s-L_0)/L_0$, where L_s is the corresponding swollen length of the specimen, and L_0 is the original length (at ambient humidity, 50% RH).

6.2.7 Transport Properties

In-plane ionic conductivity measurements of the composite membranes were made using a custom machined PEEK sample holder with two platinum wire electrodes spaced 1 cm apart. The samples were immersed in 18.2 MΩ deionized water before drying to ensure the removal of excess ions. Testing specimens were then cut into approximately 1.5 cm x 2 cm rectangles and placed on top of a glass slide. The PEM specimen was placed on the sample holder across the electrodes and clamped down to ensure good continuous connection between the wires and the membrane. Temperature and humidity were controlled using a chamber from Electro-tech Systems, Inc. Impedance values were determined by electrochemical impedance spectroscopy with a Solartron 1260 impedance analyzer, measuring from 100 kHz down to 10 Hz. The thickness of the composite membrane was measured using a Mitutoyo digital micrometer at a constant force of 0.5 N.

Through-plane proton conductivity measurements were made using a two electrode Swagelok cell with two 12 mm diameter aluminum plates as electrodes [33]. A diagram illustrating the through-plane conductivity-testing cell is shown in Figure 6-1. The composite membrane testing specimens were soaked in 18.2 MΩ deionized water and cut into 12 mm diameter disks. Excess water was removed from each sample with a Kim-wipe, and the specimen was placed between two 10 mm diameter fine wire meshes to decrease the contact resistance. The assembly was then placed in the Swagelok cell between two steel plate electrodes to a set electrode distance controlled by the applied force of the spring component. Impedance values were determined using a Solartron 1260 impedance analyzer as described earlier; the membrane resistance was calculated as the total resistance minus the resistance contribution of the Swagelok cell and the two wire meshes. The through-plane membrane conductivity was then calculated by the following equation:

$$\sigma = \frac{h}{\Omega \bullet A} \qquad \text{(Equation 6-3)}$$

where σ is the through-plane conductivity, h is the membrane thickness (as measured by a micrometer with a constant 0.5 N force), Ω is the membrane resistance (total cell resistance minus the resistance contribution of the Swagelok cell and the wire meshes), and A is the cross-sectional area of the membrane.

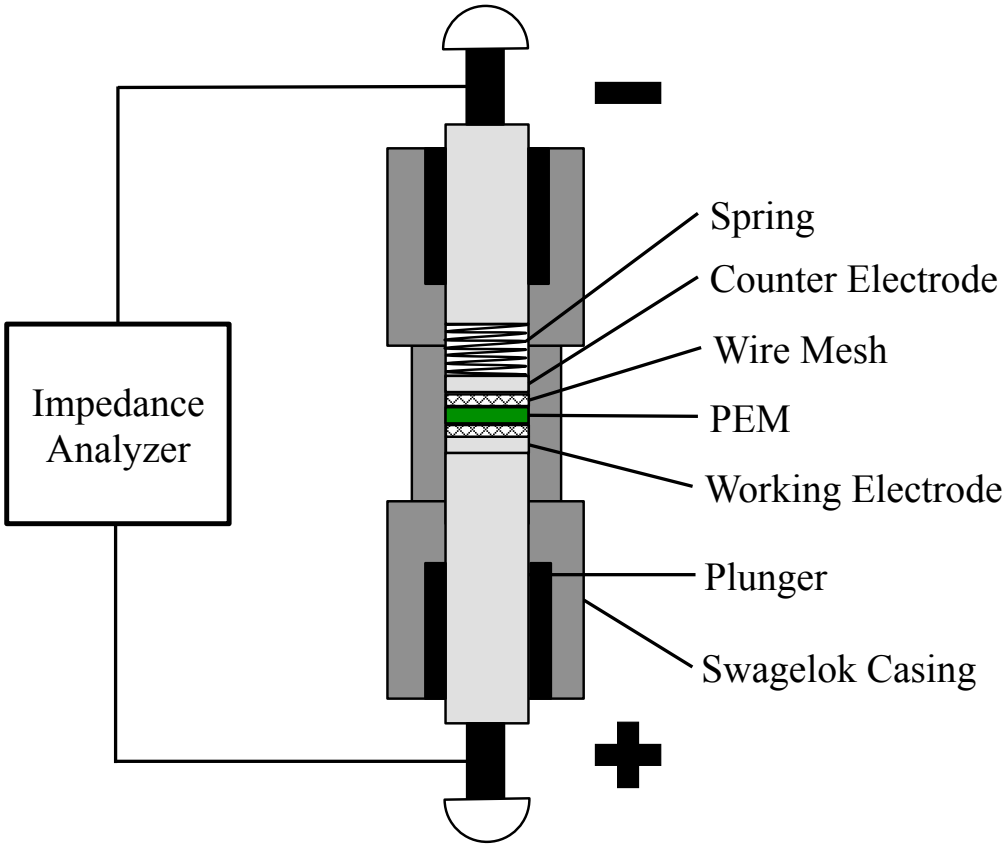

Figure 6-1. Diagram of a two electrode Swagelok cell used for measuring through-plane conductivity of composite PEMs. The spring applies a constant force to the wire mesh, ensuring good contact with the PEM specimen.

Methanol permeability values were determined by using a dual chamber apparatus, where the membrane sample is the separator between 250 mL of 90% methanol/water (v/v) and 250 mL of pure water as described previously [21]. A schematic of the methanol permeation apparatus is shown in Figure 6-2. The liquids in both chambers were stirred, and the increase in methanol concentration of the pure water side as a function of time was determined by the changes in the refractive index of the solution using a Waters 2414 Refractive Index Detector. The following equation was used to calculate the methanol permeability through the membrane:

$$c_B(t) = \frac{A}{V_B} \bullet \frac{P}{L} c_A(t - t_0) \qquad \text{(Equation 6-4)}$$

where c_B is the methanol concentration of the initially pure water solution, A is the exposed membrane area, V_B is the volume of initially pure water, P is the methanol permeability of the membrane, L is the thickness of the membrane, and c_A is the initial concentration of the methanol solution.

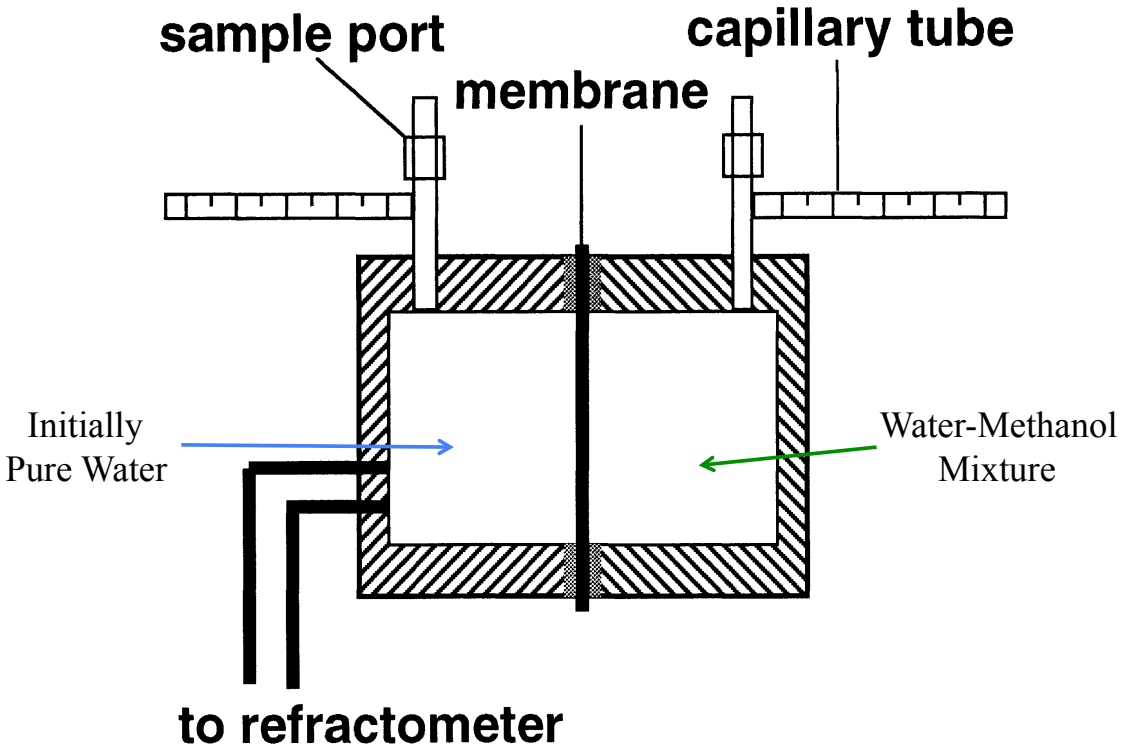

Figure 6-2. Schematic of the dual chamber apparatus used for methanol permeation measurements. The composite LbL membrane separates a 90% methanol/water (v/v) (right side) from pure water (left side). The increase in methanol concentration in the initially pure water side is monitored versus time, and methanol permeability values are determined from Equation 5-2 (schematic adapted from [34]).

6.2.8 Direct Methanol Fuel Cell Testing

The membrane electrode assemblies (MEA) were fabricated by sandwiching a 16 mm diameter circular cut-out composite PEM between two 12 mm diameter GDLs containing catalyst coating and hot-pressing at 135 °C and a force of 5 kN for 5 minutes using a Carver Hot Press. Commercial E-Tek GDL's containing Pt and Pt:Ru were used for the cathode side and anode side of the MEA, respectively. Custom catalyst coating was generated containing PDAC/sPPO binder to improve compatibility and adhesion between PEM and GDL. Catalyst slurry was prepared by adding a specified amount of Pt or Pt:Ru to a 20 wt.% sPPO in water solution, followed by addition of 1:1 IPA:water and 5 wt.% PDAC in water. The slurry was then stick sonicated for five pulses of 1 minute each or until catalyst was well dispersed, by visual inspection. 50 µL of slurry were then deposited onto individually cut 12 mm diameter carbon cloth circles using a pipette and allowed to dry. Measurements of GDL mass were taken before

and after catalyst deposition to confirm addition of 4-5 mg of catalyst per sample. Two 8 cm x 8 cm square gasket layers (250 μm thick PTFE-coated fiberglass sheets, VWR) were used to align the positions of the PEM and GDL during hot-pressing and to transfer the assembly to the DMFC. The MEAs were then tested using DMFC hardware obtained from Fuel Cell Technologies, Inc. Methanol (10% v/v in water) was fed to the anode at a flow rate of 4 mL/min using a peristaltic pump and humidified air was supplied to the cathode at 60 mL/min. Samples were allowed to equilibrate in the testing chamber under humidified air for 1 hour before flowing methanol through and taking measurements. Polarization curves were generated from a Gamry PCI750 potentiostat connected to the DMFC hardware.

6.3 Results and Discussion

6.3.1 Composite Proton Exchange Membrane Fabrication

Fabrication of the composite LbL-EFM proton exchange membrane consisted of the following steps: 1) the electrospinning of a nanofiber matrix (with optional thermal annealing); 2) spray-coating LbL deposition of polyelectrolytes on the fibers using a vacuum pulled across the membrane to create conformal coatings (vacuum-assist); 3) hot-pressing the composite membrane to increase solidity; 4) spray-coating LbL deposition of polyelectrolytes on the composite membrane without vacuum, to provide a continuous capping layer on the top of the PEM. Figure 6-3 shows a diagram illustrating the main steps of composite PEM fabrication, as well as a representative cross-sectional SEM micrograph of a completed composite membrane. Composite LbL-EF proton exchange membranes using PA 6(3)T electrospun fibers and PDAC/sPPO LbL polyelectrolyte coatings that successfully block methanol and possess greater mechanical integrity than a free-standing LbL film have been reported previously by us [22]. The vacuum-assisted LbL deposition penetrates through the entire depth of the electrospun mat, coating all the fibers with a uniform and controllable thickness of PDAC/sPPO at low fill percentages. The membrane solidity (defined as 1–porosity) after successively higher numbers of polyelectrolyte bilayers was found to increase up to about ~70-80 % with 200-250 bilayers, at which point further increases in solidity with additional bilayers were not observed. We hypothesize that the residual porosity was due to closing off of unfilled pores prematurely ("bottle-necking") and non-uniformity of pressure drop through the entirety of the membrane. In

order to reduce the remaining porous interstices of the fiber matrix (and thus create a dense composite membrane), the coated membranes are hydrated in deionized water and hot-pressed at 100 °C at 50 kN for 30 minutes. This process allows the compliant hydrated LbL to collapse the remaining pore space between coated fibers, thus increasing the overall PEM solidity.

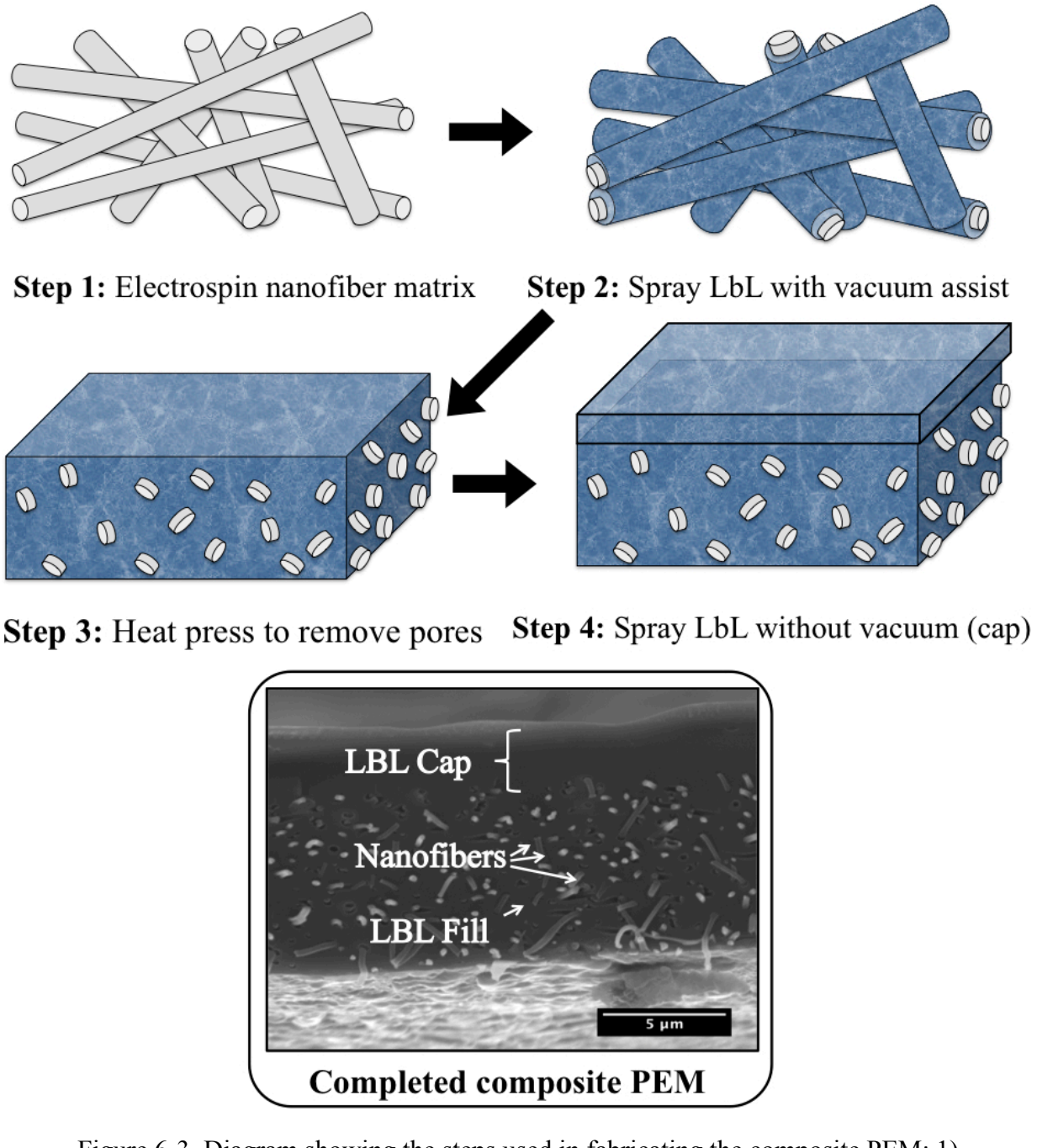

Figure 6-3. Diagram showing the steps used in fabricating the composite PEM: 1) electrospinning of nanofiber matrix; 2) spray-coat fibers with LbL polyelectrolytes using a vacuum assist; 3) hot pressing membrane to remove voids; 4) continue spray-coating LbL without vacuum to provide a capping layer to top of PEM. Scale bar of SEM micrograph is 5 µm.

Optional thermal annealing of the underlying electrospun fiber matrix at 130, 150, and 170 °C was used to improve the mechanical properties of the composite PEM. Annealing at temperatures close to the glass transition (T_g) of PA 6(3)T was found to increase the mechanical strength while also increasing the solidity of uncoated EF mats from about 11-14% for mats annealed below 150 °C, up to 35% for mats annealed at 170 °C [29]. After coating 200 bilayers of PDAC/sPPO using vacuum-assisted spray-LbL, all membranes plateaued at 68-76% solidity. Hot pressing of the hydrated membranes was used to push the membrane solidity up to 88-93%, with the EF mats originally annealed at 130 °C and 150 °C exhibiting the highest overall solidities after fabrication. Figure 6-4 shows the solidity of the composite membranes after each step in the fabrication process, as a function of the annealing temperature of the EF mat prior to LbL deposition. It should be noted that despite the fact that all of the composite membranes exhibit comparable solidities after hot-pressing, the solidity for the 170 °C thermally annealed fiber mats before coating is much higher; therefore, since there is less pore volume to fill with conducting polyelectrolyte, the ratio of LbL:EF would be lower than the other membranes, which is detrimental to the transport properties of the PEM.

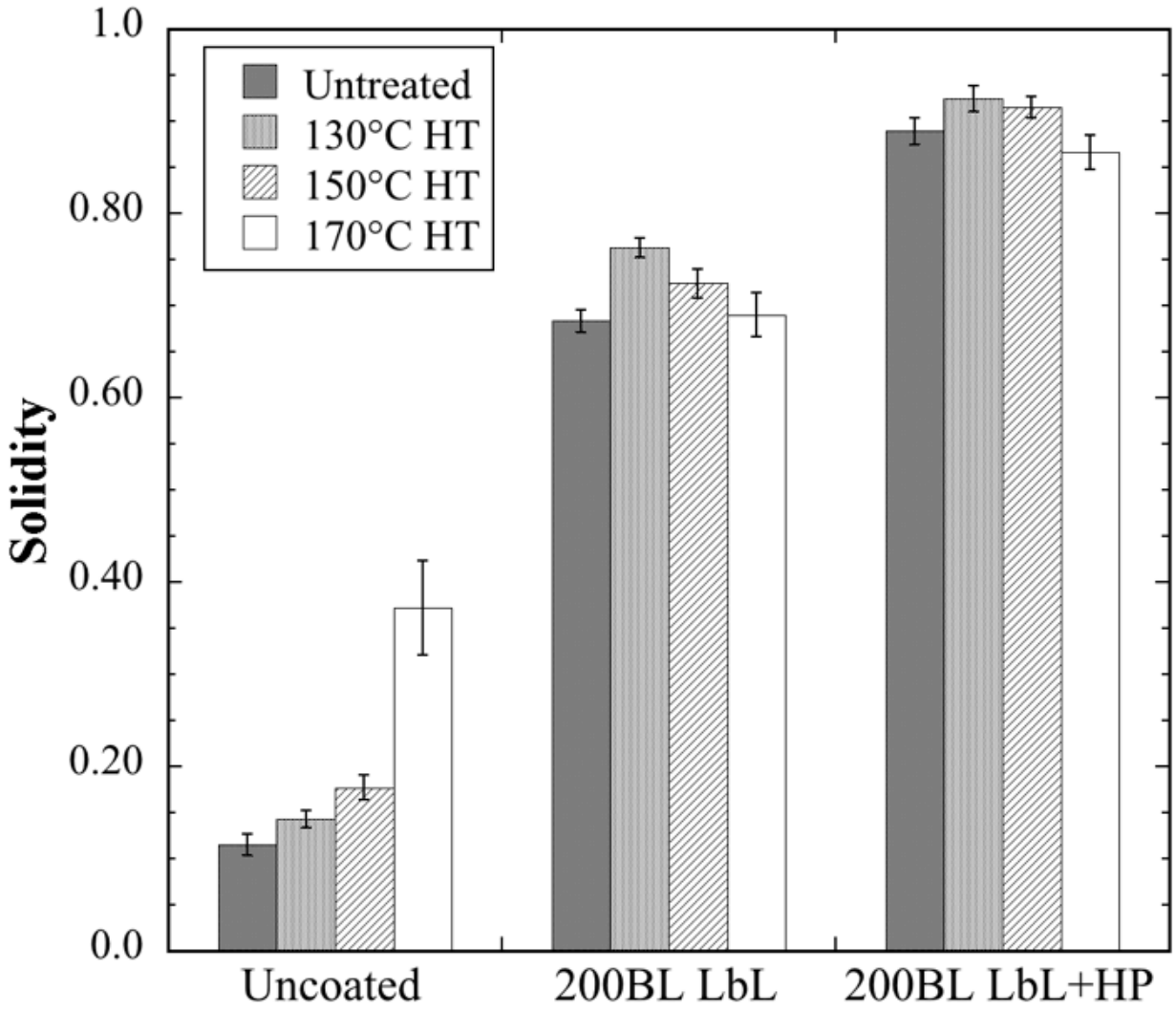

Figure 6-4. Histogram of solidity of PA 6(3)T EFMs annealed at various temperatures, after each step of the fabrication process: thermal treatment of uncoated EFM, after deposition of 200 bilayers (BL) of PDAC/sPPO, and after hot-pressing (HP) of the hydrated composite membranes. Average fiber diameter was 463±64 nm.

Representative SEM images of the composite PEM at different stages of fabrication are shown in Figure 6-5. PA 6(3)T nanofibers that have been conformally coated with 50 bilayers of PDAC/sPPO are shown in Figure 6-5a,b; there remains a significant amount of pore space between the coated fibers. SEM micrographs of a cross-section of the hot-pressed composite membranes with 250 bilayers of PDAC/sPPO spray-coated LbL are shown in Figure 6-5c,d; the PDAC/sPPO can be seen completely filling the interstices between the PA 6(3)T fibers due to compression of the hydrated LbL system into the void space during pressing. Before pressing,

the composite membrane was an opaque, whitish color, which turns clear after being hydrated and hot-pressed, as a result of the elimination of residual air pockets that scatter light.

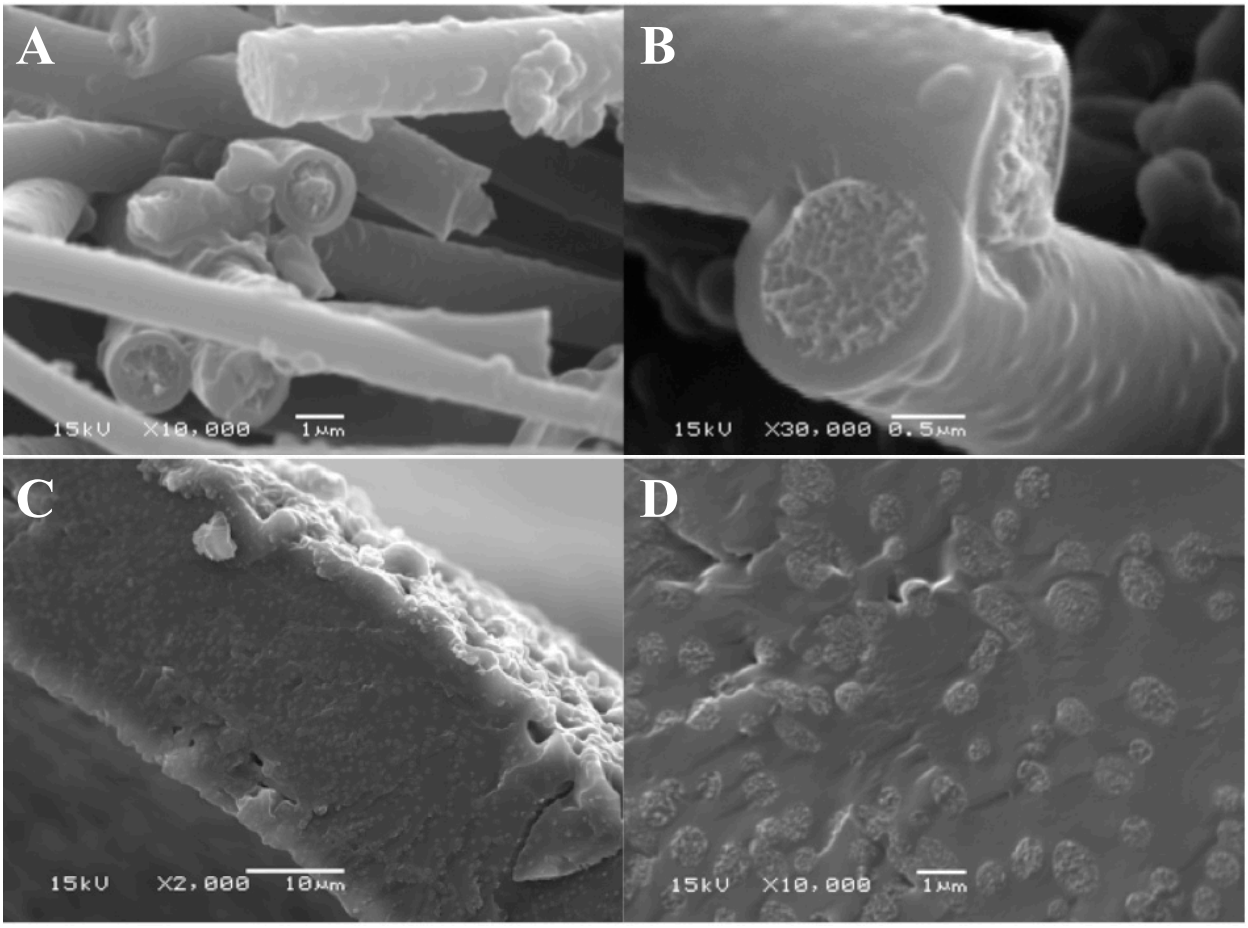

Figure 6-5. SEM micrograph of ~800 nm diameter PA 6(3)T fibers coated with 50 bilayers of PDAC/sPPO (A & B). SEM Micrograph of composite PEM, consisting of PA 6(3)T fibers whose interstices are completely filled with PDAC/sPPO (250 BLs with vacuum assist) after being hot-pressed while fully hydrated. Scale bars for A & D are 1 μm; scale bar for B is 0.5 μm; scale bare for C is 10μm.

6.3.2 Mechanical Properties

We have previously shown that the mechanical properties of the composite LbL-EFM membranes in the hydrated state depend primarily on the nonwoven fiber "endoskeleton", while those of the composite membranes in the dry state are stiff and brittle, like the LbL film itself [22]. The mechanical properties of uncoated nanofiber mats have also been investigated extensively, and can be controlled by various post-spin treatments [29,35,36]. Annealing of the PA 6(3)T nanofiber mats, in particular, improves the mechanical properties of the EFMs by a factor of 5-6 fold over the as-spun mats. Here we show that these improvements survive

hydration and are reflected in the composite PEMs as well; all mechanical testing results are listed in Table 6-1. Under dry conditions, the Young's moduli of the composite membranes range from 383 ± 43 MPa for the composite PEM based on the unannealed PA 6(3)T electrospun fiber mat, and up to 482 ± 71 MPa for the composite PEM based on the EF mat annealed at 150 °C. Yield stresses range from 8.9 ± 3.5 MPa to 12.3 ± 3.3 MPa for these same composite PEMs. The values for Young's modulus and yield stress are comparable to the values for the free-standing PDAC/sPPO film, at 610 ± 113 MPa and 12.8 ± 4.5 MPa, respectively. Even though the Young's moduli and yield stresses of the composite PEMs are greater than those of Nafion, all of the LbL systems are still brittle at 25 °C and 50 %RH; therefore, the composite PEMs exhibit strains-to-break on the order of 0.05-0.10 mm/mm, significantly lower than that of Nafion, which can extend well over 2.00 mm/mm before breaking at ambient conditions.

During processing, as well as in an operational DMFC, the composite PEMs are in a hydrated state; therefore, tensile testing was also conducted on membranes that have been pre-conditioned in water for 24 hours. An increase of up to 5-6 fold in the Young's modulus and yield stress of the hydrated composite PEM can be observed for the composite PEMs as a result of annealing the underlying PA 6(3)T fiber mat. The improvements to the mechanical properties of the fully hydrated composite LbL-EF PEMs are comparable to the response of the uncoated PA 6(3)T fibers mats under the same testing conditions, confirming that the mechanical response of the composite PEM is controlled by the underlying electrospun nonwoven fiber structure. At 150 °C heat-treatment, the mechanical properties of the hydrated composite PEM are comparable to that of hydrated Nafion N112, with Young's moduli of 80.2 ± 9.9 MPa and 74.3 ± 5.7 MPa, and yield stresses of 3.39 ± 0.37 and 5.56 ± 0.22 MPa, respectively. It was reported previously that these increases in the mechanical response of the underlying nanofiber matrix occur at the expense of porosity; however, there was not a significant drop in the porosity of the electrospun mats from the unannealed state to the 150 °C thermally annealed EF mat: 82% vs. 88% porosity [29].

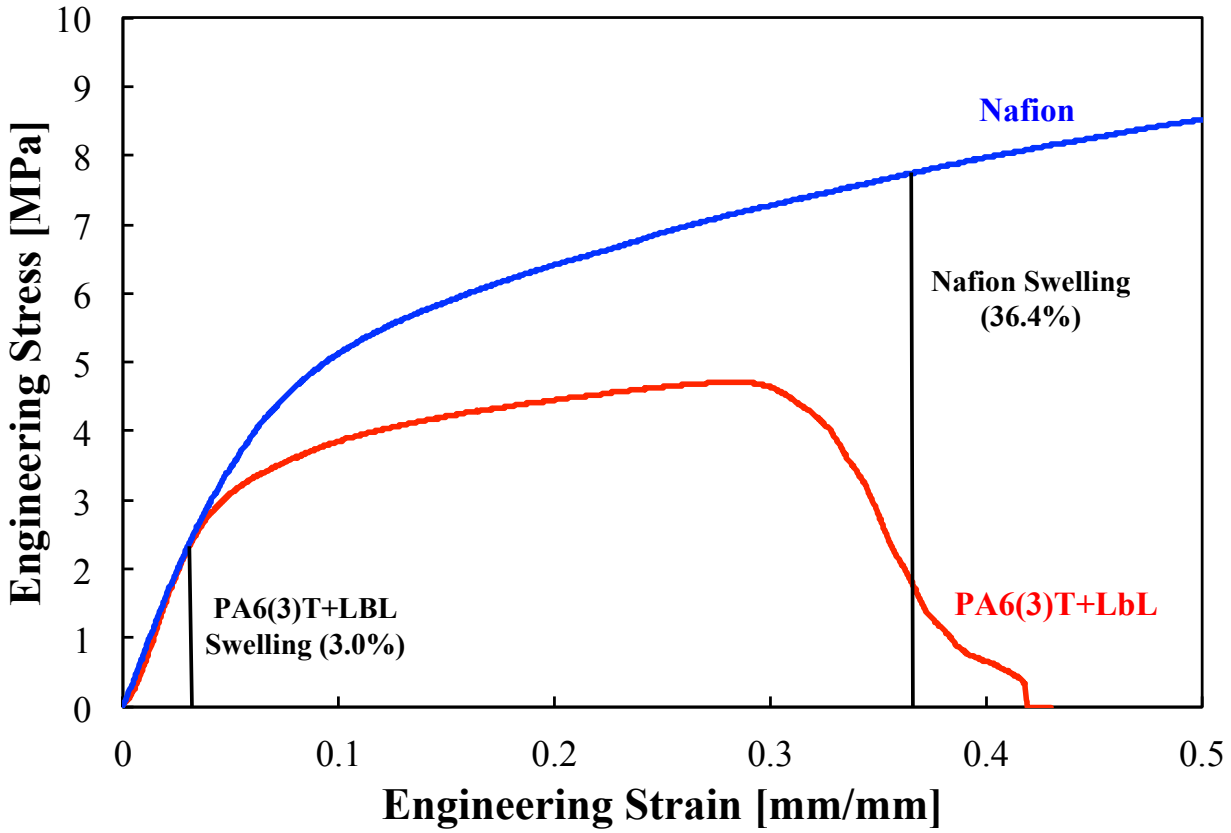

Figure 6-6. Representative stress-strain plots for hydrated membranes of Nafion and a 150 °C heat-treated PA 6(3)T nanofiber mat composite PEM along with their respective swelling strains. Note that the Nafion swelling strain penetrates significantly into the plastic deformation region, while the composite PA 6(3)T+LbL membrane exhibits swelling confined to the elastic region.

Figure 6-6 compares the data for engineering stress vs. engineering strain for a typical composite membrane (underlying PA 6(3)T mat was annealed at 150°C) vs. Nafion in the fully hydrated state. Vertical lines have been drawn in the plot to denote the typical extent of linear swelling each membrane experiences from the dry to fully hydrated state. When coated onto the heat-treated PA 6(3)T electrospun fiber scaffold, the composite membrane exhibits the improved mechanical response of the underlying thermally annealed EF mat and exhibits very small swelling strains as compared to Nafion (~0.03 mm/mm vs. ~0.36 mm/mm). At low strains (<0.05 mm/mm), the mechanical response of the composite membrane is nearly identical to that of the hydrated Nafion membrane, and maintains its integrity through the plastic deformation region (>0.05 mm/mm).

6.3.3 Swelling Behavior

In an operational fuel cell, the PEM undergoes repeated swelling and de-swelling cycles, which can significantly decrease the lifetime of the membrane [10,37]. Perfluorosulfonic acid (PFSA)-based proton exchange membranes, such as Nafion, exhibit substantial swelling in water. However, Nafion typically exhibits an elongation-to-break greater than 2.00 mm/mm, so that this swelling does not lead to failure of the membrane immediately. Nevertheless, cyclic swelling does often lead to mechanical failure/fracture as a result of pinhole formation or membrane thinning due to repeated straining of the membrane into the inelastic (plastic deformation) regime [10,38]. Greater swelling also usually results in the formation of larger water channels within the membrane, leading to higher methanol crossover, which results in a decrease in the overall fuel cell output [39]. Therefore, PEMs that swell less offer some advantages in a polymer electrolyte membrane fuel cell due to their potential for increased service lifetime. Figure 6-7 shows that the composite membranes fabricated in this work have significantly greater dimensional stability than both the Nafion and the free-standing LbL film during a swelling experiment under the same conditions. We hypothesize that the significant decrease in linear swelling for the composite PEM is due to constraint of the LbL film within the electrospun fiber matrix; the LbL film is electrostatically bound to the fiber surfaces and is unable to expand because the film is mechanically weaker than the supporting fiber matrix. The results confirm this hypothesis since the linear swelling of the composite membranes decreases with increasing annealing temperature of the underlying EF mat. Figure 6-7 also shows a comparison of the tensile strain-to-break of the PEMs at 50% RH and 25 °C. The composite membranes exhibited both a moderate increase in the strain to break at 50% RH (0.06 mm/mm for the free-standing LbL to 0.10 mm/mm for the composite system), and a more than three-fold decrease in the linear swelling from 0.17 mm/mm for the free-standing LbL to 0.03-0.05 mm/mm for the composite PEM (depending on the temperature of EF mat annealing). The linear swelling strains of all of the LbL systems were found to be significantly lower than Nafion, which swelled to 0.36 ± 0.04 mm/mm, nearly an order of magnitude larger than the composite PEMs. A summary of the strain to break and linear swelling properties can be found in Table 6-1.

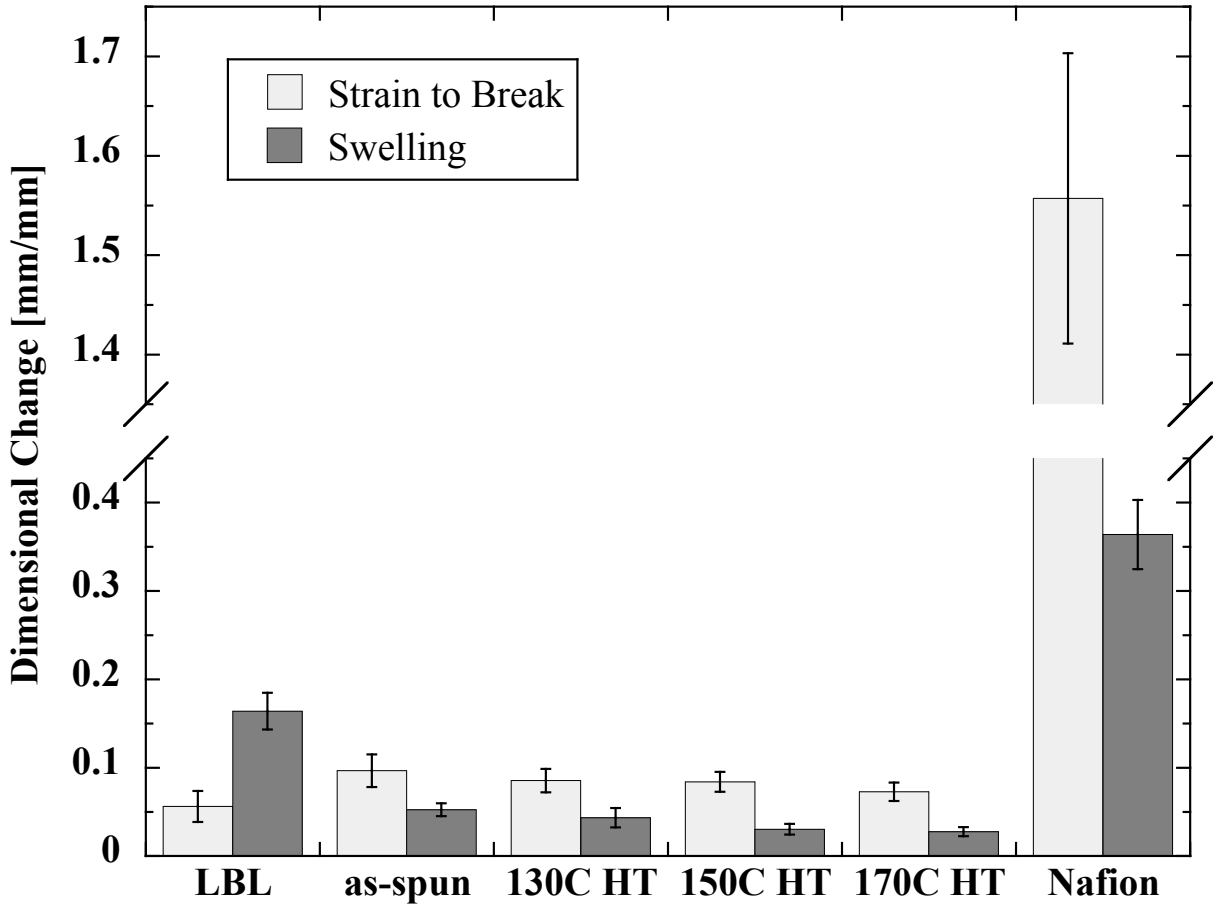

Figure 6-7. Dimensional change in the strain to break (at 50% RH) and linear swelling of composite PEMs and Nafion after boiling in water for 1 hour.

The mechanical durability of PEMs in a hydrated fuel cell is directly linked to its tensile strain to break and its linear swelling in the same direction after exposure to liquid water. Membranes undergo significant swelling when humidified and may fail mechanically if membrane stresses experienced during hydration cycling exceed the tensile strength of the membrane; therefore, larger membrane breaking strains are desirable. The hydration stability factor is a metric that was developed in recent years for evaluating the likelihood that a membrane can withstand repeated humidity cycling [8], and is defined as:

$$\mathrm{HSF} = \frac{\text{strain at break [mm/mm] (25 °C, 50 \%RH))}}{\text{linear swelling [mm/mm] (100 °C in } H_2O)} \qquad \text{(Equation 6-5)}$$

This metric has proven to be a convenient measure for assessing various membranes and to predict their relative durability in the accelerated mechanical humidity cycling test. Figure 6-8 shows the hydration stability factor of the composite membranes as well as the HSF for the free-standing LbL film and for Nafion. A value of HSF<1 indicates that the membrane is not robust

enough to survive humidity cycling, which highlights the weakness of the free-standing PDAC/sPPO film whose HSF is 0.34 ± 0.11. All of the composite LbL/EF membranes are seen to have HSF values that are 5-6 times larger than that for the free-standing LbL, and only ~30% or so less than Nafion; these results indicate that the composite LbL/EF PEMs possess sufficient mechanical integrity to withstand humidity cycling in an operational fuel cell.

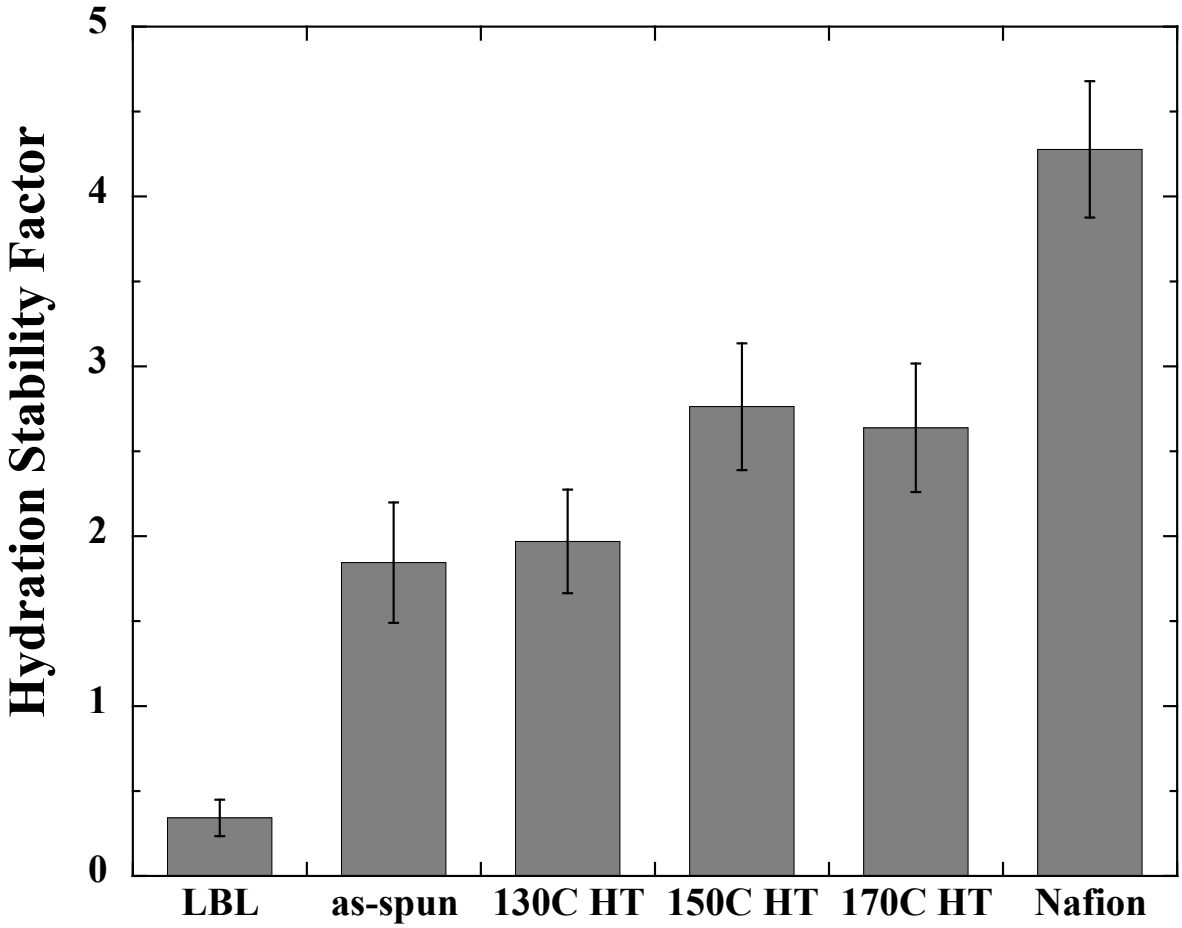

Figure 6-8. Comparison of Hydration Stability Factor for the free-standing LbL film, composite PEMs (as-spun EFM at 3 different annealing temperatures prior to LbL coating), and Nafion.

Table 6-1. Summary of Mechanical and Swelling Properties of Composite PEM at 25 °C.

	Young's Modulus (100% RH) [MPa]	Yield Stress (100% RH) [MPa]	Strain to Break (50% RH) [mm/mm]	Linear Swelling [mm/mm]	Hydration Stability Factor (HSF)	Hysteresis (1 Swelling Cycle) (100% RH) [%]
PDAC/sPPO Film	1.70 ± 0.95	0.11 ± 0.04	0.06 ± 0.02	0.16 ± 0.02	0.34 ± 0.11	N/A
As-spun+LbL	36.1 ± 5.1	1.07 ± 0.14	0.10 ± 0.02	0.05 ± 0.01	1.84 ± 0.35	47.5 ± 6.3
130 °C HT+LbL	52.1 ± 10.8	1.69 ± 0.10	0.09 ± 0.01	0.04 ± 0.01	1.97 ± 0.31	36.8 ± 5.6
150 °C HT+LbL	80.2 ± 9.9	3.39 ± 0.37	0.09 ± 0.01	0.03 ± 0.01	2.76 ± 0.37	37.0 ± 5.2
170 °C HT+LbL	197.7 ± 54.2	6.51 ± 0.63	0.07 ± 0.01	0.03 ± 0.01	2.64 ± 0.37	39.2 ± 5.4
Nafion® N112	74.3 ± 5.7	5.56 ± 0.22	1.56 ± 0.15	0.36 ± 0.04	4.28 ± 0.40	62.9 ± 3.9

The comparable values of HSF for the composite PEMs and Nafion suggest that the PA 6(3)T+LbL membranes may exhibit similar humidity fatigue cycling lifetimes to Nafion; however, the HSF does not fully capture the significant advantage of the dimensional stability (reduced linear swelling) of the composite PEMs. To evaluate quantitatively the durability of the composite LbL-EF membranes with respect to cycles of swelling and de-swelling, two resiliency metrics were utilized: the mechanical hysteresis (energy loss during swelling cycle) and the strain ratio (the ratio of the swelling strain to the yield strain). Figure 6-9 shows a comparison of the single load-unload stress-strain curves for Nafion and the composite LbL/EF membrane under extension. The membranes are extended up to a total strain equivalent to the linear deformation caused by swelling in boiling water for 2 hours. It is important to note that the strain reached by Nafion upon swelling (~0.36 mm/mm) extends well beyond the yield strain (~0.08 mm/mm) of Nafion, indicating that there is likely to be a significant amount of permanent deformation with each swelling cycle. A membrane that is repeatedly deformed beyond the yield point loses its mechanical integrity, thinning at points of high stress and leading to increased fuel cross-over and possible mechanical failure within an operational fuel cell. Conversely, the composite membrane exhibits a linear strain upon swelling of only ~0.03-0.05 mm/mm. This is below the yield point of the composite membranes (0.05-0.08 mm/mm), which therefore deforms elastically and reversibly with each cycle.

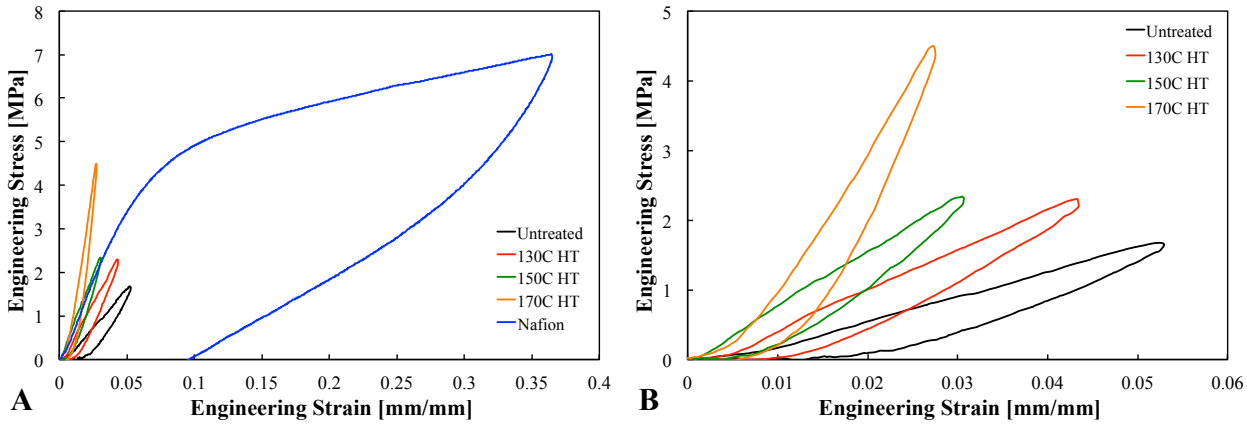

Figure 6-9. Single load-unload mechanical hysteresis stress-strain plots of Nafion and PA6(3)T+LbL (A), and a close-up of the composite PA 6(3)T+LbL membranes (B). Each sample was extended to their respective mean swelling strain. All tests conducted at 100 %RH.

To quantify the energy loss during a swelling cycle, the mechanical hysteresis for a single cycle of loading and unloading (up to the measured swelling strain) was determined for each composite membrane sample and compared to that of Nafion. The area contained between the load-unload curves is an indication of the work performed on the membrane with each swelling cycle; Nafion exhibits significantly larger hysteretic losses as compared to the LbL-EF membranes. A quantitative comparison of the percent of mechanical hysteresis for each PEM and Nafion are shown in Figure 6-10. All of the composite LbL-EF membranes exhibit lower percent mechanical hystereses relative to that of Nafion. The 130 °C and 150 °C heat-treated PA 6(3)T+LbL samples exhibit the lowest hysteretic losses, at 36.8 ± 5.6 % and 37.0 ± 5.2 %, respectively, compared with 62.9 ± 3.9 % for Nafion.

To quantify the irreversible deformation a membrane would experience with each swelling cycle, we propose the following "swelling strain ratio", which we define as:

$$\text{Strain Ratio} = \frac{\text{linear swelling [mm/mm] (100 °C in } H_2O)}{\text{yield strain [mm/mm] (25 °C, 50 \%RH)}} \qquad \text{(Equation 6-6)}$$

If the swelling strain ratio is less than 1, then the swelling occurs entirely within the elastic regime, and repeated cycling should be mostly recoverable; however, if the swelling strain ratio is greater than 1, then the sample deforms plastically during each cycle; the greater the ratio is above one, the greater the deformation the membrane would exhibit during hydration cycling. All of the composite PEMs exhibit swelling strain ratios of ~1 or lower (0.92 ± 0.19 for the 150 °C annealed sample), indicating that the strains induced on the membranes by swelling are equal to or slightly below the yield point, and thus highly recoverable, as shown in Figure 6-10.

The swelling strain ratio of Nafion is found to be 4.18 ± 0.45, which corresponds to large plastic (unrecoverable) deformation after each swelling cycle. The greater dimensional stability and lower mechanical hysteresis of the composite LbL-EF proton exchange membrane demonstrate the potential for longer operational lifetimes relative to Nafion.

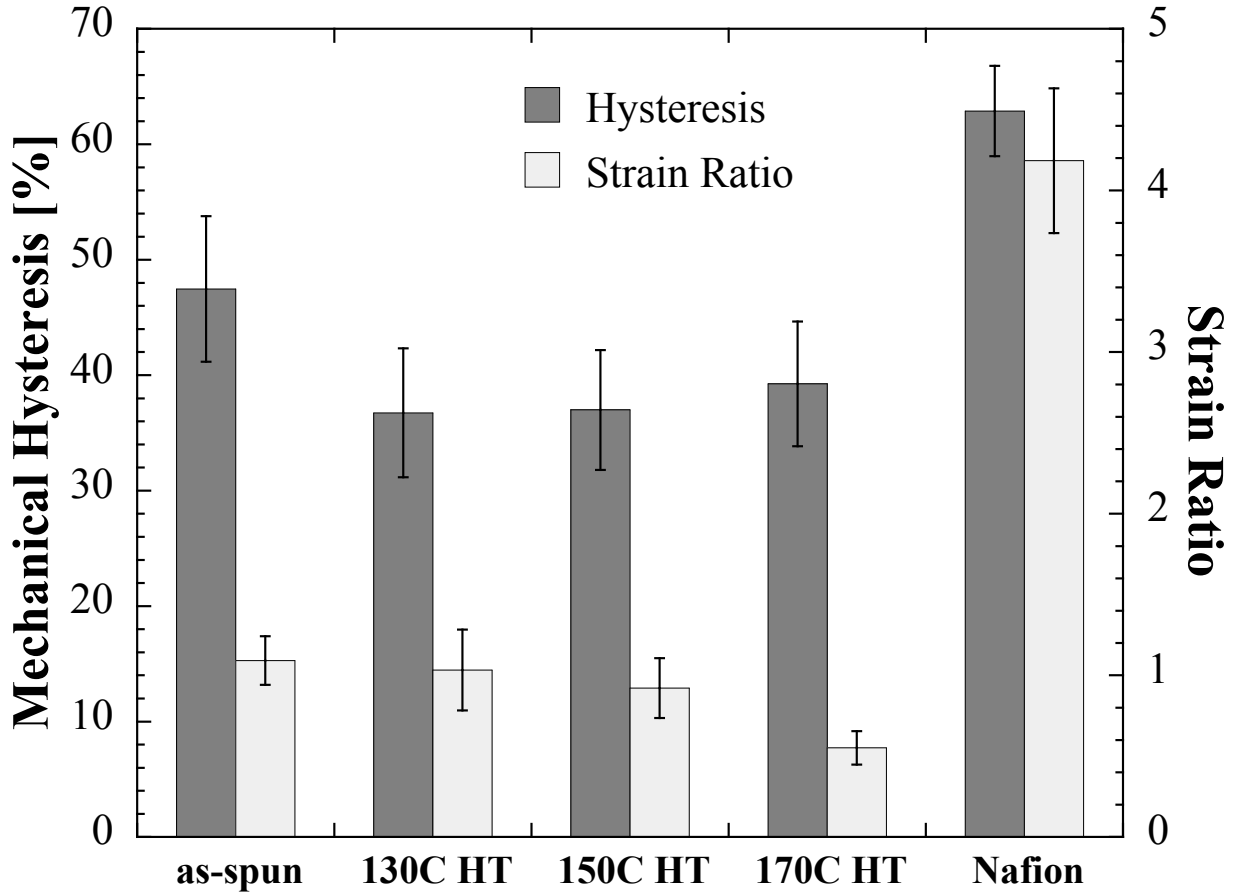

Figure 6-10. Comparison of the mechanical hysteresis and strain ratio for composite PA 6(3)T+LbL membranes with varying levels of heat-treatment and Nafion.

6.3.4 Transport Properties

In-plane conductivities of the composite PEMs assembled using the various thermally treated PA 6(3)T electrospun scaffolds as well as the free-standing LbL-deposited film were measured to quantify their dependence on humidity as seen in Figure 6-11(A). All of the composite PEMs and the pristine LbL thin-film show similar humidity dependence; the proton conductivity improves by approximately an order of magnitude with every 20% increase in the relative humidity. The dependence is also similar to that of pristine sPPO films and the previously investigated PDAC/sPPO dip-coated LbL films [25], indicating that the proton

conduction mechanism of the LbL films is analogous to that of sulfonate groups in sPPO; the assembly method or the supporting scaffold does not significantly affect proton transport. The PA 6(3)T electrospun mats annealed at 130 °C yielded composite PEMs with a higher protonic conductivity than those annealed at 150 °C or 170 °C. The slight porosity decrease of the fiber mats with annealing temperature is not enough to explain the significant drop in ion transport. This difference in the conductivity is most likely due to difficulty in coating merged fibers and weld points, resulting in bottle-necking of the spray-LbL before complete filling of pore space. The conductivity of the composite PEMs in the fully hydrated (100 %RH) and acidic medium (pH 2) are on the order of 10-20 mS/cm, close to 50% of the 35.3 mS/cm ionic conductivity of the pure free-standing PDAC/sPPO film [21]. Lower total resistances can be achieved by utilizing thinner proton exchange membranes in DMFCs and in the composite LbL-EF PEMs. Figure 6-11(B) shows the effect of using electrospun mats of various thicknesses (80, 60, 40, and 25 μm thick before coating and pressing) for fabrication of the composite PEM. All of these PA 6(3)T mats were annealed at 130 °C. The thinner membranes exhibited increased protonic conductivity due more complete impregnation of polyelectrolytes, with the thinnest membrane (25 μm) possessing conductivities comparable to that of a 5 μm thick pure LbL film when fully hydrated.

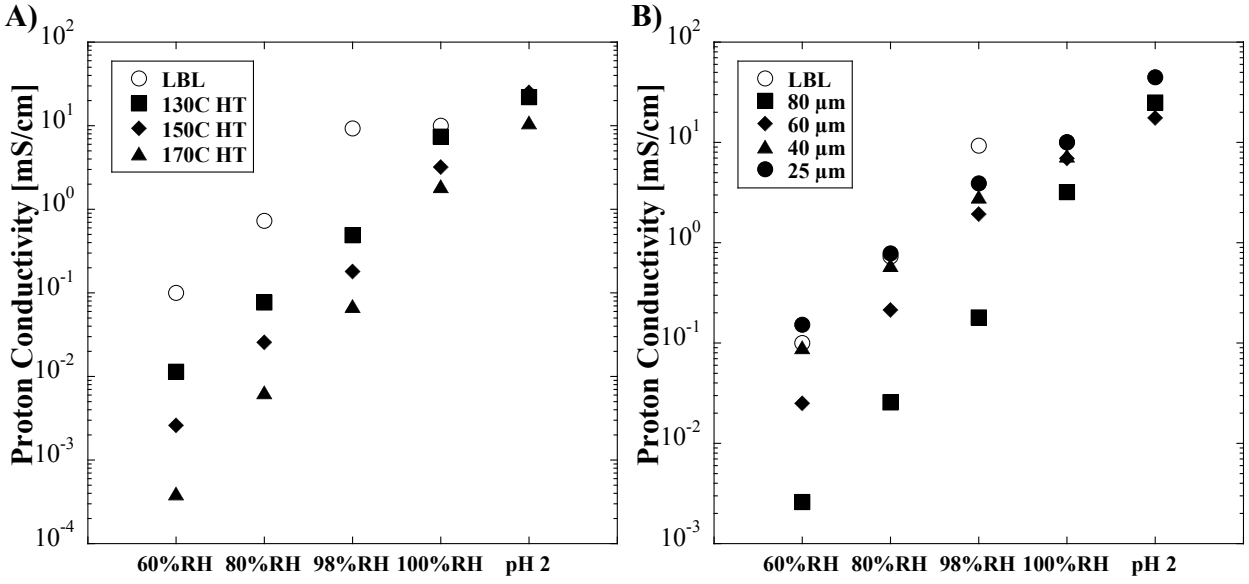

Figure 6-11. (A) Humidity dependence on the proton conductivity of the composite PEMs assembled on various thermally treated EFMs and free-standing LbL film (all samples 40 μm thick). (B) Humidity dependence of the composite PEM proton conductivity for membrane thicknesses [all EF mats annealed at 130 °C for 2 hours].

To better estimate how well the complete composite PEM would perform in a fuel cell and to observe the effect of capping on the proton conduction, the through-plane and in-plane conductivities were measured for uncapped and capped PEMs, as shown in Figure 6-12. While the in-plane conductivity of the capped PEM showed a marked, four-fold increase from the uncapped PEM, the through-plane conductivity of the capped PEM was only slightly more conductive than the uncapped PEM, which was already comparable to the pristine LbL film. We hypothesize that the uncapped composite PEM exhibits a low in-plane conductivity due to proton transport occurring along the length of the randomly aligned electrospun fibers, and the large increase in the in-plane conductivity after the addition of the capping layer was the result of the conduction through the LbL deposited capping film increasing the connectivity of the individually coated fibers in-plane; thus providing a less tortuous path for the proton conducting channels. Conversely, the uncapped composite PEM exhibited a high through-plane conductivity because the LbL was already well connected through the thickness of the fiber matrix as a result of the vacuum-assisted LbL deposition process and subsequent hot-pressing. The through-plane path within the mat for proton transport was not significantly altered due to the capping process; therefore, the conductivity measurements through-plane did not change significantly before and after LbL capping. Note that despite the anisotropic morphology of the capped composite PEM, the measured conductivity through-plane and in-plane are quite similar. This is in contrast to homogenous Nafion membranes, where the ion channels are aligned anisotropically from membrane processing, resulting in Nafion's through-plane conductivity being about 1/3 to 1/4 of its in-plane conductivity [5].

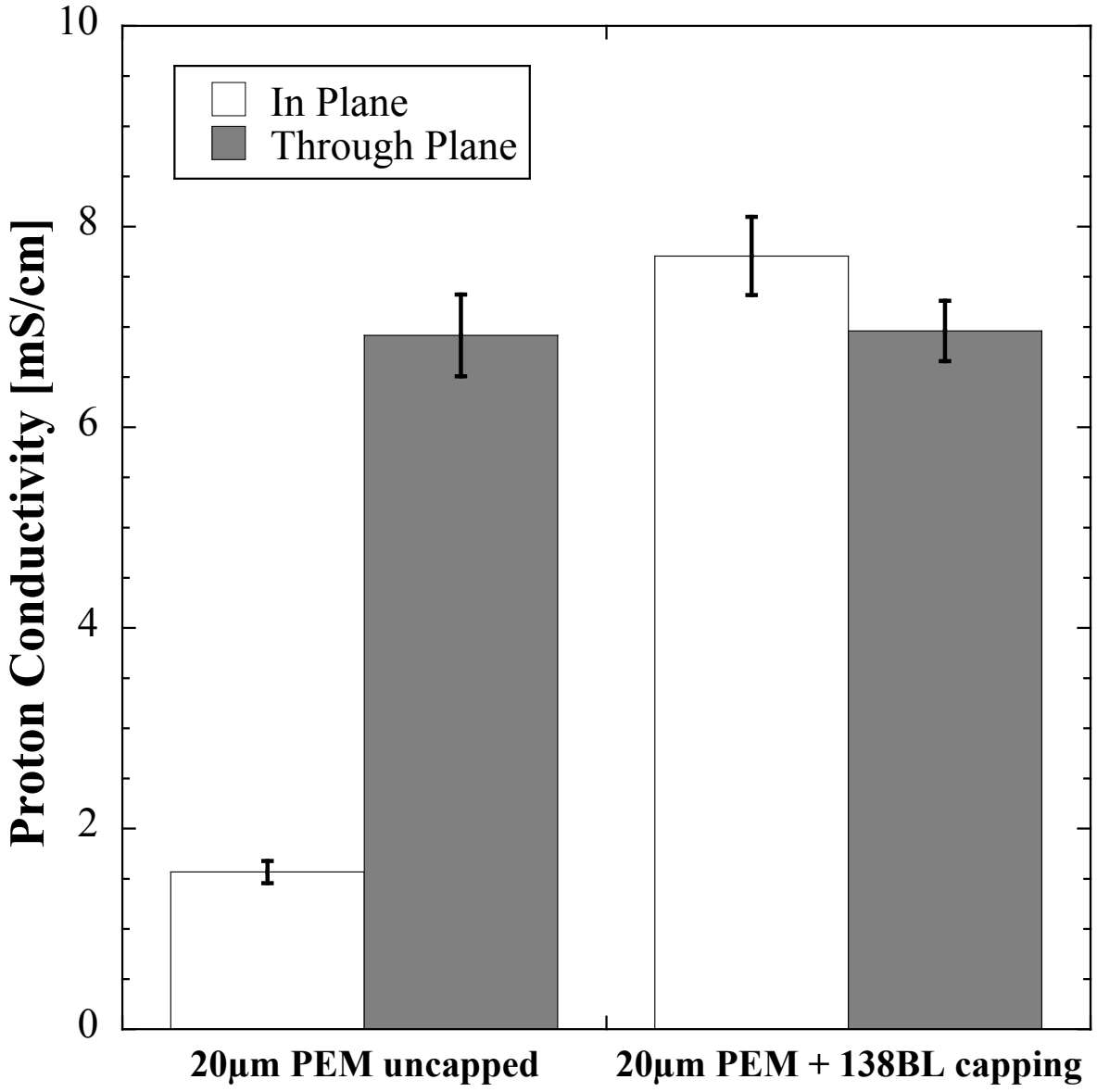

Figure 6-12. Comparison of in-plane and through-plane proton conductivity of uncapped (20 µm thickness) and capped (30 µm total thickness) composite PEMs. Samples tested at 25 °C and 100% RH.

Methanol permeability was measured for spray-LbL electrospun mats to evaluate the effectiveness of the LbL films in reducing methanol crossover. When vacuum was applied during the spray-assisted LbL process, the resultant composite membrane (with 30% void space) was highly permeable to methanol. However, when there was no vacuum applied during the spray-assisted LbL process, the pore-bridging film was able to significantly reduce methanol permeability. Figure 6-13 shows the methanol permeability of the composite membrane after a

certain number of bilayers have been sprayed onto an electrospun mat without vacuum. With as little as 100 BLs (2 μm) on an 80 μm thick electrospun mat, a fully bridged film is formed and the overall methanol permeability is already lower than that of Nafion. As the number of bilayers deposited increases, a thicker LbL capping film is sprayed and the overall methanol permeability decreases. Thus, with the spray LbL fabrication technique, the methanol permeability of the composite membrane may be varied independently of the mechanical properties and proton conductivity.

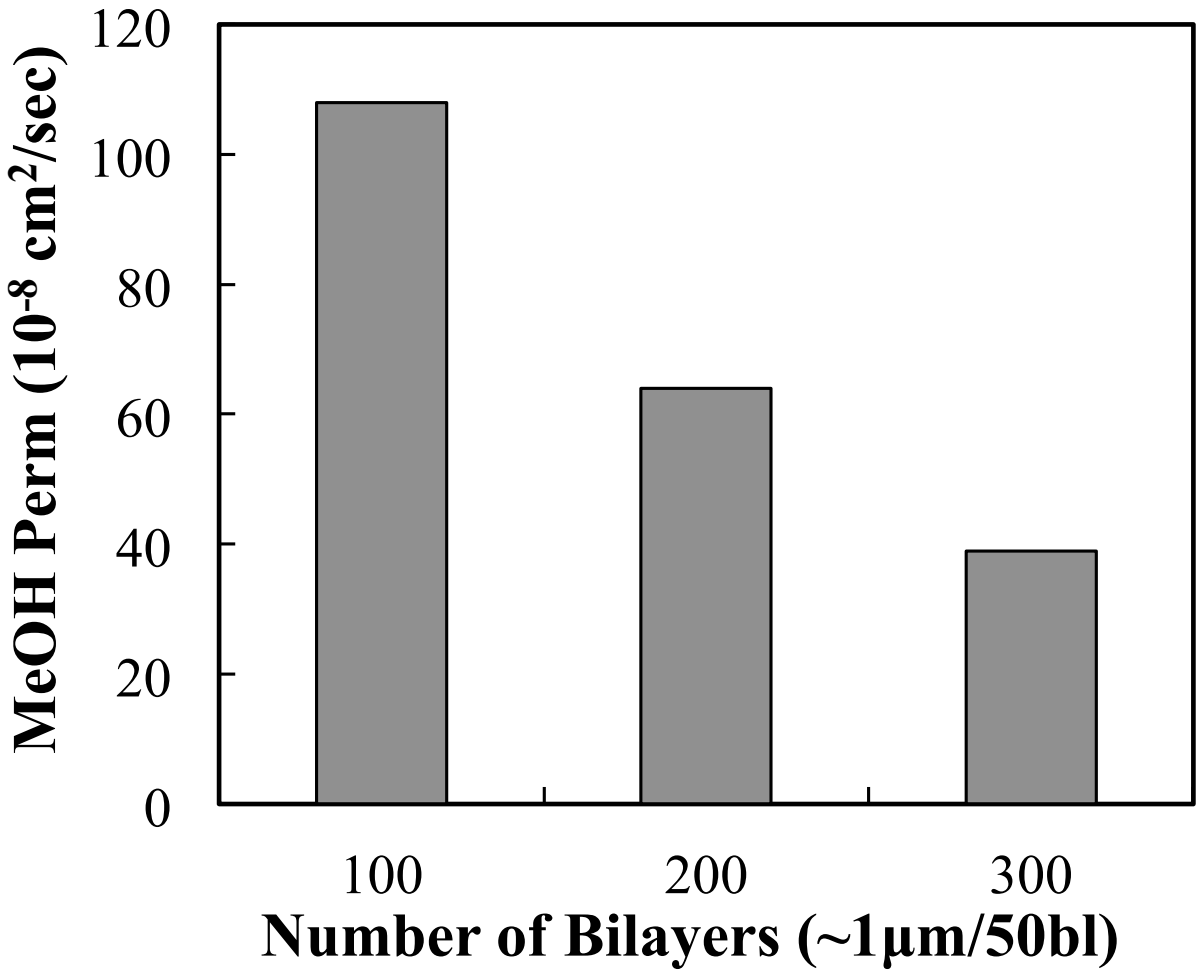

Figure 6-13. Methanol permeability of the composite membrane as a function of LbL film thickness for spray-coated electrospun mats. The spray conditions for the PDAC/sPPO films were pH = 2.0, 1.0 M NaCl in all solutions. As more bilayers are applied, the overall methanol permeability decreases.

To verify that the decrease in methanol permeability comes from the PDAC/sPPO pore-bridging top film on the electrospun mat and not from the bulk membrane, we compared the

methanol permeability of the composite membranes with that of PDAC/sPPO supported on track-etched nucleopore membranes, as published previously [21]. Table 6-2 lists the overall as well as the normalized MeOH permeability measured for the composite membranes with different numbers of bilayers. The overall permeability is the measured rate of methanol crossover multiplied by the total thickness of the composite membrane (LbL film and the electrospun mat). The normalized permeability is defined as the permeability based solely on the thickness of the blocking LbL coating, ignoring the electrospun mat base. The thickness of the LbL coating on the fibers is estimated from the film growth curve as determined on a planar glass substrate and confirmed by cross sectional SEM. As seen in Table 6-2, the overall permeability of the composite membrane drops with increasing number of bilayers; however, the adjusted permeability remains the same indicating that the inherent transport properties of the LbL film does not change with the number of bilayers. These numbers are similar to what was previously published on pure PDAC/sPPO films alone [21]. This proves that the primary blocking component for methanol crossover is a linearly growing PDAC/sPPO film on top of the electrospun mat.

Table 6-2. Methanol Permeability of Composite Membranes with Varying Number of Spray-Assisted Capping Bilayers of PDAC/sPPO.

# of Bilayers	**Overall Permeability**[a] **(10^{-8} cm^2/sec)**	**Thickness of LbL film (μm)**	**Normalized Permeability**[b] **(10^{-8} cm^2/sec)**
100[c]	108	2.0	2.7
200[c]	64	4.0	3.2
300[c]	39	6.0	2.9
PDAC/sPPO film [21]	2.18	On Nucleopore	2.18
Nafion	282	N/A	282

[a] Defined as methanol flux multiplied by the total thickness of the membrane divided by the concentration gradient.

[b] Defined as methanol flux multiplied by thickness of blocking layer (LbL or Nafion) divided by the concentration gradient.

[c] Spray conditions: pH=2, 1.0 M NaCl in all solutions without vacuum on a 75 μm thick electrospun mat.

While the high through-plane proton conductivity of the composite PEM provides an indication of the membrane's ability to sustain high currents in a fuel cell, the methanol permeability ultimately determines its potential for DMFC applications. Lower crossover limits fuel loss and permits the use of a higher methanol feed concentration, leading to a higher overall cell voltage, power density, and efficiency. In the context of DMFCs, the "selectivity", defined as the ratio of proton conductivity to methanol permeability, is a useful metric for predicting the performance of a PEM [2]. Protons and methanol have similar molecular transport mechanisms in sulfonic acid-containing PEMs. As a consequence, it is generally difficult to improve membrane selectivity significantly, even with substantial modifications to the membrane's ion content, water content, or polymer chemistry, architecture or morphology [39]. However, because PDAC/sPPO films possess such a low methanol permeability (due to the ionic cross-linking between the anion sPPO and cationic PDAC) and comparable protonic conductivity compared to Nafion, it is possible to significantly decrease methanol crossover of the composite PEM by capping the PEM with additional polyelectrolyte bilayers. The resultant PEM maintains its inherently high through-plane conductivity and exhibits selectivity higher than Nafion. Table 6-3 shows a summary of the proton conductivity, methanol permeability, and calculated selectivity of the composite PA6(3)T+PDAC/sPPO membrane compared with Nafion and other highly selective composite PEMs reported in the literature.

The capped composite PEM was made from a 20 μm thick EF mat that was thermally treated at 130 °C, coated by the vacuum assisted spray LbL method and subsequently capped with 5 μm of PDAC/sPPO on both sides. The resultant PEM had a through-plane conductivity one fourth that of Nafion (7 vs. 26 mS/cm), methanol permeability twenty times lower than that of Nafion (9.7 vs. 198 x 10^{-8} cm^2/s), and selectivity five and a half times greater than that of Nafion (7.2 vs. 1.3 x 10^7 $mS \bullet sec/cm^3$). Even correcting for the thinness of the composite membrane (30 μm) relative to the Nafion membrane (180 μm), the composite PEM's conductance (conductivity / thickness) is actually higher than that of Nafion (by 60%) and its permeance (permeability / thickness) is still lower than that of Nafion (by 3.4 times). The selectivity of the PA6(3)T+PDAC/sPPO composite membrane is higher than many other state-of-the-art membranes (including Nafion), making it a viable alternative PEM for direct methanol fuel cells in terms of electrochemical transport.

Table 6-3. Summary of Transport Properties of Select Composite PEMs.

Membrane	**Through-plane Proton Conductivity* (σ) [mS/cm]**	**MeOH Permeability ($Px10^{-8}$) [cm^2/s]**	**Selectivity ($S=\sigma/Px10^{-8}$) [$mS \cdot sec/cm^3$]**
PA6(3)T+PDAC/sPPO [this work]**	7.0	9.7	0.72
Nafion N112 [2]	26	198	0.13
Sulfonated poly(styrene-b-ethylene-r-butadiene-b-styrene) block copolymer [40]	23	82	0.28
Phosphotungstic acid/poly(vinyl alcohol) composite [41]	6	45.4	0.13
Nafion/poly(vinyl alcohol) blend [42]	20	65	0.31
PVOH/PVP blend [43]	1.4	10	0.14
SPEEK/cyclodextrin [44]	48	76	0.63

*100 % Relative Humidity

** 20 μm PA6(3)T+150BL PDAC/sPPO spray with additional 138 BL dip-coated cap

6.3.5 Direct Methanol Fuel Cell Performance

Despite the apparent potential of the composite PEM, fabrication of a membrane electrode assembly (MEA) from the composite PA6(3)T+PDAC/sPPO membrane proved to be a challenge. This difficulty was traced to incomplete bonding of the PEM to the GDL during MEA assembly. The difficulty in determining optimum hot-pressing conditions for adhesion of the PEM to the catalyst layers was exacerbated by the incompatible thermal expansion and swelling of the composite PEM versus the catalyst. A cross-sectional SEM of a typical MEA is shown in Figure 6-14. Large fibrous sections on the top and bottom of the MEA (A in Figure 6-14) are the carbon fiber sections of the GDL, which allow for efficient gas transport to the catalyst. The light-gray sections contacting the border between the PEM (C in Figure 6-14) and the GDL are the thin catalyst layers (B in Figure 6-14), typically contained within a Nafion binder. The catalyst is well bonded to the PEM in this SEM and does not penetrate deeply into the GDL; there are also no large through-plane fractures or thinning of the PEM due to hot-pressing.

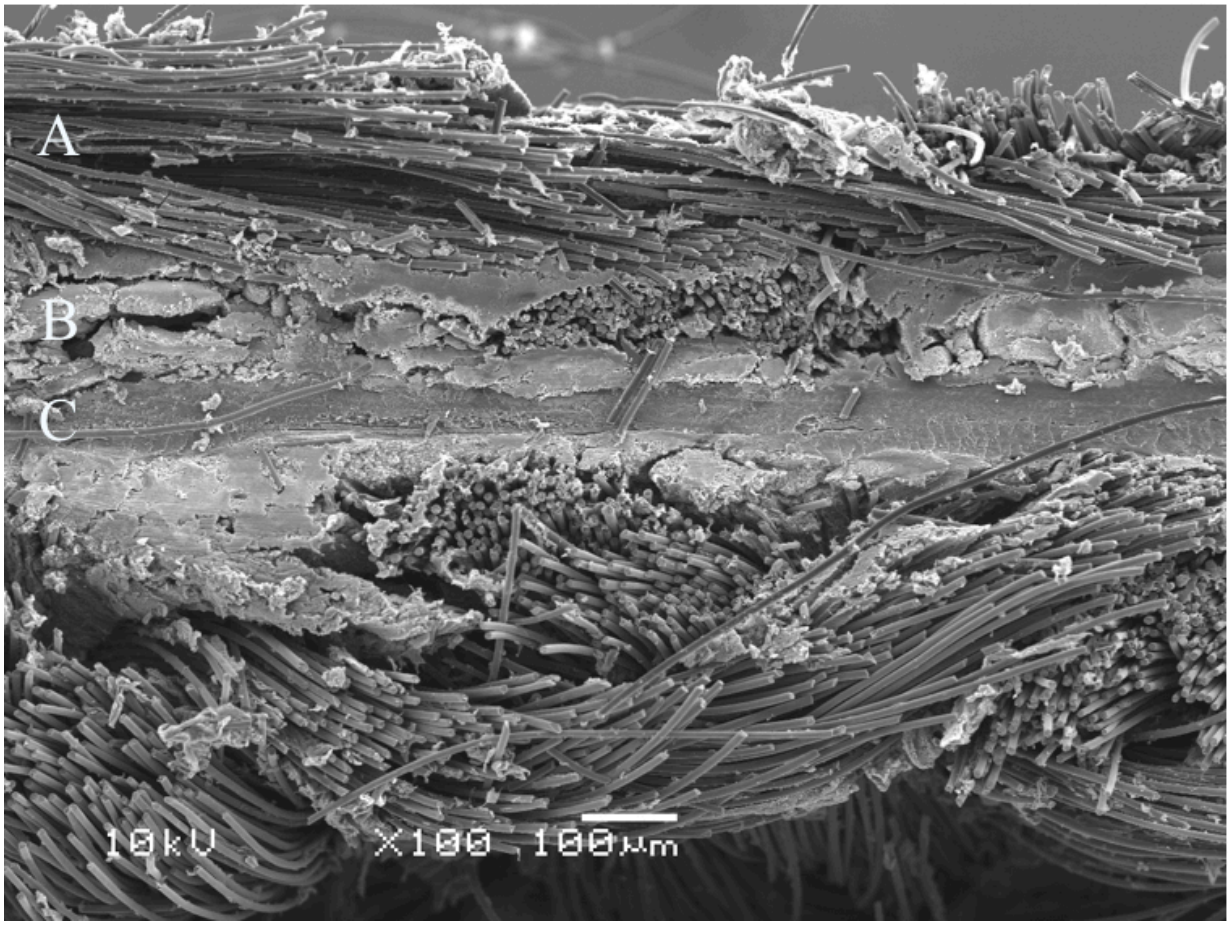

Figure 6-14. Cross-sectional SEM of Membrane Electrode Assembly showing the different components: GDL (A), Catalyst (B), and PEM (C). Scale bar for image is 100 µm.

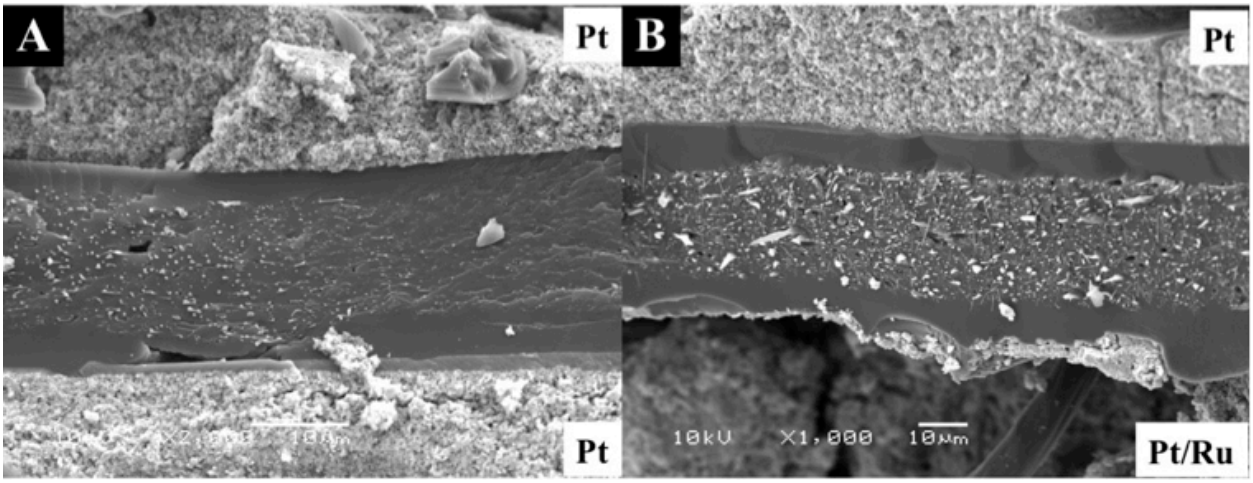

Figure 6-15. Cross-sectional SEM of MEA showing catalyst layer, PEM (with top & bottom capping layers), and Nafion binder. (A) PA 6(3)T+LbL composite PEM sandwiched between two Pt catalyst GDLs exhibiting good adhesion on both sides, (B) PA 6(3)T+LbL sandwiched between a Pt (Cathode) and Pt/Ru (Anode) GDL exhibiting fracture on the anode side leading to poor DMFC performance (scale bar for each micrograph is 10µm).

The Pt catalyst-coated GDL (cathode side) was found to adhere well to the LbL-EF composite PEM after MEA hot-pressing, as shown in Figure 6-15 (a); however, the Pt/Ru catalyst-coated GDL (anode side) was found to delaminate frequently from the PEM, as shown in Figure 6-15 (b), leading to increased cell resistances and greatly reduced catalyst activation as observed previously with other Nafion-free PEMs [45]. Several techniques to remedy this issue were attempted: adjusting the hot-pressing conditions (temperature, time, wet or dry PEM), adding a thin layer of Nafion paint as binder, coating catalyst directly onto the PEM, or even synthesizing a custom batch of Pt/Ru catalyst slurry using PDAC/sPPO as the polymer binder. In each case, the MEA exhibited high cell resistances and/or inhibited/slow catalyst activation, resulting in poor DMFC performance despite the high selectivity of the composite LbL-EF PEM. A summary of the various MEA construction methods is shown in Table 6-4 along with the resultant cell resistances and comments on methanol break-through.

The through-plane resistance of the PA6(3)T+PDAC/sPPO membranes were measured to be 0.4-0.7 Ω from Section 6.3.4, and the added cell resistance for the MEA should be ~0.1-0.2 Ω, yielding an expected total cell resistance of 0.6-0.8 Ω; this expected value is much lower than all of the resistances measured in Table 6-4, varying from 2.66 Ω up to 25 Ω. We hypothesize that the increase in cell resistance occurs as a result of poor contact between the PEM surface and catalyst due to the fact that the catalyst binder is Nafion which does not bond well with the PDAC/sPPO. Despite the unexpectedly high resistances, some useful trends were observed in MEA construction. Hot-pressing was observed in all situations to improve contact and, on average, reduced resistances by half; however, membranes would exhibit fuel cross-over/break-through if they were wet. Wet assembly of the cell (either by depositing the ink on the membrane or by using wet membranes during assembly of the MEA) further improves contact and prevents delamination (upon drying), but the methanol tended to penetrate the capping layer of the membranes. Use of excess Nafion paint helped reduce the fuel crossover of the PEMs, but not completely. The lowest cell resistances were observed when the Pt catalyst was used for both the anode and the cathode GDL, indicating that improved contact can be achieved with a Pt/Pt system; however, there will be a lower Open Circuit Voltage (OCV) due to the inefficient methanol catalysis at the Pt anode. Qualitatively, the composite PEM and Nafion performance can be compared utilizing the sub-optimized Pt/Pt catalyst system until a superior Pt-Ru catalyst slurry can be generated that will bond well the PDAC/sPPO.

Table 6-4. Summary of Membrane Electrode Assembly Fabrication Parameters.

Membrane Condition	Anode Catalyst*	Heat Press	Cell Resistance [Ω]	Comments
Wet	N/A	N/A	0.38	Membrane Resistance
Dry	Pt/Ru (E-TEK)	Yes	25.54	Fuel blocking
Dry flat	Pt/Ru (E-TEK)	No	18.26	Fuel blocking
Dry flat	Pt/Ru (E-TEK)	Yes	10.88	Fuel blocking
Dry flat	Pt/Ru (wet deposit)	No	10.43	MeOH break-through
Dry flat	Pt/Ru (wet deposit)	Yes	5.32	MeOH break-through
Wet	Pt/Ru (E-TEK)	No	7.03	MeOH break-through
Wet	Pt/Ru (custom ink)	No	4.60	MeOH break-through
Wet	Pt/Ru (E-TEK)	Yes	3.06	3x Nafion paint, reduced break-through
Dry flat	Pt (E-TEK)	Yes	2.66	Fuel blocking

*Pt (E-TEK) used for cathode catalyst of all MEA's

An example voltage-current (V-I) polarization curve of a MEA fabricated using the composite PA6(3)T+PDAC/sPPO PEM with Pt/Ru E-Tek catalyst for the anode side exhibiting very high cell resistances (~18 Ω) is shown in Figure 6-16. Note that while the composite PEM successfully blocks methanol transport (as indicated by the high OCV ~530 mV), the cell resistance is so high that no power can be drawn through at currents greater than 1-2 mA. Even after systematically modifying the assembly procedure to optimize the cell resistance with Pt-Ru anode catalyst, fuel cell performance of the composite PEM consistently fell unexpectedly short of Nafion. Improvements to the bonding between the commercial catalyst ink (containing Nafion as binder) and the Nafion-free composite PEM would decrease cell resistance and allow better evaluation of the efficacy of the LbL-EFM proton exchange membranes.

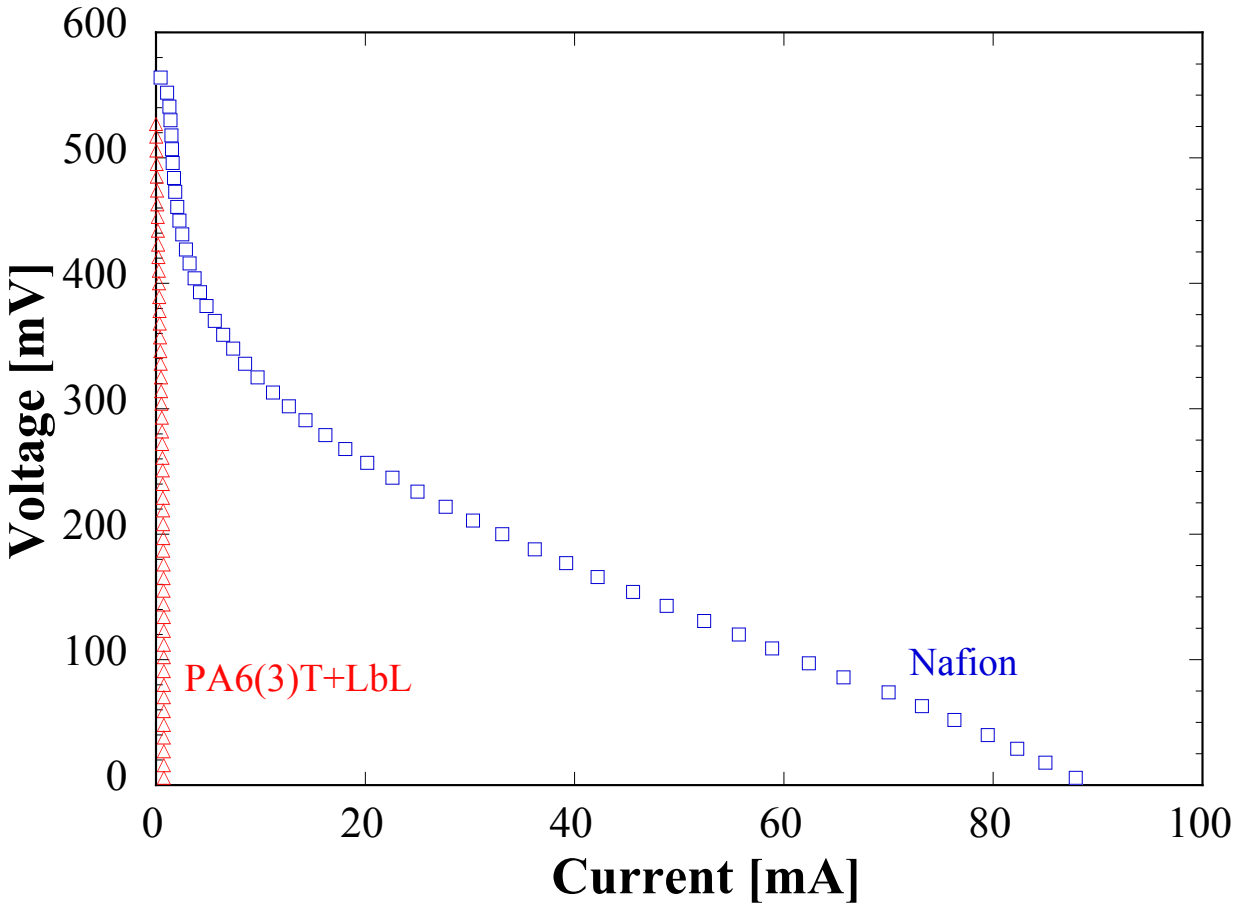

Figure 6-16. V-I polarization curves for Nafion and PA6(3)T+LBL composite membrane using Pt/Ru catalyst in Nafion binder for the anode side and Pt catalyst in Nafion binder for the cathode side. Sweep generated using 10 wt.% methanol/water solution as fuel.

Since the Pt/Ru catalyst could not be successfully integrated into the MEA containing the composite LbL-EF PEM, a sub-optimal system consisting of Pt-catalyst coated GDL sandwiched around both sides of the PEM was used to provide a reliable measure of the DMFC performance. The activation of Pt catalyst in methanol is lower than Pt/Ru, corresponding to a lower OCV; however, the PEM transport should be unaffected. The overall performance of the composite PEM relative to that of Nafion constructed with the same Pt(anode)/Pt(cathode) catalyst assembly provides a useful measure of the improvement in operational DMFC performance. Figure 6-17 shows voltage-current polarization curves as well as power density curves for a 100 µm thick Nafion PEM and the 25 µm thick PA6(3)T+PDAC/sPPO composite PEM in a DMFC using 10 wt.% methanol in water as the fuel. The MEA with composite PEM exhibits a higher

OCV than does the MEA with Nafion (270 mV vs. 257 mV), indicating that methanol is blocked more efficiently by the composite PEM. The MEA with composite PEM also draws a current of 5.8 mA at 100 mV, comparable to the 9.4 mA at 100 mV for the MEA with Nafion. Even with the Pt catalyst, the total cell resistance was still worse than expected (2.66 Ω vs. ~0.5 Ω), indicating that MEA adhesion was still not optimal. The DMFC performance of the composite PEM could be further improved with the proper catalyst designed for the composite PEM and a cell assembly technique that does not require drying or high pressures to merge the catalyst with the PEM. Additionally, improvements could be achieved with MEA conditioning procedures (temperature optimization and cell pre-loading) as well as using a higher methanol concentration fuel since the composite PEM has lower methanol permeability, the DMFC output will not decrease with increasing fuel density as it does with Nafion.

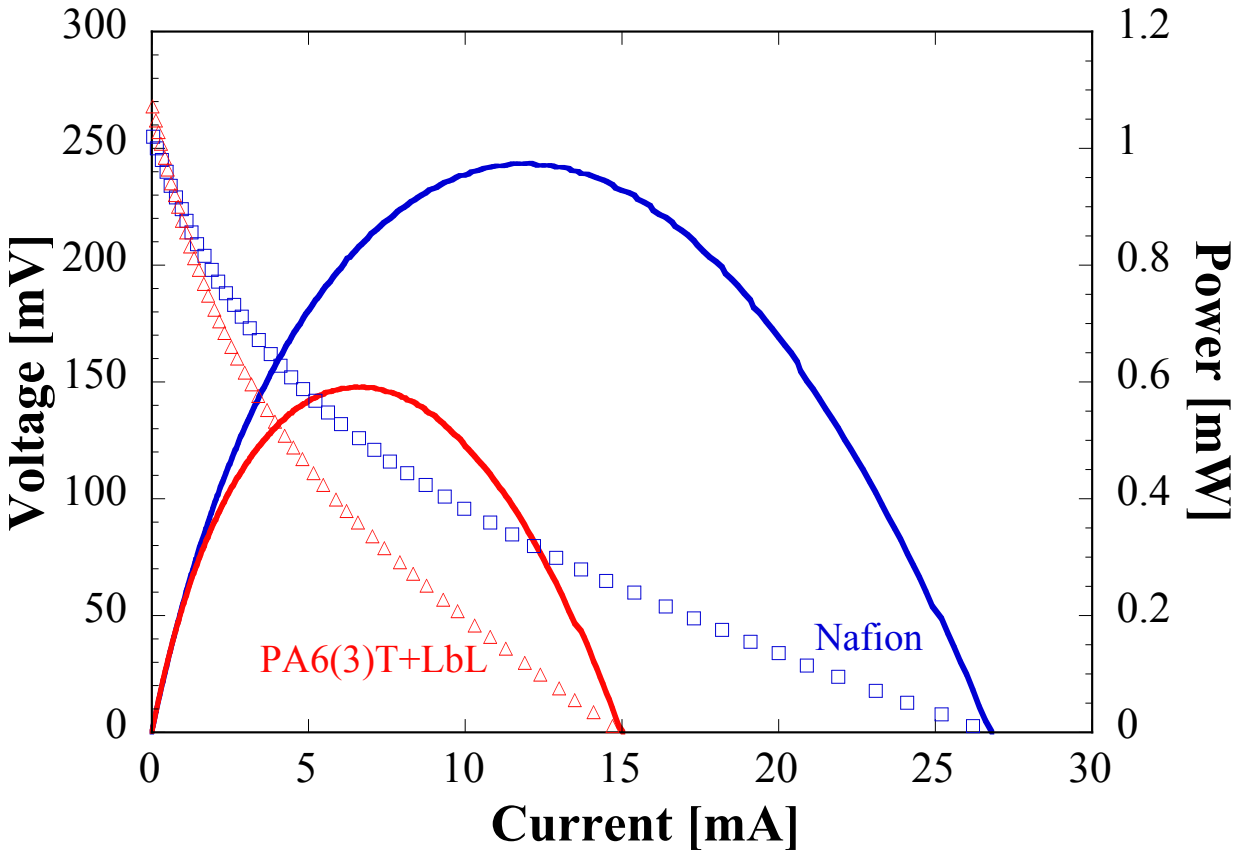

Figure 6-17. V-I polarization curves for Nafion and PA 6(3)T+LbL composite membrane using Pt catalyst for both the anode and cathode GDL in 10 wt.% methanol/water solution as fuel.

6.4 Concluding Remarks

Composite membranes of highly conductive LbL films and electrospun fiber mats were fabricated and characterized for mechanical strength and electrochemical selectivity in this chapter. To create a proton-conducting, fuel-blocking layer and to fill in the void space throughout the porous electrospun matrix, the spray-LbL assembly method (with and without vacuum-assist) was used to form LbL films rapidly. These membranes consist of highly selective poly(diallyl dimethyl ammonium chloride)/sulfonated poly(2,6-dimethyl 1,4-phenylene oxide) (PDAC/sPPO) thin films. The mechanical properties of the spray coated electrospun mats are shown to be superior to the LbL-only system, and can be further improved by thermal annealing of the underlying fiber mat. The composite PEMs exhibited a Young's modulus of 80.2 MPa and a yield stress of 3.39 MPa when the EF mat was annealed at 150 °C, comparable to the mechanical properties of Nafion under the same testing conditions (74.3 MPa Young's modulus and 5.56 MPa yield stress). Modifications to the mechanical response of the composite PEM could be achieved independently of the LbL fabrication process by thermal treatment of the underlying EF mat, allowing for precise control of membrane properties. The composite PEMs also swell less than Nafion under hydration cycling; the greater dimensional stability also means lower mechanical hysteresis and less strain into the plastic deformation regime, which promises longer operational lifetimes. The composite PEMs exhibited similar in-plane proton conductivities to the free-standing LbL films and the methanol permeability was controlled by the thickness of the capping layer. The composite PEMs also exhibited through-plane proton conductivities as high as 7.0 mS/cm at 100 %RH and a corresponding methanol permeability of 9.7×10^{-8} cm^2/sec, indicating a membrane selectivity of 7.2×10^7 $mS \bullet sec/cm^3$; this is over five times greater than the selectivity of Nafion ($S=1.3 \times 10^7$ $mS \bullet sec/cm^3$). Despite the superior transport properties of the composite PEM, high cell resistances were observed when the membranes were tested in an operational direct methanol fuel cell utilizing standard Pt/Ru and Pt catalysts for the anode and cathode, respectively. Further DMFC testing showed the potential for higher OCVs (270 mV vs. 257 mV) and comparable cell resistances to membrane electrode assemblies containing Nafion for the PEM when using Pt/Pt catalyst for both the anode and the cathode. An optimized catalyst system for the novel composite proton exchange membranes would be required to realize the improved fuel cell performance over Nafion.

6.5 Acknowledgments

Funding for this portion of the thesis was provided by the Masdar Institute, the U.S. Army through the Institute for Soldier Nanotechnologies (ISN) under AROW911NF-07-D-0004 and Samsung Advanced Institute of Technology. The author would like to thank Jonathon Harding for assistance preparing catalyst inks, Prof. Mary C. Boyce for useful discussions, and the MIT Institute of Soldier Nanotechnology for use of facilities.

6.6 References

[1] F. De Brujin, The current status of fuel cell technology for mobile and stationary applications, Green Chemistry 7 (2005) 132-150.

[2] N.W. Deluca, Y.A. Elabd, Polymer electrolyte membranes for the direct methanol fuel cell: A review, Journal of Polymer Science Part B-Polymer Physics 44 (2006) 2201-2205.

[3] M. Ulbricht, Advanced functional polymer membranes, Polymer 47 (2006) 2217-2262.

[4] S.G. Chalk, J.F. Miller, Key challenges and recent progress in batteries, fuel cells, and hydrogen storage for clean energy systems, Journal of Power Sources 159 (2006) 73-80.

[5] K.A. Mauritz, R.B. Moore, State of understanding of Nafion, Chemical Reviews 104 (2004) 4535-4585.

[6] C. Chen, G. Levitin, D.W. Hess, T.F. Fuller, XPS investigation of Nafion membrane degradation, Journal of Power Sources 169 (2007) 288-295.

[7] Y.-H. Lai, C.K. Mittelsteadt, C.S. Gittleman, D.A. Dillard, Viscoelastic stress analysis of constrained proton exchange membranes under humidity cycling, Journal of Fuel Cell Science and Technology 6 (2009) 021002.

[8] S.M. MacKinnon, T.J. Fuller, F.D. Coms, M.R. Schoenweiss, C.S. Gittleman, Y.-H. Lai, R. Jiang, A.M. Brenner, Proton exchange membrane fuel cells – membranes: design and characterization Encyclopedia of Electrochemical Power Sources (2009) 741-754.

[9] M.N. Silberstein, P.V. Pillai, M.C. Boyce, Biaxial elastic-viscoplastic behavior of Nafion membranes, Polymer, 52 (2011) 529-539.

[10] M.N. Silberstein, M.C. Boyce, Hygro-thermal mechanical behavior of Nafion during constrained swelling, Journal of Power Sources, 196 (2011) 3452-3460.

[11] F.Q. Liu, B.L. Yi, D.M. Xing, J.R. Yu, H.M. Zhang, Nafion/PTFE composite membranes for fuel cell applications, Journal of Membrane Science 212 (2003) 213-223.

[12] K.M. Nouel, P.S. Fedkiw, Nafion-based composite polymer electrolyte membranes, Electrochimica Acta 43 (1998) 2381-2387.

[13] E. Chalkova, M.V. Fedkin, D.J. Wesolowski, S.N. Lvov, Effect of TiO2 surface properties on performance of Nafion-based composite membranes in high temperature and low relative humidity PEM fuel cells, Journal of the Electrochemical Society 152 (2005) A1742-A1747.

[14] C. Yang, P. Costamagna, S. Srinivasan, J. Benziger, A.B. Bocarsly, Approaches and technical challenges to high temperature operation of proton exchange membrane fuel cells, Journal of Power Sources 103 (2001) 1-9.

[15] Y.-H. Liu, B. Yi, Z.-G. Shao, D. Xing, H. Zhang, Carbon nanotubes reinforced Nafion composite membrane for fuel cell applications, Electrochemical and Solid-State Letters 9 (2006) A356-A359.

[16] H. Cai, K. Shao, S. Zhong, G. Zhao, G. Zhang, X. Li, H. Na, Properties of composite membranes based on sulfonated poly(ether ether ketone)'s (SPEEK)/phenoxy resin (PHR) for direct methanol fuel cell usages, Journal of Membrane Science 297 (2007) 162-173.

[17] Y.-W. Chang, E. Wang, G. Shin, J.-E. Han, P.T. Mather, Poly(vinyl alcohol) (PVA)/sulfonated polyhedral oligosilsesquioxane (sPOSS) hybrid membranes for direct methanol fuel cell applications, Polymers for Advanced Technologies 19 (2007) 535-543.

[18] P. Piboonsatsanasakul, J. Wootthikanokkhan, S. Thanawan, Preparation and characterizations of direct methanol fuel cell membrane from sulfonated polystyrene/poly(vinylidene fluoride) blend compatibilized with poly(styrene)-b-poly(methyl methacrytlate) block copolymer, Journal of Applied Polymer Science 107 (2008) 1325-1336.

[19] S.-H. Yun, J.-J. Woo, S.-J. Seo, L. Wu, D. Wu, T. Xu, S.-H. Moon, Sulfonated poly(2,6-dimethyl-1,4-phenylene oxide) (SPPO) electrolyte membranes reinforced by electrospun nanofiber porous substrates for fuel cells, Journal of Membrane Science 367 (2011) 296-305.

[20] T.R. Farhat, P.T. Hammond, Designing a new generation of proton-exchange membranes using layer-by-layer deposition of polyelectrolytes, Advanced Functional Materials 15 (2005) 945-954.

[21] A.A. Argun, J.N. Ashcraft, P.T. Hammond, Highly conductive, methanol resistant polyelectrolyte multilayers, Advanced Materials 20 (2008) 1539-1543.

[22] D.S. Liu, J.N. Ashcraft, M.M. Mannarino, M.N. Silberstein, A.A. Argun, G.C. Rutledge, M.C. Boyce, P.T. Hammond, Spray Layer-by-Layer Electrospun Composite Proton Exchange Membranes, Advanced Functional Materials (2013) [In Press].

[23] G. Decher, Fuzzy nanoassemblies: toward layered polymeric multicomposites, Science 277 (1997) 1232-1237.

[24] P.T. Hammond, Form and function in multilayer assembly: New applications at the nanoscale, Advanced Materials 16 (2004) 1271-1293.

[25] J.N. Ashcraft, A.A. Argun, P.T. Hammond, Structure-property studies of highly conductive layer-by-layer assembled membranes for fuel cell PEM applications, Journal of Materials Chemistry 20 (2010) 6250-6257.

[26] J. Doshi, D.H. Reneker, Electrospinning process and applications of electrospun fibers, Journal of Electrostatics 35 (1995) 151-160.

[27] G.C. Rutledge, S.V. Fridrikh, Formation of fibers be electrospinning, Advanced Drug Delivery Reviews 59 (2007) 1384-1391.

[28] S.V. Fridrikh, J.H. Yu, M.P. Brenner, G.C. Rutledge, Controlling the fiber diameter during electrospinning, Physical Review Letters 90 (2003) 144502.

[29] M.M. Mannarino, G.C. Rutledge, Mechanical and tribological properties of electrospun PA 6(3)T fiber mats, Polymer 53 (2012) 3017-3025.

[30] K.C. Krogman, J.L. Lowery, N.S. Zacharia, G.C. Rutledge, P.T. Hammond, Spraying asymmetry into functional membranes layer-by-layer, Nature Materials 8 (2009) 512-518.

[31] W. He, Z.W. Ma, T. Yong, W.E. Teo, S. Ramakrishna, Fabrication of collagen-coated biodegradable polymer nanofiber mesh and its potential for endothelial cells growth, Biomaterials 26 (2005) 7606-7615.

[32] X. Zhu, W. Cui, X. Li, Y. Jin, Electrospun fibrous mats with high porosity as potential scaffolds for skin tissue engineering, Biomacromolecules 9 (2008) 1795-1801.

[33] D. Guyomard, J.M. Tarascon, Li metal−free rechargeable $LiMn_2O_4$/Carbon cells: their understanding and optimization, Journal of the Electrochemical Society 139 (1992) 937-948.

[34] B.S. Pivovar, Y. Wang, E.L. Cussler, Pervaporation membranes in direct methanol fuel cells, Journal of Membrane Science 154 (1999) 155-162.

[35] C.-L. Pai, M.C. Boyce, G.C. Rutledge, On the importance of fiber curvature to the elastic moduli of electrospun nonwoven fiber meshes, Polymer 52 (2011) 6126-6133.

[36] M.N. Silberstein, C.-L. Pai, G.C. Rutledge, M.C. Boyce, Elastic-plastic behavior of non-woven fibrous mats, Journal of the Mechanics and Physics of Solids 60 (2012) 295-318.

[37] M.N. Silberstein, M.C. Boyce, Constitutive modeling of the rate, temperature, and hydration dependent deformation response of Nafion to monotonic and cyclic loading, Journal of Power Sources 195 (2010) 5692-5706.

[38] R. Borup, J. Meyers, B. Pivovar, Y.S. Kim, R. Mukundan, N. Garland, D. Myers, M. Wilson, F. Garzon, D. Wood, P. Zelenay, K. More, K. Stroh, T. Zawodzinski, J. Boncella, J. E. McGrath, M. Inaba, K. Miyatake, M. Hori, K. Ota, Z. Ogumi, S. Miyata, A. Nishikata, Z. Siroma, Y. Uchimoto, K. Yasuda, K. I. Kimijima, N. Iwashita, Scientific aspects of polymer electrolyte fuel cell durability and degradation, Chemical Reviews 107 (2007) 3904-3951.

[39] Y.A. Elabd, E. Napadensky, C.W. Walker, K.I. Winey, Transport properties of sulfonated poly(styrene-b-isobutylene-b-styrene) triblock copolymers at high ion-exchange capacities, Macromolecules 39 (2006) 399-407.

[40] B. Kim, J. Kim, B. Jung, Morphology and transport properties of protons and methanol through partially sulfonated block copolymers, Journal of Membrane Science 250 (2005) 175-182.

[41] L. Li, L. Xu, Y. Wang, Novel proton conducting composite membranes for direct methanol fuel cell, Materials Letters 57 (2003) 1406-1410.

[42] N. Deluca, Y Elabd, Direct methanol fuel cell performance of Nafion/poly(vinyl alcohol) blend membranes, Journal of Power Sources 163 (2006) 386-391.

[43] Y.F. Huang, L.C. Chuang, A.M. Kannan, C.W. Lin, Proton-conducting membranes with high selectivity from cross-linked poly(vinyl alcohol) and poly(vinyl pyrrolidone) for direct methanol fuel cell applications, Journal of Power Sources 186 (2009) 22-28.

[44] T. Yang, C. Liu, SPEEK/sulfonated cyclodextrin blend membranes for direct methanol fuel cell, International Journal of Hydrogen Energy 36 (2011) 5666-5674.

[45] H.-Y. Jung, K.-Y. Cho, K.A. Sung, W.-K. Kim, J.-K. Park, The effect of sulfonated poly(ether ether ketone) as an electrode binder for direct methanol fuel cell (DMFC), Journal of Power Sources 163 (2006) 56-59.

7. Conclusions and Future Work

7.1 Research Conclusions

7.1.1 Controlling of Terminal Fiber Diameter in Electrospinning

The first objective of this thesis was to elucidate the relationship between electrospun fiber morphology and the fabrication process; more specifically, how to manipulate terminal fiber diameter based on the solution properties and processing parameters. The scaling model presented in Chapter 2 predicted a reduced terminal jet radius during electrospinning by combining previous work of balancing surface charge repulsion with surface tension and incorporating visco-elastic-capillary thinning by empirical evidence of measured fiber-size correlation with solution viscoelasticity. Previously, the prediction of fiber size and morphology of electrospun nanofibers based on solution properties and operating parameters alone was difficult to evaluate accurately as changes in a single fluid or processing parameter can affect the jet and/or fiber formation through several mechanisms; however, a reliable universal scaling law would be of high utility for process control and materials design in the nanofiber industry. The final result for the scaling law determined in Chapter 2 was $h_t=C'[De/Oh]^{1/2}[\gamma\varepsilon Q/E^2K]^{1/3}$, where C' is a constant, De is the Deborah number of the system, Oh is the Ohnesorge number of the system, γ is the surface tension, ε is the permittivity, Q is the flow rate, E is the electric field, and K is the solution conductivity. The novel scaling relationship was found to correlate well with the terminal jet diameter of electrospun fibers based on measurable solution properties and processing parameters not accounted for in previous scaling laws. The scaling presented in this thesis accurately predicted terminal jet diameter for over two orders of magnitude and is applicable for aqueous, organic, and acidic solutions over a wide range of concentrations, conductivities, viscosities, surface tensions, and relaxation times.

7.1.2 Mechanical and Tribological Properties of Electrospun Fiber Mats

The second objective for this thesis was to investigate the mechanical and tribological properties of electrospun fiber mats and to determine methods of improving their durability. Quantification of tribological properties and development of an accurate wear mechanism for

amorphous and semi-crystalline nonwoven polymeric fiber mats had not been previously reported before the work contained in this thesis. The tribological and mechanical responses of thermally treated electrospun PA 6(3)T nanofiber mats were investigated in Chapter 3. The Young's moduli and yield stresses of the nonwoven mats were found to improve dramatically with an increase in the temperature of heat-treatment at or above the glass transition temperature, at the expense of mat porosity. The Young's modulus increased significantly from 40 MPa for the untreated PA 6(3)T nanofiber mat, to 82 MPa and 117 MPa after 130 °C and 150 °C heat-treatment, respectively, without suffering a significant loss of porosity; the modulus could be increased further to >400 MPa after 170 °C heat-treatment, but at a substantial loss to the mat porosity (88% to 63%). The annealed nanofiber mats also exhibited less mechanical hysteresis under low-strain deformations than the as-spun mat, indicating that the heat-treated mats can recover more readily and have significantly improved fatigue resistance. In addition to gains in mechanical integrity, there was also an improvement in the wear resistance of the nanofiber mats with thermal treatment. Annealing at 150°C results in an order of magnitude decrease in the effective wear rate relative to that of the as-spun mats, from 2.14 x 10^{-5} g/cm to 3.66 x 10^{-6} g/cm at 1.0 N applied load, while the porosity decreases only modestly, from 88% to 82%. The effective wear rate of nanofiber mats was well-described by a modified Ratner-Lancaster relationship for wear rate of polymeric materials, $W \sim (\rho \mu L)/(\sigma_y \varepsilon_y)$, suggesting that the mechanism of wear is primarily due to the breakage of fibers that is also responsible for yield in these nonwoven mats. Post-spin treatments such as thermal annealing close to the relevant thermal transition temperature (e.g. the glass transition) served to weld the fibers and form additional inter-fiber junctions, significantly improving the mechanical and tribological properties of the electrospun mats and greatly improving their utility and service lifetime.

The tribological and mechanical response of thermally annealed semi-crystalline electrospun PA 6,6 fiber mats were investigated in Chapter 4. The crystallinity of the fiber mats was observed to exhibit small changes as a function of the annealing temperature, with more pronounced increases to the percent crystallinity, according to WAXD, when samples were treated above the Brill transition, T_B. Significant changes to the crystal morphology and orientation were observed within the PA 6,6 fibers as molecular alignment changed from parallel to the fiber axis to perpendicular for samples treated above T_B. The change in molecular orientation is most likely due to the initial strain alignment when forming the crystallites as a

result of the jet stretching during the electrospinning process. During the thermal annealing process above T_B, the molecular orientation relaxes as the chains become more mobile. The Young's modulus, yield stress, and toughness of the nonwoven mats were found to change with an increase in the annealing temperature through the glass transition, Brill transition, and crystalline melting points, at the expense of mat porosity. The yield stress increased modestly from 2.9 MPa for the untreated PA 6,6 nanofiber mat, to 4.5 MPa for the 170 °C heat-treatment, without suffering a significant loss of porosity. The yield stress could then be increased further up to 7.1 MPa after 270 °C heat-treatment (above the T_m), at a substantial loss to the mat porosity (90% to 72%). In addition to gains in mechanical integrity, there was also an improvement in the wear resistance of the semi-crystalline electrospun fiber mats with thermal treatment. Annealing at 240 °C results in a significant decrease in the effective wear rate relative to that of the as-spun mats, from 8.10 x 10^{-6} g/cm to 3.01 x 10^{-6} g/cm at 0.5 N applied load, while the porosity decreases only modestly, from 90% to 86%. The mechanical and tribological properties of the thermally annealed PA 6,6 fiber mats were found to exhibit significant improvements through the Brill transition temperature, comparable to the improvements observed when annealing amorphous PA 6(3)T electrospun mats near the glass transition temperature. The effective wear rate of the electrospun PA 6,6 fiber mats was well-described by the modified Ratner-Lancaster relationship for wear rate of electrospun fiber mats, $W \sim (\rho \mu L)/(\sigma_y \varepsilon_y)$, for samples annealed below the T_m, suggesting that the mechanism of wear is primarily due to the breakage of fibers that contributes to yield in these nonwoven mats. Only the sample annealed at 270 °C exhibits a wear rate that deviated significantly from the proposed scaling. The deviation from the modified Ratner-Lancaster correlation is most likely due to the changes observed in the crystal orientation and morphology; these changes could affect the individual fiber properties such as the fracture mode and breaking strain of the individual fibers, resulting in a lower mechanical energy required to remove material from the surface. The mechanical and tribological properties of electrospun fiber mats are found to be inter-related, and the effects of crystallinity and crystal morphology within semi-crystalline polymeric fiber mats are significant with respect to the wear resistance.

7.1.3 Composite Layer-by-Layer/Electrospun Proton Exchange Membranes

The final objective of this thesis was to incorporate the knowledge learned in the first two objectives to utilize finely controlled, robust electrospun fiber mats as a structural scaffold for

layer-by-layer deposition of polyelectrolytes to produce composite proton exchange membranes for fuel cell applications. Part of this objective included an exploration of the fabrication process for these novel composite LbL-electrospun fiber proton exchange membranes and evaluation of how the transport and mechanical properties of the composite PEM compared with a free-standing LbL polyelectrolyte film and the industry standard, Nafion. Electrochemical selectivity, dimensional stability, and mechanical properties of the composite PEM were manipulated and ooptimized in order to compare the performance of the composite membrane against Nafion in an operational direct methanol fuel cell.

Composite polymeric membranes of highly conductive layer-by-layer assembled films on electrospun fiber mats were fabricated and characterized for mechanical strength and selectivity in Chapter 5. These membranes consisted of highly conductive, methanol impermeable poly(diallyl dimethyl ammonium chloride)/sulfonated poly(2,6-dimethyl 1,4-phenylene oxide) (PDAC/sPPO) layer-by-layer deposited thin films. Free-standing PDAC/sPPO LbL-assembled films were found to have elastic moduli of up to 1100 MPa and a maximum yield stress of 40 MPa when tested at ambient conditions. The PDAC/sPPO films assembled with higher concentrations of salt in the assembly baths exhibited improved mechanical properties due to the more favorable cross-linked network that was formed. The mechanical properties of PDAC/sPPO free-standing films were on par with commercial proton exchange membranes such as Nafion at moderate to low relative humidity conditions; however, the PDAC/sPPO films were found to break at extremely low strains (~ 0.07 mm/mm) and became gel-like with low elastic moduli and yield stresses when fully hydrated. The mechanical response of the highly conducting PDAC/sPPO LbL-assembled films were improved by depositing the LbL matrix onto a highly controllable and robust electrospun fiber scaffold by the dip-LbL assembly method. Coating of Polycaprolactone (PCL) and PA 6(3)T electrospun fiber mats with PDAC/sPPO using the LbL dipping process produced composite membranes with interesting webbed morphologies that spanned adjacent fibers, but did not fully clog the pore space to prevent methanol permeation. The in-plane ionic conductivity of the composite membrane was found to be similar to the pristine LbL system beyond a critical number of bilayers.

To fill in more of the void space throughout the electrospun fiber matrix and thus create a fuel-blocking layer, the spray-LbL assembly method was utilized as a means for the rapid formation of LbL films. When the spray-LbL technique was used along with an applied pressure

gradient across the electrospun mat during assembly, the resulting LbL/electrospun mat composites were found to have conformal coatings on the individual fibers throughout the bulk of the mat. When the spray-LbL technique was used without vacuum, the resulting LbL film bridged across the pores of the electrospun mat, forming a continuous fuel-blocking layer with properties similar to the free-standing LbL. The mechanical properties of the spray coated electrospun mats were shown to be superior to the LbL-only system, particularly at hydrated conditions. These results illustrated the versatility of the spray-LbL system to successfully fabricate composite membranes with finely tuned morphology and properties.

The composite proton exchanges membranes were further optimized and tested for performance in an operational direct methanol fuel cell in Chapter 6. In addition to possessing improved mechanical properties under hydrated conditions, the composite PEMs were also found to possess reduced hydration swelling relative to Nafion when cycled between dry and fully hydrated states. This greater dimensional stability corresponded to lower mechanical hysteresis under hydration cycling and less chance of pinhole formation and membrane fracture, which promises longer operational lifetimes. The composite PEMs exhibited similar in-plane proton conductivities to the free-standing LbL-assembled films and the methanol permeability was controlled by the thickness of the capping layer. The composite PEMs also exhibited through-plane proton conductivities as high as 7.0 mS/cm at 100 %RH and a corresponding methanol permeability of 9.7×10^{-8} cm^2/sec, indicating a membrane selectivity of 7.2×10^7 $mS \bullet sec/cm^3$, a substantial improvement over the electrochemical selectivity of Nafion ($S=1.3 \times 10^7$ $mS \bullet sec/cm^3$). Despite the superior transport properties of the composite PEM, high cell resistances were observed when the membranes were tested in an operational direct methanol fuel cell when using standard Pt/Ru and Pt catalyst systems for the anode and cathode, respectively. Further DMFC testing showed the potential for higher OCVs (270 mV vs. 257 mV) and comparable cell resistances to membrane electrode assemblies containing Nafion for the PEM when using commercial Pt catalyst for both the anode and the cathode. These results confirmed the successful fabrication of a robust, highly selective composite proton exchange membrane that could be used in DMFCs; however, due to the catalyst bonding issues encountered, an optimized catalyst system for the novel composite proton exchange membranes would be required to achieve the improved performance over Nafion.

7.2 Recommendations for Future Work

7.2.1 Controlling of Terminal Fiber Diameter in Electrospinning

The novel scaling relationship determined in Chapter 2 was found to be an accurate correlation of the terminal jet diameter of electrospun fibers with measurable solution properties and processing parameters. To help confirm the validity of the proposed scaling law, additional experiments should be conducted with a wider range of polymers, solvents, and processing parameters. A lack of useable data from the literature to fit the proposed model was a significant drawback due to the fact that most researchers do not report the same solution and processing parameters. One important fluid parameter that was not commonly reported is the solution relaxation time obtained from extensional rheometry (CaBER), which was found to have a significant effect on the terminal fiber diameter in this work. If more data could be collected on electrospun fiber diameters with all of the required solution and processing parameters recorded, then it would become easier to determine the proper scaling. It was also found that there might be limits to the range of utility for the proposed scaling law. This is because the proposed correlation was based on a balance of charge repulsion, surface tension, and visco-elastic forces; if the regime of the electrospinning process becomes dominated by one or more of these driving forces, then the proposed scaling law may break-down. Further experiments to determine the parametric limits of the proposed scaling would prove to be useful for the fiber spinning industry to determine the terminal diameter fabrication capabilities. A more advanced theoretical fluids model could also help to explain the complex jet thinning mechanism during electrospinning. Understanding of the process is further complicated by the fact that viscoelastic fluid properties are changing as a function of time due to solvent evaporation and electrically induced strain hardening; therefore, incorporating such time-dependent parameters into a theoretical model could better elucidate the terminal diameter scaling.

7.2.2 Mechanical and Tribological Properties of Electrospun Fiber Mats

The tribological and mechanical properties of thermally annealed amorphous and semi-crystalline polyamide electrospun nanofiber mats were investigated in Chapters 3 and 4. Quantitative evaluation of the tribological properties of electrospun mats had not been published prior to the work reported in this thesis on PA 6(3)T and PA 6,6; the proposed wear model was determined empirically based on their tribological responses to abrasion. There are a number of

recommendations for possible future experiments to further investigate nanofiber mat durability and tribology. The tribology work conducted for this thesis only covered two polymeric nanofibrous materials (PA 6(3)T and PA 6,6), therefore additional experiments could be conducted on other polymeric materials to ensure that the proposed wear rate correlation applies to all nonwoven mats, independent of the polymer used. Furthermore, only one mean fiber diameter was used for each set of experiments in this thesis; therefore, wear testing could be conducted on electrospun mats using a wider range of fiber diameters from tens of nanometers up to several microns to determine if there is any fiber size dependence on the wear response (similar to the work of Pai et al. on the relationship between fiber size and mechanical properties). Numerous testing parameters and geometries were kept fixed for all tests conducted in this work; however, the tribological response of nonwoven mats could change for different testing speeds, contact areas or fiber mat thicknesses. Additionally, only one type of wear (abrasive) was investigated in this work; however, further experiments could be conducted to determine the tribological response of electrospun mats to adhesive, surface fatigue, fretting, or erosive wear by utilizing alternative wear testers to the Taber Abraser. Other important nanofiber mat durability tests could also be investigated in the future, including (but not limited to): laundering, bursting strength, fatigue, resiliency, tear resistance, and chemical swelling. Further quantitative tribological and durability testing of electrospun fiber mats would be invaluable to the development and commercialization of nanofibers.

7.2.3 Composite Layer-by-Layer/Electrospun Proton Exchange Membranes

Composite membranes of highly conductive layer-by-layer films and electrospun fiber mats were fabricated, characterized for mechanical strength and selectivity, and tested in an operational direct methanol fuel cell. Several fabrication techniques were manipulated in order to increase the conductivity of the layer-by-layer polyelectrolyte system (degree of sulfonation, addition of salts to solution baths, control of pH during assembly, dip/spray times and conditions, etc.); however, the protonic conductivity of the sPPO and subsequent LbL-assembled films could potentially be increased further with continued tuning of the synthesis and assembly process. For example, recently it has been shown that utilizing alternative polycations into the PDAC/sPPO assembly to create a tetra-layer system could potentially improve the conductivity by 2-4 fold depending on the degree of hydration. In addition, using different mean fiber diameters for the underlying electrospun mats and optimizing the LbL-assembled capping layer could lead to

further improvements to the electrochemical selectivity. While these PEM improvements would serve to increase the performance modestly, the biggest issue for these composite membranes is the compatibility with current Nafion-binder Pt/Ru catalyst systems. If future work is focused on creating a new catalyst system for DMFCs, which can successfully utilize sPPO (or other non-Nafion based polymers) in the binder, then a completely Nafion-free membrane electrode assembly could be fabricated with the composite PEMs proposed in this thesis. The obvious benefits of a Nafion-free MEA would be reduced swelling and significantly lower methanol permeation, which could result in higher concentration methanol fuel solutions (less added weight to the fuel cell system). Another alternative to developing an entirely new catalyst system for the composite PEMs developed in this work would be to use the current membranes in a hydrogen (H^+) fuel cell. The composite PEMs would need to have their assembly parameters manipulated to operate in the lower humidity range and higher operational temperatures of H^+ fuel cells. The major advantage, however, is that both the anode and cathode side of the MEA in a H^+ fuel cell contain only Pt catalyst in Nafion binder; therefore, no further modification to the catalyst system would be required to accommodate the composite PEM.

And in the end, the love you take
Is equal to the love you make

-Paul McCartney